

University of Strathclyde  
Department of Naval Architecture, Ocean and Marine  
Engineering

**VIV studies in hydrodynamic testing of towed long slender  
cylinders**

Francisco Melchor Castillon Valverde

A thesis presented in fulfilment of the requirements for the  
degree of Doctor of Philosophy

2018

*This thesis is the result of the author's original research. It has been composed by the author and has not been previously submitted for examination which has led to the award of a degree.*

*The copyright of this thesis belongs to the author under the terms of the United Kingdom Copyright Acts as qualified by University of Strathclyde Regulation 3.50. Due acknowledgement must always be made of the use of any material contained in, or derived from, this thesis.*

Signed:

Date:

## **Acknowledgements**

I certainly give my heartfelt thanks to my supervisor, Prof. Nigel Barltrop, for his invaluable support and guidance during my research and experimental work, thank you for making each meeting a stimulating discussion both academic and practical, his career and contributions to the industry have been extremely motivating during my studies and of course a great professional opportunity.

I also want to thank Prof. Shan Huang, who was my first supervisor during the beginning of my studies and with whom we defined the initial planning, receiving his encouragement for technical and field visits that were of great influence and benefit.

It would not have been possible to carry out the experimental scope of my thesis, without the support of Prof. Sandy Day, from whom I received the confidence to count on all necessary resources to investigate the application of new technologies, along with important time assignments of the towing tank in the Kelvin Hydrodynamics Laboratory, where I had the professional and always cordial support of the staff, integrated by Charles Keay, Edward Nixon, Grant Dunning, Bill McGuffie and Bill Wright, for the fabrication of models, equipment, calibration and instrumentation during each experimental set up and towing tests.

Special thanks to Edward Nixon and Mats Kanarbik from Qualisys Motion Capture Systems for making the first innovation of my research work possible with the underwater camera equipment of the optical tracking system and the opportunity to participate in the workshops held in world leading facilities for tank testing in Edinburgh and Norway, I also want to thank to my colleague Saishuai Dai, who along with Edd facilitated advice in the use of equipment and software.

Another technological innovation was possible thanks to the support and collaboration of our colleagues from the Department of Electronic and Electrical Engineering, Dr Gordon M. H. Flockhart and Dr Grzegorz Fusiek, whom I thank for the opportunity to introduce ourselves in the fibre optic sensing technology, as well as their support for facilitate interrogator equipment and their assistance during the installation of fibre optic arrays.

My studies have been possible thanks to the trust of Dr Faustino A. Fuentes Nucamendi, who has been my mentor within my employer and sponsor, Pemex Exploration and Production, of whom I am deeply grateful for his support and advice, as well as to the sponsorship and support of CONACYT, the National Council for Science and Technology in México.

Finally, I want to express that nothing would have been possible without the support of my parents and siblings, my eternal thanks for letting my family know and feel that we would not be alone, as well as the unconditional support of my lovely wife Judith, and my mother Norma, who have always been my greatest motivation to try to excel. To my sons Francisco and Beatriz who have been an example and pride with the sacrifice that involved joining this adventure and who seized the opportunity of their studies in UK successfully.

*In loving memory of Eddy and Ausencia.*

## **Notation and Nomenclature**

### **Roman symbols**

A.- Amplitude; Cross sectional area

A/D.- Non-dimensional amplitude (Amplitude/Diameter)

c.- Wave speed

.- Added mass coefficient

Cd.- Drag coefficient

CF.- Cross Flow

D.- Diameter

d.- Water depth

.- Fatigue damage

.- Design fatigue factor due to VIV

.- Accumulated fatigue damage due to VIV

.- Accumulated fatigue damage

*DFF*.- Design fatigue factor

E.- Young's module

.- Vortex shedding frequency

.- Natural frequency

.- Strouhal frequency

.- Froude number

g.- Standard gravity

H.- Wave height

.- Significant wave height

I.- Second moment of area

ID.- Internal diameter

IL.- In Line

k.- Wave number

KC.- Keulegan-Carpenter number

.- Stability parameter (also known as  $\beta$  .- Response parameter or  $\beta$  .- Scruton number)

L.- Length

m.- Mass per unit length

$m^*$

.- Mass ratio

.- Effective mass per unit length OD.-

Outside diameter

p.- periodic qp.-

quasi-periodic

R.- Scale ratio; Stress ratio

Re.- Reynolds number

S + P.- single plus pair of vortices

S.- Stress range

St.- Strouhal number

T.- Axial tension; Wave period

t.- thickness

.- Design Life

U.- Flow velocity

.- Current flow velocity

.- Non-dimensional current ( $U_c T/D$ )

.- Reduced velocity

.- Maximum wave particle velocity

w.- Wave angular frequency

## **Greek symbols**

$\alpha$  .- Current flow velocity ratio

.- Mode shape factor

.-Logarithmic decrement

$\epsilon$ .- Strain

$\theta$ .- Angle

.- Damping ratio

.- Curvature of mode shape

.- Mass density

$\sigma$ .- Stress

.- Angular frequency

.- Mode shape

## **Abbreviations**

2D.- Two-dimensional

2P.- Two pairs of vortices

2S.- Two single vortices

3D.- Three-dimensional

ADCP.- Acoustic Doppler Current Profiler

ALS.- Accidental Limit State

API.- American Petroleum Institute

BTM.- Buoyant Turret Mooring System

CFD.- Computational Fluid Dynamics

CNH.- Mexican National Hydrocarbons Commission

DNV.- Det Norske Veritas

DVA.- Direct Vertical Access

FBG.- Fibre Bragg Grating

FEA.- Finite Element Analysis

FFT.- Fast Fourier Transform

FMEA.- Failure Mode and Effects Analysis

FOSS.- Fibre Optic Sensing System

FPSO.- Floating Production, Storage and Offloading vessel

FSHR.- Free Standing Hybrid Riser

GOM.- Gulf of Mexico

HAZOP.- Hazard and operability

ISO.- International Organization for Standardization

KHL.- Kelvin Hydrodynamics Laboratory

LVDT.- Linear Variable Differential Transformer

Mbls.- Thousand barrels

MOCAP.- Motion Capture

MMSCFD.- Million standard cubic feet per day

NTP.- Network Time Protocol

PSD.- Power Spectrum Density

QTM.- Qualisys Track Manager

RMS.- Root Mean Square

SCF.- Stress Concentration Factor

SCR.- Steel Catenary Riser

SLS.- Serviceability Limit State

SLWR.- Steel Lazy Wave Riser

SPAR.- A vertical floating platform of cylindrical shape

TLP.- Tension Leg Platform

TTCR.- Top Tension Caisson Riser

ULS.- Ultimate Limit State

UTC.- Coordinated Universal Time

VIV.- Vortex Induced Vibrations

WDM.- Wavelength Division Multiplexing



# Table of Contents

List of Figures .....	vi	List	of	Tables
.....				x Abstract
.....				xii
1 Introduction .....	1			
1.1 Evolution of the offshore infrastructure for oil and gas production .....	1			
1.2 Floating production systems .....	2			
1.3 Riser Systems .....	6			
1.4 VIV effects on marine risers .....	8			
1.5 Tow-out installation methods and an introduction to simulation. ....	9			
2 Literature Review .....	15			
2.1 VIV Main concepts and parameters .....	15			
2.1.1 Amplitude response branches, transitions and associated vortex wake patterns	17			
2.1.2 VIV of long slender cylinders oscillating in CF and IL directions .....	19			
2.1.3 VIV over circular cylinders in yawed flows .....	21			
2.2 Metocean characteristics in Mexican waters of the Gulf of Mexico .....	22			
2.3 Selection of wave parameters for planning of towing tests within the scope of this research .....	30			
2.4 Relevant design codes for tow-out installation methods .....	32			

2.4.1	American Petroleum Institute .....	32
2.4.2	DNV Offshore codes .....	33
2.4.3	International Organization for Standardization .....	38
2.5	Lessons learned during design, fabrication and installation of deep water riser towers	38
2.6	Considerations to influence research and experimental work .....	39
3	Qualification of a motion capture system to study transversal vibrations/oscillations	41
3.1	Introduction .....	41
3.2	Model Analysis .....	42
3.3	Experimental Procedures .....	43
3.4	Beams properties .....	44
3.5	Test setup .....	45
3.6	Motion capture system setup .....	48
3.7	Response Prediction .....	48
3.8	Fatigue considerations for safety of the tests .....	50
3.9	Experimental Results.....	54
3.9.1	Pluck Tests .....	55
3.9.2	Dynamic Response Comparisons .....	59
3.9.3	Amplitude variations in the scotch yoke mechanism .....	66

3.9.4	Updated response comparison .....	68
3.9.5	Video capture with 3D data overlay .....	70
3.9.6	Approach to an Error Analysis through measures of reference .....	71
3.9.7	Conclusions .....	76
4	Application of underwater cameras of a motion capture system to VIV studies of slender cylindrical elements .....	77
4.1	Introduction .....	77
4.2	Model Analysis .....	78
4.2.1	Free vibration beam analysis .....	78
4.2.2	Rayleigh's method .....	79
4.2.3	Fundamental mode in vacuum (without plug or flange): .....	79
4.2.4	Fundamental mode (fully submerged in still water):.....	82
4.2.5	Estimation of the natural frequency in partially submerged conditions using Rayleigh's method: .....	83
4.2.6	Determination of the speed range for the tests .....	84
4.2.7	VIV Response Parameter.....	87
4.3	Experimental Procedures .....	88
4.4	Summary of equations .....	88
4.5	Vertical cantilever beam properties .....	89

4.6	Test setup .....	90
4.7	Motion capture system setup .....	92
4.8	Response Prediction .....	93
4.9	Experimental Results.....	96
4.9.1	Pluck Tests .....	96
4.9.2	Dynamic Response Validation .....	99
4.9.3	Drag coefficient estimation for the flexible cylinder .....	109
4.9.4	Video capture .....	110
4.10	Conclusions .....	111
5	Design of the riser towing test .....	113
5.1	Motivation .....	113
5.2	Simplified model analysis .....	113
5.3	Prototype material selection .....	114
5.4	Approach to the riser model response .....	116
5.5	Fibre optic sensing technology, the design and installation of fibre optic arrays with FBG sensors .....	119
5.6	Specification of FBG sensors and design of the fibre optic arrays .....	122
5.7	Fabrication of the riser prototype and test setup .....	125
5.8	ANSYS model of the riser prototype .....	134

5.9	Lessons learned in the fabrication of the riser prototype .....	139
5.9.1	Buoyancy sensitivity .....	139
5.9.2	Synchronisation of the FBG interrogator .....	139
5.9.3	Reflections on metallic surfaces affecting the mocap system .....	140
5.9.4	Fibre optic array design .....	140
5.10	Definition of test conditions for current and wave flows .....	141
5.10.1	Scaling concepts .....	142
5.10.2	Wave theory selection .....	145
5.11	Instrumentation systems and data acquisition.....	146
5.12	Approximation of steady drag force/coefficients for towing requirements and a method to estimate local mean drag coefficients along the axis of the model .....	147
5.13	Reduced velocity and Strouhal number for long flexible cylinders .....	150
6	Data analysis and results of the riser towing test .....	152
6.1	Data analysis .....	152
6.1.1	Load cell and MOCAP system data processing .....	152
6.1.2	Fibre Optic Sensing System (FOSS) data processing .....	152
6.1.3	Indications of vortex shedding patterns and response branch transitions .	156
6.1.4	Estimation of local flow velocities and local drag coefficients .....	162
6.1.5	Future work and potential of the FOSS/MOCAP integration .....	165
6.2	Test series results .....	168

6.2.1	Current flow alone .....	168
6.2.2	Current flow plus heading wave no. 1 .....	170
6.2.3	Current flow plus heading wave no. 2 .....	173
6.2.4	Current flow plus heading wave no. 3 .....	175
6.2.5	Current flow plus heading wave no. 1 (increment of initial tension respect 6.2.2) .....	176
6.2.6	Current flow plus heading wave no. 2 (increment of initial tension respect 6.2.3) .....	178
6.2.7	Current flow with induced turbulence .....	179
6.2.8	Current flow plus heading wave no. 1 with induced turbulence .....	182
6.2.9	Current flow plus heading wave no. 2 with induced turbulence .....	183
6.2.10	Current flow plus heading wave no. 1 with increment of initial tension and induced turbulence .....	185
6.2.11	Current flow plus heading wave no. 2 with increment of initial tension and induced turbulence .....	186
6.2.12	Tow depth change to 10 OD and 0 OD for current flow alone .....	188
6.2.13	Tow depth change to 10 OD and 0 OD for current flow plus wave no.1 .....	191
6.2.14	Tow depth change to 10 OD and 0 OD for current flow plus wave no.2 .....	194
6.2.15	General remarks of tests results .....	197
6.2.16	Towing Tests Conclusions .....	206
6.3	Integration of the FOSS, MOCAP and Load Cell data for motion response .....	210
7	Fatigue damage design .....	218
7.1	Software tools .....	218

7.2	Spectral fatigue analysis .....	219		
7.3	Extreme event fatigue analysis .....	223	8	Conclusions
	.....			224
	References			
	.....			228
Appendix A	.....	233		
A.1	Analysis of a simply supported beam with harmonic ground motion (fig. 3.1 in section 3.1.2) .....	233	Free vibration analysis	
	.....			233 Normal mode
	method .....			235 Support
	Motion .....			238
	Solution of the dynamic response .....			
	240	Damping		estimation
	.....			243
A.2	Analysis of a partially submerged cantilever beam (section 3.2.1) .....	248	Free vibration analysis (fig. 3.23 in section 3.2.2)	
	.....			248
	Rayleigh's method .....			251
A.3	Analysis of a tensioned free-free beam (section 3.3.2) .....	253		
	Free vibration analysis (fig. 3.45) .....			253

# List of Figures

Figure 1.1 Shell Perdido Project (Ju et al., 2010) .....	3
Figure 1.2 Petrobras Cascade and Chinook, (OIL & GAS JOURNAL, 2012).....	4
Figure 1.3 Shell Stones, (Shell, 2016) .....	5
Figure 1.4 FSHR and SCR systems (WoodGroupKenny, 2015) .....	7
Figure 1.5 Tow-out methods (DNV-RP-H103) .....	10
Figure 1.6 Surface tow (de la Cruz et al., 2009) .....	10
Figure 1.7 Subsurface tow (de la Cruz et al., 2009) .....	11
Figure 1.8 Dynamic analysis for combinations of waves and current flows at towing speed of 1.75 m/s .....	12
Figure 1.9 Subsurface towing simulations (Shaded graphics) .....	13
Figure 1.10 End tensions results using Orcaflex VIV time domain models in dynamic analysis with default parameters .....	14
Figure 2.1 Metocean measurement locations (CICESE, 2013b).....	24
Figure 2.2 ADCP mooring locations (CICESE, 2013a) .....	25
Figure 2.3 Pemex surface drift buoys hourly data 2007-2013 (CICESE, 2013a).....	26
Figure 2.4 NGOM surface drift buoys hourly data 2010-2013 (CICESE, 2013a). .....	26
Figure 2.5 Gulf of Mexico circulation regions according statistical behaviour (CICESE, 2013a). .....	27
Figure 2.6 Hydrodynamic Forecast Operational System (UNAM, 2013a). .....	29
Figure 2.7 SIPRONOMO (UNAM, 2013b). .....	30
Figure 3.1 Simplified model for vibration analysis .....	42
Figure 3.2 Test sketch .....	45
Figure 3.3 Beam supports .....	45
Figure 3.4 Scotch yoke mechanism .....	46
Figure 3.5 Preparation of oscillation tests .....	47
Figure 3.6 QTM viewer .....	48
Figure 3.7 Response prediction on simplified and FEA models	



.....	49	Figure 3.8	Fatigue strength of structural materials	
(Drechsler et al., 2009). .....	51	Figure 3.9	S-N curve comparing fatigue lives	
(Nanninga, 2008) .....	52	Figure 3.10	Fatigue results showing the	
effect of extrusion zones at $\sigma_A = 110$ MPa				
(Nanninga, 2008) .....				
53	Figure 3.11	PSD of pluck tests data for tube No. 1		
.....	56	Figure 3.12	PSD analysis of pluck tests data for	
tube No. 3 .....	58	Figure 3.13	Measured dynamic responses	
comparative for Tube No. 3 (carbon fibre) .....	60	Figure 3.14	Measured dynamic responses	
comparative for Tube No. 2 (aluminium) .....	61			
Figure 3.15	Measured dynamic responses comparative for Tube No. 1 (aluminium) .....			
62	Figure 3.16	Measured dynamic responses comparative for Tube No. 1		
.....	64	Figure 3.17	Measured dynamic responses comparative for Tube No.	
1 (aluminium) above				
fundamental mode. ....				
65	Figure 3.18	Scotch yoke markers		
.....	66	Figure 3.19	Measured dynamic	
responses comparative with adjusted excitation amplitudes				
.....				
69	Figure 3.20	Verification of 3D Data overlay on video		
.....	70			
Figure 3.21	Calibration frame .....			
72				
Figure 3.22	Camera configurations tested .....			
73	Figure 4.1	Simplified model for vibration analysis of a cantilever beam		
.....	78	Figure 4.2	Cantilever beam static analysis due to self-	
weight.....	79			
Figure 4.3	Cantilever beam static analysis due to submerged section added mass .....			
81				
Figure 4.4	Strouhal number vs Reynolds number in uniform flow tests (Resvanis et al., 2012)			
.....				
86				
Figure 4.5	Aerial system setup on the towing carriage .....			
91				
Figure 4.6	Integration of strain gauges instrumentation .....			
91	Figure 4.7	Installation of underwater cameras to the towing carriage		
.....	92	Figure 4.8	3D View of the Qualisys motion capture system setup	
.....	93	Figure 4.9	Oscillation decay analysis of the pluck test in air	
.....	93	Figure 4.10	Amplitude of response (Barltrop et al., 1990)	
.....	95	Figure 4.11	PSD Data analysis of pluck tests	
.....	96	Figure 4.12	Support vibrations during	
towing conditions .....	99			

Figure 4.13 Torsional springs at the beam support to match experimental frequency .....	101
Figure 4.14 RMS Amplitudes (Test No. 40) .....	102
Figure 4.15 Harmonic Analysis .....	103
Figure 4.16 Validation of underwater measurements .....	103
Figure 4.17 Validation of underwater measurements .....	105
Figure 4.18 QTM 3D trajectories .....	106
Figure 4.19 Marker trajectories of the cantilever free end (transverse instability region) .	107
Figure 4.20 Marker trajectories of the cantilever free end (in-line instability region) .....	107
Figure 4.21 In-line and transverse peak amplitudes of oscillations .....	109
Figure 4.22 Steady drag coefficient amplification .....	110
Figure 4.23 Video capture with 3D data overlay .....	110
Figure 5.1 Simplified model for vibration analysis of a tensioned free-free beam .....	114
Figure 5.2 Mode shapes, shear and bending moment diagrams .....	118
Figure 5.3 Fibre optic arrays locations .....	121
Figure 5.4 Fibre optic array diagram (4x) .....	123
Figure 5.5 Fibre optic assembly design .....	125
Figure 5.6 Fabrication of the riser prototype.....	125
Figure 5.7 Fabrication of the riser prototype.....	126
Figure 5.8 Verification/Calibration of the fibre optic sensing system .....	128
Figure 5.9 FBG Interrogator .....	129
Figure 5.10 Auxiliary carriage and supports connections .....	129
Figure 5.11 Installation of underwater cameras of the motion capture system .....	130
Figure 5.12 Lead-end and trail-end supports for the tensioned riser prototype .....	131
Figure 5.13 Plan view setup dimensions .....	131
Figure 5.14 Elevation view setup dimensions .....	132
Figure 5.15 Beam model for Ansys FEA .....	132
Figure 5.16 Riser upward deflection at 1.05 m tow depth at supports .....	132
Figure 5.17 Ansys model for FEA .....	135
Figure 5.18 Submerged Static deflection .....	136
Figure 5.19 Modal analysis .....	137
Figure 5.20 Wave particle velocities .....	146
Figure 5.21 Mean drag force estimation from load cell data .....	148
Figure 6.1 Bending strain responses due to current flow .....	

alone .....	153	Figure 6.2 PSD frequency peaks from the FOSS data, test No. 12. ....	155
Figure 6.3 PSD frequency peaks from the FOSS data, test No. 15. ....	156	Figure 6.4 IL and CF bending strain responses in test no. 16 (0.1 m/s). ....	157
Figure 6.5 IL and CF bending strain responses in test no. 17 (0.2 m/s) .....	157	Figure 6.6 IL and CF bending strain responses in test no. 18 (0.3 m/s) .....	158
Figure 6.7 IL and CF bending strain responses in test no. 19 (0.4 m/s) .....	158	Figure 6.8 IL and CF bending strain responses in test no. 11 (0.5 m/s) .....	159
Figure 6.9 IL and CF bending strain responses in test no. 12 (0.6 m/s) .....	159	Figure 6.10 IL and CF bending strain responses in test no. 13 (0.7 m/s) .....	160
Figure 6.11 IL and CF bending strain responses in test no. 14 (0.8 m/s) .....	160	Figure 6.12 IL and CF bending strain responses in test no. 15 (0.9 m/s) .....	161
Figure 6.13 IL Mean bending strain .....	162	Figure 6.14 Preliminary local drag coefficient distributions along the riser length for current flow, tow depth = 1.05 m (25 OD) .....	164
Figure 6.15 Bending strain responses due to current flow plus heading wave no. 1, tow depth = 1.05 m (25 OD) .....	172	Figure 6.16 Bending strain responses due to current flow plus heading wave no. 2, tow depth = 1.05 m (25 OD) .....	174
Figure 6.17 Bending strain responses due to current flow plus heading wave no. 3, tow depth = 1.05 m (25 OD) .....	176	Figure 6.18 Bending strain responses due to current flow plus heading wave no. 1 with tension increment, tow depth = 1.05 m (25 OD) .....	177
Figure 6.19 Bending strain responses due to current flow plus heading wave no. 2 with tension increment, tow depth = 1.05 m (25 OD) .....	179	Figure 6.20 Bending strain responses due to current flow with induced turbulence, tow depth = 1.05 m (25 OD) .....	180
Figure 6.21 Bending strain responses due to current flow plus heading wave no. 1 with induced turbulence, tow depth = 1.05 m (25 OD) .....	182	Figure 6.22 Bending strain responses due to current flow plus heading wave no. 2 with induced turbulence, tow depth = 1.05 m (25 OD) .....	184
Figure 6.23 Bending strain (induced turbulence over 6.2.5 case), tow depth = 1.05 m (25			

OD) .....	185
Figure 6.24 Bending strain (induced turbulence over 6.2.6 case), tow depth = 1.05 m (25 OD) .....	187
Figure 6.25 Bending strain responses due to current flow alone, tow depth = 0.42 m (10 OD) .....	189
Figure 6.26 Bending strain responses due to current flow alone, tow depth = 0.0 m (free surface, 0 OD) .....	189
Figure 6.27 Bending strain responses due to current flow alone, tow depth effects at 0.5 m/s. ....	190
Figure 6.28 Bending strain responses due to current flow alone, tow depth effects at 0.9 m/s. ....	190
Figure 6.29 Bending strain responses due to current flow plus wave no. 1, tow depth = 0.42 m (10 OD) .....	192
Figure 6.30 Bending strain responses due to current flow plus wave no. 1, tow depth = 0.0 m (free surface, 0 OD) .....	193
Figure 6.31 Bending strain responses due to current flow plus wave no.1, tow depth effects at 0.5 m/s. ....	193
Figure 6.32 Bending strain responses due to current flow plus wave no. 2, tow depth = 0.42 m (10 OD) .....	195
Figure 6.33 Bending strain responses due to current flow plus wave no. 2, tow depth = 0.0 m (free surface, 0 OD) .....	196
Figure 6.34 Bending strain responses due to current flow plus wave no.2, tow depth effects at 0.5 m/s. ....	196
Figure 6.35 Effect of waves on maximum bending strain responses due to VIV and wave forces. ....	199
Figure 6.36 Approximation of mean drag forces per unit length at 25 OD in different test conditions.. ....	200

Figure 6.37 Effects of induced turbulence on drag forces for current + wave flows. .... 202

Figure 6.38 Tow depth effects on bending strain responses due to VIV and wave induced forces (current and current plus wave flows). ..... 204

Figure 6.39 Tow depth effects on approximated mean drag forces for current and current + wave flows. .... 205

Figure 6.40 Chord projection angles from bending strain data ..... 210

Figure 6.41 Deflected profile from chord projections ..... 210

Figure 6.42 IL Motion response ..... 212

Figure 6.43 CF Motion response ..... 213

Figure 6.44 CF and IL RMS response amplitudes (A/D) ..... 214

Figure 6.45 RMS Amplitude responses and drag coefficients ..... 215

Figure 6.46 PSD frequency peaks from the FOSS data, test No. 15. .... 216

Figure 6.47 CF motion response against bending strain response ..... 217

Figure 7.1 Broad band spectrum, test No. 64 ..... 219

Figure 7.2 Broad band spectrum, test No. 88 ..... 220

## List of Tables

Table 2.1 Significant wave heights ( $H_s$ ) and Periods (T) ..... 32

Table 3.1 Beam properties and geometric data ..... 44

Table 3.2 Stress ratios R (Rösler et al., 2007) ..... 53

Table 3.3 Frequency measured at each marker along Tube No. 1 during pluck test ..... 55

Table 3.4 Damping ratio experimentally obtained for Tube No. 1 ..... 57

Table 3.5 Damping ratio experimentally obtained for Tube No. 3 ..... 57

Table 3.6 Natural frequency predictions against measured values ..... 58

Table 3.7 Variations of amplitudes with oscillation frequency of the scotch yoke mechanism ..... 67

Table 3.8 Calliper measurements of calibration frame markers ..... 73

Table 3.9 Comparative of motion capture tests of the calibration frame ..... 74

Table 3.10 Reprocessing of test No. 241 with selected cameras ..... 75

Table 4.1 Estimation of towing speeds ..... 85

Table 4.2 Vertical cantilever properties and geometric data ..... 90

Table 4.3 Damped natural

frequency comparative .....	97	Table 4.4	Experimental
damping ratio .....	97	Table 4.5	Differences
in RMS amplitudes of the aerial camera system (mm) .....	104	Table 4.6	Differences in RMS amplitudes of the underwater camera system (mm) .....
104			
Table 4.7 Estimation update of towing speeds .....	106		
106			
Table 4.8 In-line and transverse peak responses .....	108	Table	5.1
108			FBG
			Interrogators
.....	123	Table 5.2	FBG sensors
arrangement spec .....	124	Table 5.3	Final specs
124		Table 5.4	Averages
for fibre optic arrays .....	124	Table 5.4	Averages
124			of FBG wavelength shifts during calibration .....
127			127
Table 5.5 Riser model properties and geometric data for tests at a yaw angle about 80° .	134		
134			
Table 5.6 Experimental damping .....	138	Table	5.7
138			Measured frequency of the fundamental mode
.....	138	Table	5.8
138			FEA modal analysis
.....	138	Table	5.9
138			Testing waves
.....	143		
143			
Table 6.1 Current flow alone, tow depth = 1.05 m (25 OD), PSD analysis from marker no.3 of MOCAP system .....	152		
152			
Table 6.2 Local reduced velocities and drag coefficients, test no. 15 .....	163		
163			
Table 6.3 Local reduced velocity range and maximum drag coefficients for current flow alone .....	164		
164			
Table 6.4 Current flow (PSD analysis from FOSS data), tow depth = 1.05 m (25 OD) .....	169		
169			
Table 6.5 Current flow plus heading wave no. 1, tow depth = 1.05 m (25 OD) .....	171		
171			
Table 6.6 Current flow plus heading wave no. 2, tow depth = 1.05 m (25 OD) .....	173		
173			
Table 6.7 Current flow plus heading wave no. 3, tow depth = 1.05 m (25 OD) .....	175		
175			
Table 6.8 Current flow plus heading wave no. 1 with tension increment, tow depth = 1.05 m (25 OD) .....	177		
177			
Table 6.9 Current flow plus heading wave no. 2 with tension increment, tow depth = 1.05 m (25 OD) .....	178		
178			
Table 6.10 Current flow with induced turbulence, tow depth = 1.05 m (25 OD) .....	180		
180			
Table 6.11 Current flow plus heading wave no. 1 with induced turbulence, tow depth = 1.05 m (25 OD) .....	182		
182			
Table 6.12 Current flow plus heading wave no. 2 with induced turbulence, tow depth = 1.05			

m (25 OD) .....	183
Table 6.13 (Induced turbulence over 6.2.5 case), tow depth = 1.05 m (25 OD) .....	185
Table 6.14 (Induced turbulence over 6.2.6 case), tow depth = 1.05 m (25 OD) .....	186
Table 6.15 Current flow alone, tow depth = 0.42 m (10 OD) .....	188
Table 6.16 Current flow alone, tow depth = 0.00 m (free surface, 0 OD) .....	188
Table 6.17 Current flow plus wave no. 1, tow depth = 0.42 m (10 OD) .....	191
Table 6.18 Current flow plus wave no. 1, tow depth = 0.00 m (free surface, 0 OD) .....	192
Table 6.19 Current flow plus wave no. 2, tow depth = 0.42 m (10 OD) .....	194
Table 6.20 Current flow plus wave no. 2, tow depth = 0.00 m (free surface, 0 OD) .....	195
Table 6.21 RMS response amplitudes (A/D) and main parameters .....	214

## **Abstract**

The thesis presents experimental and theoretical work on VIV and fatigue damage during the tow operation for installation of free standing risers.

The research studies were sponsored by PEMEX, the Mexican national oil company and the Mexican Science and Technology National Council, within a professional development program, to assist with the short-term execution of deep water projects, considering the potential of important findings in the Gulf of Mexico, and the decreasing opportunities of easy access reservoirs as well as the production declination in the main oilfields in shallow waters.

A literature review on related VIV fundamentals was conducted while approaching industry leaders in the execution of tow-out installation methods, to assimilate some of the main processes during engineering, fabrication and towing operations for installation of pipe bundles and risers, which supported initial modelling works for towing simulations to explore VIV prediction tools.

After revision of industry standards and published work related to design guidelines on VIV and fatigue damage, the contribution to knowledge in the present work was focused on the evaluation and implementation of innovative technologies for instrumentation and response measurement in model testing, looking for a better understanding and characterisation of responses for more representative models of full-scale designs, with hydrodynamic parameters and coefficients required for calibration of the different prediction models used in leading software for VIV and fatigue analysis.

The experimental work used one of the first implementations of an underwater optical tracking system for motion capture, to conduct hydrodynamic studies over flexible submerged elements, as well as the first design and installation of a fibre optic sensing system in the towing tank of the University.

The successful instrumentation, allowed measurement and data processing for results which contribute to understanding of some of the response characteristics for a flexible model with a long aspect ratio, subject to selected loading conditions of interest for current



flows, regular waves, change of initial tension and tow depths, presenting indications of interesting VIV phenomena such as transition branches and vortex shedding modes, allowing the identification of velocity boundaries to avoid high response amplitudes associated to the upper branch response of VIV.

Future work and test conditions are proposed to develop the potential of the evaluated technologies to achieve a high-quality data acquisition system for further VIV studies over flexible elements.

The research work achieved a successful application of an aerial motion capture system in flexible beams and a first implementation of the technology on VIV studies using underwater cameras with integration of a fibre optic sensing system for strain/curvature measurements.

These were applied in the final experimental work over a model tested in the towing tank at the Kelvin Hydrodynamics Laboratory, with an aspect ratio about 430, a final mass ratio of 0.9, damping ratio in still fluid  $\zeta = 0.046$  ( $m^*\zeta=0.04$ ), for combinations of current and wave flows at low Keulegan-Carpenter number range of  $0.3 < KC < 5.25$ .

The results provide an insight of the response behaviour for the main fluid loading conditions during towing operations for offshore installations and route planning, as well as methods and basis for further research development with a sound potential of application.

# 1 Introduction

During the last decade, PEMEX, the Mexican national oil company, obtained authorization from the Mexican Hydrocarbons National Commission (CNH) for exploratory drilling within the area or oil province of the Perdido fold belt in ultra-deep waters of the Gulf of Mexico, with successful findings of large potential reservoirs at some locations such as Trion-1 and Supremus-1 wells at water depths of about 2540 and 2890 metres respectively (Mexican Presidency, 2012).

Recently, in the second half of 2016, the Mexican government has called for bids to select a partner for a joint operation agreement with PEP, or farm out, in order to develop the Trion block, as the first ultra-deep water oil production project (Pemex, 2016).

The Mexican government also called for the 4<sup>th</sup> bidding process of the round number 1, which encompasses 10 deep water blocks for exploration and production license contracts, where 4 blocks are located in the same oil province of the Perdido fold belt, with other important discoveries by PEMEX at nearby locations such as Maximino-1 and Exploratus-1 wells (COMISION NACIONAL DE HIDROCARBUROS, 2016).

The imminent project execution and exploitation in ultra-deep waters of the Gulf of Mexico demands an understanding of knowledge and technologies in the industry frontier for floating systems and production risers, where postgraduate studies in Naval Architecture and Marine Engineering seek to strengthen the comprehension of the technical challenge to secure reliable infrastructure within acceptable levels, while contributing to knowledge with research topics based on latest technologies.

## 1.1 Evolution of the offshore infrastructure for oil and gas production

The construction technology based in harbour and civil engineering was initially applied to take drilling equipment over piers and barges in shallow water locations to access potential oil reservoirs.

The utilisation of barges for drilling equipment and some particular conditions either in coastal or inland waters, set the requirements to conceptualise some way to stabilise the drilling platform area that a barge can provide, leading to the development of the jack-up and the submersible platform concepts (Howe, 1986).

As the drilling exploration activities progressed from coastal to offshore waters, the proved good motion response of the first submersible barges fostered the development and design of semi-submersible floating platforms, and drilling ships design and construction took place.

The success of these drilling activities demanded the installation of process facilities for oil and gas production. Near shore and offshore locations were accessed generally using fixed structures based on tubular steel members and accessed with the later development of concrete gravity platforms mainly utilised in the North Sea.

As the availability and demand for hydrocarbons pushed the exploratory efforts towards deeper waters, the technical feasibility of the fixed offshore structures and their associated costs among other factors encouraged the design and execution of the first floating production systems that had been conceptualised by the industry.

## **1.2 Floating production systems**

The description and characteristics of the main types of floating production systems, namely FPSO, Semi-Submersible, TLP and Spar platforms, has been well described (Barltrop, 1998), including relevant field and performance requirements driving the concept selection.

The imminent development of oil fields for the Mexican sector in the Perdido fold belt, at water depths ranging from 2,500 to 3,000 metres, left the TLP floating production system practically out of the scenario, considering that TLP's has showed a techno-economical boundary at about 1,500 metres of water depth in comparison with other floating systems in deeper waters.

Consequently, two of the largest drivers for a concept selection of the floating system will be either, the requirement of drilling, completion and workover rig for a direct vertical

access (DVA), which commonly has led to the selection of a SPAR concept in the Gulf of Mexico, or lacking proximity and capacity of pipeline infrastructure, which can lead to storage requirements for an FPSO solution. These main alternatives have been implemented in the three projects of reference to date, considering the location and water depths of interest, being Shell Perdido, Petrobras Cascade and Chinook and Shell Stones.

For the Shell Perdido project, a Spar moored in 2,450 metres of water depth was selected as a hub processing facility for subsea wells of three oil fields: Great White, where the Spar is located at the main drilling centre, Tobago and Silvertip. The water depths range from 2,300 to 2,800 metres. The stated production capacity of the Spar is up to 100 Mbbls per day of oil and 200 MMSCFD of gas (Ju et al., 2010).

Figure 1.1 shows the links between the Spar and the subsea infrastructure, achieved with 4 Steel Catenary Risers (SCR) for water injection, service and export pipelines, 4 dynamic umbilicals and 5 top tensioned caisson risers (TTCR) for a subsea boosting system, one of the main enabling technologies of the project, which was required to provide artificial lift given the low-pressure characteristics of the reservoir.

The boosting system was designed as an inlet assembly below each caisson riser bottom, integrated to the top of a vertical cyclonic separator with an electrical submersible pump (ESP); the separator is located inside a 350 feet caisson penetrating the seabed, in this way each TTCR provides a direct vertical access from the floating system to the ESP.

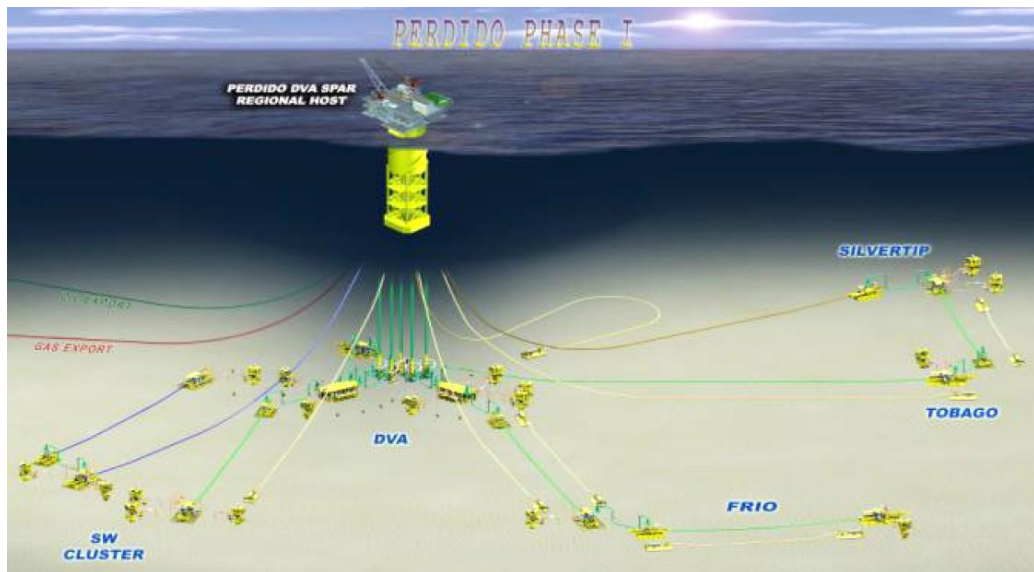


Figure 1.1 Shell Perdido Project (Ju et al., 2010)

Petrobras Cascade and Chinook project, with subsea wells in a water depth range of 2,500 to 3,000 metres, selected an FPSO system with a disconnectable internal turret buoy mooring system, linking the subsea system of each of the 2 fields with 2 Free Standing Hybrid Risers (FSHR) and 2 umbilicals with a looped arrangement, a 5<sup>th</sup> FSHR is used for a gas export pipeline. The stated production capacity is up to 80 Mbbls of oil per day and 16 MMSCFD of gas (OIL & GAS JOURNAL, 2012).

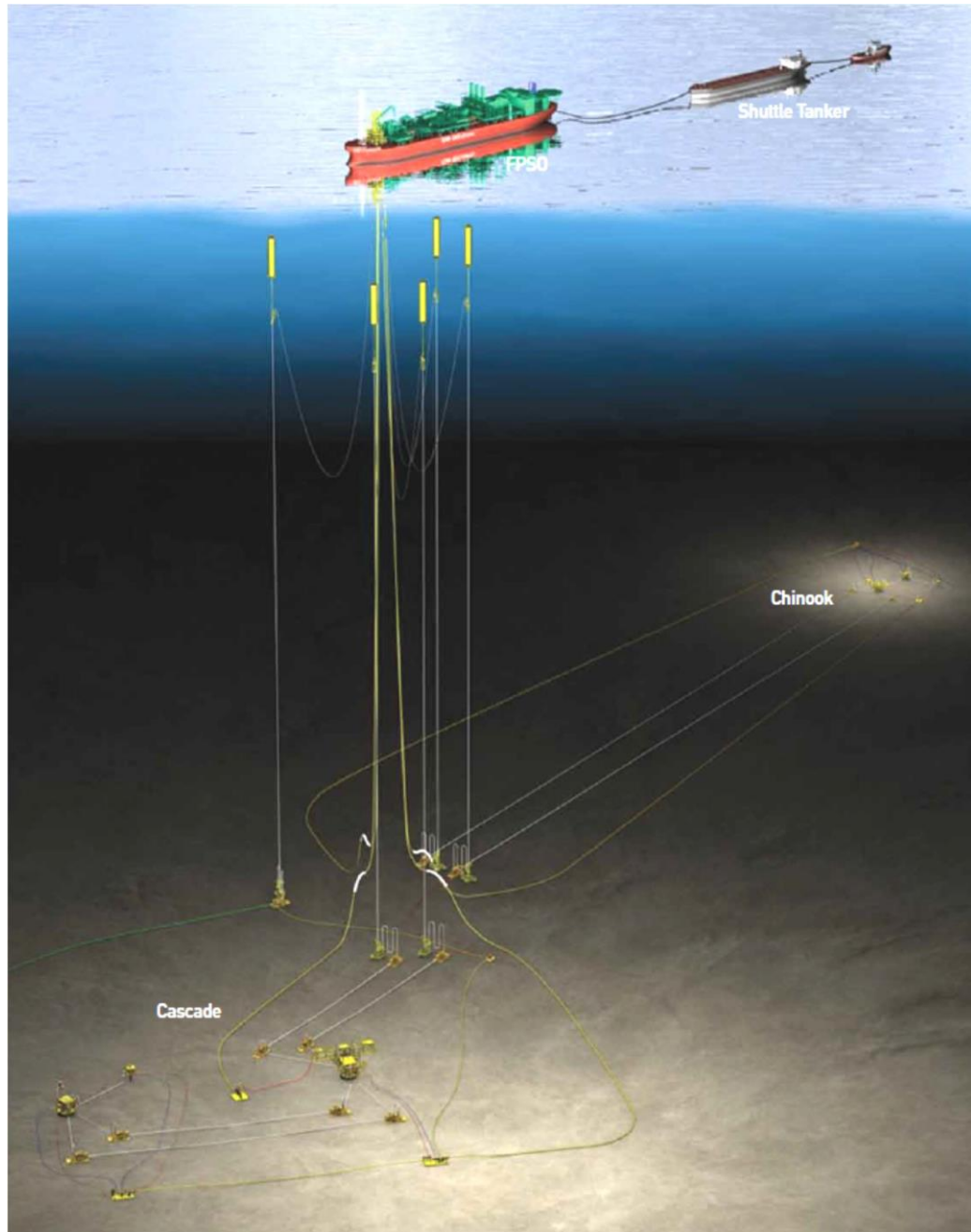
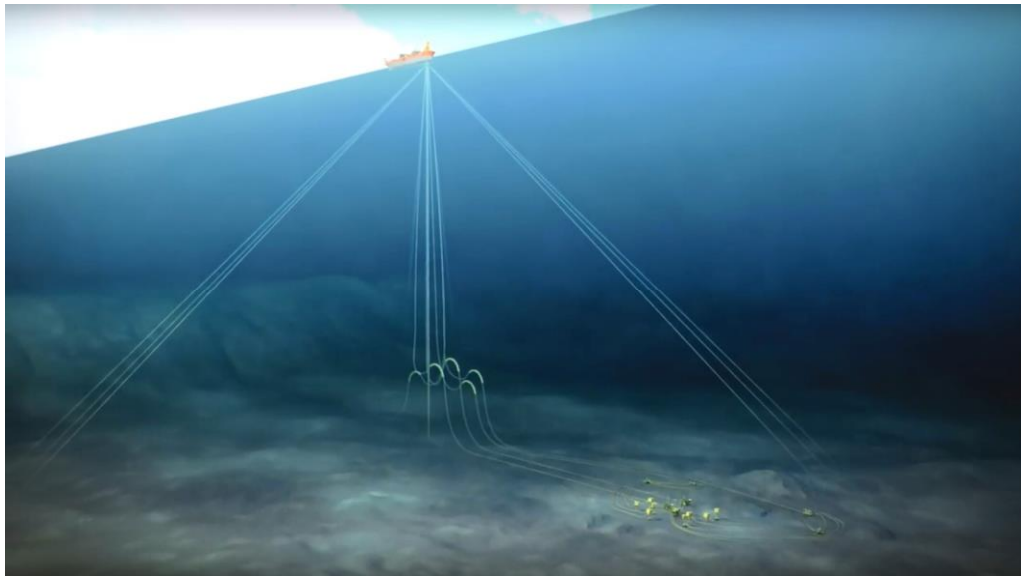


Figure 1.2 Petrobras Cascade and Chinook, (OIL & GAS JOURNAL, 2012)

Shell Stones project also selected an FPSO solution for the development of the Stones oil field at water depths of about 2,900 metres; using for a first time a disconnectable buoy turret mooring with 3 x 8” Steel Lazy Wave Risers (SLWR) and 2 umbilicals (SBM Offshore, 2016). The stated production capacity is up to 60 Mbls of oil per day and 15 MMSCFD of gas (Offshore Technology 2016).



**Figure 1.3 Shell Stones, (Shell, 2016)**

The extreme environmental conditions in the Gulf of Mexico, characterised by the presence of an annual hurricane season, had motivated the use of buoyant turret mooring system (BTM).

External and internal turrets at the forepeak are commonly designed for FPSOs, where a bearing system allows the moored vessel to rotate or “weathervane” according to external forces, such as wave, current and wind, for an equilibrium position; swivels inside the fixed turret structure can provide the fluid transfer from riser systems.

In a BTM system, the disconnectable feature is achieved through a moored buoy supporting the riser system, which can be connected inside a receptacle in the lower end of the turret; when disconnected, the buoy is designed to match the weight of mooring and riser systems in a suitable submerged position (SBM Offshore. Glossary, 2013).

### 1.3 Riser Systems

Offshore riser systems and umbilicals provide the link between the wells at seabed level or subsea infrastructure to either, fixed or floating drilling/production facilities. They conduct hydrocarbons and any of the drilling, service and control fluids, and electric power or communication/data transmission lines required by the project or drilling activity.

The main characteristics, configuration types and components for rigid and flexible risers have been well described (Barltrop, 1998); the relative term for rigid and flexible risers is highlighted, especially for riser systems in deep water where very long steel pipes can and have been designed and installed in some configuration profiles of flexible risers.

The conceptual alternatives for riser systems were studied for the potential development of ultra-deep water oil fields.

The technical feasibility and commercial viability of FSHR (see fig. 1.4) and SLWR (a lazy wave configuration profile for a steel catenary riser) as main riser concepts for deep and ultra-deep water solutions were well predicted (Sertã et al., 2001), being both alternatives implemented as riser concepts for Petrobras Cascade and Chinook and Shell Stones recent developments in the Gulf of Mexico, which are based on FPSO concepts with disconnectable turret.

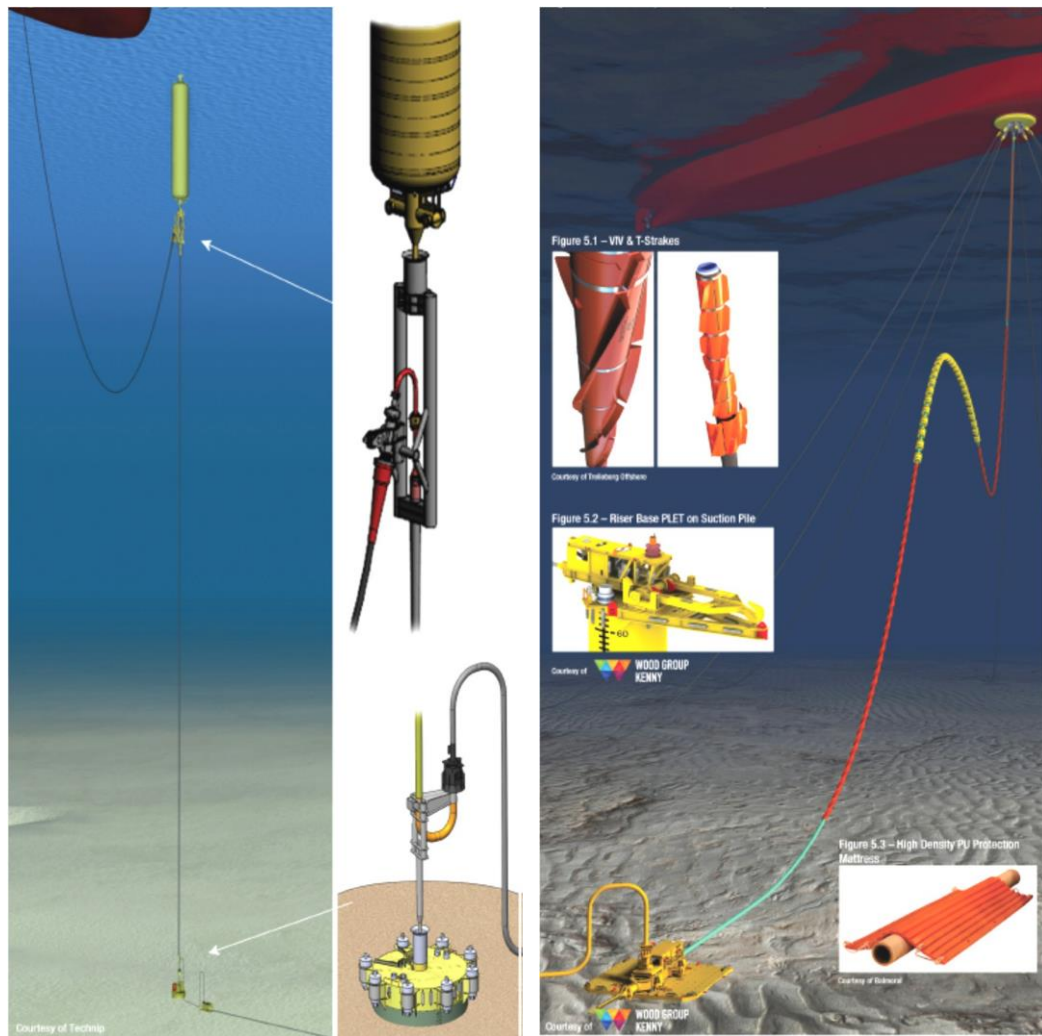


**Figure 1.4 FSHR and SCR systems (WoodGroupKenny, 2015)**

Some scenarios related with production volumes and/or storage requirements can create a potential demand for decoupling the largest part of the loading interactions of SCR from the floating system. The solution has been considered as a number of designs for the support of groups or a single SCR with a tethered subsurface buoy, such as the Tethered Leg Riser (TLR) (Petruska et al., 2002), the Tethered Catenary Riser (Legras and Pillet, 2013) or the Catenary Offset Buoyant Riser Assembly (COBRA) (Nurwanto et al., 2013).

FSHR installed as a single line riser or as a riser tower, had proved their advantages in deep water developments, located either in the west coast of Africa (Deserts, 2000) or in the Gulf of Mexico. Some of the main advantages are:



- Decoupling the floater motions from the main vertical riser with an important reduction of the loads.
- They can be installed well before the floating system to reduce vessel conflicts.
- Provides more independence, reducing engineering and construction interphases between contractors for the subsea, risers and floating production system.
- The subsea lay out benefits from more room in comparison with SCR foot prints.

The cost and fabrication complexity of the FSHR has been reported higher than that of an SCR (Sworn, 2005), although this riser system can remain competitive when the cost impact of their advantages is integrated in the specific evaluation.

One attractive advantage of the FSHR concept is represented by the large impact in local content due to the requirement of an onshore fabrication yard for the main section of the riser (Lirola et al., 2013), providing a wide range of construction, fabrication, assembly, equipment and quality assurance methods with the consequent development of supplies and services.

Moreover, the impact of the local content in this case could provide the opportunity for the development of other related solutions, like towed installation methods for SCR or pipe bundles, which has been mainly utilised in the North Sea.

One of the main concerns for the towing installation methods are related with the fatigue damage due to wave induced oscillations and/or VIV.

Even when some recommendations are given in literature on the estimation of hydrodynamic forces and coefficients for elements at a yaw angle with respect to current and/or wave flows, there was not found any publication of experimental data/results for these cases, thus the motivation to investigate current technologies and to conduct experimental work that allows an understanding of the response during horizontal towing of risers/bundles.

## **1.4 VIV effects on marine risers**

From a structural point of view, a marine riser is generally a partial or totally immersed slender cylindrical element, which must be able to withstand internal and external pressures, thermal conditions, support induced forces/motions and often vortex induced vibrations (VIV) as part of general flow induced vibrations. VIV is the least well understood mechanism and the prediction of responses cannot be made with the same level of confidence as for other loading sources during analysis and design, due to the inherent complexity of the non-linear vortex shedding process over these slender riser structures, which becomes especially relevant if we consider combinations of current and wave flows over the horizontal configuration adopted during tow-out installation methods.

Several effects can arise when bluff bodies are subject to external fluid flow conditions, some of them can be recognisable in familiar structural elements with circular cross section, as flexible cables for electric power, for communications or in bridge components; or even in more rigid elements like aerial antennas, street lights, chimneys, or dock piles to name a few.

The previous examples are often a source of evident effects between the flow and the structure in the form of oscillatory responses or vibrations and/or evidence of turbulence in the wake of the flow.

The main disciplines involved in the study of such phenomena are related with fluid and structural mechanics, where dimensionless relationships between physical quantities of the flow have been fundamental in the research for development of empirical and semiempirical response prediction models.

## **1.5 Tow-out installation methods and an introduction to simulation.**

Tow-out installation methods have been performed for long slender structural elements and offshore systems, e.g. pipelines, bundles, spools, TLP tethers and risers. The offshore code DNV-RP-H103 describes the off-bottom tow, deeply submerged or control depth tow (fig. 1.5) and the surface or near-surface tow (figs. 1.6 and 1.7) as the three main methods normally performed.

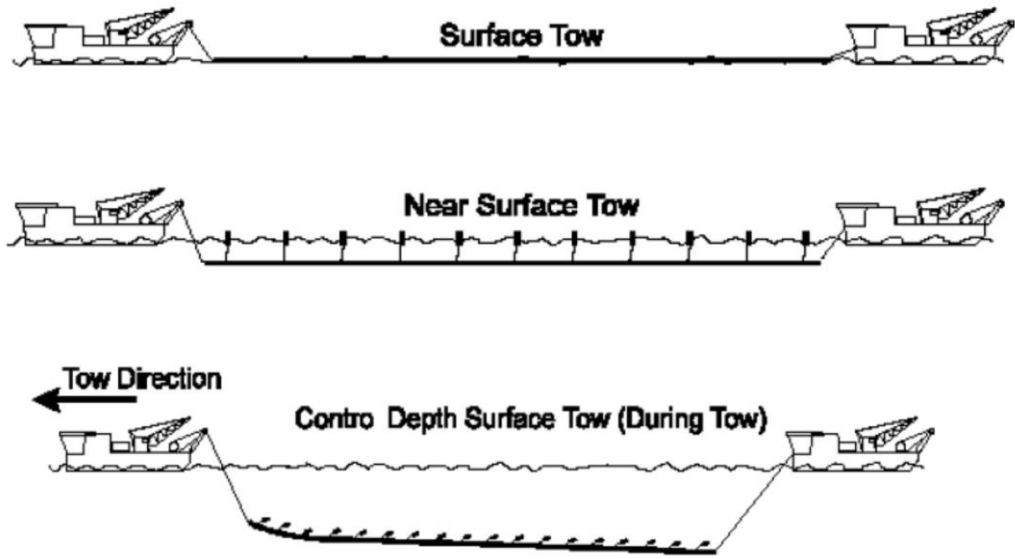


Figure 1.5 Tow-out methods (DNV-RP-H103)

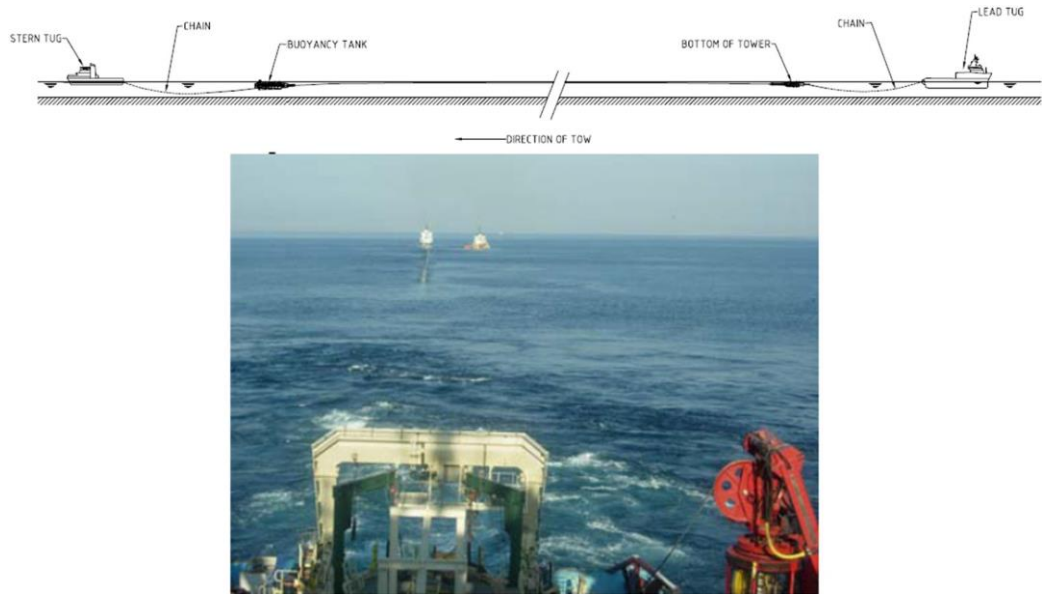
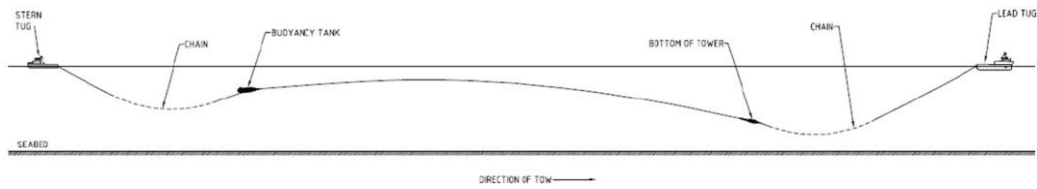


Figure 1.6 Surface tow (de la Cruz et al., 2009)



**Figure 1.7** Subsurface tow (de la Cruz et al., 2009)

In order to gain a practical insight on the onshore fabrication of pipeline/bundles, launching and tow-out operations, a visit was made to the Wick fabrication yard in Scotland, a facility owned by Subsea7, which is a world leader in subsea engineering, construction and related services.

The Wick fabrication yard has a long record in the fabrication of pipeline bundles for towout installation methods in the North Sea since 1978; the fabrication yard visit was followed with some interviews with analysts and designers at Subsea7 engineering facilities in Paris, France, for a direct contact to the company's current riser technology capabilities and conceptual designs, covering basic aspects related with the analysis of tow-out operations.

Knowledge of current capabilities and the assimilation of basic construction and operational procedures from field visits, were supportive and set the basis to perform some preliminary scenarios for towing operations, using the availability of the software Orcaflex, a leading tool for analysis of offshore marine systems.

A riser of 2,500 metre length and 1 metre of outside diameter was modelled, including weight distribution with drag chains and towing heads, setting configurations that achieve convergence of static solutions, while assimilating the effects of the towing cables lengths

and buoyancy of towing heads used to maintain a target depth during towing simulations in dynamic analysis, gaining practical experience with the use of the software (see figs. 1.8 and 1.9).

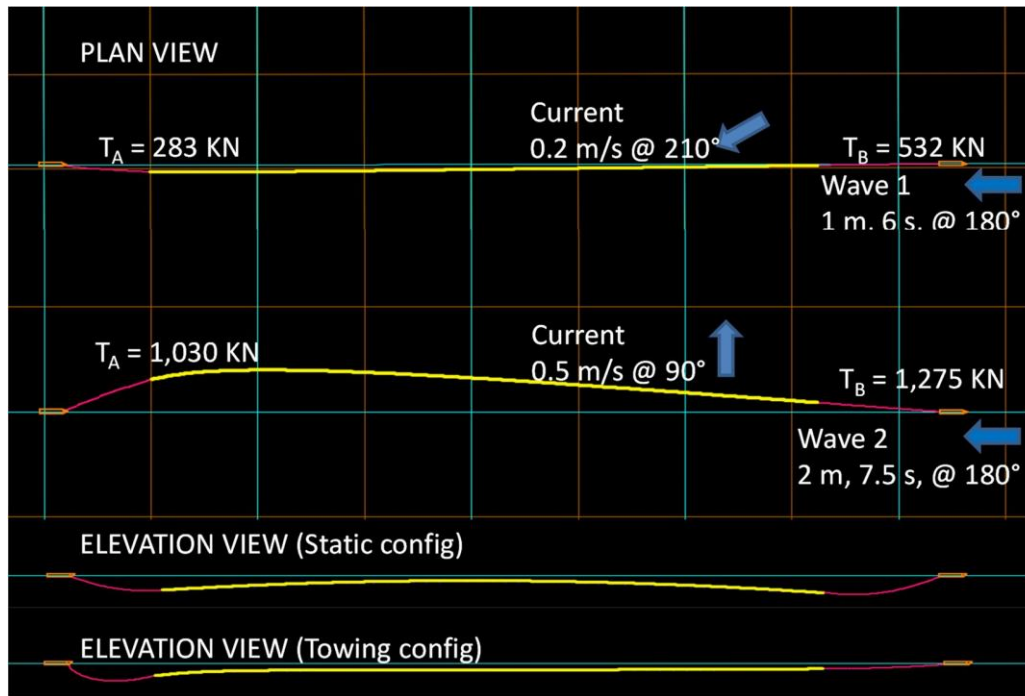


Figure 1.8 Dynamic analysis for combinations of waves and current flows at towing speed of 1.75 m/s

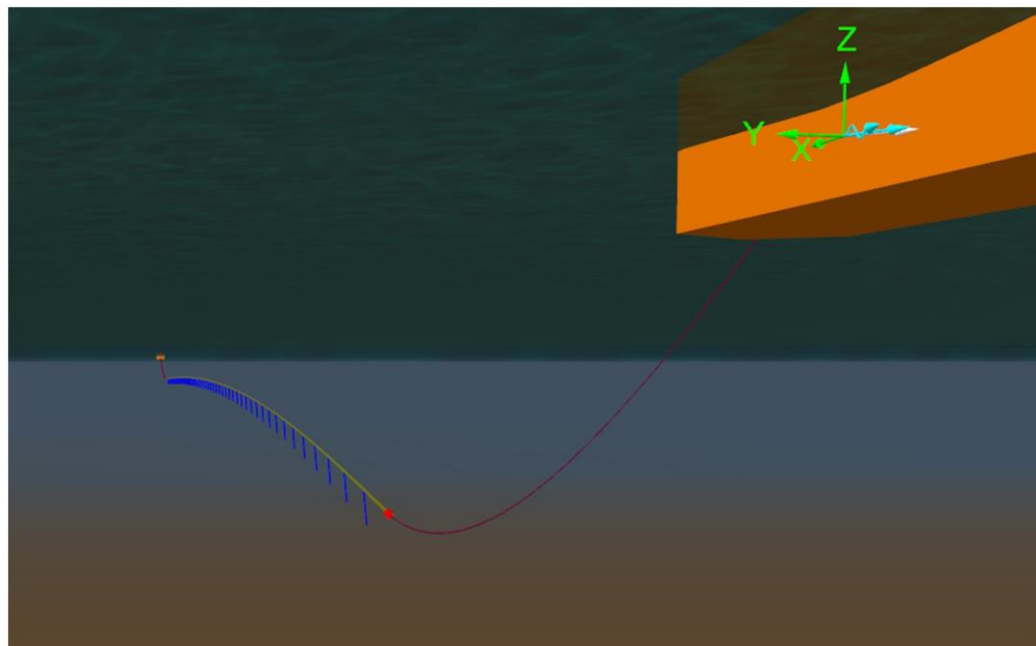


Figure 1.9 Subsurface towing simulations (Shaded graphics)

The model enabled the modal analyses for the calculation of the natural frequencies of vibration, as well as the application of the VIV toolbox for VIV prediction.

It is important to mention that although the Orcaflex VIV toolbox includes the integration and ability to work with two frequency domain models (for steady state conditions), VIVA and Shear7, these could not be tested since these are 3<sup>rd</sup> party software that require the license and installation of those independent programs, which were not available at the time of this research.

However, the VIV toolbox does include 4 time domain models within Orcaflex (for nonsteady state conditions) which are applicable to dynamic analysis, two of them based on wake oscillator models, the Milan model and the Iwan and Blevins model, and the other two based on vortex tracking models.

Both wake oscillator models were applied in dynamic analysis, to explore results of the transverse and inline vortex force per node; verifying that these models do not cause variations of significance in end tensions in comparison with the results of dynamic analysis without VIV, as shown in fig. 1.10.

On the other hand, it was noted that the application of both vortex tracking models for VIV analysis caused some increments of the end tensions results in comparison to the tensions reported in dynamic analysis without VIV tools, which was consistent with the reported tendency of these vortex tracking models to over predict VIV amplitude responses according to Orcaflex validation works (Orcina LTD., 2007).

Although it is mentioned that these models can be useful for qualitative investigations on VIV in certain shear flow conditions, which cannot be assessed with other VIV models, providing predictions of inline VIV.

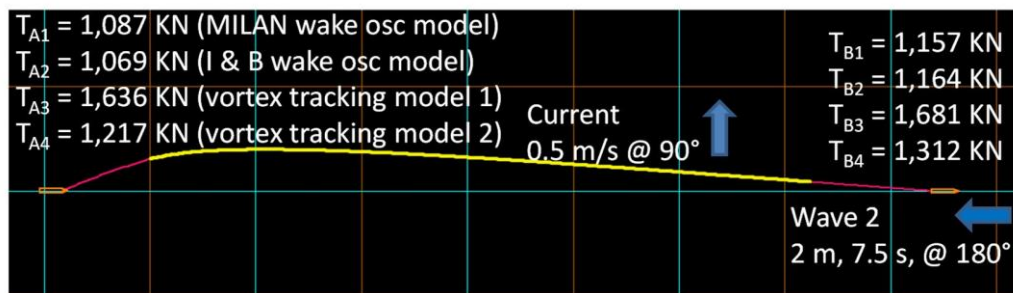


**Figure 1.10 End tensions results using Orcaflex VIV time domain models in dynamic analysis with default parameters**

The description, theory and recommendations for the use of the VIV models and the possibility for adjustment of calibration parameters when experimental data of sufficient similarity to the model is available, are well documented in section 9 of the Orcaflex software manual.

An additional visit to Subsea7's engineering offices in Aberdeen Scotland was made, verifying a good approximation of the model developed in Orcaflex with respect to one simulation that were presented by the company as an example of the analysis and simulation of towing operations for pipeline bundles.

## **2 Literature Review**

### **2.1 VIV Main concepts and parameters**

As mentioned in section 1.4, the vortex shedding processes account for VIV effects on bluff bodies subject to particular conditions of fluid flows, being circular cross section bodies of interest in several engineering applications.

Much of the main studies and research contributions about the fundamentals of the VIV phenomenon have been compiled in well-known related literature (Blevins, 1994), (Sarpkaya, 2010); here, some of the main characteristics and parameters related with the scope of this research will be summarised for cylindrical shape bodies, others parameters will be more conveniently discussed during experimental work.

The fundamental mechanism causing vortex shedding when a fluid flow pass a body with circular cross section is related to the viscous forces in the boundary layer, a thin layer of fluid close to the body surface where the fluid velocity, due to a non-slip condition, varies from zero at the surface to the velocity of the free stream, which cause a rotation in the fluid, leading to separation points of the incident flow where flow reverses, lower pressures on the afterbody leads then to drag forces (Barltrop, 1998).

Pairs of vortices form at the aft surface, remaining in place at very low Reynolds number ( $Re$ ) but as the  $Re$  increases, vortices start to be shed in a wake and form again at the aft surface of the body, imparting oscillatory drag and lift forces.

For flexible members in steady flow condition and depending on the fluid velocity, three regions of instability characterised for enhanced oscillatory responses are associated to the vortex shedding process and their interaction with the natural frequencies of the body, two in-line (IL) instability regions with oscillations parallel to the flow direction due to symmetrical and asymmetrical vortex shedding, and a third instability region in the crossflow (CF) direction due to asymmetrical vortex shedding.

The frequency at which vortices shed has been related by a robust parameter given by the Strouhal relationship  $f = St \cdot U / D$ , where  $St$  is the non-dimensional Strouhal number,  $U$  is the flow velocity normal to the member and  $D$  is the diameter of the member's cross section.

The non-dimensional Strouhal number experimentally studied over smooth fixed cylinders shows a nearly constant value about 0.2 at subcritical Reynolds numbers of practical applications. At higher  $Re$  within the critical regime, the  $St$  number shows a sharp rise, although for experiments with cylinders free to oscillate the  $St$  number remains at values near to those presented in subcritical regimes.

When cylindrical body shapes are free to oscillate and the vortex shedding frequency approaches one of the natural frequencies of the body, the vortex shedding frequency no longer follows the  $St$  relationship and adapts or synchronises itself to the natural frequency of the body; this synchronisation occurs within a range of flow velocities and is known as lock-in, lock-on, vortex or frequency capture range.

In the lock-in range the natural modes are excited and vortex shedding becomes stronger, leading to the peak responses of the instability regions.

The response frequency does not remain constant through the lock-in range for cylinders free to oscillate, since the added mass can show variations due to a number of complex interactions between the time dependant flow and the body motions, becoming even negative since the fluid and the body are subject to positive and negative accelerations or inertia (Sarpkaya, 2010) (Vikestad et al., 2000).



The reduced velocity is the parameter used to identify velocity ranges of interest for VIV and is defined as  $U^* = U / (f_n D)$ , where  $f_n$  is the n-th natural frequency of the cylinder, the typical ranges for IL and CF instability regions will be explored during design and execution of the experimental work.

The response of cylinders to VIV due to steady current flow and within the lock-in range has been characterised as a function of a mass-damping response or stability parameter  $K_s$  (some variations of the parameter can be found in literature, e.g. the Scruton number  $Sc$ ,  $\delta r$ ,  $R_p$ ), and is given by  $K_s = \frac{2m\zeta}{\rho D^2}$ , where  $m$  is the mass of the body per unit length, including added mass,  $\zeta$  is the logarithmic decrement of the damping, excluding hydrodynamic damping, with  $\gamma$  for the damping ratio and  $\rho$  the external fluid density.

The non-dimensional amplitude  $A/D$ , as function of the stability parameter, can be estimated from experimental results (Barltrop et al., 1990) (Barltrop, 1998) or empirical equations based on prediction models using experimental lift coefficients (Sarpkaya, 1979), although special care must be considered due to variability of experimental data at low or low mass ratios (Khalak and Williamson, 1999).

The mass ratio or reduced mass, is defined as the ratio of the mass per unit length, including contents, respect to the mass of the fluid displaced by the submerged element, which for cylindrical elements is given by  $m^* = (m + m_a) / (\rho D^2 / 4)$ . It is a relevant parameter for tow-out installation methods of risers and bundles, since these are generally executed at near neutrally buoyant conditions, which increases the lock-in frequency range where vortex shedding synchronises to natural frequencies.

### **2.1.1 Amplitude response branches, transitions and associated vortex wake patterns**

When plotting VIV experimental response amplitudes of elastically mounted rigid cylinders (commonly the non-dimensional amplitude  $A/D$ ) against the reduced velocity, important hysteresis effects in the response have been documented. Two branches in the response behaviour characterise the classic experiments of Feng (1968) with a high mass ratio cylinder, the initial and lower branches are relevant; whereas cylinders with a low mass ratio present responses with three branches, initial, upper and lower branches.

In the work of Khalak and Williamson (1999), the initial branch was characterised by two sub regimes of approximately quasi-periodic ' $qp$ ' and periodic ' $p$ ' behaviour, where the phase angle, the angle between the lift force and displacement, slips through 360 degrees for  $qp$ , remaining about 0 degrees for  $p$ , up to reduced velocities values about 4.4 (see figs. 3 and 14 in the referenced paper).

In the previously cited work, the transition between initial and upper branches is described with a jump of both, amplitude and frequency response, while the phase angle remained about 0 degrees, identifying a hysteretic behaviour for the jump from the initial to the upper branch going from lower to higher reduced velocities about a value of 4.7 and the jump from the upper to the initial branch from higher to lower reduced velocities at a value of about 4.5.

Despite the initial-upper transition, the transition was observed to switch intermittently with a weak lock-in between upper and lower branches in the reduced velocity range of 5.0 to 5.6, where the phase angle indicated the predominant mode, remaining for a number of periods at either values around 0 or 180 degrees, which can be observed in figs. 19 and 20 of the work by Khalak and Williamson (1999).

It is also of interest to identify the association between vortex wake patterns and the amplitude response branches during synchronisation. The main vortex wake patterns near lock-in regions 2S, S + P and 2P, their variations and associations with the response branches were described by Williamson and Roshko (1988), where the 2S mode (two single vortices per cycle) was associated to the initial branch and the 2P mode (two pairs of vortices formed per cycle) to the lower branch.

Additional work by Govardhan and Williamson (2000) identifies the association of the 2P mode to the upper branch and showed the relation of jumps in vortex phase, where the phase is measured between vortex force and displacement, to the initial-upper branch transition and corresponding 2S and 2P vortex wake modes. The upper-lower transition is then shown to be related not with a vortex phase jump but a total phase jump, the phase of the total force and displacement, since both branches presents the 2P vortex wake mode.

It is noteworthy that the cited research works in this section (which identify the response amplitude branches and their reduced velocity ranges related to the hysteretic behaviour,

jumps, switching transitions and the associated vortex wake modes) have been conducted over rigid cylinders with forced oscillations or free to oscillate, or cylinders in cantilever support conditions in current flows.

It is considered that some variations could be expected for experiments modelling horizontal towing of a long slender cylinder subject to tension forces and a number of additional non-linear effects, thus the motivation to conduct experimental work looking to enable some methods for further research, especially considering the potential of some mathematical models for improvement of VIV predictions.

A good revision of current VIV prediction models and their dependency on experimental coefficients is given by Gabbai and Benaroya (2005) and this was found also helpful for planning the experimental work within the scope of this research.

### **2.1.2 VIV of long slender cylinders oscillating in CF and IL directions**

VIV of long slender cylinders is not considered to be fully understood (Wu et al., 2012), here the authors make a comprehensive review of research work on the subject, addressing topics on complex sheared flows acting over typical slender structures in ocean environments, such as risers, tethers and mooring lines, which can cause different and competing response modes along the length of the structures, leading to multi-mode vibrations and other phenomena, e.g. unsteady lock-in, higher harmonic responses, dual resonance or a travelling wave dominant response.

The dynamic characteristics of long slender cylinders related with the domination of the tension and bending stiffness parameters are mentioned in the work of Wu et al. (2012), identifying a significant influence on response branches. The authors cite the work of Vandiver et al. (1996) about some switching vibrational modes identified during lock-in conditions, which are attributed to fluctuations in tension or flow.

Non-lock-in behaviour is also addressed and described for long cables experiments by Kim et al. (1986), where the peak of the spectrum responses identifies the vortex shedding frequency but with a broader bandwidth that can cover adjacent natural frequencies of the cables.

The dual resonance, typically associated with figure eight cylinder orbits in VIV experiments over short cylinders allowed to vibrate in both, CF and IL directions, are examined by Wu et al. (2012), mentioning that dual resonance has been found in long slender cylinders (HueraHuarte and Bearman, 2009), although different shapes in the orbits were observed along the axis of the cylinder. The authors also describe important experimental findings about the influence of tension in response branches and the prediction of response frequencies under lock-in conditions using a Strouhal number about 0.16.

Higher harmonic responses in VIV related with multi vortex patterns in the wake of the flow and their interaction with the cylinder motion under lock-in conditions has been studied for short cylinders (Dahl et al., 2007), where lift forces were found not only dominated by the fundamental response associated to the Strouhal frequency, being the higher harmonic responses significant to structural fatigue (Vandiver et al., 2009).

A possible explanation of higher harmonics is given by Wu et al. (2012) in the equations 3 to 7 of the paper, considering force coefficients for lift and drag forces at an angle with respect to x and y axes, due to the relative motion of the cylinder.

Traditionally, the non-dimensional response amplitude  $A/D$  has been used to characterise VIV responses, but as shown in the work of Williamson and Jauvtis (2004), the transfer function from force to displacement filters out higher harmonic responses; hence, it makes sense to consider strain or acceleration response characterisation for experimentation and research involving a long slender cylinder, especially considering the impact of higher harmonics in structural fatigue as mentioned above.

In the work of Williamson and Jauvtis (2004), important findings about response branches and a vortex wake mode, a triplet of vortices defined as the “2T” mode, are especially relevant for cylinders with a low mass ratio, which are of interest in this research.

In addition to the standing wave response associated to uniform flows, Vandiver et al. (2009), identified travelling wave dominant responses in long slender cylinders subject to sheared flows, the motion trajectories along the span of the cylinder showed large variations attributed to variations of the phase angle along the cylinder, which in turn is attributed to phase velocity differences due to differences in added mass between IL and

CF vibrations for a tension dominated cylinder. The influence of bending stiffness over higher harmonic responses is also discussed.

Wu et al. (2012) proposed that wave dispersion leads to phase velocity varying along the length of long slender cylinders considering the difference of frequency response between IL and CF directions, which may cause the difference between IL and CF phase velocities.

In an early investigation by Vandiver (1993), a wave propagation parameter (being the mode number and the hydrodynamic source of damping) was proposed to predict whether the response behaviour is represented by: a standing wave, a combination of standing and travelling waves or a travelling wave dominant response, for  $0.2 < < 2.0$  respectively.

From previous research, it is evident that VIV over long slender cylinders presents significant differences with respect to a much large knowledge about the phenomena over short cylinders, as reviewed for multi-mode responses, higher harmonics responses which may have important impacts in structural fatigue, variations of trajectories along the length of cylinders due to phase angle differences between IL and CF directions, especially for aspect ratios above a range of  $10^2 - 10^3$  as concluded by Wu et al. (2012).

### **2.1.3 VIV over circular cylinders in yawed flows**

The independence principle (IP) has been traditionally applied to approximate response predictions for yawed flows. For circular cylinders the principle empirically assumes that the flow dynamics are essentially determined by the normal component of the flow velocity respect to the cylinder axis, neglecting the influence of the axial component (Schlichting, 1979), the yaw angles are considered to depart from  $0^\circ$  when the cylinder axis is fully perpendicular to the flow direction, to  $90^\circ$  when the cylinder axis is fully parallel to the flow.

The validity of the IP has been studied in the past for fixed cylinders in several conditions and it was found a possibility that body inclination can lead to oblique vortex shedding, i.e. the vortex rows in the wake of the flow are not parallel to the axis of the body from which they are shed, here, the assumptions for the IP are no longer valid specially for large yaw angles (Ramberg, 2006), although for the case of cylinders allowed to vibrate transversally, the majority of the tests found parallel shedding at lock-in conditions in the previous cited work, where the vortex wakes were described by the IP.

Other research works over flexible mounted inclined cylinders (Jain and Modarres-Sadeghi, 2013) show that even when parallel shedding can be identified at yaw angles of 45° and 65° in their test conditions, they found a change in the range of reduced velocities for lock-in with respect to tests at lower yaw angles, which implies that parallel shedding do not necessarily secures the IP if the lock-in range is considered as a criterion of validity.

More recent studies (Bourguet et al., 2015), found parallel shedding in a flexible cylinder at a yaw angle of 60° subject to current flow, where the IP provided good predictions as long as the IL bending response is small.

The authors states that if the IL response is significant, the induced shear flow can lead to multi-frequency responses which deviate from the IP.

The findings of research work cited in this section for VIV in yawed flows, has been reviewed by Bourguet and Triantafyllou (2015), whom indicate that for larger yaw angles, the behaviour remains to be investigated.

In the former work, a direct numerical simulation of a tension dominated flexible circular cylinder at a yaw angle of 80° and  $Re=500$  under current flow is investigated, the main findings are related with the confirmation of IL and CF oscillations under lock-in condition, i.e. VIV, with a predominant standing wave response in all cases analysed, although a mixed response of standing waves and travelling waves are reported. The fixed rigid cylinder case is also analysed to confirm an oblique vortex shedding pattern with a large angle respect to the cylinder axis where the IP is not valid, as previous research works suggested.

The parallel or oblique vortex shedding nature of the response is found to be dependent on tension, with large differences respect to the fixed cylinder condition, showing significant reductions in the vortex shedding angles and frequencies, with a 2S pattern in the wake structure and figure eight orbits. Counter-clockwise trajectories are reported to be more favourable to body excitation and clockwise orbits to vibration damping.

Under oblique shedding, the frequency response prediction is underestimated by the IP, although for parallel shedding, the frequency response is found to be close to that predicted by the IP for the normal incidence of the flow, however, is indicated that this behaviour does not imply validity of the IP, due to major differences in oscillation and force amplitudes.

A spanwise asymmetry of the flow-structure is confirmed due to a significant shear of the local perpendicular current, which are explained by the asymmetrical profiles of the ILbending response.

## **2.2 Metocean characteristics in Mexican waters of the Gulf of Mexico**

The oil and gas industry has been an active user and contributor for the development of marine forecast services, which are required with the greatest possible level of knowledge, to conduct a safe design for the construction, installation, operation and maintenance of offshore infrastructure.

Specific meteorological and oceanographic (metocean) forecast services are commonly used to avoid the exceedance of environmental load limits, predominantly wind and waves conditions, during typical time frames related with the transport and/or installation of offshore structures, according to project specifications, operation manuals and related codes, regulations and marine warranty requirements.

For the towing installation methods of marine risers, and particularly for the specific locations of interest in the Perdido fold belt area in the Gulf of Mexico, we are interested in continental shelf circulation patterns below latitude 26°N and about 200 km to the east from the shore.

The Mexican continental shelves to the west and south of the Gulf of Mexico shows circulations associated to cold front systems coming from the northwest continental part of the United States during autumn-winter seasons and south-southeast winds during summer, these circulations are reported also to be affected by mesoscale eddy currents interacting with the slope of the continental shelf (Zavala-Hidalgo et al., 2006).

According to published work from the oceanography department of CICESE, a Mexican scientific research centre in Ensenada Baja California, hired by Pemex to conduct metocean measurements and analysis for the Gulf of Mexico, the continental circulations has been well documented only for the American part of the Gulf, precisely above 26°N, being

underrepresented in the Mexican counterpart (Dubranna et al., 2011); here the authors improve on the description of the continental shelf circulation of interest, based on measurements from seven moorings equipped with Acoustic Doppler Current Profilers (ADCP) deployed between 2007-2009, trajectories of 36 surface drift buoys on shallow waters (less than 200 m of water depth), satellite altimetry and wind models.

One of the main findings reported in the previous publication is related with the seasonal shift in the circulations along the studied continental shelves. Although some surface current values are reported, including some periods of measurement from a mooring in the area of Perdido, it is emphasised the influence of eddy currents as a cause of the variability found against the wind driven circulations.

Further work during longer periods of measurements and analysis were conducted by CICESE for Pemex, the installation of the full measurement network considered in the project consisting of four metocean measurement locations, from which three floating platforms were installed in shallow waters and one metocean buoy in deep water (see fig. 2.1), 30 moorings with ADCP (see fig. 2.2) and 444 surface drift buoys launched from 2007 to 2013 plus an agreement for the use of data transmitted by surface drift buoys launched from 2010 to 2013 in the north of the Gulf of Mexico (NGOM) and entering the Mexican waters (see figs. 2.3 and 2.4).

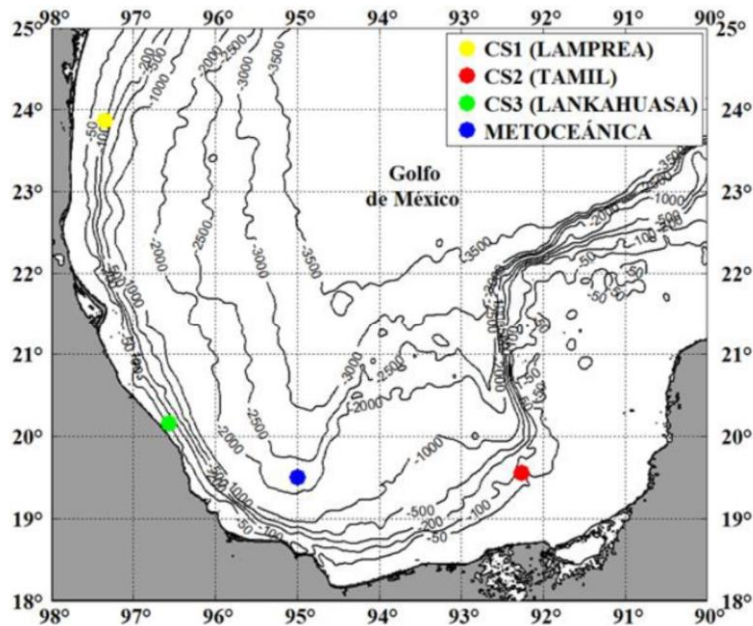


Figure 2.1 Metocean measurement locations (CICESE, 2013b).



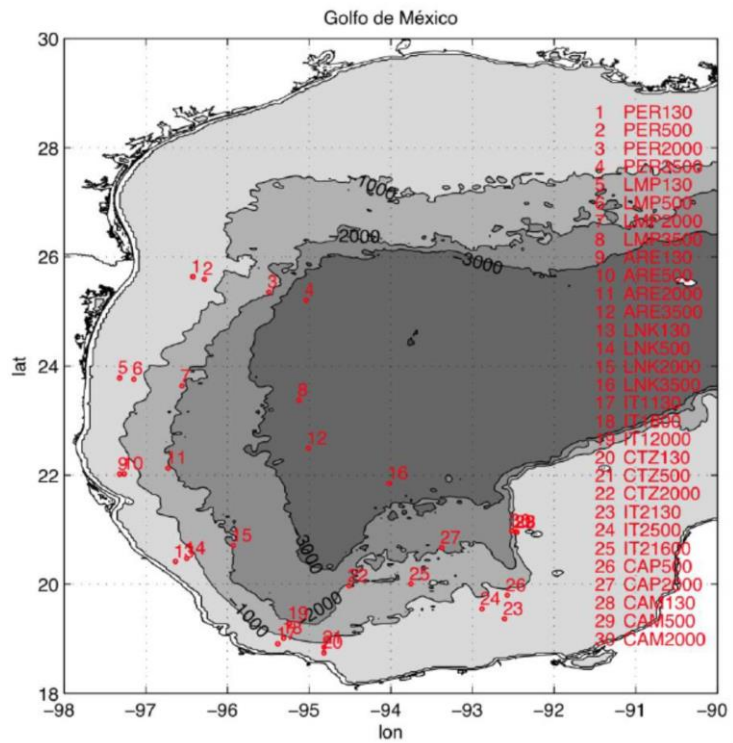


Figure 2.2 ADCP mooring locations (CICESE, 2013a)

The reports of the study had improved the knowledge of the circulation in the Mexican sector and the study of the interactions with anticyclonic eddies released from the loop current.

The statistical data of more than 6 years from the drift buoys in these studies are an unprecedented data base for the surface circulation in the Mexican sector of the Gulf of Mexico.

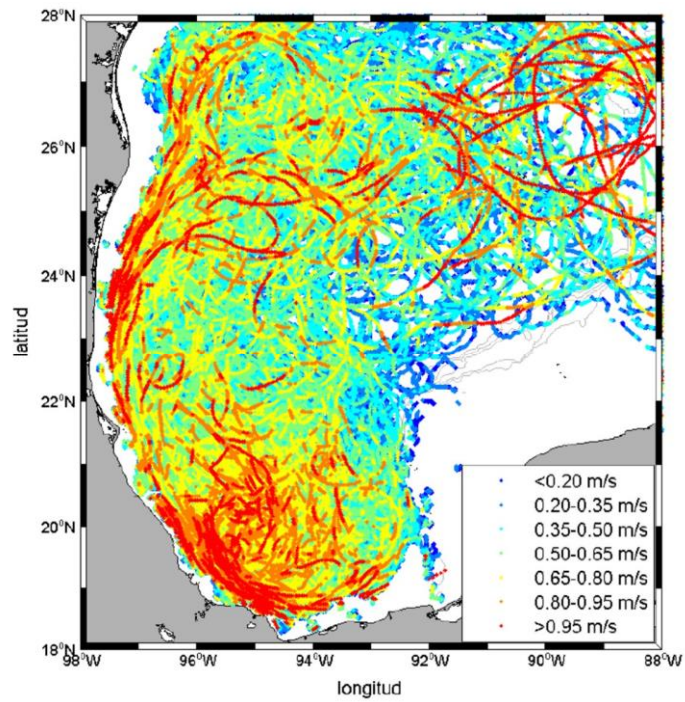


Figure 2.3 Pemex surface drift buoys hourly data 2007-2013 (CICESE, 2013a).

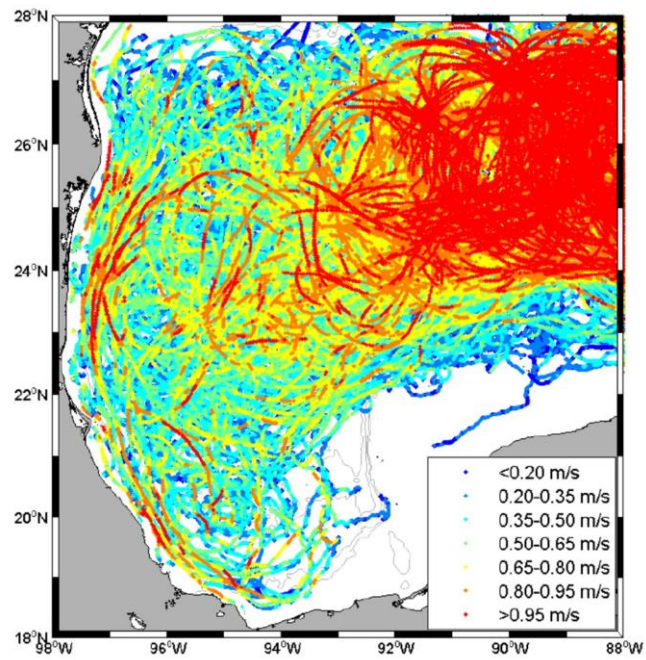


Figure 2.4 NGOM surface drift buoys hourly data 2010-2013 (CICESE, 2013a).

The statistical behaviour identifies 4 main regions for the circulation (see fig. 2.5), being region 2 of our interest and characterised by elongated standard deviation ellipses along the continental shelf.

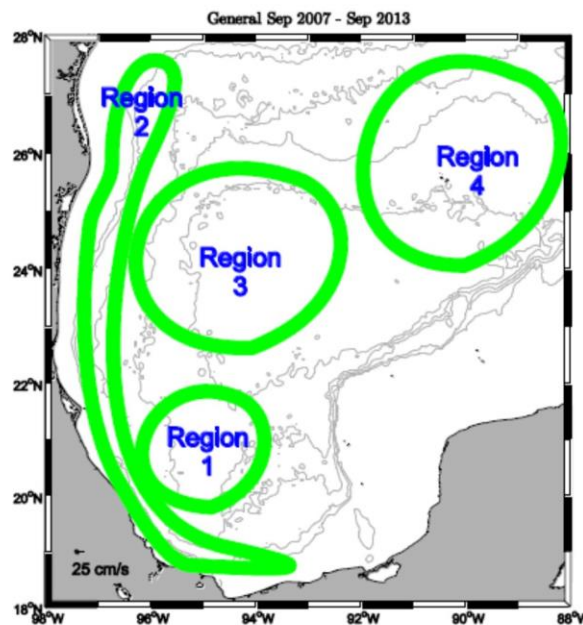


Figure 2.5 Gulf of Mexico circulation regions according statistical behaviour (CICESE, 2013a).

The reports include mean and maximum speeds for surface currents of the circulation in meshes of  $0.25^\circ$  and, standard deviation ellipses for the total period of studies and for the important seasonal behaviour, considering the identification of circulation patterns during the annual 4 seasons.

The information is found to be useful for selection of potential fabrication yard sites for risers and/or pipe bundles, being preliminary located two sites about  $25^\circ 47'N$  near Matamoros, Tamaulipas coast or  $20^\circ 50'N$  near Tuxpan, Veracruz; the lately representing 300 miles further to the south of Perdido area but a more central position for the entire Mexican sector.

One of the most interesting conclusions of the reports with respect to Perdido area, is the identification of the autumn-winter season for moderate to low circulation speeds, with mean values along the potential towing routes from the Matamoros coast, slightly below

26°N, with up to 0.3 m/s and maximum values up to 1.0 m/s, which allows the establishment of better scenarios for the planning of offshore towing operations or to evaluate the risk level and importance of eddy current watch and forecasting services.

The previous surface current values are within the same reported values from ADCP measurements of the moorings of Perdido area in the study of reference, and within specified current speeds in Pemex design norm NRF-003-2007 for transport analysis of offshore structures.

The typical speeds reported for tow-out operations of riser towers can be found up to 3.5 knots (Alliot et al., 2006), equivalent to about 1.75 m/s. In order to plan the experimental work within the scope of this research, this towing speed was chosen, and the likely scenario of a transversal current was a mean speed of 0.3 m/s.

For the previous condition, the flow vector towards a towed riser will have an approximate angle about  $(0.3/1.75) \approx 10^\circ$  which is usually referred as a corresponding yaw angle of  $80^\circ$  in VIV studies; hence, this angle will be considered as a setup angle for the riser model during the intended tests in the towing tank of the Kelvin Hydrodynamics Laboratory, in order to investigate VIV effects within a range of towing speeds and wave combinations.

The Pemex-CICESE project related with the metocean measurements and analysis for the Gulf of Mexico, included the development of a state of the art Hydrodynamic Forecast Operational System (see fig. 2.6) with high resolution for the oceanic circulation, which is based on three numerical models, the Global Forecast System (GFS), the Weather Research and Forecasting Model (WRF) and the Hybrid Coordinate Ocean Model (HYCOM), starting operations in October 2013 (UNAM, 2013a).

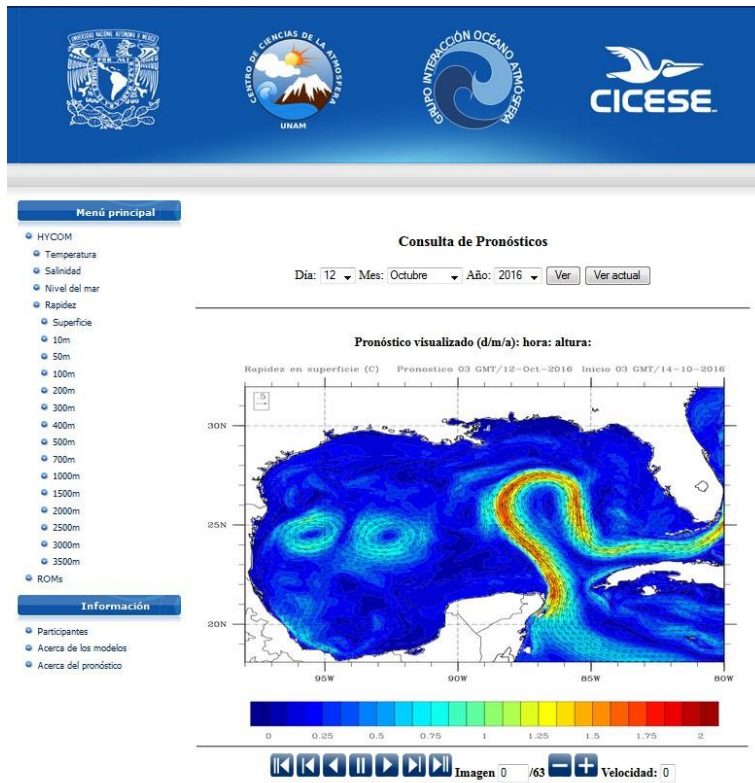


**Figure 2.6 Hydrodynamic Forecast Operational System (UNAM, 2013a).**

The Hydrodynamic Forecast Operational System constitutes an additional resource to the Numerical Operational Weather and Waves Forecast System developed also by UNAM (National Autonomous University of Mexico) in 2009 for Pemex offshore sectors, namely SIPRONOMO (see fig. 2.7), which is based on the Weather Research and Forecasting Model (WRF) for the weather forecast and the WAVEWATCH III model for the wave forecast (UNAM, 2013b).

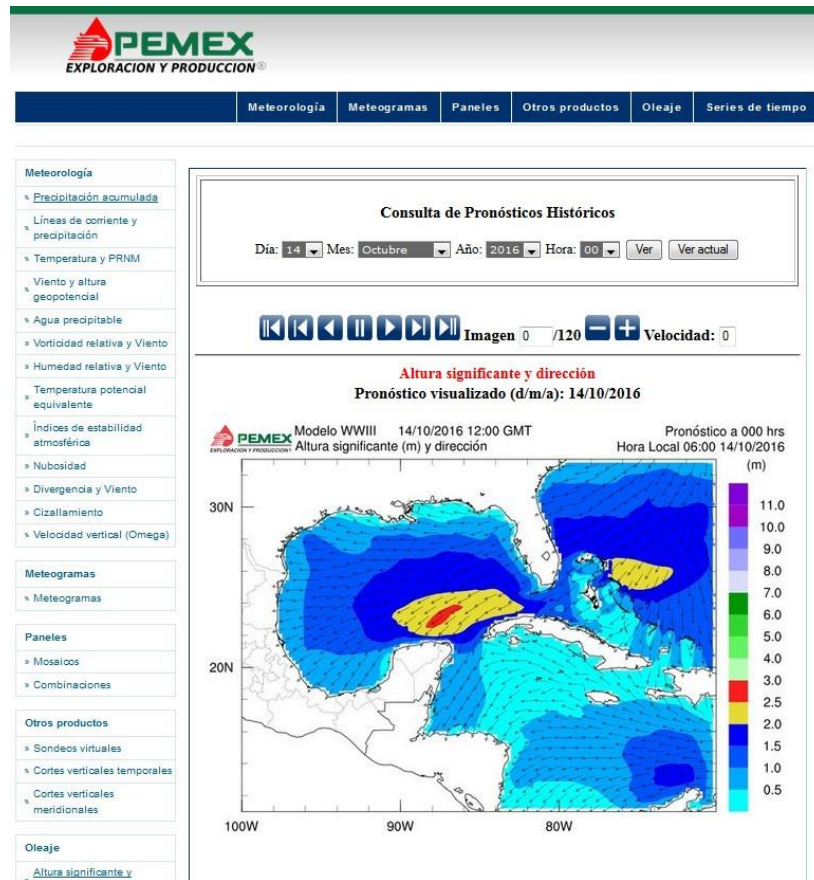


Figure 2.7 SIPRONOMO (UNAM, 2013b).

These forecasting services are already providing a valuable and reliable source of information for offshore operations in the Mexican sector, which will be of great value for the planning of future transportation and towing operations, and to provide statistical data for wave and current design parameters.

### 2.3 Selection of wave parameters for planning of towing tests within the scope of this research

During a towing installation method for riser systems, the towed riser will be subject to unavoidable combinations of wave and current flow loading, demanding the understanding of the wave flow kinematics to conduct studies of some of the effects on VIV responses.

The general characteristics of waves and the current modelling techniques for their representation are well described in offshore codes and design guides; according to a widely accepted recommended practice, DNV-RP-C205, the wave steepness parameter, shallow water parameter and Ursell number are the three main parameters used for the selection of the wave theory able to determine the relationships of the wave length, period and water particle motions within each theory limits.

Thus, the correct selection of the wave theory will provide the means to calculate the wave particle velocities interacting with current flows.

The dimensionless wave steepness  $H/gT^2$  and the dimensionless relative depth  $d/gT^2$  parameters for wave theory selection, requires a definition of the wave characteristics, in terms of the wave height  $H$ , wave period  $T$  and water depth  $d$ .

For the Mexican sector of the Gulf of Mexico, the transport operations for offshore structures are regulated by Pemex norm NRF-003-2007. The norm set the design parameters for typical transport routes along the west and south continental shelves with a significant wave height ( $H_s$ ) of 4.5 metres and spectral peak period intervals from 9 to 11 seconds.

The previous wave characteristics for offshore transport analysis and design is based on probabilistic models using metocean data to determine an exceedance rate, which describes the annual mean proportion of the significant wave height above a given wave height along discrete parts of a selected towing route (Alamilla et al., 2007); the method can be used to determine extreme values for transport routes not included in NRF-003PEMEX-2007, using the return periods according to NRF-041-PEMEX-2014.

For the towing test series planned in this research, the previous wave with  $H_s=4.5$  metres will be selected as an extreme value case, with two additional conditions representing wave heights of 1 and 2 metres, which are frequently expected for planned operations subject to marine forecast. According to tabulated oceanographic information in NRF-003-2007, the most frequent wave periods associated to those waves are about 6 and 7.5 seconds, thus, the three waves to be scaled for the investigation of VIV in the towing test series are chosen as regular waves indicated in table 2.1.

**Table 2.1 Significant wave heights ( $H_s$ ) and Periods (T)**

$H_s$ (m)	T (s)
1.00	6.0
2.00	7.5
4.50	10.0

## **2.4 Relevant design codes for tow-out installation methods**

### **2.4.1 American Petroleum Institute**

The first edition of the API-RP-2RD standard “Design of Risers for Floating Production Systems (FPSs) and Tension-Leg Platforms (TLPs)” from the American Petroleum Institute dates from June 1998, where section 6.2.3.3.1 covered the recommendations for tow-out installation methods.

It briefly provides the description and recommendations of the four main operations associated with the tow-out installation method, i.e. launch, trimming, tow-out and upending, mentioning the likelihood of severe oscillations for neutrally buoyant long bodies that requires exhaustive analysis of the current and wave flow combinations, in order to conduct a fatigue analysis considering the potential of the tow-out operation to take a large part of the fatigue life (recommended practices for fatigue design are covered in section 6.7.1.2).

Section 6.6.3 in API-RP-2RD (1998) describes typical steps for VIV analysis of risers; for the response predictions, it mentions that some models in uniform flow and low mode numbers (< 5) reviewed by Blevins (1977), presented differences within only 15%; however, it also mentions that there was not an accepted way to model VIV in high mode responses and/or sheared flows, and that the conceptual models proposed then, depend on calibrations with substantial model or field data.

The conditions mentioned above for high mode responses and sheared flows are relevant for towing operations of risers, where the long cylindrical structure are also likely to include



appendages for buoyancy/weight control, which creates an interest in this research to explore new technologies for experimental and field data acquisition, while gaining an understanding of the response characteristics, complexity and risk associated to VIV in long flexible cylinders subject to current/wave flows during towing.

In the second edition of the API-RP-2RD standard dated September 2013, brief considerations on towing methods are included in section 8.3.4.2, but additional guidance is now referred to the offshore standard DNV-OS-F101 for SUBMARINE PIPELINE SYSTEMS.

#### **2.4.2 DNV Offshore codes**

DNV offshore codes have been issued for the oil and gas industry by Det Norske Veritas, an international certification body and classification society (currently merged with another classification society, Germanischer Lloyds, as DNV-GL), in three hierarchy levels, Offshore Service Specifications (OSS), Offshore Standards (OS) and Recommended Practices (RP)

Section 10 F in DNV-OS-F101 (2010) provides the recommendations to be considered for the three towing options related with surface or near-surface, mid-depth and bottom tows. It also provides the recommendations to follow for installation manuals and operational procedures; additionally, instrumentation requirements for continuous monitoring and record of towing speeds, tensions, depth of the pipestring and position of ballast valves and recommendations for the installation of strain gauges for monitoring of stresses during towing and installation are given.

Important DNV codes related with the analysis and design aspects of tow-out installation methods were identified and referred in DNV-OS-F101 as follows:

DNV-OS-F201 (2010) DYNAMIC RISERS is particularly important since it provides the guidance and requirements for structural analysis and design of riser systems subject to static and dynamic loading; indicating the application of the global analysis methods, fatigue analysis, design criteria, components, material and documentation requirements during design, fabrication, installation and operational phases.

Specific guidance for global analysis of the riser systems referred to finite element computer codes is given in Appendix A, emphasising the need of a basic understanding of the nonlinearities of riser systems for adequate modelling, summarized in section B 401.

Fatigue analysis guidance is provided in Appendix B.

Related with the topic of this research, the Appendix E of DNV-OS-F201 proposes a fourstep method for VIV and fatigue damage assessment, being:

- 1 Simplified assessment of fatigue damage;
- 2 Multi-modal response analyses based on empirical hydrodynamic coefficients (and tests);
- 3 Computational Fluid Dynamics solving the Navier-Stokes equations;
- 4 Laboratory tests

For step 1, the standard proposes the estimation of induced fatigue damage by neglecting wave flows, assuming only current flow velocities. The planes of vibration must be identified, indicating that for cross flow vibration of symmetric risers, the planes are generally perpendicular to the flow directions, then a procedure is indicated to:

- a) Calculate the natural frequencies and mode shapes for bending in the cross-flow direction by either, analytic or numeric (finite element method) analysis.
- b) Using the Strouhal relationship, with typical St range indicated between 0.14-0.25, a band of local vortex shedding frequencies can be defined.
- c) Identify the parts of the riser where each mode frequency is within the band of local shedding frequencies defined previously.
- d) Identify the mode shapes likely to be excited by VIV and select the one with the highest curvature for a unit modal amplitude (typically the one with the highest frequency).
- e) For a given flow velocity, the amplitude of vibration for the mode selected in d) is proposed to be computed according to Sarpkaya (1979) as:

$$\bar{D} = \frac{0.32}{\sqrt{0.06 + (2K_s)^2}}$$

where  $K_s$  is the response parameter (see section 3.2.2.7), is a dimensionless mode shape factor given by:

$$\phi(\theta)$$

$$= \phi \left( \frac{1}{\phi(s)} \right)$$

being  $\phi(s)$  the mode shape at each point  $s$  over the length  $L$ .

- f) A stress range is indicated to be computed as  $S = A \cdot SCF \cdot E \cdot \kappa \cdot (D-t)$ , being  $A$  the amplitude,  $D$  the diameter,  $t$  the thickness,  $SCF$  a stress concentration factor (defined in DNV-RP-C203, section 2.10),  $E$  is the modulus of elasticity and  $\kappa$  is the

curvature of the mode shape  $\phi(s)$ , to be calculated as  $\kappa = \frac{1}{r} \left( -1 + \frac{1}{r} \right)$ , unless a FE analysis has been applied, where the stress can be computed for a unit mode shape amplitude and then the stress range can be obtained multiplying by  $2 \cdot A \cdot SCF$ .

- g) The fatigue damage is then estimated by application of the corresponding S-N curve as  $D = f_n \cdot T_L \cdot S^{-m}$ , being  $f_n$  the frequency of the relevant mode,  $T_L$  the design life, and  $S$  the stress range (which generally considers a stress concentration factor  $SCF$  and a thickness correction factor where applicable), with  $n$  and  $m$  as empirical constants experimentally established, where  $n$  represents the number of stress cycles to failure.

The code indicates that the damage must be computed as a weighted summation over long-term current distribution for velocities and direction, although for screening purposes a 1-year velocity and associated velocity profile is considered conservative.

For fatigue damage estimation during a towing operation, a number of representative blocks could be identified along the towing route to represent different VIV conditions.

Maximum incident flows can be set from route directions and planned towing speeds with respect to seasonal or 1-year return period of current velocities from oceanic circulation statistics; then the estimation of accumulated fatigue damage will be given by a summation of the damage computed for each representative block with the previous simplified assessment. The summation represents Miner's rule for accumulation of fatigue damage:

$$D = \sum_i \frac{n_i}{N(S_i)}, \text{ where } n_i \text{ is the number of stress cycles for each block range } S_i.$$

range .

If the fatigue damage found with the previous simplified procedure is significant, the next steps are indicated in the code to be applied over a generalisation of the previous procedure for multimodal response analysis using models with empirical or semi-empirical hydrodynamic coefficients.

Step 2 can be tackled using VIV models in computer codes for analysis (e.g. the VIVA and SHEAR7 programs based on frequency domain models, or time domain wake oscillator models as explored in Orcaflex software (see section 1.5).

For the step 3, the time domain vortex tracking models, as also explored in Orcaflex, can be considered; although these models are not a full CFD, they implement methods to apply boundary layer theory to model vorticity at separation points, then the vortex tracking is conducted by solving the inviscid Navier-Stokes equations in vortex tracking planes, applying a 2D fluid model normal to the line axis at each node of the riser model. However, these models are still considered as research tools, requiring further calibration with real world data (Orcina LTD., 2006), hence the importance of step 4 to conduct laboratory tests.

DNV-RP-F204 (2005) RISER FATIGUE includes aspects of fatigue design and procedures for marine risers, assessment is based on S-N curves (with further guidance in DNV-RP-C203) and, when appropriate, detailed guidance on fatigue analysis based on fracture mechanics is referred to the British Standard BS 7910, "Guide on methods for assessing the acceptability of flaws in metallic structures".

DNV-RP-F204 defines a fatigue criterion  $\cdot \leq 1.0$ , where  $\cdot$  is the accumulated fatigue damage obtained by the Palmgren-Miner rule, and  $\cdot$  is a design fatigue factor, following with a summary of the typical fatigue assessment procedure, considering all relevant cyclic load contributions to fatigue damage related with WF wave frequency, LF low frequency and VIV cyclic loads for all modes of operation.

For WF and LF fatigue damage contributions, a procedure is indicated to obtain a weighted fatigue damage accumulation as  $= \sum$ , where  $\cdot$  is the number of discrete sea states from representative blocks of the wave environment scatter diagram,  $\cdot$  is the lumped probability of occurrence for the sea states within each representative block/sea state, and  $\cdot$  is the short term fatigue damage.

Section 5.3 of the code provides methods to compute the combined damage of WF and LF, and section 5.4 indicates the conditions for the standard industry practice to sum up the VIV fatigue damage with the combined WF+LF fatigue damage.

The acceptance criteria for VIV induced fatigue in section 4.2 of the code is given as  $D_{VIV} \cdot S_{VIV} \leq 1.0$ , where  $D_{VIV}$  is the accumulated fatigue damage for VIV, and  $S_{VIV}$  is a design fatigue factor for VIV, with further guidance in section 6 of the code for the use of standard safety factors or enhanced risk based safety factors, this acceptance criteria is generalised in section 6.5 of the code to account for the implicit uncertainty of VIV analysis (e.g. Miner sum, S-N curves) and bias of the VIV analysis as:

$$D_{VIV} \cdot (S_{VIV})^{\alpha} = 1$$

Where  $(S_{VIV})^{\alpha}$  is the design life time in years,  $S_{VIV}$  is the fatigue safety factor accounting for uncertainties (which can be calculated with the risk-based criterion of section 6.3 of the code) and  $\alpha$  accounts for bias as

$$S_{VIV} = \left( \frac{h}{h_{ref}} \right)^{\alpha}$$

It's important to note that section 6.3.7 of DNV-RP-F204 makes a strong recommendation to conduct a verification of the safety factors determined during design by an expert and independent body with experience in application of enhanced risk-based safety factors.

Guidance notes in section 6.5 of the code mentions that in some cases evaluated by DNV for VIV safety factors, these presented values from 10 to 15; which means that the uncertainty for VIV predictions can surpass largely the uncertainty of other sources of dynamic responses; this is indicative of the VIV complexity and uncertainty.

Recommendations for VIV fatigue analysis conducted by state-of-practice software are given in section 4.1.2 of the code, indicating the requirement to conduct detailed sensitivity studies for the controlled input parameters of the software.

DNV-RP-H103 (2010) MODELLING AND ANALYSIS OF MARINE OPERATIONS includes towing operations in chapter 7, describing main tow methods and providing some operational

considerations for analysis, modelling, and VIV; although further guidance for VIV is referred to DNV-RP-C205.

DNV-RP-C205 (2007) ENVIRONMENTAL CONDITIONS AND ENVIRONMENTAL LOADS includes, in section 9, a valuable summary of basic concepts for vortex induced oscillations, principles for prediction of VIV and current and wave induced vortex shedding aspects among other relevant guidelines; additionally, section 10 covers a comprehensive guide for the planning and design of model testing. Section 10.6.6.2 mentions recent methods using fibre optics for VIV studies in flexible structures, which are used in this research.

DNV offshore codes are frequently reviewed and updated, thus, it is recommended to verify the latest editions, especially after the DNV GL merge, where codes could be renamed.

### **2.4.3 International Organization for Standardization**

Offshore industry efforts towards the internationalisation of codes and standards have been concentrated with ISO, the International Organization for Standardization, which has published several standards of relevance for the offshore petroleum and natural gas industries under different parts of ISO 13628. Part no. 12, related with Dynamic Production Risers, was initially proposed in 2005 for replacement of API-RP-2RD to provide guidance and requirements and it was reported to be updated as part of a joint industry project, scheduled for ISO ballot in 2010 (Sharma et al., 2010), although no further information about the status of the latest standard draft has been found nor published by ISO to date.

## **2.5 Lessons learned during design, fabrication and installation of deep water riser towers**

Planning and evaluation of riser solutions for deep and ultra-deep water oilfield development can be improved from lessons learned from previous applications of the technology; hence, every effort to investigate both, unforeseen impacts at any project stage or discipline, as well as successful and optimised practices and outcomes, should be conducted and documented by designers from the earliest project stage, with the participation of all those involved.

As a starting review of the issue, some recommendations have been shared from the relative recent experiences in the first project developments for free standing risers.

Useful guidelines were found in conference papers; the general design methodology for deep water riser solutions, and preliminary aspects for flow assurance regarding steel material, insulation and number of risers for multi-line towers were commented (SaintMarcoux et al., 2010), the authors also elaborate on some phases and conditions for risk analysis, identifying main risks during fabrication and installation phases to set the fundamentals of riser monitoring.

Another conference paper (Alliot and Legras, 2005), provides an insight on the lessons learned applied during three generations of designs for multiple-line hybrid riser towers, including the description of some concepts considering during optimisations. It also elaborates on main drivers during first stages of the design process and how the main structural issues, components and bundle arrangements have been tackled during the evolution of the designs.

The previous document highlighted the surface tow-out as a proved and reliable installation method for a project of reference, although indicates the sub-surface tow method as a method to be considered for large diameter bundles subject to specific metocean conditions. It also provides an insight of the cost parameters, a breakdown and a comparison and identification of the cost break-even point against the water depth for single riser lines and riser towers in particular conditions.

A further background on the evolution of hybrid riser towers is provided in another conference paper (Saint-Marcoux and Legras, 2011), here a summary of the advantages and disadvantages of bundle hybrid riser towers is provided, with a diagram of options based on lessons learned to be consider at the conceptual design phase of the bundle arrangement to simplify design and installation.

The characteristic data of latest riser tower projects is provided in the previous document, commenting on lessons learned for the different components of the riser, i.e. the foundation, the lower riser termination assembly, the bundle, the upper riser termination assembly, buoyancy tank and jumpers. Additionally, it emphasises the implementation of a lessons-learned data base for a continuous improvement of design processes.

## 2.6 Considerations to influence research and experimental work

Considering the previous literature review on VIV fundamentals, fluid loading, response prediction and design codes related with tow-out operations, the following aspects were regarded relevant to set the work scope in this thesis:

- The VIV response prediction for submerged cylinders with low values of the massdamping response parameter, which is likely for the near neutrally buoyant condition in a tow-out operation, shows high variability in experimental data.
- The experimental data or prediction models based on empirical equations using experimental lift coefficients has been generally obtained in short length models with different conditions to that of a long slender and flexible cylinder that can better model a riser during tow operations.
- A more representative test model of a tow-out operation could provide a characterisation to identify towing speed limits, to avoid the high responses associated with the transitions to the upper response branch, as reviewed in section 2.1.1.
- Design codes and state of practice software states that the different models to predict VIV responses rely heavily on calibration of hydrodynamic coefficients with substantial model or field data.
- The latest revisions of design codes associated to towing installation methods, mention the use of fibre optic technology for VIV studies in flexible structures.

Most of the motion response measurements in the towing tank facility of the University make extensive use of an optical tracking system for rigid body motions during model testing.

Recently, the manufacturer of this measurement technology has been adapting their cameras and systems to be used underwater, hence the experimental work will assess the potential application of the optical tracking system over slender cylindrical elements for motion capture and it will explore the integration of the fibre optic technology, aiming to set methods for hydrodynamic studies and for investigations of VIV over a more representative model subject to towing operations.



## **3 Qualification of a motion capture system to study transversal vibrations/oscillations**

### **3.1 Introduction**

The planned model testing within the scope of this research on VIV during tow operations was motivated by the need to explore alternatives for vibration/oscillation measurements in future tank testing with slender cylindrical elements to be used as riser models.

The facilities at the Kelvin Hydrodynamics Laboratory, located adjacent to the West of Scotland Science Park in the North-West of Glasgow, have the availability of a camera system for motion capture, mainly based on technology to process time series of 2D coordinate data obtained from cameras by infrared reflection; where retro-reflective material, usually spherical passive markers, are commonly attached to the body or model of interest for motion measurements.

Optical tracking systems have been widely implemented in towing tanks and ocean basins around the world with the technology development in the last two decades, mainly for rigid body motion measurements in model tests, using their non-intrusive advantage over traditional instrumentation (e.g. accelerometers, potentiometers, LVDTs).

The system has also been used successfully for motion capture in some VIV tests, using the regular spherical passive markers on aerial sections of partially submerged models.

During the start of this research; there was not found any published work or antecedent about the system implementation on VIV studies for fully submerged cylindrical elements.

The aim is to explore the possibility to adapt the system's capabilities for motion capture through control points on slender cylindrical elements, for which retro reflective tape

material, in a circular form, is intended to be used as uniformly distributed passive markers along a round tube.

To assess the precision of the system to be used in this way on continuum elements, experiments were conducted with simply supported beam elements, which were excited at one end with a controlled harmonic displacement, in a configuration such that the vertical response along its length can be calculated.

The test allows setting a simplified analytical model and to conduct a finite element analysis to compare the calculated responses against the measurements for beam models with different flexibility.

The natural frequencies of each model can also be compared against the motion capture of a series of pluck tests.

The results are assessed to determine the viability to continue with a second stage, intended to explore the implementation of the motion capture system in submerged conditions, using under water cameras.

### **3.2 Model Analysis**

A simplified model of the experiment is represented in fig. 3.1 by a simply supported beam with harmonic ground motion at one end, where Euler-Bernoulli beam theory is applied, assuming that any cross section along the beam remains plane.

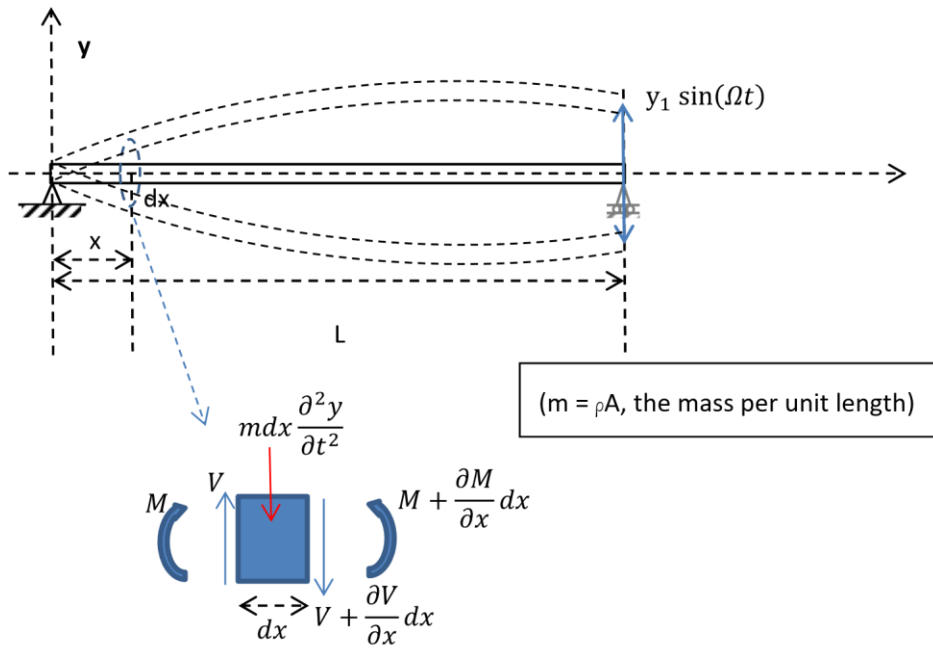


Figure 3.1 Simplified model for vibration analysis

x

A step by step derivation of the analytical solution for the vertical response can be consulted in Appendix A.1, including a revision of a damped beam model for the logarithmic decrement used during experimental evaluation.

### 3.3 Experimental Procedures

When the experimental excitation frequency is not too close to that of the natural frequency of the beam, the response can be estimated by equation no. (A.34) as:

$$= \sum_{i=1}^{\infty} \sin\left(\dots + \dots\right) \left[ \dots \right] - \dots (+ \dots - 2 \dots)$$

Eq. (A.11) will be used to calculate the natural frequencies for the geometry and properties of each beam to be tested.

In eq. (A.34), rotary inertia and shear deformation was neglected, but it can be used as a first estimation of the dynamic response profile, to be compared against a finite element analysis in ANSYS.

From eq. (A.52) and (A.51), the damping ratio can be estimated experimentally with the measure of two consecutive amplitudes.

For lightly damped systems, the precision can be increased with  $n$  cycles, taken the logarithmic decrement as:

$$= \frac{\ln(A_1/A_2)}{n} \quad (3.1)$$

The damping ratio value can then be used with eq. (A.47) to estimate the natural frequencies of the beam from a damped frequency measured in a pluck test.

It also can be used as an input data in ANSYS to calculate the dynamic beam response at excitation frequencies close to the natural frequency.

The ANSYS model will aim to represent the best estimate of the true dynamic response profile of the beams, where rotary inertia and shear deformation is considered.

Frequencies and response profiles will be then compared against data analysis from the motion capture system to assess the applicability of this system on slender cylindrical elements.

The sensitivity of the motion capture system for various flexibilities can also be explored, so the variability of the data analysis results for different configurations in length and or materials will be compared.

### 3.4 Beams properties

Aluminium and carbon fibre materials were chosen to compare the stiffness differences.

The real dimensions were measured at several points along the length and circumferentially for diameter and thickness averages.

For real density determination, each tube was measured and weighed 3 times for average values.

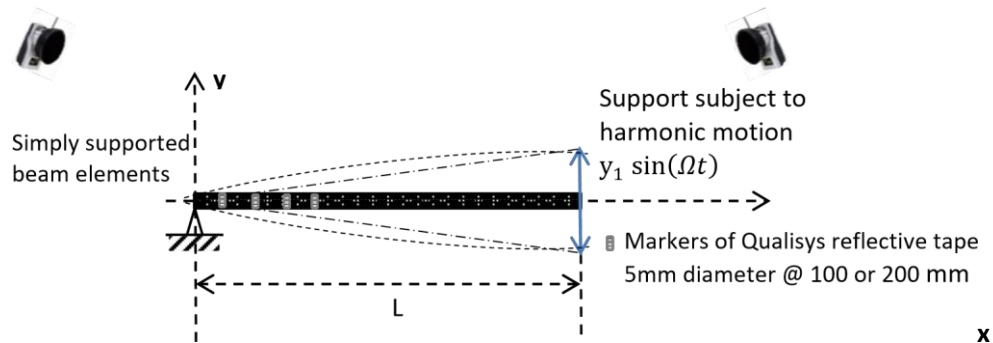
The main properties of the tube elements are shown in table 3.1.

**Table 3.1 Beam properties and geometric data**

Tube No.		1	2	3
Material		Extruded aluminium round tube 6082 T6		Carbon Fibre tube (Roll Wrapped)
Length	L (mm)	4129.00	2106.00	2066.00
Outside Diameter	OD (mm)	25.20	25.20	25.00
Internal Diameter	ID (mm)	19.00	19.00	22.20
Thickness	t (mm)	3.10	3.10	1.40
Aspect ratio	L/OD	163.85	83.57	82.64
Density	$\rho$ (kg/m <sup>3</sup> )	2728.00	2728.00	1720.00
Mass per unit length	m (gr/m)	587.00	587.00	178.60
Young's Modulus (0°)	E (Gpa)	69.00	69.00	90.00
Young's Modulus (90°)	E (Gpa)	N/A	N/A	19.00
Proof stress	$\sigma_{0.2\%}$ (Mpa)	250.00	250.00	N/A
Ultimate Tensile Strength	$\sigma_{UTS}$ (Mpa)	290.00	290.00	400.00
Bending Stiffness	EI (kNm <sup>2</sup> )	0.93	0.93	0.57

### 3.5 Test setup

#### Oscillations on slender beam elements for motion capture



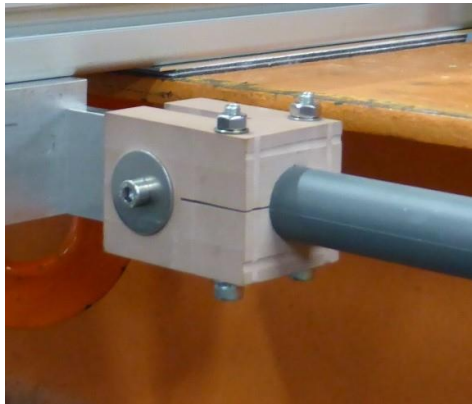
Tube No. 1.- Aluminium round tube OD = 25.2 mm x t = 19 mm x L = 4,129 mm

Tube No. 2.- IDEM No. 1 with L = 2,106 mm

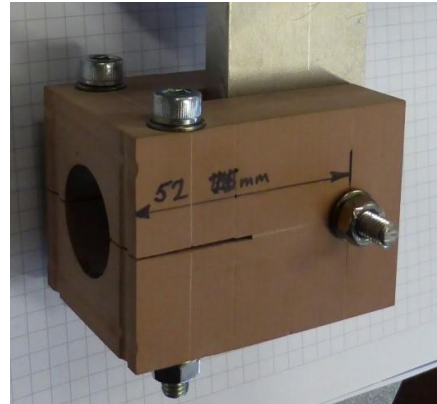
Tube No. 3.- Carbon Fibre Tube (Roll Wrapped) ID=22.2 mm x t=1.4 mm x L=2,066 mm

Figure 3.2 Test sketch

The beam supports were built from polyurethane machinable slab material Axson Prolab 65, these were pinned to structural elements for the simple support condition and partially drilled/grooved to allow the installation of the different tubes with clamping bolts, as showed in fig. 3.3.



(a) Left support



(b) Right support under excitation motor

**Figure 3.3 Beam supports**

For the sinusoidal vertical excitation of the beams, a scotch yoke mechanism was fabricated at the KHL facilities for a maximum amplitude of 25 mm, equivalent to the external diameter of the tube elements, the mechanism was directly coupled to an electrical motor of 420 watts, 3000 rpm, and 133.4 N-cm of torque; initially the torque was not enough to achieve smooth oscillations at low oscillation frequencies on tube No.1, showing smooth sinusoidal oscillations only at one fifth of the desired oscillation amplitude.

A gearbox 5:1 was implemented between the motor and the scotch yoke, using a DC Servo System for speed control, providing a maximum speed of 10 Hertz limited by the gearbox.

To keep the simply supported condition of the beam during the oscillations, the support at the excitation side was mounted under a linear motion guide to avoid axial forces over the beam due to deflections during dynamic response.



(a) Scotch yoke and DC Servo System



(b) Motor, Gearbox and linear motion guides

**Figure 3.4 Scotch yoke mechanism**

The pin support structure and the motor frame support were mounted and fixed over the stiff structure of an auxiliary carriage near the trimming dock area of the towing tank, using mechanical clamps to facilitate the mounting of the different tubes to be tested.

Once each tube was mounted, the amplitude of the scotch yoke was set to zero and a line laser tool was used for levelling the supports, see fig. 3.5.



(a) Tube No. 1, Aluminium, L = 4,129 mm



(b) Tube No. 2, Aluminium, L = 2,106 mm



(c) Tube No. 3, Carbon Fibre, L = 2,066 mm

**Figure 3.5 Preparation of oscillation tests**

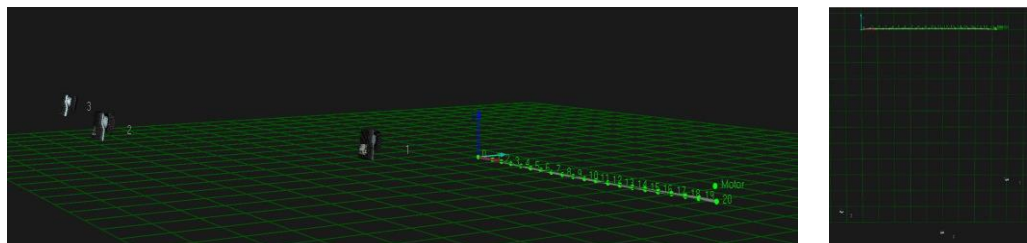
### 3.6 Motion capture system setup

The Qualisys optical tracking system available at the Kelvin Hydrodynamics Laboratory was implemented for the test, Qualisys Track Manager Software (QTM) was used to handle the motion capture process.

Three standard Oqus series 3+ cameras were used for motion capture and a fourth high speed camera of the same series was added during a specific calibration test and to include the capture of synchronized video frames to the 3D coordinates derived by the system for a visual revision.

To perform calculations from 2D data to locate markers in 3D, QTM software must determine the location and orientation of each camera in the setup; this is done by one of the calibration procedures of the system.

The positions of the cameras relative to each tube tested can be visualised from the data files, see fig. 3.6.



(a) QTM Perspective view

(b) QTM Top view

**Figure 3.6 QTM viewer**



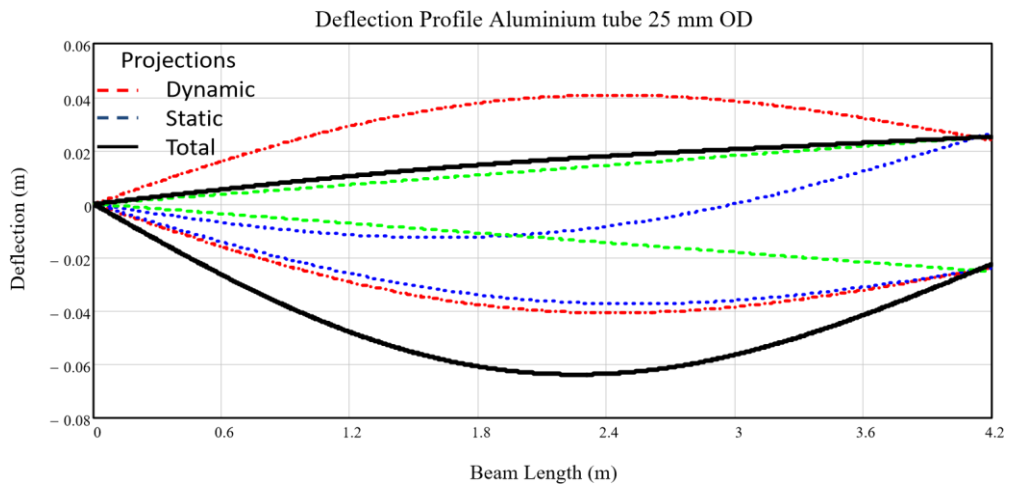
### 3.7 Response Prediction

The calculation of natural frequencies and a set of deflections along the beams for a range of excitation frequencies were executed in Mathcad, according to the equations derived in Appendix A.1 from the simplified model of section 3.1.2.

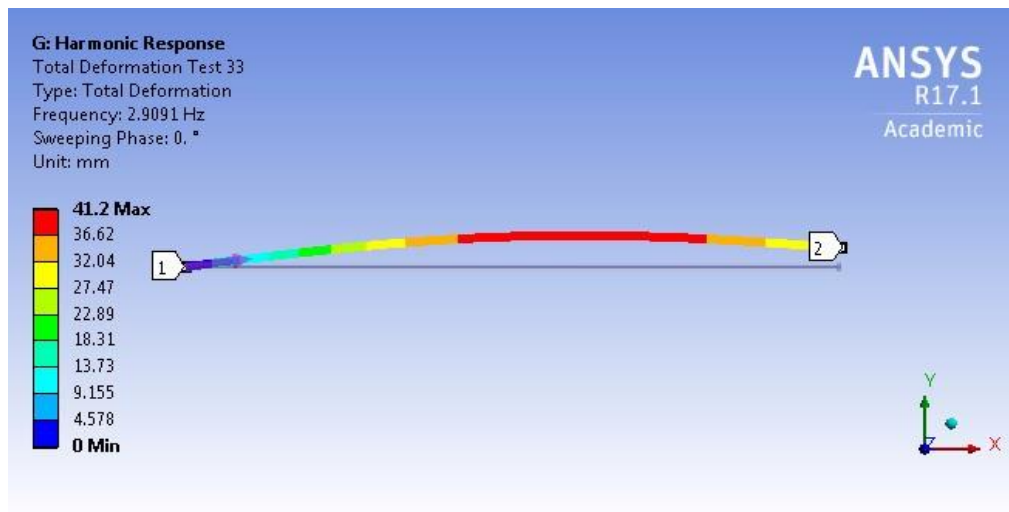
The estimation of maximum stresses and test cycles were reviewed against allowable stresses and cycle dependent fatigue strength of aluminium tubes for safety measures.

Finite Element Analyses of the beams, including details for the supports were performed in ANSYS for static, modal and harmonic response.

The predicted results of both models (see fig. 3.7) were compared against the measured response.



(a) Simplified model response (Mathcad)



(b) Dynamic harmonic response, FEA model (Ansys)

**Figure 3.7 Response prediction on simplified and FEA models**

### 3.8 Fatigue considerations for safety of the tests

It is necessary to perform the experiments with excitation frequencies other than the natural frequencies of vibration of the tubes to prevent excessive deflections due to resonance, which can represent a danger.

As mentioned, the maximum oscillation speed delivered by the motor-gearbox assembly to be used in the test series is 10 Hz.

The fundamental frequencies of vibration of the tubes No. 2 and 3 are well above the maximum speed of the oscillation mechanism, thus, there is no risk of resonance for the tests on these tubes.

On the other hand, the fundamental frequency of vibration for the more flexible tube No. 1 is around 4 Hz. This gives the possibility to test excitation frequencies above the first mode of vibration, allowing a dynamic deflection mode with a node within the beam length; the excitation frequency during the test can be adjusted to approximate the observable location of the node above a marker on the tube, for comparison purposes of capture data against calculations.

It can be expected that a low excitation frequency will produce a beam motion close to a rigid body motion of the static deflection of the tubes, so it is desirable to perform tests with excitation frequencies that generate sufficient dynamic response, taking the necessary precautions near the frequency of the fundamental mode for the tube No. 1.

Considering that the tubes will be subjected to cyclic stresses, it is convenient to verify fatigue aspects on the beams as a safety measure. The analytical calculations used to estimate the dynamic deflections along the beams for different excitation frequencies, can be also used to calculate the distribution and maximum stresses expected for the series of oscillations to be induced on each tube.

This makes it necessary to define a fatigue strength value according to the material characteristics of the tubes.

Unlike ferrous metals such as steel, carbon fibre reinforced polymers, in general, are recognized as being essentially insensitive to cyclic loading, see fig. 3.8, which typically reach endurance fatigue limit values above 40% of their ultimate strength (Drechsler et al., 2009).

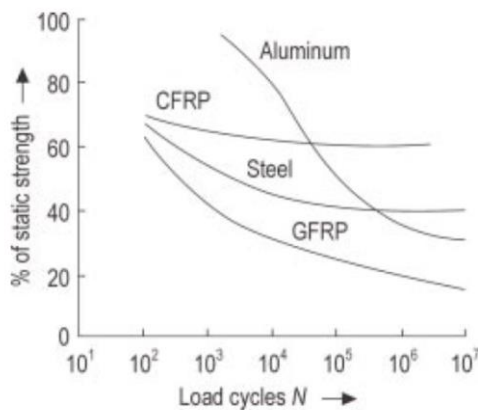


Figure 3.8 Fatigue strength of structural materials (Drechsler et al., 2009).

Non-ferrous metals such as aluminium, while reducing its slope in high cycle zones, are characterized by not having a distinctive limit, and the fatigue strength is associated to the number of cycles before failure.

To estimate the maximum number of cycles that the aluminium tube will undergo, no more than 100 tests of 3 minute are considered, in a frequency range of up to 7 Hz, thus, conservatively the number of oscillations would be about  $(100)(3 \text{ min})(60 \text{ sec/min})(7 \text{ cycles/sec}) = 1.26 \times 10^5$  cycles.

Moreover, the aluminium tube was previously tested when the mechanism was not able to provide smooth oscillations, and the same tube will be used for a third series of tests with a shorter length to be identified as tube No. 2, so the maximum number of oscillations expected would be of the order of  $(1.26 \times 10^5 \text{ cycles})(3) = 4 \times 10^5$  cycles.

S-N curves consulted in a dissertation (Nanninga, 2008) for extruded elements in aluminium 6082 T6, which is the material spec of the tubes to be tested, show a fatigue strength amplitude  $\approx 115$  MPa for specimens longitudinally oriented and  $\approx 95$  MPa for specimens transversally oriented to the extrusion direction. The dissertation states that the most obvious factor of this difference is due to the die lines produced during extrusion, which are parallel to the extrusion direction, see fig. 3.9.

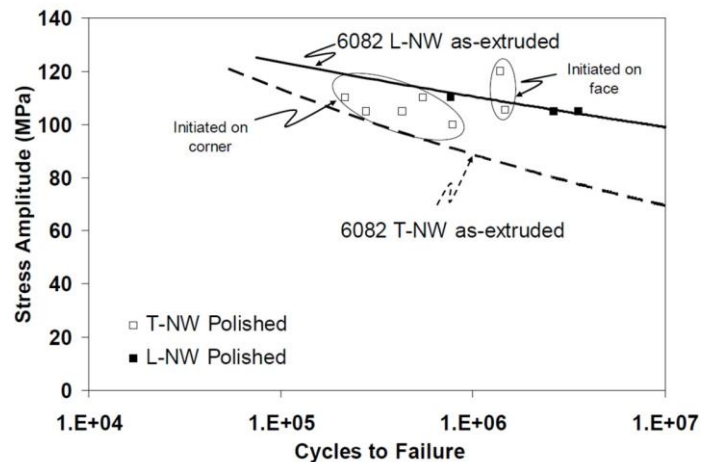


Figure 3.9 S-N curve comparing fatigue lives (Nanninga, 2008)

In the aluminium extrusion processes, heated cast billets of aluminium alloys are discretely loaded into a press, which forces the billets to flow at high pressure and high temperature through die orifices to form a desired shape; the billet to billet interface forms a “charge” weld by the effects of pressure and temperature.

For hollow sections, such as a round tube, hollow dies with a stationary mandrel are generally used, which cause the material flow of the billets to split around the mandrel supports, the metal then re-join in the weld chamber of the die and form an extrusion or “seam” weld by pressure and temperature.

The effects on fatigue lives due to seam and charge welds of the extrusion process were evaluated in the dissertation of reference, stating that seam welds show a minor effect on fatigue lives, while charge welds show more scatter in the results and moderate drops for specific charge zones.

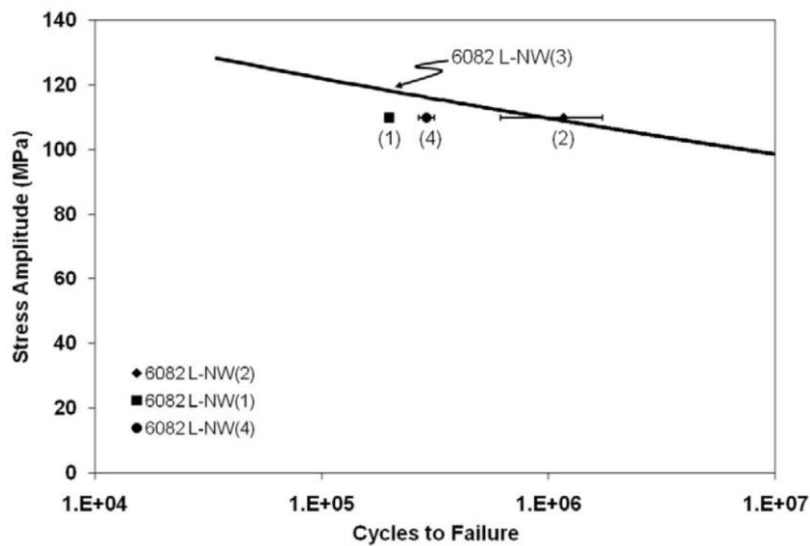
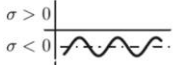
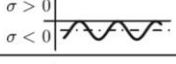
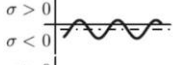
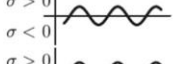
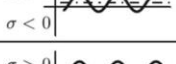
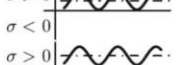




Figure 3.10 Fatigue results showing the effect of extrusion zones at  $\sigma_A = 110$  MPa (Nanninga, 2008)

Considering the above, fatigue strength = 100 was set as a parameter to verify that the maximum bending stresses during induced oscillations remain below the fatigue strength.

It is noteworthy that the consulted curves are constructed from pulsating in tension tests, see table 3.2, with stresses ratios  $R = \sigma_{\min}/\sigma_{\max} = 0.1$ ; that is, the mean stress is a tension.

Table 3.2 Stress ratios R (Rösler et al., 2007)

pulsating in compression		$\sigma_{\max} < 0$	$R > 1$
zero-to-compression		$\sigma_{\max} = 0$	$R = -\infty$
reversed		$\sigma_m < 0$	$-\infty < R < -1$
fully reversed		$\sigma_m = 0$	$R = -1$
reversed		$\sigma_m > 0$	$-1 < R < 0$
zero-to-tension		$\sigma_{\min} = 0$	$R = 0$
pulsating in tension		$\sigma_{\min} > 0$	$0 < R < 1$
static		$\sigma_{\min} = \sigma_{\max}$	$R = 1$

For fully reversed stress ( $R = -1$ ), the fatigue strength is improved over positive mean stress cases ( $-1 < R < 1$ ), which cause a detriment in fatigue life.

There was not found available information for S-N curves of aluminium extrusions with  $R = 1$ ; some empirical relationships consulted, suggest a fatigue strength increase of the order of 20 % from  $R = 0$  to  $R = -1$ . Thus, the fatigue strength = 100 is considered conservative for revision purposes.

A special case is represented by the tube No. 1 with a natural frequency around 4 Hz, it was verified that frequencies around 3 and 5 Hz can be tested securely, by means of a quick speed change in the excitation motor, in order to pass over the natural frequency without excessive responses on the beam due to resonance.

The calculations showed maximum bending stresses of the order of 30 MPa for the range of frequencies to be tested on the aluminium tubes, thus there is not expected any risk of failure during tests due to fatigue under previous considerations.

If further series of tests were required, an assessment of the cumulative damage could be estimated by the Miner's rule method or a more suitable probabilistic model.

### 3.9 Experimental Results

The motion capture system was installed and calibrated about the trimming dock area of the towing tank in KHL, the system's manual sets some considerations to be followed for camera positioning and calibration procedures; after the calibration procedure is performed, the system reports the calibration results as average residuals per camera, which were in the order of 0.2 to 0.6 mm during our tests. The system also controls trajectories during processing of 3D tracking with two parameters for maximum residual and prediction error.

### **3.9.1 Pluck Tests**

A series of pluck tests were performed for natural frequency and damping analysis, the vertical "Z" position from 3D data files were exported and analysed with the software Spike2 to compare the frequency obtained from each reflective point or marker along the beam, to assess the degree of consistency in the captured data.

The consistency, in each marker frequency, obtained from sinusoidal fitting of captured data is shown in table 3.3 for the Tube No. 1. It was evident that the greater motion of the central markers showed a better precision, thus for stronger plucks (order of 2 OD instead of 1 OD) the agreement improves due to the increment in the oscillation amplitude, although a small increment of damping (and the consequent small reduction in the damped frequency measured) becomes evident.

**Table 3.3 Frequency measured at each marker along Tube No. 1 during pluck test**

Marker No.	Damped Nat Freq (Spike data fit) Pluck No. 1 (1 OD)	Damped Nat Freq (Spike data fit) Pluck No. 2 (1 OD)	Damped Nat Freq (Spike data fit) Pluck No. 3 (2 OD)
	Hz	Hz	Hz
1	3.6576	3.6594	3.6551
2	3.6587	3.6582	3.6552
3	3.6587	3.6581	3.6551
4	3.6585	3.6581	3.6551
5	3.6586	3.6581	3.6551
6	3.6587	3.6582	3.6552
7	3.6586	3.6581	3.6551
8	3.6586	3.6581	3.6551
9	3.6586	3.6581	3.6551
10	3.6586	3.6581	3.6551
11	3.6586	3.6581	3.6551
12	3.6585	3.6580	3.6551
13	3.6585	3.6580	3.6551
14	3.6585	3.6580	3.6551
15	3.6585	3.6580	3.6551
16	3.6585	3.6579	3.6551
17	3.6584	3.6580	3.6551
18	3.6586	3.6582	3.6551
19	3.6582	3.6577	3.6551
$\mu$	3.6585	3.6581	3.6551
$\sigma$	0.0003	0.0003	3.0E-05

The complete Z position data was also analysed with the power spectrum tool in Spike2 software, which uses a Fast Fourier Transform (FFT) to convert data into a power spectrum density (PSD), with the agreement of

previous results as shown in Fig. 3.11. It is worth to mention that a Hanning window was selected to compute spectra for this and all subsequent PSD analysis in this thesis.



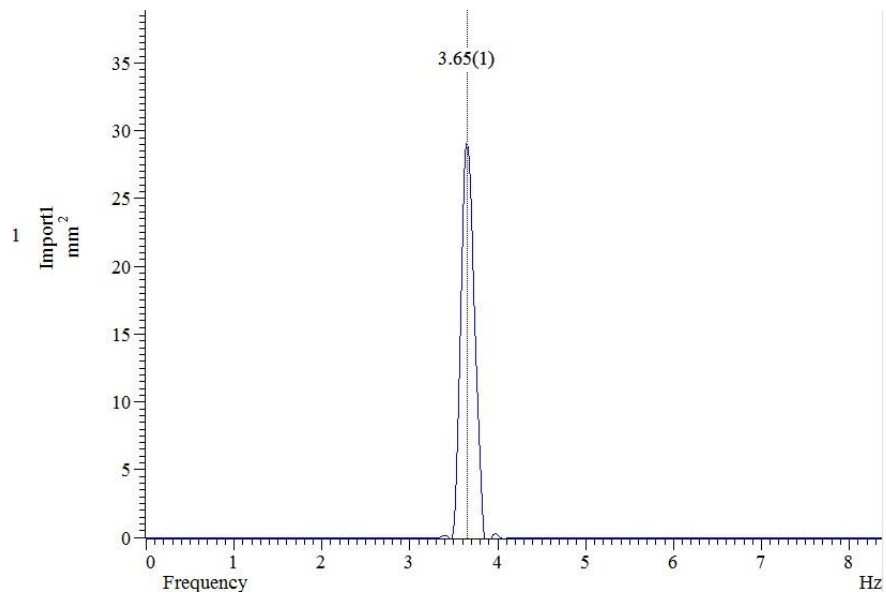


**Figure 3.11 PSD of pluck tests data for tube No. 1**

Once the frequency consistence between markers was reviewed, the value of the damped natural frequency of each beam was set from the data analysis of a central reflective point or marker. The next step requires the experimental determination of the damping ratio for each beam, in order to get the natural frequency of each beam to be compared against calculations.

The damping ratio of the beams was determined from decay analysis of captured data for each pluck test, using the logarithmic decrement method.

The low damping observed in the response of the aluminium tubes, allowed the setting of 20 cycles for a better precision in the decay analysis to estimate the damping ratio, the final value was set as an average of results from three test, as showed in table 3.4.

**Table 3.4 Damping ratio experimentally obtained for Tube No. 1**

Pluck Test No.	Amp @ cycle 1	Amp @ cycle 21	$\delta$ 0-20	$\zeta$ 0-20
	(mm)	(mm)		

1	23.2300	9.0179	0.0473	0.0075
2	22.2592	8.2886	0.0494	0.0079
3	23.9899	9.7595	0.0450	0.0072
		$\mu$	0.0472	0.0075
		$\sigma$	0.0022	0.0004

On the other hand, for the combination of the high stiffness and length of the carbon fibre beam (Tube No. 3), only small initial deflections were achievable during plucks, where a higher damped response in the form of a quick decay with just 4 to 5 cycles after each pluck was experienced, with very small amplitudes after the first cycle, thus the estimation of the damping was set as an average of a series of pluck tests (13) considering the decay of the first cycle in the response as shown in table 3.5.

**Table 3.5 Damping ratio experimentally obtained for Tube No. 3**

Pluck Test No.	Time (s)		Damp Freq (Hz)	Amplitude (mm)		Log Dec $\delta$ 1-2	$\zeta$ 1-2	Nat Freq (Hz)
	x1	x2		x1	x2			
1	0.8152	0.8598	22.4316	4.6196	2.8097	0.4972	0.0789	22.5017
2	3.8521	3.8970	22.2717	5.3096	3.4895	0.4197	0.0667	22.3214
3	6.7180	6.7627	22.3864	4.1598	2.3301	0.5796	0.0918	22.4814
4	9.6529	9.6985	21.9202	5.7598	3.9697	0.3722	0.0591	21.9586
5	12.8270	12.8722	22.1239	5.7198	3.9397	0.3728	0.0592	22.1628
6	15.4324	15.4776	22.1239	5.4095	3.4596	0.4470	0.0710	22.1798
7	18.0940	18.1391	22.1729	5.4896	3.5894	0.4249	0.0675	22.2236
8	20.9939	21.0392	22.0751	4.9897	2.9298	0.5324	0.0844	22.1542
9	24.2190	24.2643	22.0751	5.7294	4.1096	0.3323	0.0528	22.1059
10	26.7554	26.8009	21.9780	6.3094	4.4594	0.3470	0.0551	22.0115
11	29.7885	29.8339	22.0264	5.3497	3.1296	0.5361	0.0850	22.1065
12	32.6810	32.7259	22.2370	5.7598	3.7998	0.4160	0.0661	22.2857
13	35.5816	35.6271	21.9780	5.8095	3.9494	0.3859	0.0613	22.0194
$\mu$			<b>22.1385</b>			<b>0.4356</b>	<b>0.0692</b>	<b>22.1933</b>
$\sigma$			<b>0.1571</b>			<b>0.0784</b>	<b>0.0124</b>	<b>0.1684</b>

For the high stiffness of this Tube No. 3, the amplitudes and frequencies measured for each pluck test, shows greater variability than those obtained for the more flexible aluminium

beams; although this variability represented less than 1% respect to the estimated natural frequency.

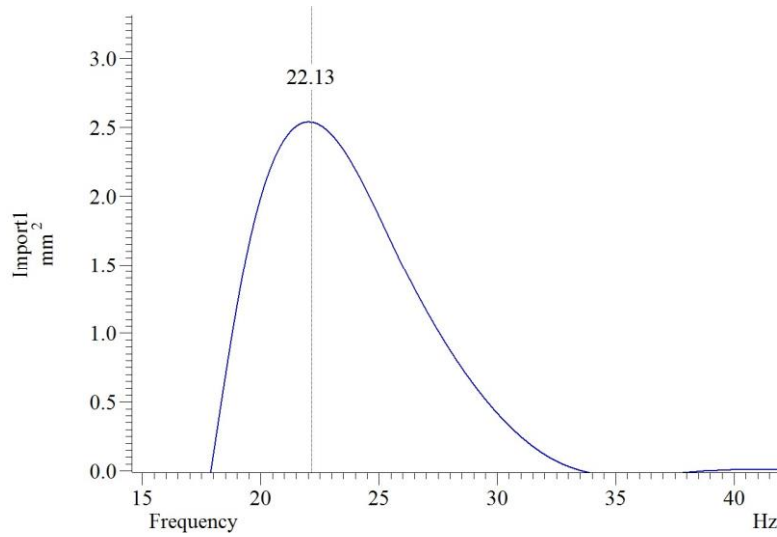


Figure 3.12 PSD analysis of pluck tests data for tube No. 3

Table 3.6 shows the values obtained from the experimental data and those calculated by analytical and finite element methods for the three tubes tested:

Table 3.6 Natural frequency predictions against measured values

Beam Material	OD (mm)	ID (mm)	Length (mm)	Pluck test values MOCAP Data			Calculations	
				Damped Freq. (Hz)	Damping ratio (%)	Nat Freq. (Hz)	Nat Freq. Mathcad (Hz)	Nat Freq. Ansys (Hz)
Tube No. 1 Al	25.2	19.0	4129.0	3.657	0.752	3.657	3.656	3.653
Tube No. 2 Al	25.2	19.0	2106.0	14.01	1.275	14.012	14.052	14.036
Tube No. 3 CF	25.0	22.2	2066.0	22.14	6.92	22.193	22.247	22.164

From the analysis of the above data to determine the frequency and damping ratios of the beam models, it was found that:

- The motion capture system demonstrates a very good consistency for all markers along the tube elements.
- Precision of the captured frequency among markers along the beam, improves at the markers with the highest oscillation amplitudes.

- The fundamental vibration frequencies obtained from captured data demonstrate a good agreement against calculated values, considering the inherent variability in experimental pluck tests.

### **3.9.2 Dynamic Response Comparisons**

The simplified model showed a good approximation for response predictions below the fundamental modes of vibration for each tube, although as indicated in the derivation of the response equations, the damping effects for excitations close to natural frequencies, shear deformations and rotational inertia were not considered.

A best estimate was conducted with a finite element analysis (FEA), modelling the beams and support details in ANSYS for the series of harmonic analysis at the frequency ranges tested, considering the damping ratios experimentally obtained for each tube.

During tests and as expected, after a short transient response, the steady motion response due to the transversal harmonic excitations was harmonic along the beams, where the transversal displacements originates from the static equilibrium position, i.e. from the initial transversal position of any point along the beam due to static deflection.

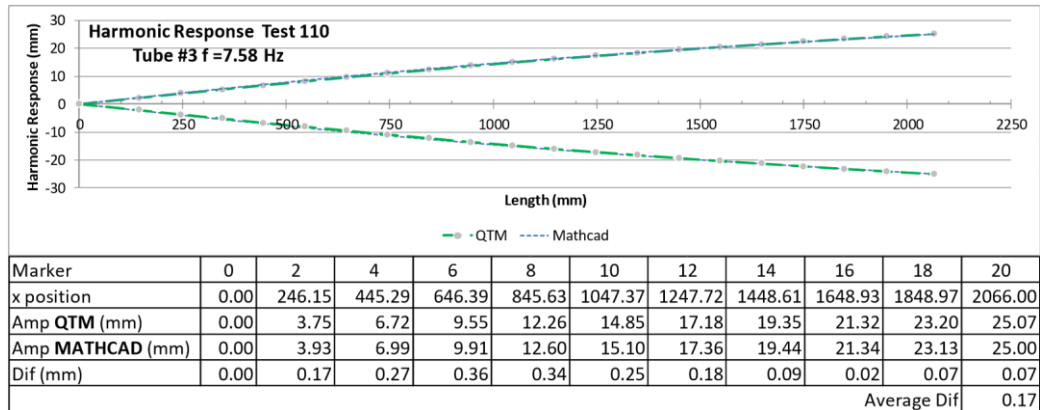
For comparative purposes, the motion capture data describing the oscillatory response of each marker on the beam was analysed in Spike2 software to get their amplitude and frequency values using sinusoidal data fitting, the results were verified by sinusoidal data fit in Mathcad. These results were compared against the amplitude response calculated for each marker position along the beam for each test.

The motion capture system requires the selection and setting of the capture frequency for data acquisition, so a series of motion capture tests were performed for different capture frequencies, finding that sinusoidal data fit demands about 24 data points per marker oscillation for consistency, which provided a guide to set a ratio of 24:1 for the minimum capture frequency respect to the excitation frequency to be tested.

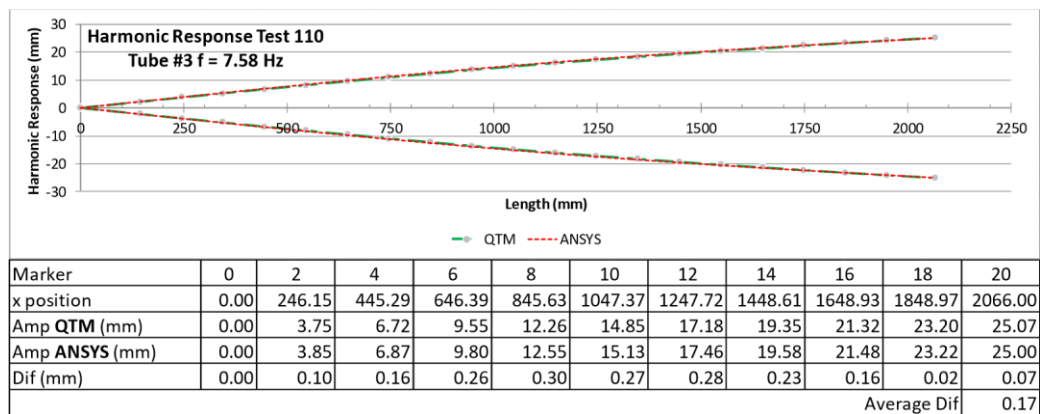
The larger the capture frequency, the better the data resolution, although an unnecessary large frequency will increase the data size to be processed and stored, so the computational demands during motion capture must be assessed accordingly.

The figures 3.13, 3.14 and 3.15 shows the comparison of the dynamic response of the beams at marker locations for excitation frequencies able to produce large deflections but below the fundamental mode, these were chosen since the set of results for lower frequencies on the excitation of the beams were of better precision.

The amplitude comparison corresponds to data analysis of the motion capture system, against the calculations from the simplified analytical model and the FEA model respectively.



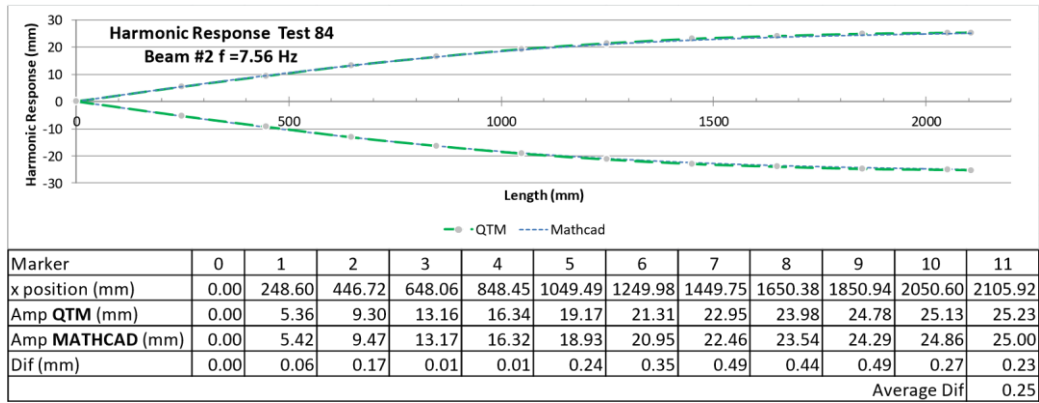
(a) Against simplified model predictions



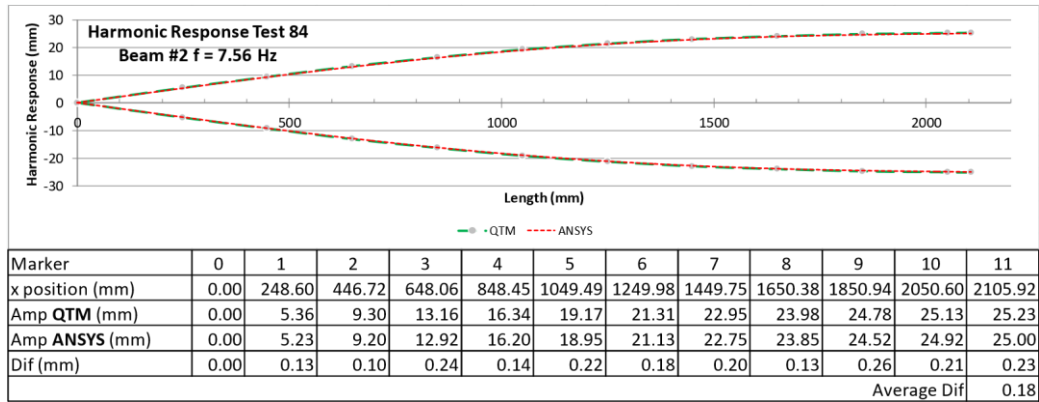
(b) Against FEA model predictions

**Figure 3.13 Measured dynamic responses comparative for Tube No. 3 (carbon fibre)**

The oscillation amplitude captured for each marker location on Tube No. 3, shows a good agreement with respect to the calculated values in both models.



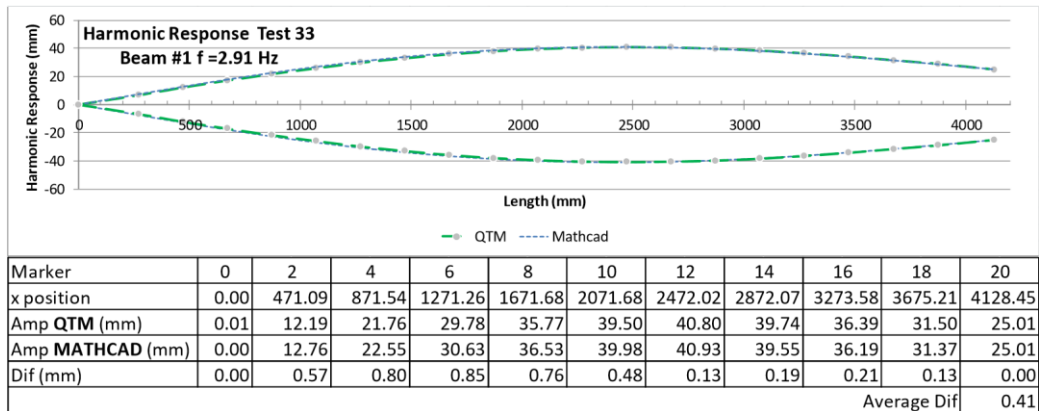
(a) Against simplified model predictions



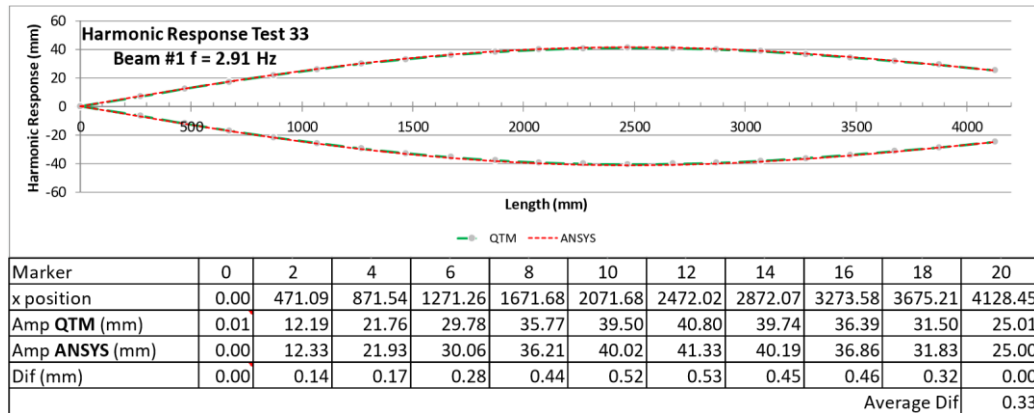
(b) Against FEA model predictions

**Figure 3.14 Measured dynamic responses comparative for Tube No. 2 (aluminium)**

For tube No. 2, the oscillation amplitude captured also shows a good agreement with respect to the calculated values in Fig. 3.14.



(a) Against simplified model predictions



(b) Against FEA model predictions

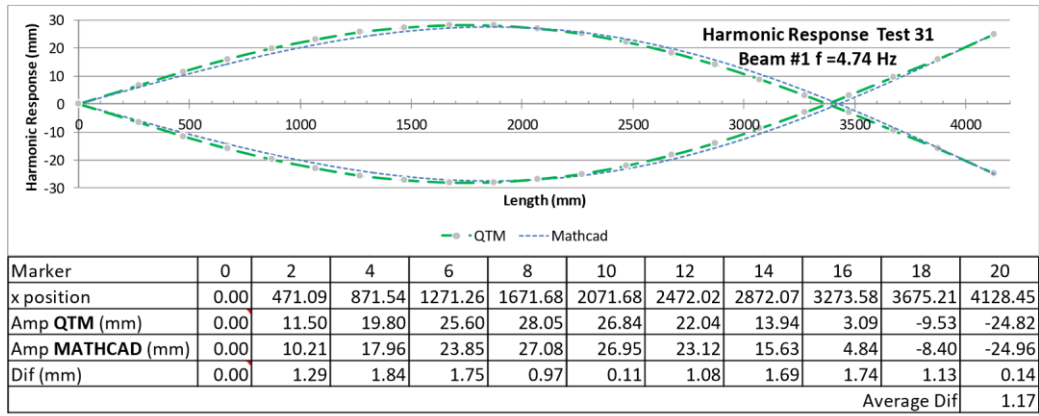
**Figure 3.15 Measured dynamic responses comparative for Tube No. 1 (aluminium)**

The oscillation amplitude captured along the beam also agree reasonably well with the calculated values, although in this case of large dynamic deflections with an excitation frequency ratio of 0.80 with respect to the first natural frequency of the beam, the differences approach the magnitude of calibration residuals reported by the motion capture system.

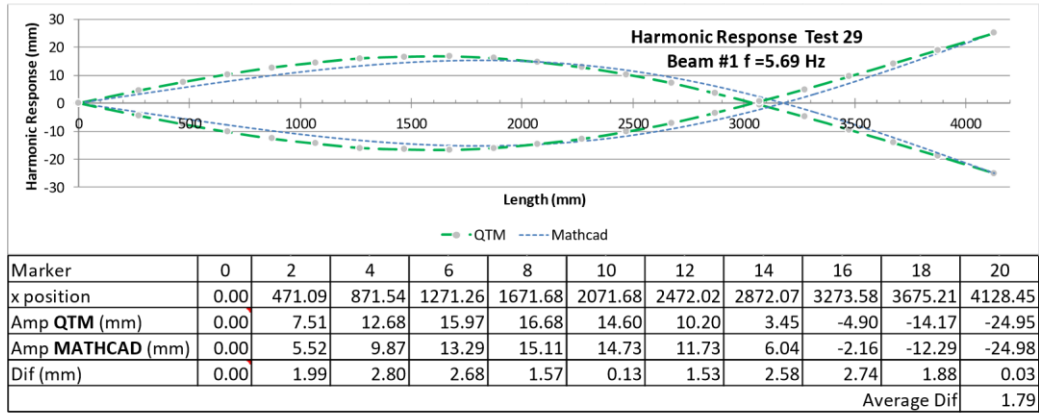
The greater slenderness of Tube No. 1 was convenient for testing frequencies above the frequency of his fundamental mode.

Considering that an excitation frequency above the first natural frequency will produce an internal node; a series of frequencies were also tested between the first and second mode, starting slightly above the first mode to get large oscillations.

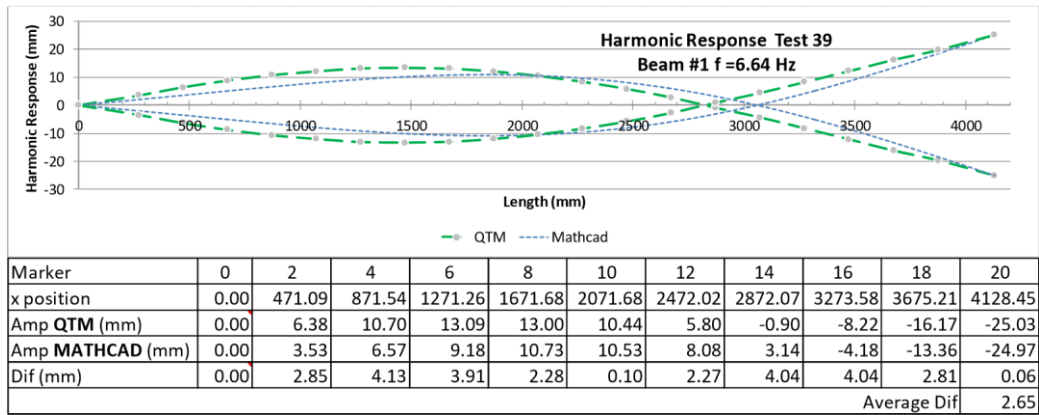
The excitation frequency was then increased so that the internal node position was visually set as close as possible to one marker, to include a comparative of the captured node position against calculations.



(a) Against simplified model predictions for  $f = 4.74$  Hz.



(b) Against simplified model predictions for  $f = 5.69$  Hz.



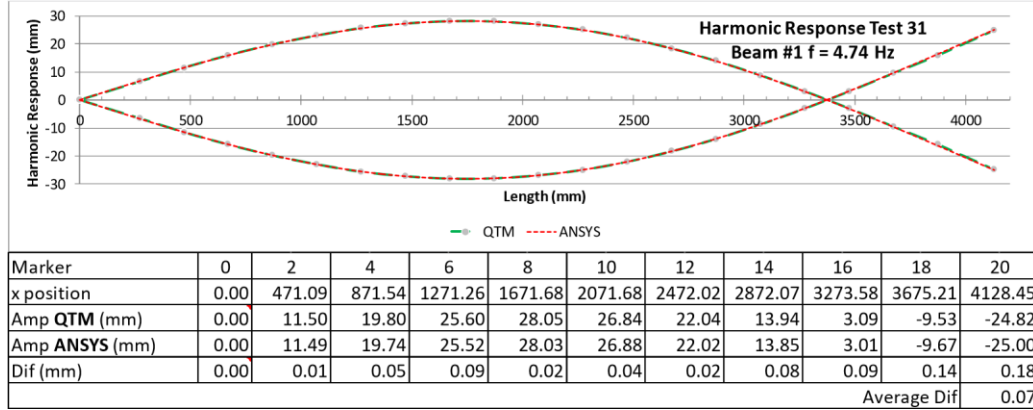
(c) Against simplified model predictions for  $f = 6.64$  Hz.

**Figure 3.16 Measured dynamic responses comparative for Tube No. 1**

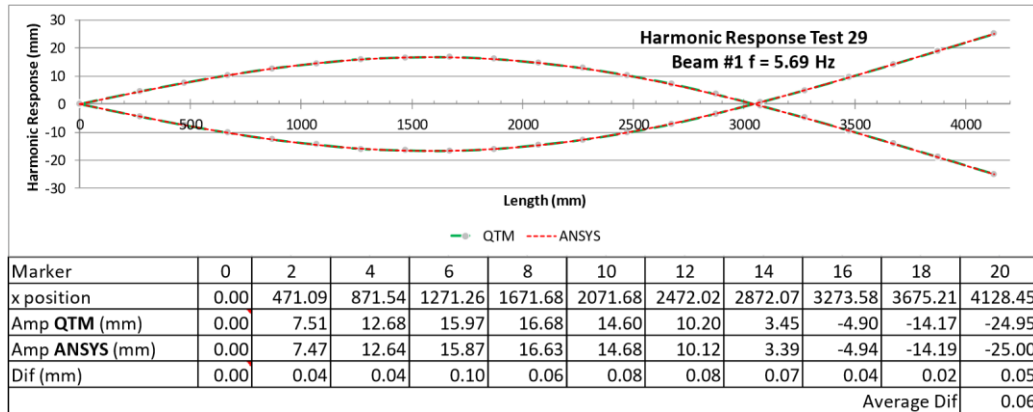
Taking as reference the response from data analysis of the captured motion, the simplified model approximation for the three cases in figure 3.16 is only similar at supports and at the



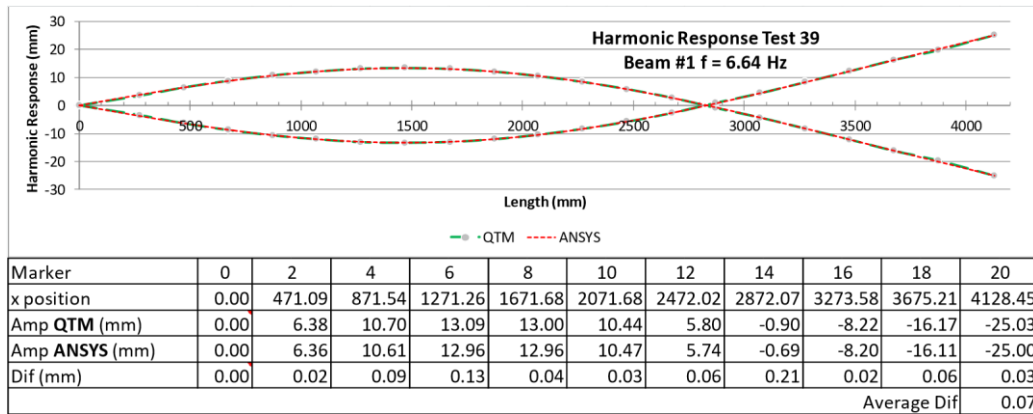
mid length (i.e. at  $x=0$ ,  $x = L$  and  $x = L/2$ ), underestimating oscillation amplitudes along the first half and showing an offset in the prediction of the internal node location; it is also evident that these differences increases as the excitation frequency on the beam was increased.



(a) Against FEA model predictions for  $f = 4.74$  Hz.



(b) Against FEA model predictions for  $f = 5.69$  Hz.



(c) Against FEA model predictions for  $f = 6.64$  Hz.

**Figure 3.17 Measured dynamic responses comparative for Tube No. 1 (aluminium) above fundamental mode.**

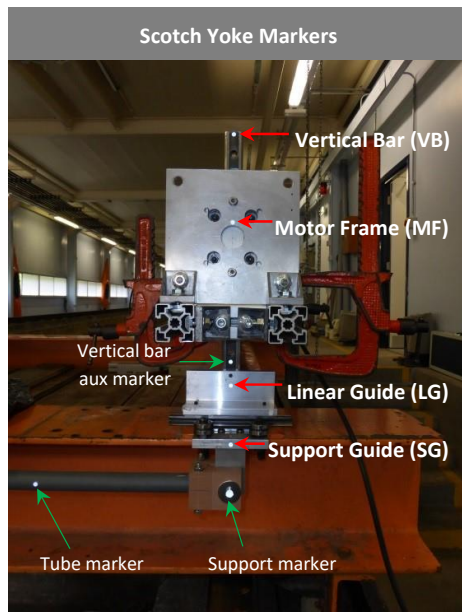
Unlike the simplified model, the expected response and node location calculated in the FEA model, shows a better agreement compared against the captured response for the three cases in figure 3.17; the amplitude differences found are in average of the order of 0.07 mm, which represents a small fraction of the average camera residuals reported by the motion capture system.

Due to speed limitations in the excitation mechanism, it was not possible to explore comparisons with the simplified model for frequencies above the second mode of vibration.

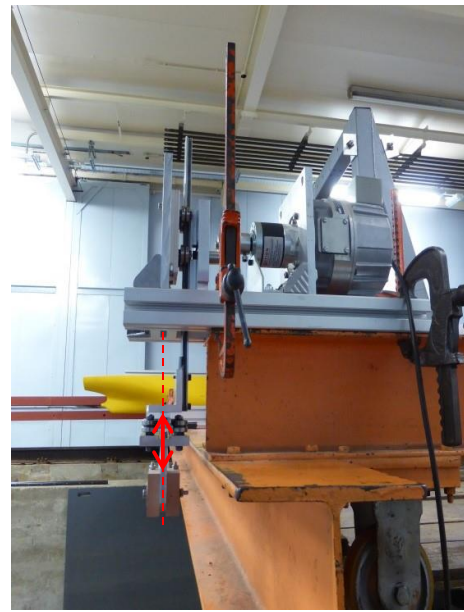
### **3.9.3 Amplitude variations in the scotch yoke mechanism**

During data analysis, it was noted that the captured amplitude of the excited support presented a slight variation, as can be verified in data tables of Fig. 3.13 to 3.17, which increases with the oscillation speed. After careful inspections, it was found a faulty fixing of markers used at the beam supports, and probable deformations in the mechanism of the scotch yoke.

The spherical markers at supports were replaced by retro reflective tape markers as the ones used over the tubes, including additional markers along the mechanism of the scotch yoke.



(a) Front view



(a) Lateral View

**Figure 3.18** Scotch yoke markers

A series of motion capture tests were performed for a range of oscillation frequencies to assess the variation of the vertical amplitudes (Z axis) along the scotch yoke mechanism, and possibly transversal oscillations (Y axis) due to the eccentricity caused by the angle profile of the support guide.

**Table 3.7** Variations of amplitudes with oscillation frequency of the scotch yoke mechanism

TEST No.	FREQ.		MARKER OSCILLATION AMPLITUDE (mm)									
	(rad/s)	(Hz)	SUPPORT		SG		LG		M		VB	
			Z	Y	Z	Y	Z	Y	Z	Y	Z	Y
204	1.11	0.18	24.88	0.15	24.89	0.15	24.75	0.15	0.00	0.00	24.85	0.30
203	6.76	1.08	24.93	0.10	24.95	0.10	24.76	0.20	n/a	n/a	24.90	0.30
202	12.79	2.04	24.98	0.10	25.01	0.10	24.81	0.22	n/a	n/a	24.94	0.30
201	19.07	3.03	25.07	0.20	25.09	0.20	24.87	0.25	n/a	0.03	24.99	0.40
200	25.30	4.03	25.16	0.20	25.18	0.20	24.93	0.30	n/a	0.03	25.05	0.50

198	31.43	5.00	25.21	0.40	25.24	0.35	24.97	0.35	n/a	0.03	25.08	0.50
199	37.68	6.00	25.30	0.50	25.33	0.40	25.01	0.40	0.03	0.06	25.11	0.65
197	43.83	6.98	25.38	0.95	25.40	0.60	25.05	0.55	0.03	0.07	25.13	0.80
Max increment (mm)			0.50	0.80	0.51	0.45	0.30	0.40	0.03	0.07	0.28	0.50

From the results of the data analysis which are shown in table 3.7, it was found that:

- a) The vertical oscillation amplitude “Z” of the top marker at the vertical bar (VB) increases around 0.04 mm per Hz, this can be due to deformations of the motor support frame and/or tolerances in the gearbox shaft and the slot of the sliding yoke. The maximum increment was 0.28 mm in the excitation frequencies tested.
- b) The vertical oscillation amplitude of the marker over the linear guide (LG) increases with the oscillation frequency similarly as the VB marker, although the amplitude is around 0.1 mm lower than VB for all frequencies; with these results, it can be assumed that there is no vertical deformation of significance along the bar. In this case, the difference of amplitude at LG could be explained by interference of metallic surfaces of the angle profile located between the infra-red light source and the marker location, although the magnitude is below the residuals reported by the system.
- c) A small transversal deflection “Y” at the support guide (SG) and at the support marker (SUPPORT), increases as the oscillation frequency increases. This variation can be explained by rotational deflection of the angle profile, which is subject to eccentricity loads between the vertical bar of the scotch yoke and the vertical axis of the support (see Fig. 4.3.1b); the effect is the transmission of the small transverse deflections along the vertical bar to LG and VB markers, and a vertical deflection component, down to the support.
- d) Finally, the vertical oscillation amplitude at the support marker (the excitation amplitude for the tubes), increases as the oscillation frequency increases, which can be explained by a summation of the causes stated in previous paragraphs, with an increment up to 0.5 mm within the range of frequencies tested.

From the above, a modification is recommended to avoid the eccentricity at the support guide under the vertical bar, using an inverted double T profile instead of an angle.

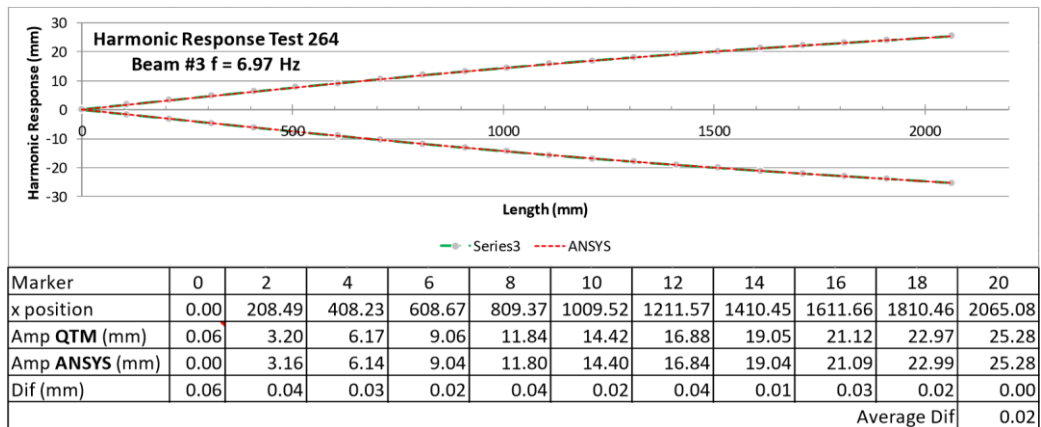
Also, a reinforcement of the stiffness in the support frame of the scotch yoke, gear-box and motor assembly, to mitigate the variations of the oscillation amplitudes in the mechanism of excitation.

Even so, this verification of variations provides an insight on accuracy and precision issues of the motion capture system and some input to error analysis.

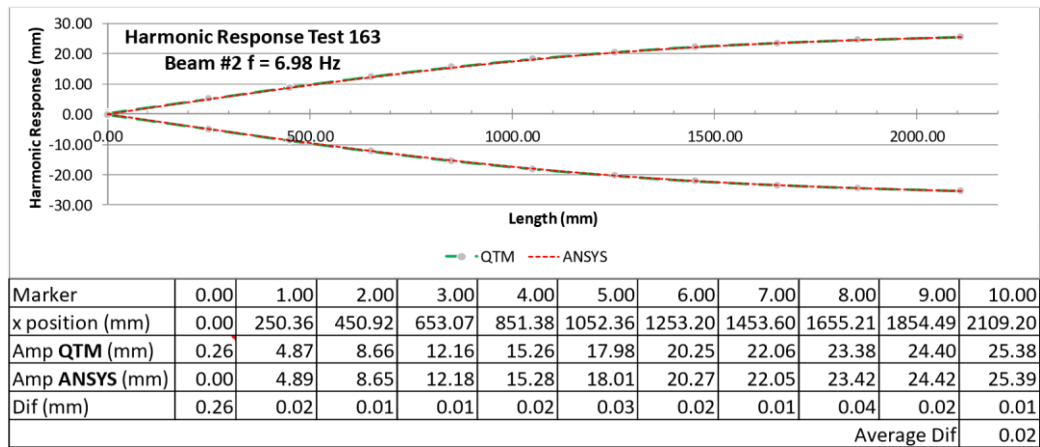
### 3.9.4 Updated response comparison

Assuming that the measured amplitude of excitation at the support marker is reasonably accurate with respect to the real value for each frequency tested, the update of the calculated responses for the tubes Nos. 3 and 2 are shown below for an excitation frequency around 7 Hz.

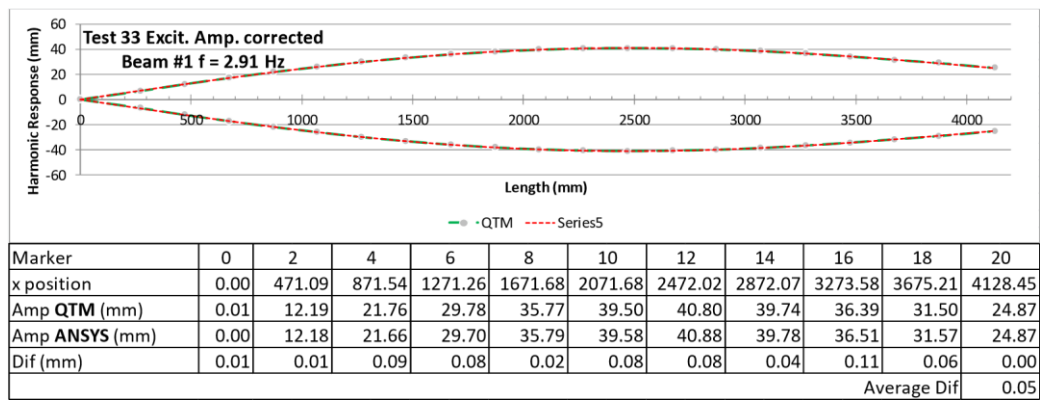
For the tube No. 1, the calculations are updated for the amplitude and frequency measured at the scotch yoke in the test No.33.



(a) Tube No. 3



(b) Tube No. 2



(c) Tube No. 1

**Figure 3.19 Measured dynamic responses comparative with adjusted excitation amplitudes**

It was verified that if the support details are removed from the FEA model to represent the beam elements just as a simply supported cylindrical element, the differences on the calculated results for static deflections, natural frequencies and maximum dynamic deflections on the three tubes are negligible (smaller than 0.01 mm or 0.01 Hz).

The differences in the FEA model after specifying the experimentally obtained damping ratio as a stiffness coefficient based on damping vs frequency were also negligible; even for the case shown in Fig. 3.19c, the maximum amplitude difference between analysis results of the damped model against the undamped model, was around 0.03 mm.

It was also found that if the measured oscillation amplitude of each marker is determined by approximation of the root mean square value of data (RMS) about their mean value, =

$RMS\sqrt{2}$ , instead of sinusoidal data fitting, the average differences indicated in Fig. 3.19 increase around 0.06 mm.

From previous results, it is considered that the FEA model responses, represents the best estimate of the true response of the beams.

### 3.9.5 Video capture with 3D data overlay

The Qualisys system can add cameras with the optional feature of high-speed video to the system setup, allowing 3D data overlay which can be shown on the video data files.

The availability of one of these cameras was used on the carbon fibre tube, to get a visual record of the system capability over continuum elements.

A series of video files were processed, showing an excellent visual position and synchronisation between 3D projections of the motion capture data for each marker against the markers position in the video, for a range of excitation frequencies from 2 to 8 Hz.

The video playback speed with data overlay can be adjusted and frozen in the QTM software for a visual verification of the test as shown in figure 3.20a.

The camera with the high-speed video feature was relocated within the system guidelines and recommendations, performing the new calibration of the system setup to repeat the video capture, without observing variations or negative effects during 3D data overlay on the new video files, see figure 4.6b.

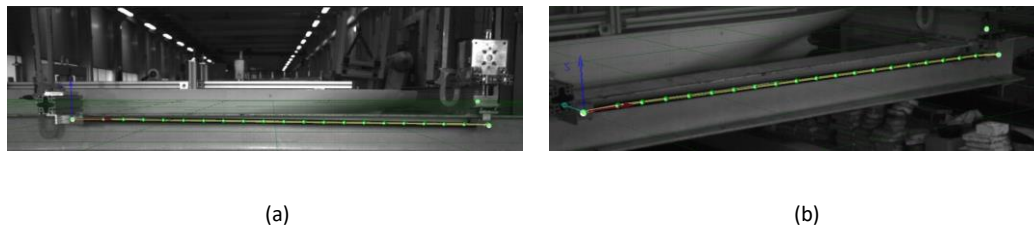


**Figure 3.20** Verification of 3D Data overlay on video

### **3.9.6 Approach to an Error Analysis through measures of reference**

Accuracy and precision of motion capture systems has a large dependence on the system setup, being sensitive to modifications (Windolf et al., 2008), the authors cite some of the elements and system properties influencing performance, mentioning literature about investigations related to specific system setups.

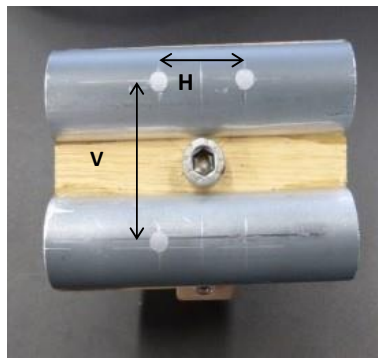
The general system calibration procedures, like the wand calibration method used in Qualisys systems, are required by the QTM software to determine the position and orientation of each camera, which is used to derive 3D coordinates from the 2D camera projections. The residuals reported by the system represent an average of the closest distances between each 3D point derived and the cameras ray projections.

The relevant point is that no significant correlation was found in the cited work (Windolf et al., 2008) between calibration residuals and overall accuracies, which agrees with our findings in section 3.1.9.2, where the differences of the experimental measurements against the best estimation were a small fraction of the residuals reported by the QTM software of the MOCAP system.

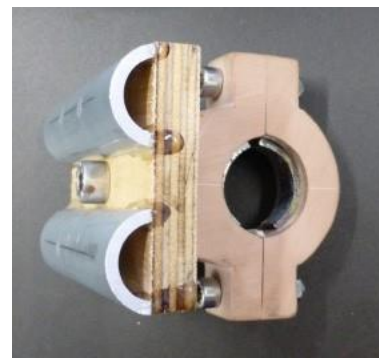
Additionally, our application of the system implied the acceptability of retro reflective tape as circular markers on the curved surface of the tubes, unlike the spherical markers commonly utilised for rigid body motion capture; therefore, it was considered convenient to define a specific calibration method to assess the accuracy and precision for the experimental conditions to explore the setup dependences.

A small calibration rigid frame was built to allocate three markers of the same retro reflective tape over two small sections of the tube used in the experiment, in a way that the horizontal and vertical distances between the markers could be set with the extreme accuracy of a digital calliper; it includes a clamp to allow an installation along the tube elements about the positions where the motion capture of the markers of each model was performed.





(a) Front view



(b) Lateral View

**Figure 3.21 Calibration frame**

A series of motion captures of the calibration frame mounted over the tubes in oscillation conditions were made to compare the differences between the reference horizontal and vertical marker separation distances obtained with the digital calliper, and those obtained from motion capture data, where the corresponding coordinates can be subtracted per time frame to obtain a mean distance and the standard deviation during each test.

The comparisons explored the distance variations for the following changes in the setup of the motion capture system and the test:

- Different camera positions
- Oscillation speed
- Capture rate frequency
- Calibration frame position along the tube
- Recalibration of the Qualisys camera system

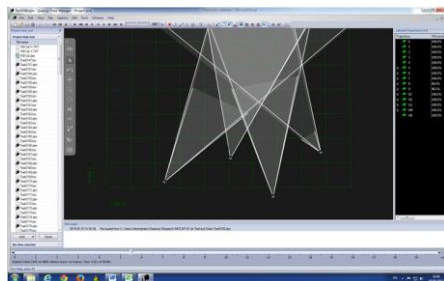
Several measurements with the digital calliper were made to set the horizontal and vertical distances between the centres of the markers.

The digital calliper has a rated accuracy of 0.02mm, with a resolution of 0.01 mm; however, the measurement was subject to visual approximation of the Vernier jaws to the internal and external soft borders of the markers, where no pressure contact can be applied, leading to the results shown in table 3.8 ( $\text{Dist @ centre} = \text{Int} + (\text{Ext} - \text{Int}) / 2$ )

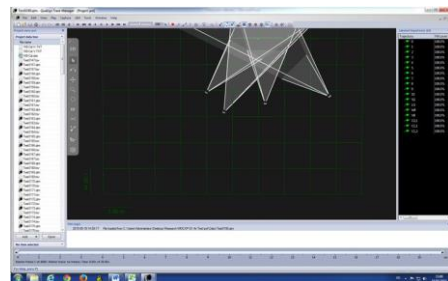
**Table 3.8 Calliper measurements of calibration frame markers**

HORIZONTAL DISTANCE (mm)			VERTICAL DISTANCE (mm)		
Ext	Int	Dist @ centre	Ext	Int	Dist @ centre
31.11	19.62	25.37	46.14	34.63	40.39
31.14	19.50	25.32	45.85	34.50	40.18
30.96	19.38	25.17	46.09	34.58	40.34
31.09	19.50	25.30	45.91	34.43	40.17
30.93	19.39	25.16	46.07	34.54	40.31
30.95	19.56	25.26	45.95	34.64	40.30
30.75	19.48	25.12	45.98	34.50	40.24
31.00	19.69	25.35	45.92	34.62	40.27
30.79	19.75	25.27	46.03	34.47	40.25
30.85	19.73	25.29	45.93	34.67	40.30
	$\mu$	<b>25.26</b>		$\mu$	<b>40.27</b>
	$\sigma$	<b>0.08</b>		$\sigma$	<b>0.07</b>

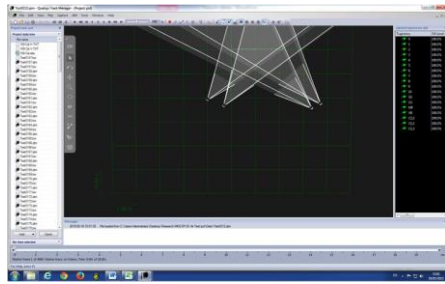
Four different camera positions were tested, conducting a wand calibration procedure for each configuration; table 3.9 shows the average distance (from the camera to the tracking markers) and the average residual of each camera reported by QTM software, and a top view of the cameras configuration are shown in Fig. 3.22.



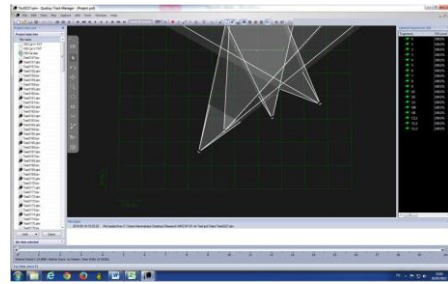
(a) Test No. 180



(b) Test No. 190



(c) Test No. 212



(d) Test No. 227

**Figure 3.22 Camera configurations tested**

For the motion capture with the configurations shown in Fig. 3.22, the calibration frame was mounted over tube No. 2 at the centre of the length, setting an excitation frequency of 3 Hz.

Once the best camera configuration was chosen, as in test No. 227, additional motion capture tests were performed, tests Nos. 226, 228 and 229, for a change in oscillation speed and a change in the capture rate frequency.

The calibration frame was then repositioned along the beam near to the left support, where oscillation amplitudes are smaller, and to the right support where the oscillation amplitudes are close to the excitation amplitude, with results according to tests Nos. 233 and 234.

Finally, a recalibration of the system with the wand calibration procedure was conducted on the last system setup for an additional motion capture test No. 241, which was done to register the influence of system recalibrations on the performance.

Table 3.9 shows the results and comparative of measures on the calibration frame, from the motion capture tests mentioned above.

**Table 3.9 Comparative of motion capture tests of the calibration frame**

Test No.	Osc freq. (Hz)	Capture rate (Hz)	Horizontal distance (mm)		Vertical distance (mm)		H dif (mm)	V dif (mm)	Camera 1		Camera 2		Camera 3		Camera 4	
			$\mu$	$\sigma$	$\mu$	$\sigma$			Avg dist	Avg res	Avg dist	Avg res	Avg dist	Avg res	Avg dist	Avg res
			(mm)	(mm)	(mm)	(mm)			(mm)	(mm)	(mm)	(mm)	(mm)	(mm)	(mm)	(mm)
Vernier			25.26	0.08	40.27	0.07										
180	3	244	25.28	0.04	40.08	0.18	-0.02	0.19	6400.00	1.00	6900.00	2.00	5000.00	1.60	5200.00	1.20
190	3	244	25.22	0.03	40.23	0.04	0.04	0.04	2700.00	0.30	3200.00	1.10	3300.00	0.20	3400.00	0.30
212	3	244	24.78	0.06	39.94	0.09	0.48	0.33	3400.00	1.30	3000.00	0.60	3000.00	0.10	3300.00	0.30
227	3	244	25.26	0.03	40.21	0.06	0.00	0.06	3200.00	0.30	5000.00	0.40	4000.00	0.30	3500.00	0.40
226	1	244	25.26	0.03	40.22	0.05	0.00	0.05	3200.00	0.30	5000.00	0.40	4000.00	0.30	3500.00	0.40
228	3	64	25.24	0.03	40.22	0.05	0.02	0.05	3200.00	0.30	5000.00	0.60	4000.00	0.40	3500.00	0.40
229	1	64	25.23	0.03	40.24	0.05	0.03	0.04	3200.00	0.20	5000.00	0.60	4000.00	0.30	3500.00	0.40
233	1	244	25.21	0.02	40.23	0.08	0.05	0.04	3200.00	0.10	5000.00	0.40	4000.00	0.30	3500.00	0.60
234	1	244	25.20	0.05	40.27	0.10	0.06	0.00	3200.00	0.10	5000.00	0.70	4000.00	0.30	3500.00	0.40
241	1	244	25.23	0.02	40.28	0.09	0.03	0.00	3200.00	0.20	5000.00	0.60	4000.00	0.20	3500.00	0.30

From results in table 3.9, it was found that:

- a) A configuration avoiding narrow angles among cameras, as in test no. 190, and/or a change of the camera distance if the increase of angles is not possible, as in test no. 227, shows lower differences among the reference values of comparison, being the camera configuration in the setup the largest influence of performance of the motion capture system.
- b) The increase of capture frequency and the oscillation speed of the body, as in tests Nos. 226, 228 and 229, show negligible differences.
- c) The position of the calibration frame along the beam shows very low differences, of the order of 0.06 mm; tests Nos. 233 and 234 represent the position of the calibration frame close to each tube support, for the lower and the maximum oscillation amplitudes of motion.
- d) The measured horizontal distance of the calibration frame during the tests was slightly and constantly better than the vertical distance; a possible cause is that the vertical curvature of the markers, originates more vertical variations of the retroreflection captured by the cameras during the motions.

It must be mentioned that the previous results agree with the recommendations for camera positioning and 3D tracking test of the system's manual, indicated to perform wand

calibration procedures until the average residuals becomes as uniform and as low as possible, to improve the accuracy performance. The manual guidelines for the adjustment of exposure time and marker threshold settings were also relevant to achieving low residuals.

Among the reprocessing options in QTM software, one or more cameras in the set up can be disabled to reprocess 3D coordinates from data files, thus a series of reprocessing operations was conducted for the test No. 241, to explore the results of different camera combinations, with results indicated in table 3.10.

**Table 3.10 Reprocessing of test No. 241 with selected cameras**

Test No.	Osc freq. (Hz)	Capture rate (Hz)	Horizontal distance (mm)		Vertical distance (mm)		H dif (mm)	V dif (mm)	Camera 1		Camera 2		Camera 3		Camera 4	
			$\mu$	$\sigma$	$\mu$	$\sigma$			Avg dist	Avg res	Avg dist	Avg res	Avg dist	Avg res	Avg dist	Avg res
			(mm)	(mm)	(mm)	(mm)			(mm)	(mm)	(mm)	(mm)	(mm)	(mm)	(mm)	(mm)
Vernier			25.26	0.08	40.27	0.07										
241 C1&C3	1	244	25.21	0.05	40.27	0.11	0.05	0.00	3200.00	0.00			4100.00	0.00		
241 C2&C4	1	244	25.28	0.07	40.22	0.12	-0.02	0.05			5400.00	0.00			3400.00	0.00
241 C3&C4	1	244	25.25	0.03	40.28	0.07	0.01	-0.01					4100.00	0.00	3400.00	0.00
241 C1,C2&C3	1	244	25.21	0.05	40.28	0.12	0.05	-0.01					4100.00	0.00	3400.00	0.00

The results showed that the reprocessing with a selection of cameras can improve the system performance.

Either way, after that the four camera configurations were tested to select the best performance (after the first 4 tests in table 3.9), all the measurements were within the small standard deviation of the values of reference. The motion capture system shows an even better performance in the standard deviation of the measurements with respect to those obtained statically with the digital calliper for the calibration frame.

### 3.9.7 Conclusions

Although the simplified analytical model based on Euler beam theory, provides an understanding of the system and good predicted responses for oscillation frequencies

below the fundamental mode, the model based on finite element analysis in ANSYS enables solutions for a detailed discretisation of the beam model based on the Timoshenko beam theory, including the shear deformation and rotational inertia effects in the response.

Based on the studies and comparison of experimental results, it is concluded that the FEA model, including the input of experimental values of damping, provides the best estimation of the dynamic response to validate the practical application of the motion capture system on the slender cylindrical elements tested on air.

The closeness among calculations of the harmonic response along the beams for the excitation frequencies tested, the captured response by the system, and the calculations of the fundamental modes against the experimental values from the pluck tests, shows an excellent applicability within studied parameters, where small amplitude differences were identified well below the calibration residuals, so it is considered that under this methodology, the motion capture system is reliable for use in trials involving frequencies and displacements over continuous elements in air.

Based on the foregoing, it was considered that this study provided enough foundation toward the second experimental stage, to verify the system capability for measurement of underwater oscillations on slender cylindrical elements, by means of underwater cameras.

## **4 Application of underwater cameras of a motion capture system to VIV studies of slender cylindrical elements**

### **4.1 Introduction**

This experimental work represents a second stage and it follows the work of the previous section.

In order to investigate the applicability of the system, an experiment was performed with an aluminium tube as a vertical cantilever, fixed at the upper end and partially submerged at the bottom for towing tests, looking for VIV due to flow velocity around the submerged section of the tube.

Underwater cameras of the motion capture system were installed in selected positions under the towing tank carriage and integrated to standard cameras for the aerial section as a twin system to facilitate the performance assessment of the submerged measurements.

Following the procedures of the first stage experiment, a simplified model was derived considering a constant added mass for the submerged section, to assist the understanding of the mechanical fundamentals and to estimate some of the expected responses to design the test parameters; the predicted response was then compared against a Finite Element Analysis model.

To assess and work towards the validation of the measurement capability of the underwater system, the motion captured by the aerial camera system above water (oscillation frequencies and amplitudes of the transversal and in-line VIV responses) was compared against the motion captured by the underwater camera system, considering the good performance assessed for the aerial system in the first stage.

## **4.2 Model Analysis**

For a cantilever beam, a simplified model for free vibration analysis can be represented in fig. 4.1, where Euler-Bernoulli beam theory is also applied, assuming that any cross section along the beam remains plane.

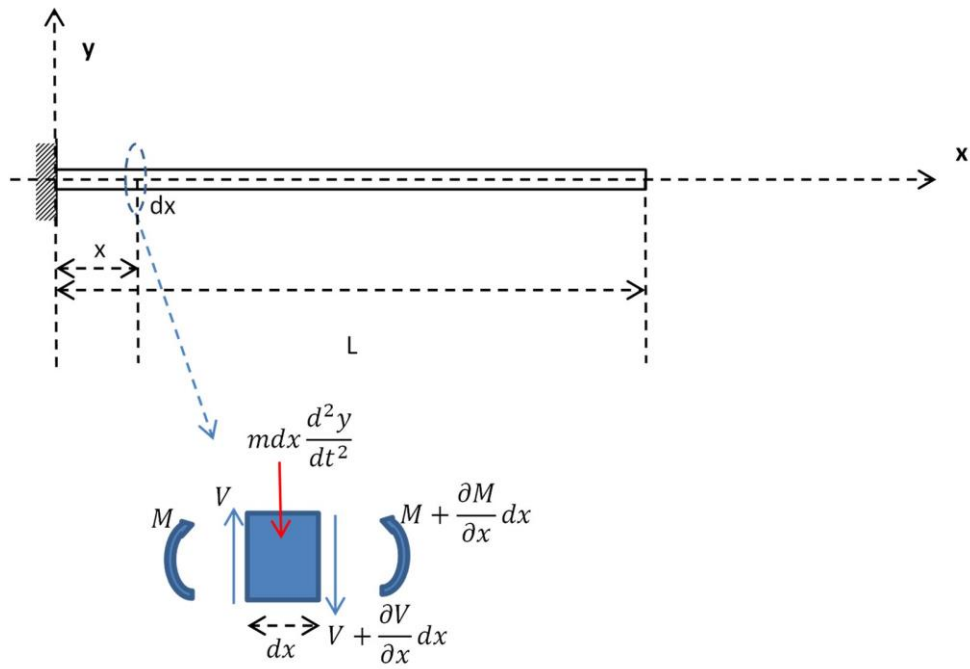


Figure 4.1 Simplified model for vibration analysis of a cantilever beam

#### 4.2.1 Free vibration beam analysis

A step by step derivation of the analytical solution for the natural frequency in vacuum and the mode shape can be consulted in Appendix A.2.

The natural frequency in vacuum is given by eq. (A.59) as  $\omega_n = \frac{\lambda_n^2}{2} \sqrt{\frac{EI}{m}}$ , where  $\lambda_n = (1.875, 4.694, 7.855, 10.996\dots)$ .

The mode shape is given by eq. (A.60) as:

$$y(x) = \frac{1}{\lambda_n^3} \left[ \cosh \lambda_n x - \cos \lambda_n x + \left( \frac{\sinh \lambda_n L}{\lambda_n L} - \frac{\sin \lambda_n L}{\lambda_n L} \right) \left( \sin \lambda_n x - \sinh \lambda_n x \right) \right]$$

Where  $C_n = \frac{\cosh \lambda_n L - \cos \lambda_n L}{\lambda_n L \left( \frac{\sinh \lambda_n L}{\lambda_n L} - \frac{\sin \lambda_n L}{\lambda_n L} \right)}$



### 4.2.2 Rayleigh's method

An approximation for the fundamental angular frequency of the partially submerged cantilever is derived in Appendix A.2 using Rayleigh's method, and given by eq. (A.63) as:

$$\omega = \frac{\omega''}{\omega'}$$

In this method, the approximation of the frequency increase with a reasonable assumption of the shape for the elastic curve of the beam, and it is considered that the deflected shape due to the loads of the beam applied statically is a very good assumption.

### 4.2.3 Fundamental mode in vacuum (without plug or flange):

The estimation of the natural frequency for both, in vacuum and in a partially submerged condition, was calculated in Mathcad and ANSYS models, considering the cantilever properties in section 4.5 and the deflected shapes for the three following load cases:

(a) Uniformly distributed mass ( $\rho A$ ) due to the self-weight along the beam length

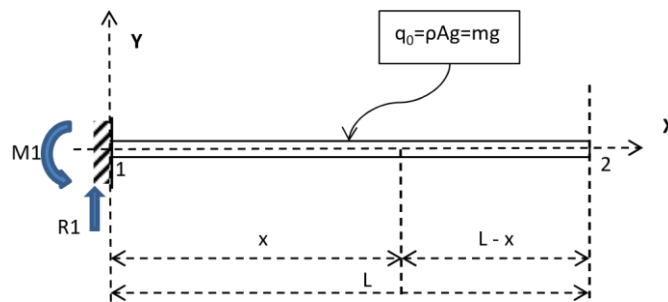


Figure 4.2 Cantilever beam static analysis due to self-weight

Taking moments at x in fig. 4.2:

$$\frac{d^2 y}{dx^2} = (-), \text{ from bending theory, } \omega'' = \omega', \text{ then:}$$

$$\omega'' = \frac{mg}{2} ( -2 + )$$

$$\omega' = \_ - + \_ +$$

$$= \frac{2}{2} \left( \frac{2}{2} - \frac{3}{3} + \frac{3}{12} + \dots \right)$$

B.C.:  $y'(0)=0$  and  $y(0)=0$ , so,  $A=B=0$ , then:

$$() = \frac{1}{24} ( - 4 + 6 )$$

(b) Uniformly distributed added mass at the submerged section

When a submerged body oscillates, it accelerate/decelerate and moves some volume of surrounding fluid, which adds inertia to the system.

For simplicity, this has been usually modelled as an added mass of the body, considering the mass of some volume of the fluid moving with the object.

The experimentally determined average value of this added mass normal to the axis of fully submerged cylinders in water, with length to diameter ratios from 9 to  $\infty$  is about 0.96 to 1.00 times the fluid mass displaced by the body. It is emphasized that this values are valid for a brief moment after the onset of the acceleration-deceleration and before the flow separation and viscous effects set in and for very small amplitudes (Sarpkaya, 2010).

The length to diameter ratio  $L/D$  for the experiment is about 20, thus an added mass coefficient of 1.00 times the fluid mass displaced per unit length by the submerged section of the cantilever will be considered for still water.

Approximating preliminary the added mass as a uniformly distributed load " $q_2$ " along the submerged section:

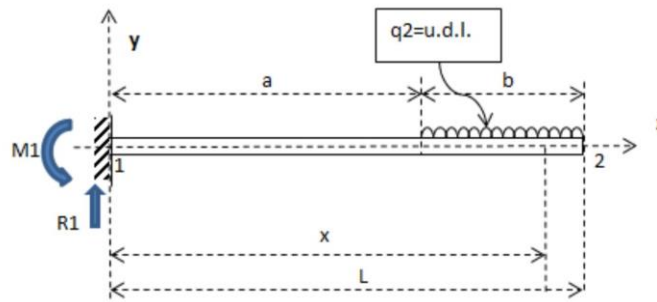


Figure 4.3 Cantilever beam static analysis due to submerged section added mass

From static equilibrium in fig. 4.3:  $\sum F_x = 0$  and  $\sum F_y = 0$ ; using Macaulay method and taking moments to the left of  $x$ :  $\sum M_x = 0$ , where

$\delta(x-a)$  is the step function ( $= 0$  for  $x < a$  or  $= x-a$  for  $x > a$ ), which must be integrated in a way to preserve the identity of the bracket. Since  $M = EIy''$ :

$$EIy'' = M1 - R1x + \frac{q_2}{2}(x-a)^2 - \frac{q_2}{6}(x-a)^3$$

$$y'' = \frac{M1}{EI} - \frac{R1}{EI}x + \frac{q_2}{2EI}(x-a)^2 - \frac{q_2}{6EI}(x-a)^3$$

$$y' = \frac{M1}{EI}x - \frac{R1}{2EI}x^2 + \frac{q_2}{2EI}\left(\frac{2}{3}(x-a)^3\right) - \frac{q_2}{6EI}\left(\frac{1}{4}(x-a)^4\right) + A$$

$$y = \frac{M1}{2EI}x^2 - \frac{R1}{6EI}x^3 + \frac{q_2}{2EI}\left(\frac{1}{2}(x-a)^4\right) - \frac{q_2}{6EI}\left(\frac{1}{5}(x-a)^5\right) + Bx + C$$

B.C.:  $y'(0)=0$  and  $y(0)=0$ , so,  $A=B=0$ , then:

$$y(0) = \frac{M1}{2EI}(0)^2 - \frac{R1}{6EI}(0)^3 + \frac{q_2}{2EI}\left(\frac{1}{2}(0-a)^4\right) - \frac{q_2}{6EI}\left(\frac{1}{5}(0-a)^5\right) + C = 0$$

$$C = -\frac{q_2}{24EI}(2a^4 - 3a^5)$$

(c) End load due to the weight of a plug/flange at the end of the cantilever

For a concentrated weight  $W$  at the cantilever end, at any point  $x$ ,

$$EIy'' = M1 - R1x + W\delta(x-L)$$

$$y'' = \frac{M1}{EI} - \frac{R1}{EI}x + \frac{W}{EI}\delta(x-L)$$

$$y' = \frac{M1}{EI}x - \frac{R1}{2EI}x^2 + \frac{W}{EI}\delta(x-L) + A$$

$$y = \frac{M1}{2EI}x^2 - \frac{R1}{6EI}x^3 + \frac{W}{EI}\delta(x-L) + Bx + C$$

B.C.:  $y'(0)=0$  and  $y(0)=0$ , so,  $A=B=0$ , then:

$$y(0) = \frac{M1}{2EI}(0)^2 - \frac{R1}{6EI}(0)^3 + \frac{W}{EI}\delta(0-L) + C = 0$$

$$C = -\frac{W}{EI}\delta(0-L)$$

From eq. (A.59):

$$= \frac{\lambda^2}{\sqrt{\frac{E_A I}{}}} = 3.919 \qquad = 3.916$$

Using Rayleigh’s method, we can consider the shape due to self-weight:

$$y(x) = \frac{b_m g}{24 E_A I} (x^4 - 4 L x^3 - 6 L^2 x^2)$$

$$F n_{vRM} = \frac{1}{\sqrt{\frac{E_A I \int_0^L (y'')^2 dx}{b_m \int_0^L y(x)^2 dx}}} = 3.935 \text{ Hz}$$

$$\frac{h}{h} \left( \frac{3.919}{3.935} \right) = 3.916$$

**4.2.4 Fundamental mode (fully submerged in still water):**

Mass for submerged tube = + +

No internal fluid allowed, the tube will be fitted with a bottom plug and a flange of 2.5 OD to mitigate 3D/ending effects.

Mass of internal fluid:

$$= 0$$

Added mass:

Added mass coefficient = 1.0

$$\left( \frac{1}{4} \right) = \frac{-}{4}$$

$$= + \left( \frac{1}{4} \right) = 3.338 \text{ ---}$$

$$\frac{\lambda^2}{\sqrt{\frac{E_A I}{}}} \frac{1}{2} == 2.456$$

For the ANSYS model, an equivalent density for the submerged section of the beam was used as:

$$= \frac{6.875 \times 10^{-4}}{2.8} = 2.454$$

#### 4.2.5 Estimation of the natural frequency in partially submerged conditions using Rayleigh's method:

For a vertical cantilever, the deflected shape is assumed by superposition of the cases for added mass in the submerged section and the end load of a plug/flange derived in section 4.2.3:

$$2 = \frac{Added_{mass}(C_a)g}{24E_A I} * \left[ \begin{cases} 0 & \text{if } x < a \\ (x-a)^4 & \text{otherwise} \end{cases} - 4bx^3 + 6bx^2(2a+b) \right] + \frac{(Flange)g}{6E_A I} (3 - \frac{2x}{h})$$

The mass as function of x, is defined according to the lengths where the beam mass, the added mass and the end masses are acting:

$$m(x) = \begin{cases} m_{beam} & 0 \leq x < a \\ m_{beam} + m_{added} & a \leq x < L \\ m_{beam} + m_{added} + m_{plug} + m_{flange} & x = L \end{cases}$$

The 1<sup>st</sup> mode of the natural frequency in still water can be finally estimated from eq. (A.63) as:

$$(C_a) = \frac{1}{2\pi} \sqrt{\frac{E_{AI} \int_0^L \left(\frac{d^2}{dx^2} y(x, C_a)\right)^2 dx}{\int_0^L \text{mass}(x, C_a) * y(x, C_a)^2 dx}}$$

$$( ) = 2.686$$

The calculation of the first natural frequency in the FEA model in ANSYS, including the modelling of the plug, the end flange and the equivalent density for the submerged section to account for the added mass was:

$$= 2.659$$

It was verified that if the contribution of the end masses (plug/Flange) are removed from the elastic curve and the mass distribution, as in y1 and mass1 functions above, the difference in the estimation of the fundamental frequency is negligible.

If the contribution of the end masses (Plug/Flange) is removed in the elastic curve in Rayleigh's method:

$$(x, C_a) = \frac{\text{Added}_{\text{mass}} C_a g}{24E_{AI}} \left[ \left[ (x - a) \text{otherwise} \right] - 4bx^3 + 6bx^2(2a + b) \right]$$

$$Fn_{\text{swRM1}}(C_a) = \frac{1}{2\pi} \sqrt{\frac{E_{AI} \int_0^L \left(\frac{d^2}{dx^2} y_1(x, C_a)\right)^2 dx}{\int_0^L \text{mass}(x, C_a) * y_1(x, C_a)^2 dx}}$$

$$Fn_{\text{swRM1}}(C_a) = 2.686 \text{ Hz} \quad ( )$$

$$0 <$$

If the contribution of the end masses (Plug/Flange) is removed in the mass distribution:

<

$$( ) = + ( ) \geq$$

$$(C_a) = \frac{1}{2\pi} \sqrt{\frac{E_{AI} \int_0^L \left(\frac{d^2}{dx^2} y_1(x, C_a)\right)^2 dx}{\int_0^L \text{mass}_1(x, C_a) * y_1(x, C_a)^2 dx}}$$

$$( ) = 2.687$$

So, the method approximates well the solution with reasonable deflected shapes, since any assumed amplitude is cancelled in the equation.

#### 4.2.6 Determination of the speed range for the tests

In uniform steady flow, three regions of instability defined by empirical rules for flexible cylinders can be identified by the reduced velocity  $U_r = U/[(f_n)(D)]$  (Bartrop, 1998).

First instability region for in-line oscillations due to symmetric vortex shedding in the range of  $1.2 \leq U_r \leq 2.5$ , with maximum response at  $U_r = 2.1$ .

Second instability region for in-line oscillations due to asymmetric vortex shedding in the range of  $2.7 \leq U_r \leq 3.8$ , with maximum response at  $U_r = 3.2$ .

Third instability region for transverse oscillations due to asymmetric vortex shedding in the range of  $4.8 \leq U_r \leq 8.0$ , with maximum response at the range of  $6.5 \leq U_r \leq 8.0$ , or  $U_r \approx 7.25$ .

Therefore, the range of towing speed for the test can be estimated as:  
 = , which are indicated in table 4.1.

**Table 4.1 Estimation of towing speeds**

Instability Regions	Ur range			fn (Hz)	D (m)	U=U <sub>r</sub> f <sub>n</sub> D		
	Ur <sub>a</sub>	Ur <sub>b</sub>	Ur <sub>peak</sub>			U <sub>a</sub> (m/s)	U <sub>b</sub> (m/s)	U <sub>peak</sub> (m/s)
1 In-line oscillations	1.20	2.50	2.10	2.686	0.051	0.164	0.341	0.287
2 In-line oscillations	2.70	3.80	3.20	2.686	0.051	0.368	0.519	0.437
3 Transverse oscillations	4.80	8.00	7.25	2.686	0.051	0.655	1.092	0.989

From the previous results, the maximum speed for the experiment was set to 1.2 m/s.

A verification of the fluid flow regime from the Reynolds number associated to the maximum speed is given by:

$$= 1.2 \text{ — } = \frac{0D \cdot V_{max}}{\nu} = 5.54 \times 10^4$$

For  $300 < < 3 \times 10^5$ , the regime is classified as subcritical, where the wake is completely turbulent but the boundary layer separation is still laminar (Blevins, 1994).

For fixed circular cylinders, the vortex shedding frequency due to the fluid separation flow around the body can be estimated by the Strouhal number relationship  $St = f_{vs} D / U$ . In subcritical regions, the Strouhal number  $St$  is about 0.2 (Sarpkaya, 2010).

For a body in motion, the vortex shedding frequency, denoted as  $f_{vs}$ , behaves with some differences with respect to that of fixed cylinders. "*In the lock-in range,  $f_{vs}$  becomes increasingly smaller than  $f_{st}$  until the lockout*" (Sarpkaya, 2010), which means that the Strouhal number decrease as Reynolds number increases.

We are interested in explore the lock-in range, where  $U_r \approx 7$ ; as mentioned above, if the peak value of transverse oscillations occurs around a reduced velocity value of  $U_r=7.25$ , we can estimate the Strouhal number for the maximum response of transverse oscillations in lock-in as  $St = f_{vs} D / U = (f_{vs} D / U_r) \cdot U_r / U = (f_{vs} D / U_r) \cdot U_r / (U_r \cdot 7.25) = (f_{vs} D / U_r) / 7.25$ ; so,  $St = 0.138$ .

This preliminary value is in the range of experimental data of reference showed in Fig. 4.4 below (Resvanis et al., 2012).



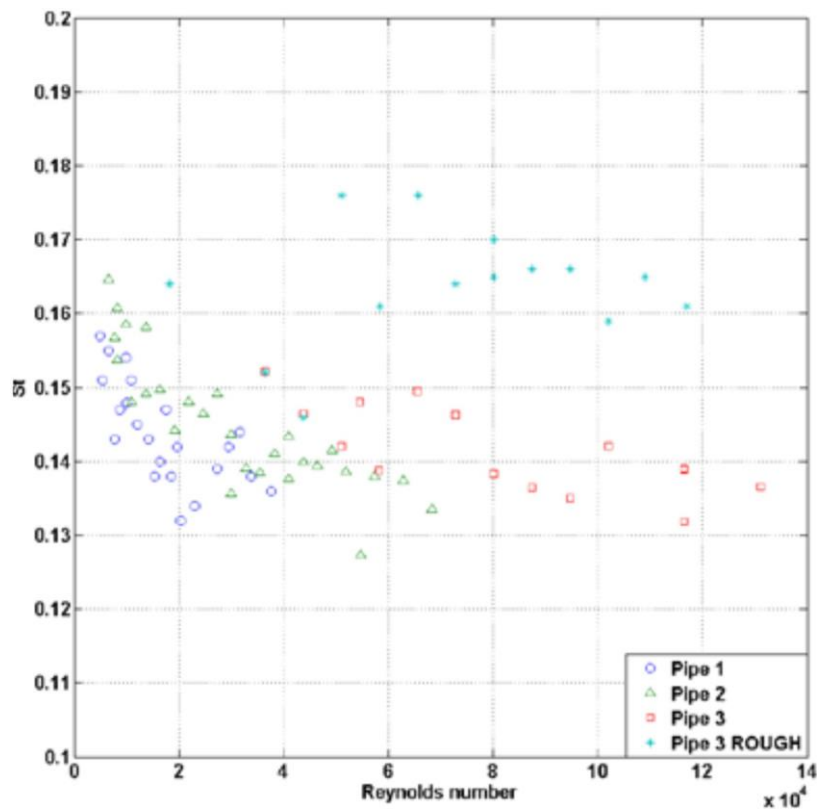


Figure 4.4 Strouhal number vs Reynolds number in uniform flow tests (Resvanis et al., 2012)

The Rayleigh's method used in the simplified model, implies that computed frequencies will be slightly higher than the real fundamental frequency since a definite shape is assumed, this represent a constraint which increases the stiffness of the system (Timoshenko, 1974).

Additionally, it can also be expected that the measured value of the natural frequency in a pluck test (damped frequency), occurs below the calculated value due to the real structural support stiffness and damping forces in the system, since the perfect restraint assumed in the model for the fixed support is very difficult to achieve in practice.

Thus, the estimated towing speeds indicated above must be updated with the natural frequency of the cantilever beam obtained experimentally.

#### 4.2.7 VIV Response Parameter

The locked-on response amplitude of VIV depends on the member properties. The Scruton number is recognized as a response parameter to estimate the amplitude of the dynamic response (Barltrop et al., 1990).

This parameter is proportional to the structural damping and to the ratio of the equivalent mass to the mass of the water displaced by the element, and is defined as:

$$S_n = \frac{2 \zeta \omega_n}{\rho D} \sqrt{\frac{m}{m_a}}$$

Where

$m$  is the effective mass per unit length (including hydrodynamic added mass),  $\zeta$  is the log decrement of structural damping in air,  $\rho$  is the density of water and  $D$  is the external diameter.

For the effective mass, the real cantilever beam is equated to an equivalent element, where the cross section, mode shape, natural frequency and inertial properties remains the same, but the length of the element is equal to the length of the section exposed to vortex formation.

### 4.3 Experimental Procedures

One-week availability of the underwater cameras was achieved due to the support of Qualisys systems, during a Qualisys Marine Workshop at the Kelvin Hydrodynamics Laboratory in May of 2014, with the participation of delegates from 12 European laboratories.

The installation of the underwater cameras and the setup of the twin system on the towing carriage of KHL was conducted with a huge support from the laboratory staff.

A series of towing tests was conducted with the vertical cantilever partially submerged, at incremental speeds, to identify vortex induced in-line and transverse oscillations,

performing measurements and data acquisition with strain gauges and the motion capture system, using above and underwater cameras in a twin system configuration.

The measurements of the underwater motion capture were then compared against the measurements of the aerial camera system and against the strain gauges instrumentation for validation.

The estimated natural frequency in the partially submerged condition with the simplified and the FEA model will be compared to that obtained experimentally in still water from a pluck test.

The natural frequency measured in still water will be used to update reduced velocities, according to section 4.2.6.

The predicted in-line and transverse oscillation by the response parameter will be compared with the measurements of the motion capture system.

#### **4.4 Summary of equations**

Eq. (A.63) of the simplified model was used to calculate the natural frequency for the beam properties in the partially submerged condition, comparing results with a FEA model of the beam.

The logarithmic decrement in air was calculated as in eq. (3.1):

$$= \frac{1}{\dots}$$

For the response prediction, the response parameter and equivalent mass were estimated as indicated in section 4.2.7.

#### **4.5 Vertical cantilever beam properties**

Aluminium extruded round tube was the beam material chosen to facilitate any connection with the structural accessories available at KHL.

A preliminary dimension design for diameter, thickness and length was conducted, to obtain natural frequencies within the range of towing speeds, considering the installation of the underwater cameras, and a convenient flexibility to allow for oscillations induced by the vortex shedding.

The selected diameter was of 50.8 mm which represents twice the diameter used in the previous experimental work, therefore the marker diameter was increased to 10 mm to maintain the angular ratio of the arc covered by one marker over the tube.

To choose the beam thickness, an approximated static load was considered for the submerged section, equivalent to the drag force over a cylinder for the maximum towing speed, in a way that the maximum deflection was around 1.5 times the external diameter to secure enough flexibility for oscillations.

The retro reflective material used for the aerial part was the same used in the first stage.

For the submerged section, Qualisys recommended the use of a SOLAS grade retro reflective tape.

The real dimensions of the supplied extruded aluminium tube were measured at several points along the length and circumferentially for diameter and thickness averages.

For real density determination, the tube was measured and weighed 3 times; the geometric data is shown in table 4.2.

**Table 4.2 Vertical cantilever properties and geometric data**

Tube Material		Extruded aluminium round tube 6082 T6
Length (Cantilever)	L (mm)	3500.00
Outside Diameter	OD (mm)	50.80
Internal Diameter	ID (mm)	44.30
Thickness	t (mm)	3.25
Aspect ratio	L/OD	68.90
Aluminium density	$\rho$ (kg/m <sup>3</sup> )	2710.00
Mass per unit length	m (gr/m)	1316.00
Flange weight at tube end	(gr)	56.00
Young's Modulus (0°)	E (Gpa)	70.00
Proof stress	$\sigma_{0.2\%}$ (Mpa)	250.00
Ultimate Tensile Strength	$\sigma_{UTS}$ (Mpa)	290.00
Bending Stiffness	EI (kNm <sup>2</sup> )	9.65
<b>Plug material at tube end</b>		<b>Axson prolab 65</b>
Plug Length	(mm)	50.00
Plug weight	(gr)	50.09

#### 4.6 Test setup

The partially submerged vertical cantilever had a length of 3.5 metres; the top support was 2.5 metres above the water level and connected structurally to the towing carriage, leaving 1 metre of the free end for the submerged condition.



(a) Aerial camera system

(b) Vertical cantilever

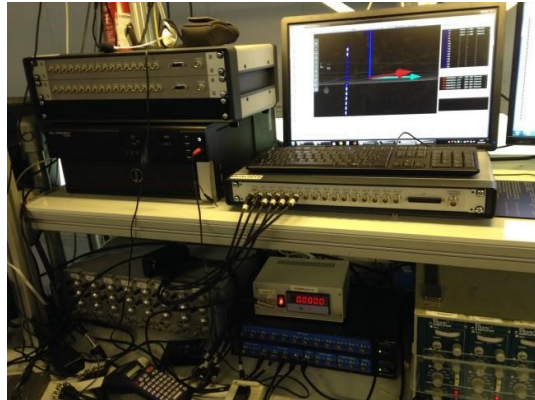
**Figure 4.5 Aerial system setup on the towing carriage**

Two pairs of strain gauges were installed at 55 centimetres below the top fixed support and connected to a DC strain signal amplifier and to the CED 1401 (mkII) data acquisition system, using CED Spike2 software for data file storage, processing and analysis.

Both systems, the Qualisys motion capture twin system and the data acquisition from strain gauges, were set and synchronised to start data acquisition from external triggering.

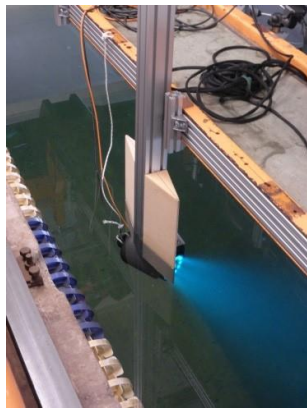


(a) Top support of the vertical cantilever



(b) Data acquisition rack

**Figure 4.6 Integration of strain gauges instrumentation**



(a) Underwater camera



(b) Markers on tube

**Figure 4.7 Installation of underwater cameras to the towing carriage**

## 4.7 Motion capture system setup

The Qualisys optical tracking system available at the Kelvin Hydrodynamics Laboratory was implemented as the main camera system for the aerial section of the beam (2 x Oqus 310p+, 2 x Oqus 300p+ and 2 x Oqus 300p+).

Structural supports connected to the towing carriage were implemented for the mounting of three Qualisys underwater cameras (2 x Oqus 310+, 1 x Oqus 510).

The underwater cameras were integrated as a slave system in QTM using the twin system feature in the software.

The wand calibration method was conducted in 2 stages, for the aerial (main) and the underwater (slave) camera system, both being integrated by the QTM software.

To link the coordinate system, a Qualisys’s custom marine dual calibration frame with reference markers at both sides, above and underwater, was moored to the tank walls to perform the wand calibration procedures.

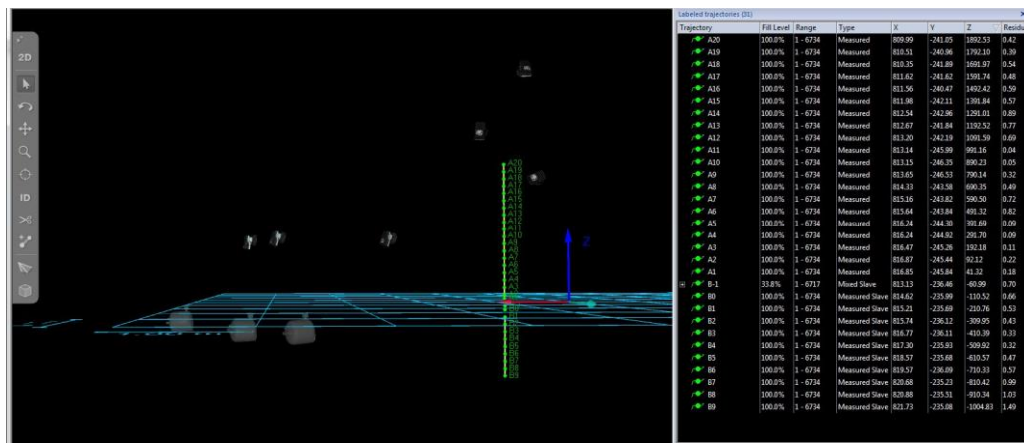
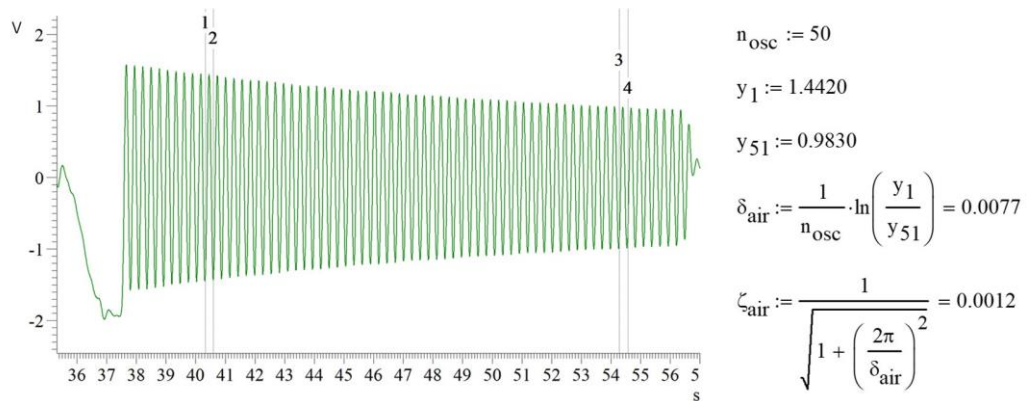


Figure 4.8 3D View of the Qualisys motion capture system setup

The first setup of the system after calibration is shown in fig 4.8, all the markers for the submerged section are within the field of view of the underwater cameras; the location provided for the aerial cameras on the towing carriage do not allowed the visibility for all the markers above water, the top visible marker A20 is located about 1900 mm above the tank water level and 600 mm under the fixed support of the cantilever.

## 4.8 Response Prediction

The log decrement in air for this experiment was obtained experimentally by a pluck test through the strain gauges instrumentation, observing a lightly damped response as shown in fig 4.9.



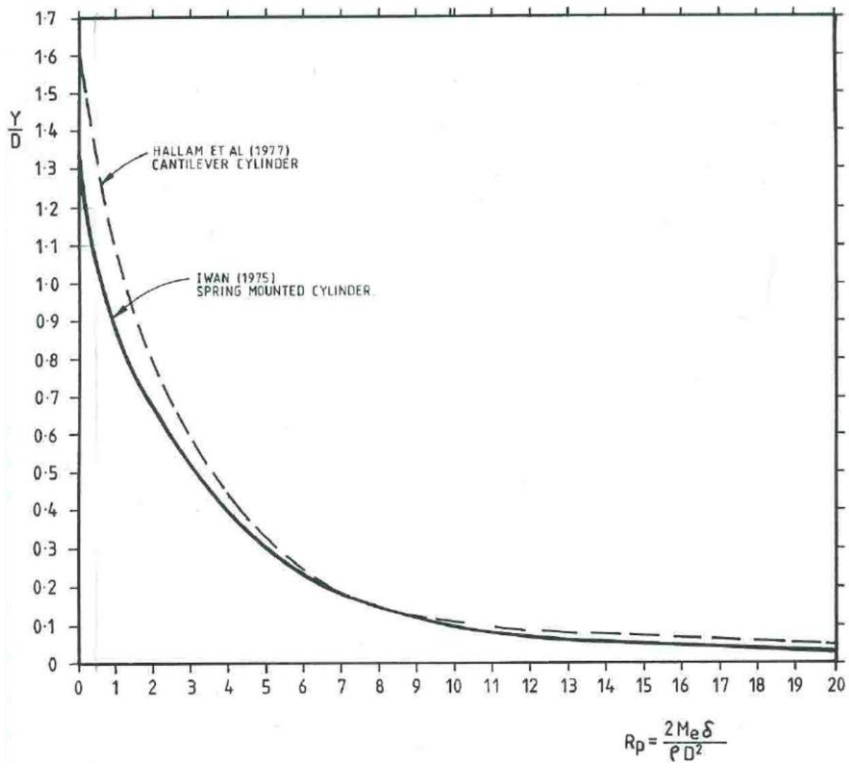
**Figure 4.9 Oscillation decay analysis of the pluck test in air**

Using the elastic curvature and mass distribution functions from section 4.2.5 and the response parameter equation from section 4.2.7, we get:

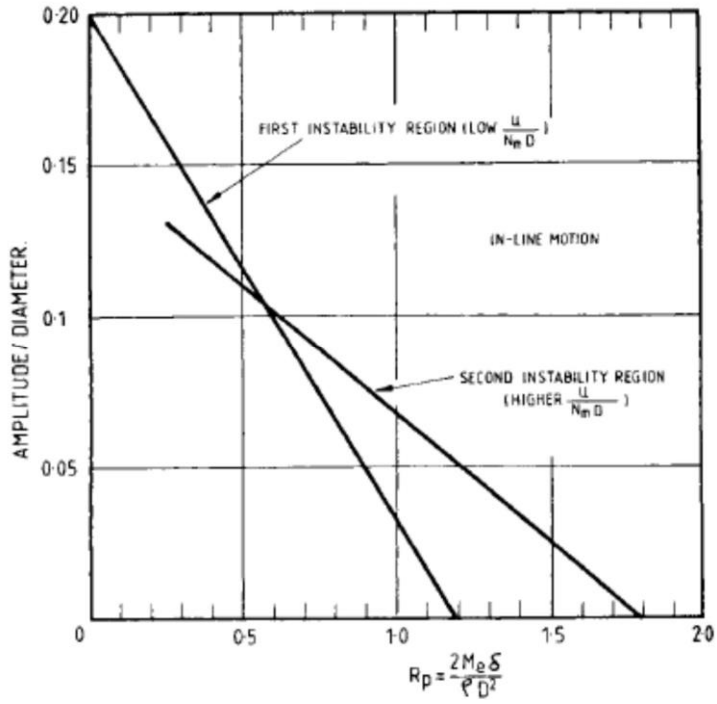
$$= \frac{\dots}{\dots} = 2.804 \dots = \dots = 0.017$$

Although not a rigorous parameter, the amplitude of response for transverse and in-line oscillations of a cantilever cylinder can be estimated with the response parameter (Bartrop et al., 1990); subject to the conditions stated in this reference.





a) Cross flow motion



b) In-line motion

Figure 4.10 Amplitude of response (Bartrop et al., 1990)

From fig. 4.10, the response amplitude of transverse oscillations can be expected to be slightly below  $A/D = 1.6$ , when the vortex shedding frequency approaches the natural frequency of the cantilever measured in still water.

The response amplitude for in-line oscillations within the first and second instability regions can be expected to be below  $A/D = 0.2$ .

## 4.9 Experimental Results

### 4.9.1 Pluck Tests

A series of pluck tests for the damped fundamental frequency in still water of the vertical cantilever were conducted for a first performance assessment.

The data analysis was conducted in Spike2 software, a sinusoidal fitting of each decay response gives a frequency value verified in a PSD analysis of the same signal (see fig. 4.11).

The response frequency from the aerial cameras, underwater cameras and the strain gauges instrumentation was analysed in this way.

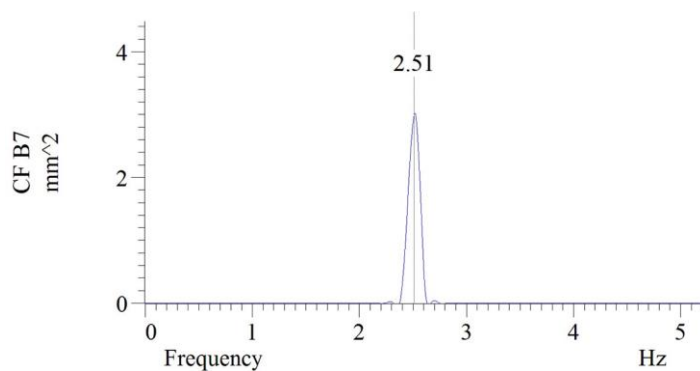


**Figure 4.11 PSD Data analysis of pluck tests**

The table 4.3 shows the frequency obtained from the motion capture of one selected marker of each camera system and the strain gauges data during the pluck tests.

**Table 4.3 Damped natural frequency comparative**

Test No.		MOCAP aerial (Hz)	MOCAP underwater (Hz)	Strain gauges (Hz)
<b>Test No. 99</b> <b>X Axis</b> <b>(Drag dir)</b>	Pluck 1	2.522	2.522	2.521
	Pluck 2	2.519	2.518	2.518
	Pluck3	2.516	2.517	2.516
	Pluck 4	2.515	2.515	2.516
	<b>Average</b>	<b>2.518</b>	<b>2.518</b>	<b>2.518</b>
<b>Test No. 100</b> <b>Y Axis</b> <b>(Lift dir)</b>	Pluck 1	2.507	2.509	2.509
	Pluck 2	2.510	2.510	2.510
	Pluck3	2.513	2.513	2.513
	Pluck 4	2.510	2.512	2.512
	<b>Average</b>	<b>2.510</b>	<b>2.511</b>	<b>2.511</b>

The results show an excellent agreement between aerial, underwater and strain gauges data.

Table 4.4 shows a comparative of the experimental damping ratio in the transversal direction, using the logarithmic decrement method in the data analysis of the three systems, with a very good agreement.

**Table 4.4 Experimental damping ratio**

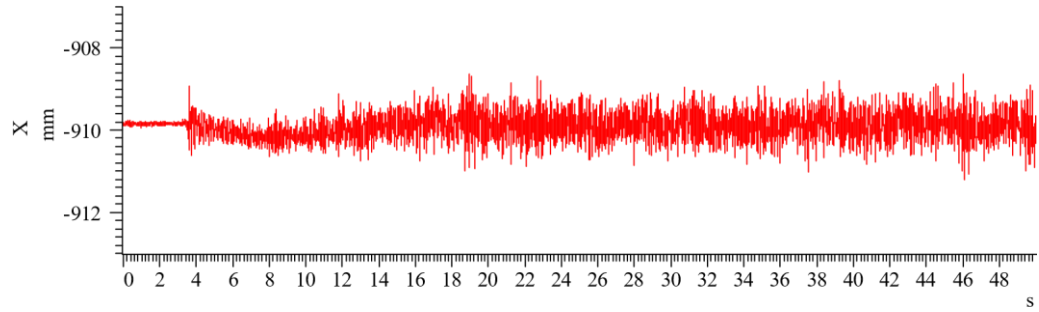
Pluck Test No.	Marker	System	Amp @ cycle 1	Amp @ cycle 21	$\delta$ 0-20	$\zeta$ 0-20	
			(mm)	(mm)			
1	B7	UW	18.9890	1.7194	0.1201	0.0191	
2	B7	UW	17.3291	1.6306	0.1182	0.0188	
3	B7	UW	16.6397	1.7496	0.1126	0.0179	
					$\mu$	0.1170	<b>0.0186</b>
					$\sigma$	0.0039	0.0006
1	A3	AERIAL	12.5299	1.2401	0.1156	0.0184	
2	A3	AERIAL	11.4203	0.9901	0.1223	0.0195	
3	A3	AERIAL	10.8600	1.2003	0.1101	0.0175	
					$\mu$	0.1160	<b>0.0185</b>
					$\sigma$	0.0061	0.0010
1	SG	SG	2.6208	0.2600	0.1155	0.0184	
2	SG	SG	2.3907	0.2063	0.1225	0.0195	
3	SG	SG	2.2791	0.2496	0.1106	0.0176	
UW.- UNDER WATER					$\mu$	0.1162	<b>0.0185</b>
SG.- STRAIN GAUGES					$\sigma$	0.0060	0.0010

The natural frequency estimated by the simplified and the FEA model were 2.686 Hz and 2.659 Hz respectively, which represents a difference around 7% and 6% with respect to the damped frequency measured, as shown in table 4.3.

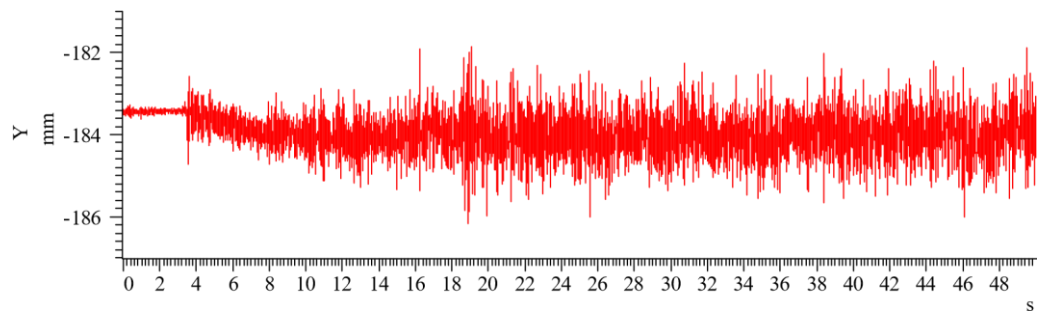
Two of the main causes for the previous variations can be due to a higher added mass than that assumed in analysis for an added mass coefficient of  $= 1.0$ , and to the real stiffness of the cantilever support condition. Considering the light damping shown in table 4.4 and the small frequency difference found between X and Y axis shown in table 4.3, the experimental support condition of the cantilever was first reviewed.

A spherical marker was installed over the support location, the figure 4.12 shows the vibration of the support over X and Y axis plotted from the motion capture system, the static noise is visible at the start of the test until transverse and in-line responses transmit vibrations to the support.

The amplitudes were of the same order of magnitude over the towing speed range of the tests, but a lower restraint over the Y axis cannot be conclusive, since transversal amplitudes of oscillations due to vortex shedding are greater than the in-line amplitudes, although a structural reinforcement of the support can be attempting to mitigate vibrations.



(a) In-line support vibrations (X axis)



(b) Transversal support vibrations (Y axis)

**Figure 4.12 Support vibrations during towing conditions**

#### 4.9.2 Dynamic Response Validation

Considering that the performance of the motion capture system in air was evaluated during a first stage over controlled oscillations of slender cylindrical elements, with excellent results for the frequencies, amplitudes and geometric parameters tested, the following methodology was set to assess the performance of the underwater cameras.

It consisted in the harmonic analysis performed in the FEA model, inducing one harmonic displacement corresponding to any marker location above water, with an amplitude obtained from data analysis of the aerial camera system for any chosen marker in a given

test; in this way the calculated amplitudes of the deflected profile, including the submerged section, can be compared.

Since the vortex induced oscillation amplitudes have their natural peak variations, the RMS amplitude is used for each marker data about the second half of the time series, allowing the setting of the oscillations experienced in the towing test.

This provides a measured profile of RMS amplitudes during a towing test. The RMS amplitudes data from both, above and underwater markers can then be compared against the calculated profile of the harmonic analysis mentioned in the previous paragraph, as the proposed method of validation.

Additionally, the response prediction indicated in section 4.8 can be examined against 2D trajectories of the measured response at the cantilever free end.

### **FEA Model Adjustment**

The mathematical model assumes for a fixed support condition, that displacements and rotations at the support are identically zero, which in practice is difficult to achieve, especially on a towing carriage.

One approach, to update the model to match the experimental natural frequency, is to relax the mathematical condition of the fixed support for angular displacements.

This approach is to find a finite rotational spring constant which matches the fundamental mode of the model with the experimental result, as a representation of the real conditions (Ritto et al., 2008).

Considering the above, the FEA model was modified in a modal analysis, to change the fixed support condition of the cantilever for a simply support with torsional springs, setting the stiffness values to match the fundamental modes obtained experimentally for both directions, as shown in figure 4.13.

The results of the modal analysis show negligible differences if the experimental damping ratio is introduced in the FEA model or not.

Also, the differences in results of deflection profiles were negligible during harmonic analysis within the frequencies tested, whether the experimental damping ratio is considered or not.

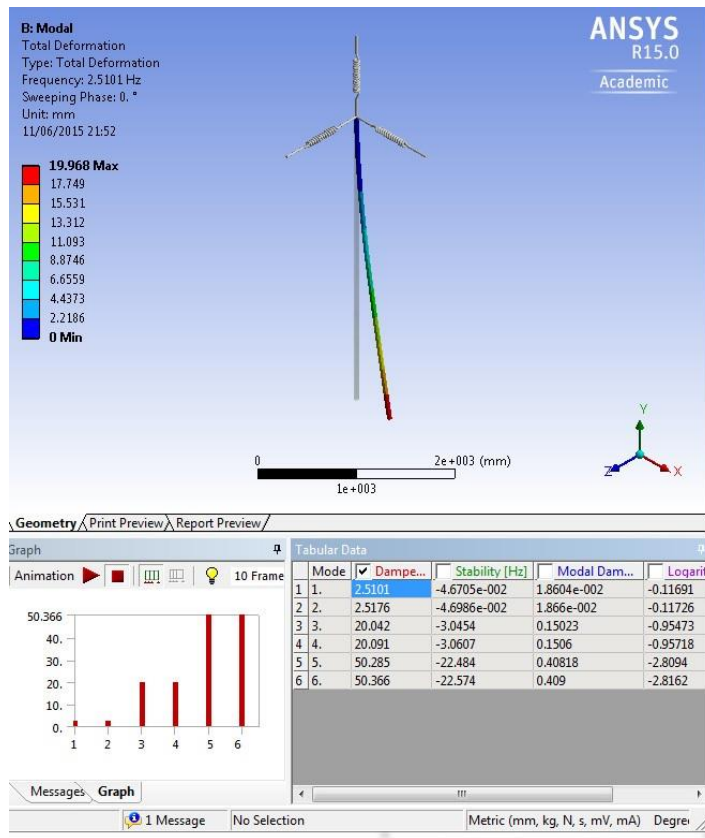
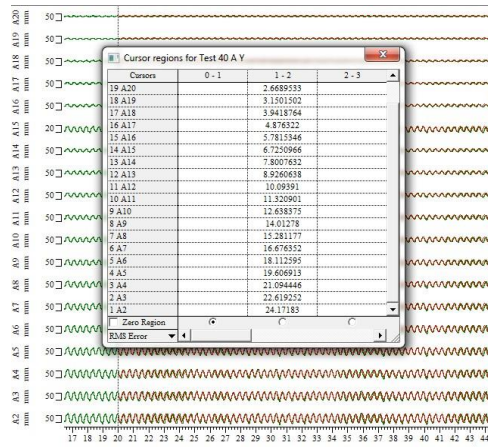


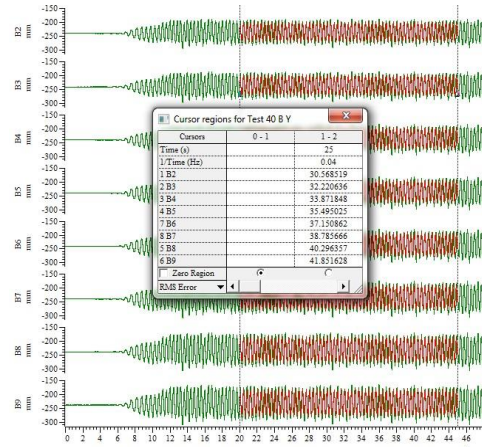
Figure 4.13 Torsional springs at the beam support to match experimental frequency

### Test selection for MOCAP data analysis to obtain RMS transverse amplitudes

The test No. 40 at towing speed of 1.05 m/s ( $U_r \approx 8.2$  m/s) was chosen, considering that the transverse vortex shedding frequency approach the value of the natural frequency measured in still water, being this one of the required conditions to be satisfied for the use of the response parameter (Barltrop et al., 1990).



(a) Aerial markers



(b) Underwater markers

**Figure 4.14 RMS Amplitudes (Test No. 40)**

### Harmonic analysis for validation

The RMS amplitude measured at marker A2, a marker located 100 mm above the water level and 2400 mm below the support of the cantilever, was chosen as the harmonic displacement input in the model to calculate the harmonic response profile along the beam.

Added mass coefficients of 1.0 and 0.0 were considered for the water volume displaced by the submerged section.

Fully submerged flexible cylinders with low mass ratio generally exhibit a drop of the average added mass at increasing reduced velocities, although for this experiment setup, the free surface, 3D effects of the cantilever free end and the largest part of the cantilever, which is not exposed to hydrodynamic but inertial forces, are likely to have a particular behaviour due to the discontinuity of the mass ratio between the structural mass and the mass of the fluid volumes displaced by the cylinder.



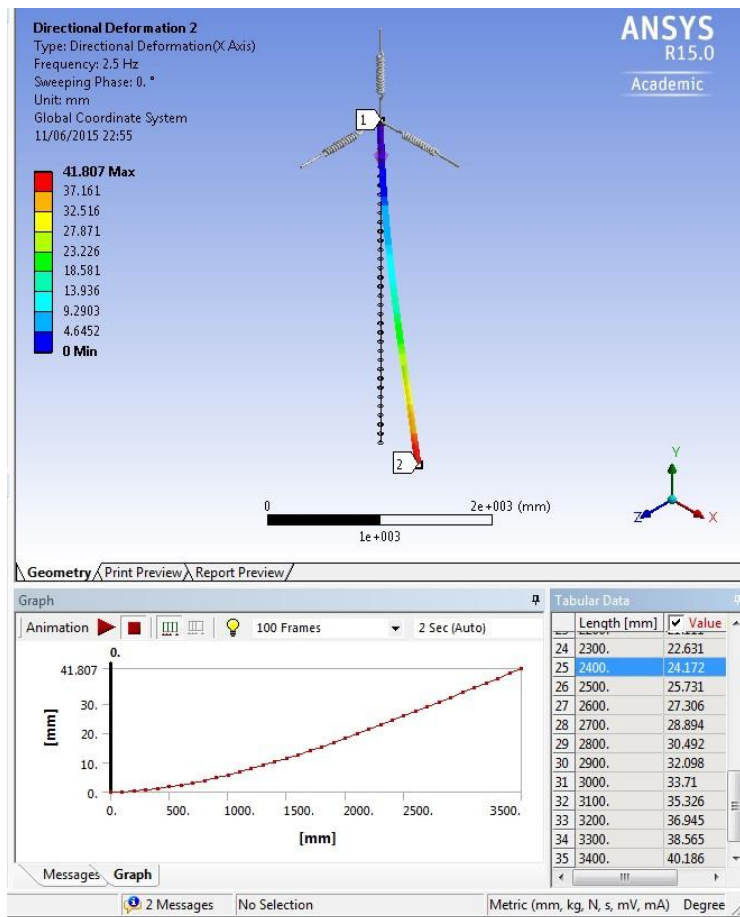


Figure 4.15 Harmonic Analysis

The response profile of the harmonic analysis shown in Fig. 4.15 was compared against the RMS amplitude values obtained from measurements of the motion capture system, as shown in Fig. 4.14.

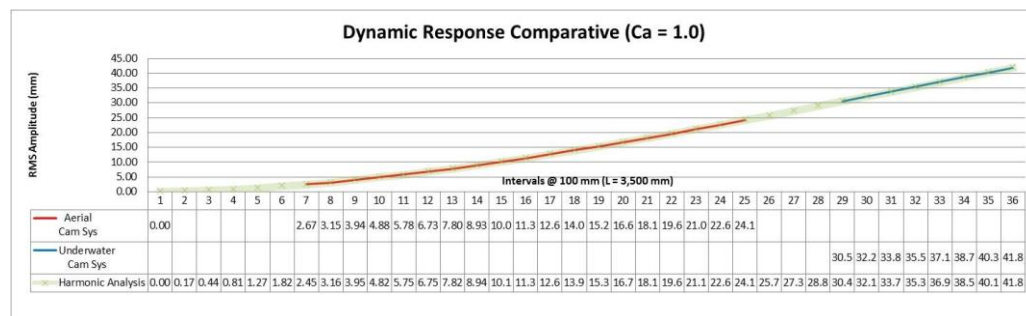


Figure 4.16 Validation of underwater measurements

The differences of the RMS amplitudes are summarised in tables 4.5 and 4.6.

**Table 4.5 Differences in RMS amplitudes of the aerial camera system (mm)**

Marker	Position from support	RMS A Markers	RMS A Harmonic Analysis	Difference
A20	600.00	2.67	2.45	<b>-0.22</b>
A19	700.00	3.15	3.16	<b>0.01</b>
A18	800.00	3.94	3.95	<b>0.01</b>
A17	900.00	4.88	4.82	<b>-0.06</b>
A16	1000.00	5.78	5.75	<b>-0.03</b>
A15	1100.00	6.73	6.75	<b>0.03</b>
A14	1200.00	7.80	7.82	<b>0.02</b>
A13	1300.00	8.93	8.94	<b>0.01</b>
A12	1400.00	10.09	10.12	<b>0.02</b>
A11	1500.00	11.32	11.35	<b>0.03</b>
A10	1600.00	12.64	12.63	<b>-0.01</b>
A9	1700.00	14.01	13.95	<b>-0.06</b>
A8	1800.00	15.28	15.31	<b>0.03</b>
A7	1900.00	16.68	16.71	<b>0.04</b>
A6	2000.00	18.11	18.15	<b>0.04</b>
A5	2100.00	19.61	19.62	<b>0.01</b>
A4	2200.00	21.09	21.11	<b>0.02</b>
A3	2300.00	22.62	22.63	<b>0.01</b>
A2*	2400.00	24.17	24.17	<b>0.00</b>
A2* Induced displacement in harmonic analysis			$\mu$	-0.01
			$\sigma$	<b>0.06</b>

**Table 4.6 Differences in RMS amplitudes of the underwater camera system (mm)**

Marker	Position from support	RMS A Markers	RMS A Harmonic Analysis	Difference
B2	2800.00	30.57	30.49	<b>-0.08</b>
B3	2900.00	32.22	32.10	<b>-0.12</b>
B4	3000.00	33.87	33.71	<b>-0.16</b>
B5	3100.00	35.50	35.33	<b>-0.17</b>
B6	3200.00	37.15	36.95	<b>-0.21</b>
B7	3300.00	38.79	38.57	<b>-0.22</b>
B8	3400.00	40.30	40.19	<b>-0.11</b>
B9	3500.00	41.85	41.81	<b>-0.04</b>
			$\mu$	-0.15
			$\sigma$	<b>0.06</b>

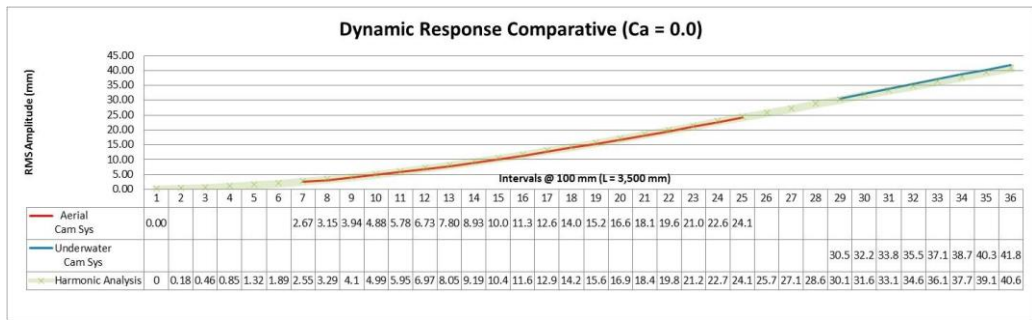


Figure 4.17 Validation of underwater measurements

The calculated results for deflections assuming added mass coefficients of 1.0 and 0.0 (figs. 4.16 and 4.17) do not show enough sensitivity for this test setup; however, additional work could determine an average added mass coefficient for the model including force sensors at the support, to calculate the inertial and hydrodynamic components from the total force.

The residuals reported by the motion capture system were consistent from start to finish of each test, which do not suggest vibrations of the underwater camera enclosures due to fluid flow within our towing speed range; although, further work can explore whether the fluid flow over the enclosure of the underwater cameras can cause vibrations influencing accuracy/precision of the measurements.

This can be done by installation of a fixed submerged marked in the towing tank, conducting measurements at a range of speeds and with different camera angle positions against the towing tank longitudinal axis, to assess potential vibrations of the underwater enclosures.

Nonetheless, it is considered that the adjusted FEA model provides a very good estimate of the true response of the cantilever beam for the validation of measurements obtained from the underwater cameras of the motion capture system, considering the agreement of the predicted response against the measurements in the aerial section (table 4.5).

**Revision of predicted response and flow velocities in sections 4.8 and 4.2.6**

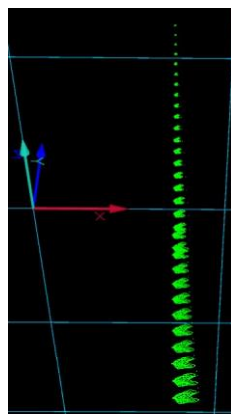
The flow velocities in section 4.2.6 for in-line and transverse instabilities were updated with the measured frequency of the fundamental mode in still water, as shown in table 4.7.

**Table 4.7 Estimation update of towing speeds**

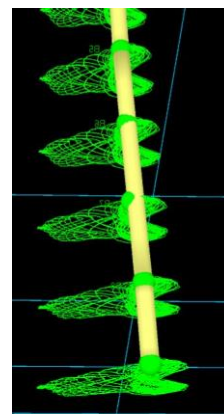
Instability Regions	Ur range			f <sub>n</sub> (Hz)	D (m)	U=U <sub>r</sub> f <sub>n</sub> D		
	U <sub>ra</sub>	U <sub>rb</sub>	U <sub>rpeak</sub>			U <sub>a</sub> (m/s)	U <sub>b</sub> (m/s)	U <sub>peak</sub> (m/s)
1 In-line oscillations	1.20	2.50	2.10	2.51	0.051	0.153	0.319	0.268
2 In-line oscillations	2.70	3.80	3.20	2.51	0.051	0.344	0.485	0.408
3 Transverse oscillations	4.80	8.00	7.25	2.51	0.051	0.612	1.020	0.924

The response analysis in section 4.8 predicted transverse oscillations slightly below of  $A/D = 1.6$ , when vortex shedding frequency approach the natural frequency of the cantilever measured in still water, and in-line oscillations between first and second instability regions below  $A/D = 0.2$ .

The 3D trajectories of the mocap data in QTM, as shown in Fig. 4.18, were useful to identify the motion pattern at different towing speeds.



(a) Marker trajectories



(b) Free end trajectories

**Figure 4.18 QTM 3D trajectories**

The mocap data of the marker at the underwater free end was plotted for a range of towing speeds to visualize the transition between in-line and transverse instabilities.

2D trajectories are commonly plotted in the non-dimensional quantities  $A/D$  and reduced velocity ; the trajectories shown in Figs. 4.19 and 4.20 were plotted in their measured data values to facilitate the comparison against the towing velocity estimated for in-line and

transverse instability regions in section 4.8, although the gridlines spacing are indicative of one external diameter.

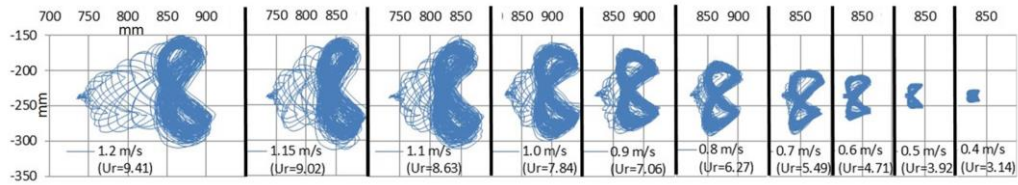


Figure 4.19 Marker trajectories of the cantilever free end (transverse instability region)

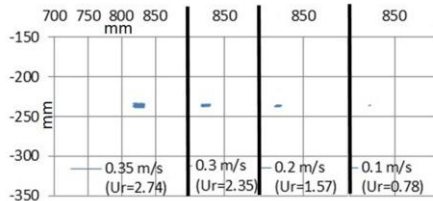


Figure 4.20 Marker trajectories of the cantilever free end (in-line instability region)

Table 4.8 summarizes the mocap data analysis for transverse and in-line peak amplitudes found within a range of towing speeds. The reduced velocity is calculated with the value of the natural frequency measured in still water as: = \_\_\_\_\_

Table 4.8 In-line and transverse peak responses

Test No.	Towing Speed (m/s)	Reduced Velocity	In-line oscillation		Transverse oscillation		Mean Drag displacement (mm)	Cd
			$A_{max(P2P/2)}$ (mm)	$A_{max}/OD$	$A_{max(P2P/2)}$ (mm)	$A_{max}/OD$		
43	1.20	9.41	38.29	0.75	79.27	1.56	133.23	3.12
42	1.15	9.02	41.67	0.82	79.94	1.57	120.13	3.06
41	1.10	8.63	45.24	0.89	79.53	1.57	105.40	2.94
38	1.00	7.84	41.68	0.82	69.55	1.37	83.34	2.81
36	0.90	7.06	35.64	0.70	59.81	1.18	65.51	2.73
34	0.80	6.27	33.95	0.67	53.76	1.06	49.59	2.61
21	0.70	5.49	29.39	0.58	45.73	0.90	36.55	2.51
16	0.60	4.71	21.27	0.42	32.27	0.64	21.62	2.02
14	0.50	3.92	12.97	0.26	17.58	0.35	12.54	1.69
12	0.40	3.14	11.23	0.22	9.31	0.18	6.44	1.36
11	0.35	2.74	9.27	0.18			4.17	1.15

9	0.30	2.35	7.87	0.15			2.51	0.94
7	0.20	1.57	4.99	0.10			0.45	0.38
5	0.10	0.78						

Comparing the predicted response peaks against data analysis of the measured motion, as showed in Fig. 4.19, 4.20, 4.21 and table 4.8, it was found that:

1. The initial in-line instability was observed and measured at towing speeds of 0.2 to 0.35 m/s, within the predicted range.
2. The peak in-line non-dimensional amplitude of oscillation, was found at  $A/D = 0.18$ , within predicted values for the initial in-line instabilities in section 3.2.8.
3. The peak transversal non-dimensional amplitude of oscillation was found at  $A/D = 1.57$ , also within predicted values in section 3.2.8.
4. Transverse oscillations were identified from a towing speed of 0.4 m/s, which corresponds to a reduced velocity  $U_r = 3.14$ .
5. Peak transversal response was found around a towing speed of 1.15 m/s, which corresponds to a reduced velocity  $U_r = 9.02$ .
6. In this case, the maximum in-line and transverse oscillations were very close each other around a reduced velocity  $U_r = 9$ .

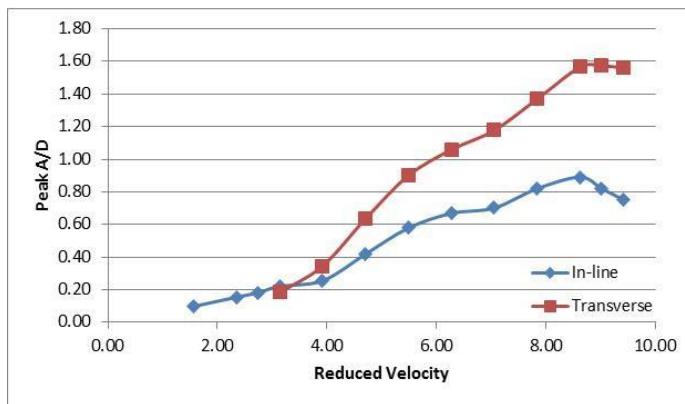


Figure 4.21 In-line and transverse peak amplitudes of oscillations

#### 4.9.3 Drag coefficient estimation for the flexible cylinder

As previously mentioned, the free surface and the 3D effects at the free end are likely to affect the real drag fluid loading distribution along the submerged section of the cantilever.

Using Morison's equation for an equivalent mean drag force per unit length = 0.5 acting over the submerged section of the cantilever, the mean drag coefficient can be approximated assuming a uniform distributed load, as derived in section 4.2.3 as:

$$= \frac{24EIy(L)}{2(L-a)^4 - 4bL^3 + 6bL^2(2a+b)} \cdot 0.5$$

The displacements corresponding to the steady or mean drag component at the free end, ( $y$ ), were obtained considering the mean value of the in-line time varying oscillations for each towing speed with respect to the initial position at rest; these displacements and the resulting drag coefficients are included in table 4.8.

The main variations of the drag coefficients and reduced velocities against the response for this experiment are shown in Fig. 4.22.

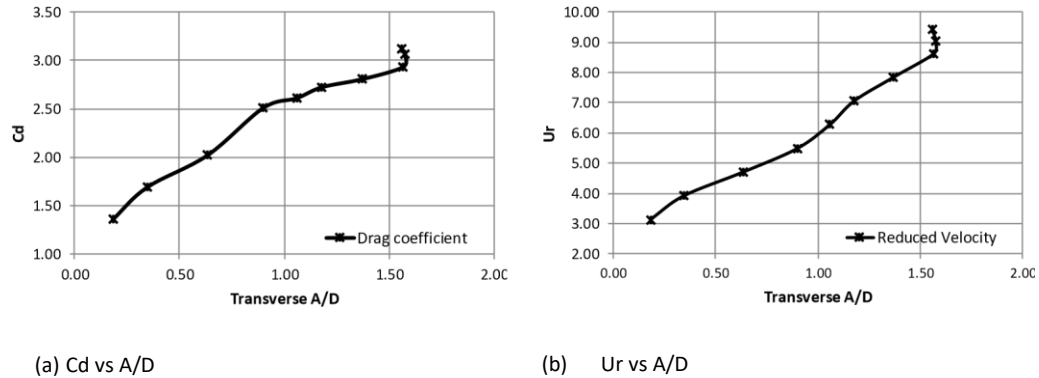
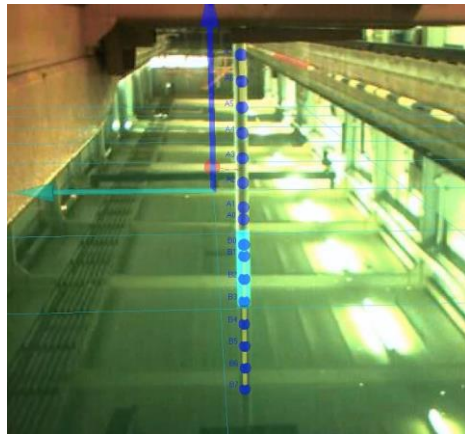
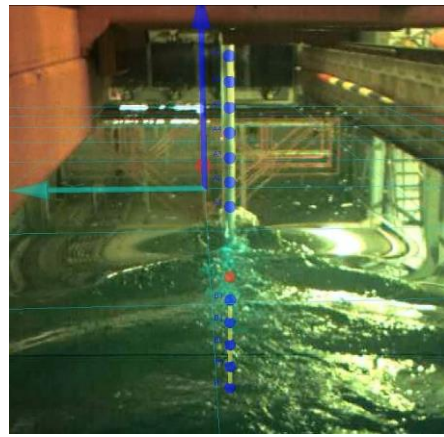


Figure 4.22 Steady drag coefficient amplification

#### 4.9.4 Video capture



(a) At rest ( $U = 0$  m/s)



(b) During VIV ( $U = 1.05$  m/s)

**Figure 4.23** Video capture with 3D data overlay

The Qualisys system can add cameras with the optional feature of high-speed video to the system setup, allowing 3D data overlay which can be shown on the video data files.

An oqus 210c camera was available and used below the towing carriage for some tests, to get a visual record of the system capability over the vertical cantilever.

A series of video files were processed, showing an excellent visual position and synchronisation between the vertical cantilever and the 3D projections of the motion capture data for both camera systems, aerial and underwater.

Nonetheless, it can be observed that at high towing speeds, the splash zone at the free surface caused the loss of reflexion for the marker A0, located at 50 mm above water; additionally, air bubbles generated below the water free surface caused the loss of reflexion for the marker B0, located at 50 mm below the tank water level and intermittent loss of reflexion for the marker B1 and occasionally B2, located at 100 and 200 mm below the water level respectively (see fig. 4.23b).

## 4.10 Conclusions



The performance of underwater cameras in the motion capture system was validated with excellent results for the analysis of natural frequencies and experimental damping values of the vertical cantilever beam used in the tests, comparing the motion captured with the aerial camera system previously evaluated and independent strain gauges instrumentation.

The measurements allowed that the FEA model could be updated, to match the real support conditions of the cantilever beam tested.

Test data were processed to obtain RMS amplitudes of in-line and transversal oscillations, to perform the harmonic analysis proposed to validate the dynamic response measured by underwater cameras during VIV. The methodology provided a good estimation of the elastic curvature of the beam to validate the system performance as discussed in section 4.9.2.

3D and 2D trajectories were plotted using QTM and exported data to verify in-line and transversal peak amplitudes of oscillations during tests and successfully compared against the peak response predictions in section 4.8.

The experimental data were also used to estimate the variation of the steady drag coefficient at a range of towing speeds, showing dependences respect to the reduced velocity and the transversal oscillations.

The video capture feature was reviewed for visual validation, identifying some issues related with the loss of visualisation for markers nearby the free surface.

Future work to obtain additional hydrodynamic parameters and the accuracy dependence on vibration of underwater cameras due to fluid flow were discussed, although these should be assessed for each test setup.

Based on the test findings and previous comments, it is considered that the underwater camera system under towed conditions is viable as a non-intrusive optical system for motion capture over continuum elements, although some considerations must be taken for limitations of marker visibility nearby the water free surface, possible effects of high flow

speeds over the enclosure of underwater cameras that could compromise accuracy and the distance range depending on water quality and marker sizes.

## 5 Design of the riser towing test

### 5.1 Motivation

The onshore fabrication process of a riser tower or pipe bundle to be towed offshore, demands a launching operation, where sections or the whole length of the structure is required to remain for time periods at the free surface of the sea for weight/buoyancy verifications and adjustments or component assembly activities until the towing operation can be started.

The structure is then likely to be towed near the free surface until the tow depth can offer conditions for an alternative control depth or sub-surface towing technique; hence the interest to investigate the responses close to the free surface and subject to current and wave flows.

The limitations of aerial and/or underwater motion capture system for response measurements of immersed continuum elements near the water free surface in the towing tank were evident in the previous experimental work.

Additionally, the response along a slender cylinder in laboratory conditions can demand a prohibitive number of underwater cameras to be integrated in a motion capture system, which motivates the interest to investigate alternative technologies for the studies.

### 5.2 Simplified model analysis

Following the ideas in sections 3.2 and 4.2 for the previous experiments, a simplified model was developed to gain an understanding of the structural response fundamentals for the riser prototype to be towed, this was initially represented by a tensioned free-free beam (fig. 5.1), where Euler-Bernoulli beam theory is applied again, assuming that any cross section along the beam remains plane.

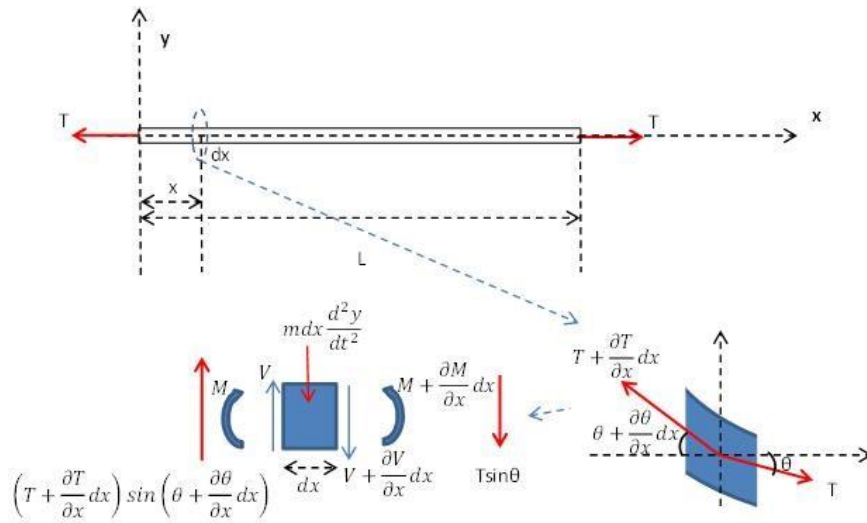


**Figure 5.1 Simplified model for vibration analysis of a tensioned free-free beam**

A step by step derivation of the analytical solution for the natural frequencies and the mode shape equation can be consulted in Appendix A.3.

The natural frequencies of the beam are given by eq. (A.85) as  $\omega = \frac{B_l^2}{L} \sqrt{EI}$

Where  $B_l$  is given by eq. (A.72), using eq. (A.67) to solve the characteristic equation (A.84) for  $k$  roots, then eq. (A.74) and (A.86) are used for the mode shape given by eq. (A.87) as:

$$y(x) = \frac{1}{2} E \cosh(kx) + \frac{1}{2} \sinh(kx) + \cos(kx) + \sin(kx)$$

### 5.3 Prototype material selection

It was considered to assume a full-scale riser with an outer diameter about 20 inches (0.508 m) to be scaled for the model test.

The model scaling laws requires geometrical, dynamic and kinematic similarities to be hold.

For geometrical similarity, the linear dimensions must be within the same scale ratio, this scale ratio is given between linear dimensions of the full-scale structure and the model structure ( $R=L_f/L_m$ ). As a first approach, a scale ratio of  $R=10$  was considered for the riser model design, the external diameter of the model was preliminary scaled to  $D_m = D_f/R = 508 \text{ mm}/10 = 50.8 \text{ mm}$ .

To achieve a neutrally buoyant condition for the experiment within a reasonable tube thickness, copper material was chosen given its high material density.

For the intended diameter, the commercial dimensions available were found according to the following properties:

Copper round tube R250, half-hard (BS EN 1057), external diameter  $D = 42 \text{ mm}$ , thickness  $t = 1.2 \text{ mm}$ , mass per unit length  $m = 1.369 \text{ kg/m}$ , Young's modulus  $E = 117 \text{ GPa}$ , tensile strength =  $250 \text{ MPa}$ , proof stress =  $150 \text{ MPa}$ .

The previous dimensions give a mass ratio (tube mass per unit length respect to mass per unit length of the water displaced by the tube in fully immersed conditions with no internal fluid) of  $0.988$ , which practically provides a neutrally buoyant condition.

The updated scale ratio was  $R = 508\text{mm}/42\text{mm} = 12.095$

In section 2.2, it was identified a potential scenario for a typical towing speed of  $3.5 \text{ knots}$  ( $1.75 \text{ m/s}$ ) with transversal currents about a mean speed of  $0.3 \text{ m/s}$  giving a flow vector angle of about  $10 \text{ degrees}$ .

The KHL towing tank has a width of  $15 \text{ feet}$ ; subtracting  $1 \text{ foot}$  per side for vertical supports under the towing carriage, the maximum length of the model string to achieve the intended angle of  $10 \text{ degrees}$  is about:

$$= \frac{13 (0.3048 / )}{(10^\circ)} = 22.82$$

The maximum commercial length found for the copper tube was  $6 \text{ m}$ , thus, it was decided to fabricate the riser prototype with  $3 \text{ tube sections}$  for a length about  $18 \text{ m}$ , leaving an approximate length about  $2.4 \text{ m}$  at the tube ends for cable sections as part of a tensioning system, giving a model with ratio  $L/D \approx 429$ .

## 5.4 Approach to the riser model response

The geometric and physical properties of the copper tube as a beam, with some practical pre-tension values to be applied during tests (about 100-200 N) can be substituted in the equations mentioned in section 5.2 for the mode shapes.

The mode shapes in eq. (A.87) also requires an approximated value for the proportional amplitude  $C_4$ , a first estimation can be obtained from the response parameter for steady flows.

For the case of wave and current flows, the incident flow velocity becomes intermittently in the lock-on range, and the response parameter of section 4.2.7 becomes:

$$= \text{---} \quad (5.1)$$

The new factor  $P$  is  $\leq 1$  and is given in (Barltrop et al., 1990) as  $P=Q\delta/\pi$ , where  $Q$  is a dynamic magnification of the response to a fluctuating lift force, being a function of the number of decay cycles “ $m$ ”, forcing cycles “ $f$ ” and damping.

An equilibrium value for  $Q$  is derived, where the increase of amplitude during locked-on oscillations is balanced by the reduction of damped oscillations during the fluctuating response, so:

$$= \quad (5.2)$$

From eq. 5.1,  $Q$  (and  $P$ ) decreases as the number of decay cycles increases for a given number of forcing cycles, thus the response parameter increases and can originate a reduction in the relative amplitudes of response due to vortex shedding in current plus wave flows (see fig. 4.10).

For steady flow, the number of cycles can be taken as infinite, where  $P=1$ , the logarithmic decrement was preliminary assumed with a low value of  $\delta=0.05$ , the mass of the copper tube per unit length plus the added mass is taken as the equivalent mass  $M_e$  and the tube

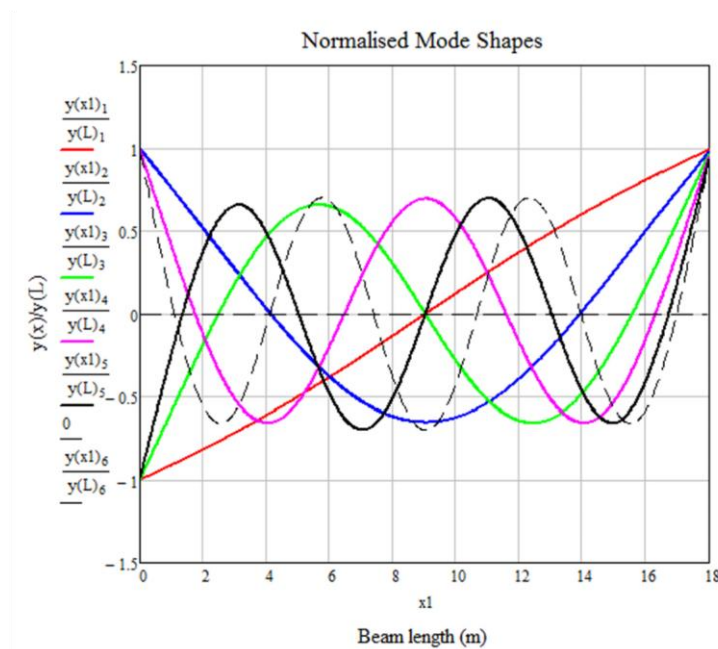
properties in section 5.4 are substituted in eq. 5.1 for a response parameter result of  $R_p=0.149$ .

For current plus wave flows, it was explored a case of 1 force cycle and up to 10 decay cycles, then  $P=0.07$  (a larger number of forcing cycles or lower number of decay cycles will increase  $P$  values), with this value, the response parameter increases up to  $R_p=2.128$ .

From fig. 4.10, the relative amplitude response is estimated about 1.2D for current flows ( $R_p=0.149$ ) and an expected reduction about 0.6D for wave plus current flows ( $R_p=2.128$ ), thus the relative amplitude of 1.2D was considered for the constant  $C_4$  in eq. (A.87).

The mode shape equation (A.87), allows shear diagrams to be plotted as  $\frac{d^2y}{dx^2}$  to identify zero crossings distances, which are used to solve for maximum bending moments from

$EI \frac{d^2y}{dx^2}$ , the corresponding stress is given by  $\sigma_{max} = \frac{M_{max}(\frac{x}{L})}{I}$  (see fig. 5.2), then the maximum bending strain can be found for each mode by  $\epsilon_{max} = \frac{\sigma_{max}}{E}$ .



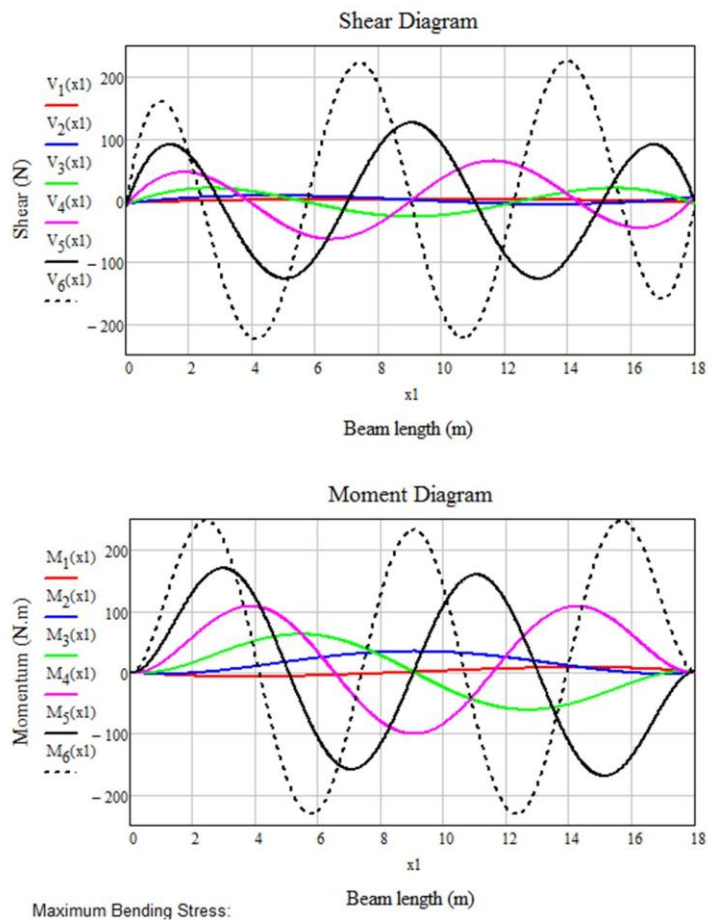


**Figure 5.2 Mode shapes, shear and bending moment diagrams**

The proof stress of the copper tube is given as  $\sigma_{0.2\%}=150$  MPa, thus the associated bending strain can be determined as  $\epsilon_{0.2\%} = \sigma_{0.2\%}/E = 1282.05 \mu\epsilon$ .

The intended pre-tension values for the towing test generates low strains values about 15  $\mu\epsilon$ .

Applying the procedure for a simplified assessment of fatigue, as reviewed in section 2.4.2 (DNV-OS-F201, Appendix E, B101-106), the most likely mode shapes to be excited were identified for the range of towing speeds up to the third mode in CF direction.

For the relative amplitude of 1.2D, the bending stress and strain corresponding to the third mode was calculated for values of  $\sigma_{3\max CF} = 44.44$  MPa and  $\epsilon_{3\max CF} = 379.82 \mu\epsilon$  respectively; assuming a 2 x response for the IL direction (6<sup>th</sup> mode) for a typical maximum amplitude



about 0.2D, the corresponding values were estimated for the IL response as  $\sigma_{6\max\text{IL}} = 29.71$  MPa and  $\epsilon_{6\max\text{IL}} = 253.94 \mu\epsilon$ .

From previous calculations, the maximum expected strain in the CF direction represents less than 30% respect to the bending strain corresponding to the proof stress of the copper tube.

There was no available fatigue strength information or S-N curves for the copper tube, although the standard fatigue strength for copper alloys, i.e. the value of stress at which failure occurs after N cycles, is generally reported for  $10^8$  cycles, decreasing approximately one half of the static tensile strength (Kutz, 2006).

The copper tube tensile strength is specified as 250 MPa, thus a fatigue strength was preliminary assumed for a value of 125 MPa, where the maximum bending stress expected  $\sigma_{3\max\text{CF}} = 44.44$  MPa represents about 36% respect to that of the fatigue strength.

Even considering a maximum amplitude of 1.2OD for a higher 4<sup>th</sup> mode shape, the calculated values of bending stress and strain ( $\sigma_{4\max\text{CF}} = 77.48$  MPa and  $\epsilon_{4\max\text{CF}} = 662.22 \mu\epsilon$ ) are still well below both, the fatigue strength and the maximum strain associated to the proof stress.

Assuming tests with 200 seconds runs in the towing tank up to the 4<sup>th</sup> mode (see fig. 3.62) at 1.32 Hz of frequency response for max CF amplitudes, the number of tests to reach the number of cycles associated to the copper fatigue strength will be about  $10^8 / (200)(1.32) = 3.78 \times 10^5$  tests; hence, the intended towing tests can be conducted safely with no expected risk related to fatigue failure.

## **5.5 Fibre optic sensing technology, the design and installation of fibre optic arrays with FBG sensors**

To deal with measurement responses along slender cylindrical elements, recent research work has resorted to the use of fibre optic sensing technology (Vandiver et al., 2009), which encouraged the investigation of this technology to be applied in the intended towing tests.

The technology is based on Fibre Bragg Grating (FBG) sensors, a microstructure written in the core of a fibre optic to construct a periodic variation of the refracting index over a short

length of the fibre core, using transversal radiation of laser beams to form a wavelength selective mirror.

The FBG sensor can then reflect a specific frequency of a broadband light source in the fibre optic, this narrowband reflected frequency is known as the Bragg wavelength  $\lambda_b = 2n\Lambda$ , where  $n$  is the effective refracting index and  $\Lambda$  is the grating period or space between gratings; the sensor is highly sensitive to any strain affecting the grating space and to temperature which produce mainly variations in the FBG refracting index, causing wavelength shifts when the sensor reflects frequencies from the light source (Werneck et al., 2013).

According to National Instruments (2016), the Bragg wavelength can be expressed as:

$$\frac{\Delta\lambda}{\lambda} = (1 - p_e)\epsilon + (\alpha_\Lambda + \alpha_n)\Delta T \quad (5.3)$$

Where  $\Delta\lambda$  is the wavelength shift,  $\lambda$  is the initial wave length,  $\epsilon$  is the strain,  $\Delta T$  is the temperature variation,  $p_e$  is a strain-optic coefficient,  $\alpha_\Lambda$  is a thermal expansion coefficient and  $\alpha_n$  is a thermo-optic coefficient; thus, the terms  $(1 - p_e)$  and  $(\alpha_\Lambda + \alpha_n)$  in eq. 5.3 represents the FBG's strain and temperature sensitivities respectively.

The strain and temperature sensitivities of FBG sensors are specified by manufacturers, with typical values of:

$$\begin{aligned} (1 - p_e) &= 7.8 \times 10^{-6} & (\alpha_\Lambda + \alpha_n) &= 6.5 \times 10^{-6} \\ &\text{Measured at room temperature} & &\text{Measured between 0 - 70}^\circ\text{C} \end{aligned}$$

Then, the wavelength shift can be estimated from eq. 5.3 as:

$$\Delta\lambda = [(7.8 \times 10^{-6})\epsilon + (6.5 \times 10^{-6})\Delta T] \quad (5.4)$$

The FBG sensors can be manufactured with a different Bragg wavelength by changing the grating period, which allows multiple sensors to be allocated in daisy chain over the same fibre optic.

The sensors must be "interrogated" to identify the Bragg wavelength shifts due to changes in strain and/or temperature; one of the most used techniques for interrogation is the wavelength division multiplexing (WDM) method.

The FBG interrogator is the instrument connected at one end of the fibre optic to provide the light source and measure the Bragg wavelength of each FBG sensor, this is connected to a computer to convert the identified wavelengths into desired measurements through dedicated software.

As a complement of the Qualisys motion capture system, the fibre sensing technology received support for a first application in the Kelvin Hydrodynamics laboratory for hydrodynamic research, to obtain bending strains and frequency responses along the span of a towed riser prototype, allowing measurements for test conditions near to the water free surface.

To get the bending strains for in-line and cross flow directions, four fibre optic arrays were considered along the riser model to be bonded in the four main quadrants (see fig. 5.3). The number of sensors per array were limited to 15 FBG sensors per array due to budget constraints for the test.

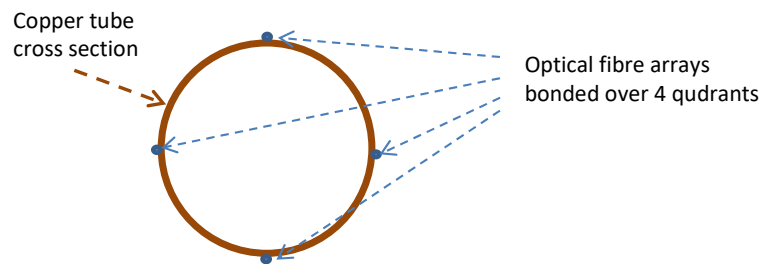


**Figure 5.3 Fibre optic arrays locations**

The main advantage to design the installation of the 4 fibre optic arrays over the tube quadrants, instead of the possible minimal arrangement with 3 arrays, is that the temperature and axial strains can be compensated by differential measurement.

Being two FBG sensors diametrically opposed at the same location along the tube, the bending strains and consequent wavelength shifts will be identical in opposite directions, whereas the wavelength shifts due to temperature and axial strains are considered the same and in the same direction since they are very close each other.

Hence, the wavelength shifts due to bending strains can be obtained by a simple subtraction between measurements of diametrically opposed FBG sensors divided by 2, then, the bending strains at each point along the model axis are processed from equation

5.4 as 
$$\epsilon = \frac{\Delta \lambda_1 - \Delta \lambda_2}{2 \lambda_0}$$
, where  $\Delta \lambda_1$  and  $\Delta \lambda_2$  are any diametrically opposed

FBG sensors.

In the same way, the wavelength shifts due to axial strains can be obtained by addition of measurements of diametrically opposed FBG sensors divided by 2, although it is important to consider that in case of environments with relevant temperature variations, dedicated FBG sensors for temperature measurement will be required for compensation.

## 5.6 Specification of FBG sensors and design of the fibre optic arrays

The FBG sensors must be specified within a wavelength range to be written accordingly in the core of the fibre optic, the range must be wide enough to cover the maximum and minimum expected strains and temperature changes from the manufactured conditions to the intended application.

Additionally the wavelength range of the sensors must consider avoiding an overlap of spectral responses for an adjacent sensor when they are subject to opposite strains, one in tension and the adjacent in compression, which is a potential case during oscillations or vibrations along slender structural elements; thus, our colleagues from the Centre for Microsystems and Photonics recommended a common practice to set the wavelength of the grating for the maximum-minimum expected shifts during measurements plus a safety margin.

For a WDM interrogation method, the FBG's centre wavelength  $\lambda$  must consider the number of sensors to be distributed within the wavelength range of the interrogator.

The availability of interrogation equipment from the Centre for Microsystems and Photonics of the Department of Electronic and Electrical Engineering in the University of Strathclyde

was restricted to any of two possible units due to the time window assigned in the KHL towing tank for the experimental work, the main characteristics of these units are indicated in table 5.1.

**Table 5.1 FBG Interrogators**

Interrogator	Wavelength range (nm)	Max sampling freq. (Hz)	No. of channels
National Instruments (PXIe-4844)	1510-1590	10	4
Smart Fibres (SmartScan)	1528-1568	2500	4

The SmartScan interrogator model has the lower wavelength range of 40 nm, thus for 15 sensors per channel, the wavelength range of each sensor should not be greater than about  $40 \text{ nm}/15=2.66 \text{ nm}$  to avoid any risk of wavelength shift overlap, which allows a max-min wavelength shift of 1.33 nm.

For the max-min strains obtained at the end of section 5.4 ( $\epsilon_{4\text{maxCF}} = 662.22 \mu\epsilon$ ) and considering up to 10 Kelvin degrees of temperature variation, the wavelength shift can be calculated for a value of 0.9 nm; thus, if we define a wavelength range for the FBG sensors of 2.5 nm, the safety margin for the wavelength shift is about 39% ( $1.25\text{nm}/0.9\text{nm}$ ). In this way, the FBG sensors can be interrogated by any of the two available instruments.

Four fibre optic arrays were designed to distribute 15 FBG sensors along bare optic fibres to be bonded on each quadrant along the 18 m length of the riser model to measure in-line and cross flow responses; the optic fibres then continue with a protected download section up to the data acquisition rack on the towing tank carriage.

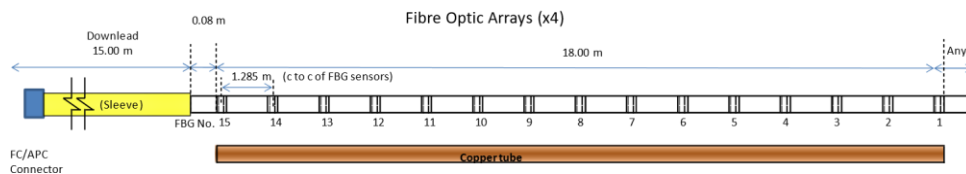


**Figure 5.4 Fibre optic array diagram (4x)**

The general arrangement for the FBG sensors and the final specification for the fibre optic arrays are summarised in tables 5.2 and 5.3 respectively.

**Table 5.2 FBG sensors arrangement spec**

FBG sensor #	CW $\lambda$ (nm)	FBG C TO C distance (m)	Cummulative distance (m)
1	1530.0	1.285	17.990
2	1532.5	1.285	16.705
3	1535.0	1.285	15.420
4	1537.5	1.285	14.135
5	1540.0	1.285	12.850
6	1542.5	1.285	11.565
7	1545.0	1.285	10.280
8	1547.5	1.285	8.995
9	1550.0	1.285	7.710
10	1552.5	1.285	6.425
11	1555.0	1.285	5.140
12	1557.5	1.285	3.855
13	1560.0	1.285	2.570
14	1562.5	1.285	1.285
15	1565.0	1.285	0.000
FBG wavelength range 2.50 nm			
FBG CW distribution for SmartScan Interrogator (1528 - 1568 nm)			
The arrays can also work with NI interrogator (1510 - 1590 nm)			

After a market research for latest technologies of manufacture, Femtofibertec/Loptek in Germany was selected due to cost reduction, higher tensile strength and immunity to humidity, among other benefits against conventional FBG sensors, which is offered by their inscription methods based on infrared femtosecond laser technology, where the FBG can be written through the fibre coating, avoiding typical stripping and recoating processes to the fibre (Femtofibertec, 2016).

**Table 5.3 Final specs for fibre optic arrays**

Fibre Manufact.	Fibre type	Core diam. ( $\mu\text{m}$ )	Cladding diam. ( $\mu\text{m}$ )	Coating	Fibre length (m)
Fibercore	SM1250SC (10/125)P	10	125	Polyimide	33

FBG

FBG length (mm)	Reflectivity (%)	3dB Bdwth (nm)	SNR (dB)
< 5	>20%	~0.5	>20

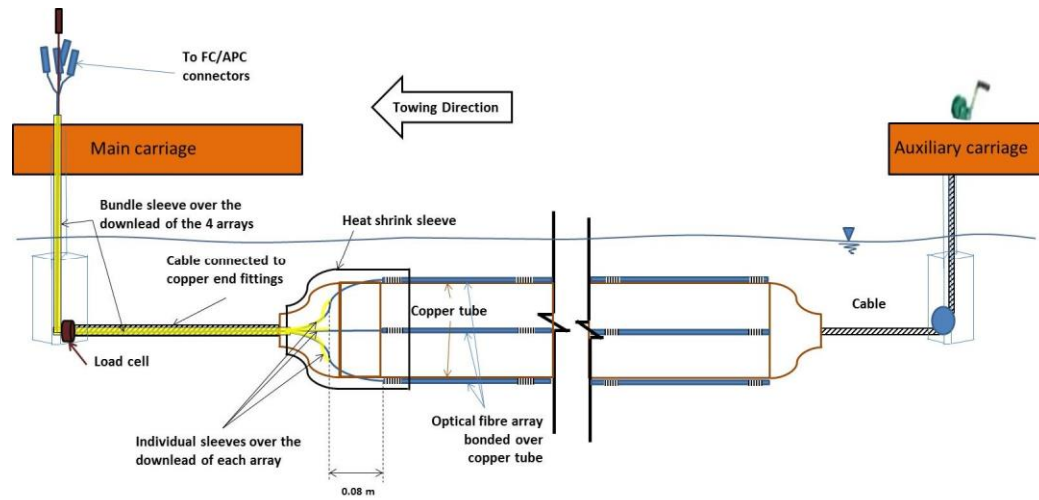


Figure 5.5 Fibre optic assembly design

## 5.7 Fabrication of the riser prototype and test setup

The riser model was fabricated along the towing tank with solder joints, using three sections of the copper tube, 4 straight fittings, 2 reducer fittings (42x15 mm) and 2 short copper studs of 15 mm diameter at the ends to seal the interior from water and allow connections for tensioning.



**Figure 5.6 Fabrication of the riser prototype**

The 4 quadrants of the model were marked for the installation of the fibre optic arrays, bonding the FBG sensors with cyanoacrylate glue “super glue” according to recommended practices (HBM, 2010), which has been successfully evaluated as a good bonding method by Chen et al. (2009) and Chien-ching (2008). Retro-reflective tape markers were also installed for the motion capture system as showed in fig. 5.7.

Preliminary, one independent fibre optic containing one FBG sensor was bonded and tested over a tube section, performing a measurement for the bending strain due to own weight deflection in a simply supported beam condition.

A simple protection of the bare fibres with magic tape along the instrumented riser prototype was tested and utilised considering the test time frame assigned, although an alternative for using a heat shrink sleeve over the whole length was ready available. A small length of this heat shrink sleeve was used to secure the fibres at one end of the tube for the down lead of the fibre optic arrays.



**Figure 5.7 Fabrication of the riser prototype**



The Fibre optic arrays were connected to the Smartscan interrogator for verification of the system, conducting a calibration by measurements of statically induced constant curvatures nos. 1 and 2 with an arc height or sag of  $s_1=100$  mm and  $s_2=150$  mm, being the length of the tube the arc length, see fig 5.8 and 5.9, so the radius of the induced curvatures are obtained solving the eq.  $\frac{1}{R} = \frac{8s}{L^2}$  for  $R_1=405.951$  m and  $R_2=270.62$  m.

The curvatures were applied to opposite sides and identified as 1a and 2a in the calibration test and for both transversal axes of the copper tube according to the fibre array quadrants, considering that these will be oriented in the IL and CF directions during VIV tests.

The calibration method was set as 3x20 seconds measurements of the FBG wavelengths in the straight condition and repeated for each curvature applied to both sides of the plane, to impose tension and compression deformations in the two horizontal fibre optic arrays nos. 2 and 4 subject to bending; the model was then rotated 90 degrees to repeat the operation for arrays nos. 1 and 3.

The measured wavelengths for 20 seconds were averaged for the 5 central FBG sensors bonded in the central copper tube section of the model subject to bending and subtracted from each strained/unstrained condition to determine the associated FBG wavelength shift; the results were also compensated for temperature by differential measurement of the opposite fibre optic arrays, as indicated at the end of section 5.5, with summarised results in table 5.4.

**Table 5.4 Averages of FBG wavelength shifts during calibration**

	Arrays 2-4 (nm)	Arrays 1-3 (nm)	$\mu$ 2-axes (nm)	$\sigma$ (nm)
Curvature 1	0.0622	0.0623		
Curvature 1a	0.0622	0.0610		
$\mu$	0.0622	0.0617	0.0619	0.0006
Curvature 2	0.0955	0.0937		
Curvature 2a	0.0933	0.0899		
$\mu$	0.0944	0.0918	0.0931	0.0024

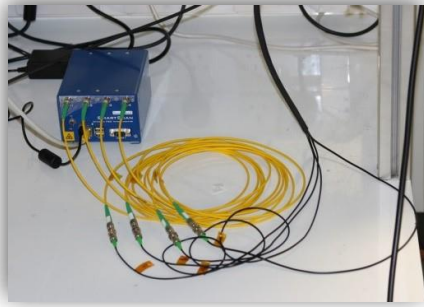
Since FBG sensors are bonding directly to the external diameter of the copper tube, the theoretical strains due to the imposed curvatures 1 and 2 are determined by dividing the radius of the copper tube by the radius of curvature,  $\epsilon = \frac{r}{R}$ , to get the values of  $51.73 \mu\epsilon$

and  $77.60 \mu\epsilon$ . Using the typical FBG strain sensitivity  $(1 - \nu) = 7.8 \cdot 10^{-5}$  in the first term of eq. 5.4, the estimated wave length shifts associated to previous calculated strains are of 0.0624 and 0.0936 nm, which represents a negligible difference respect the average measurements indicated in table no. 5.4 of 0.0005 nm or 0.5 pm.

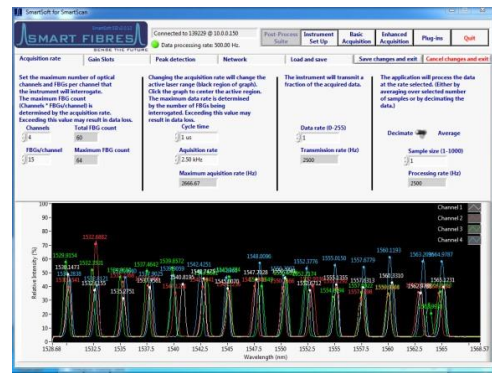
Considering that the previous result is within the experimental standard deviation found in the measurements, it was concluded that the typical strain sensitivity is adequate for be used during measurements of bending strains in the riser prototype.



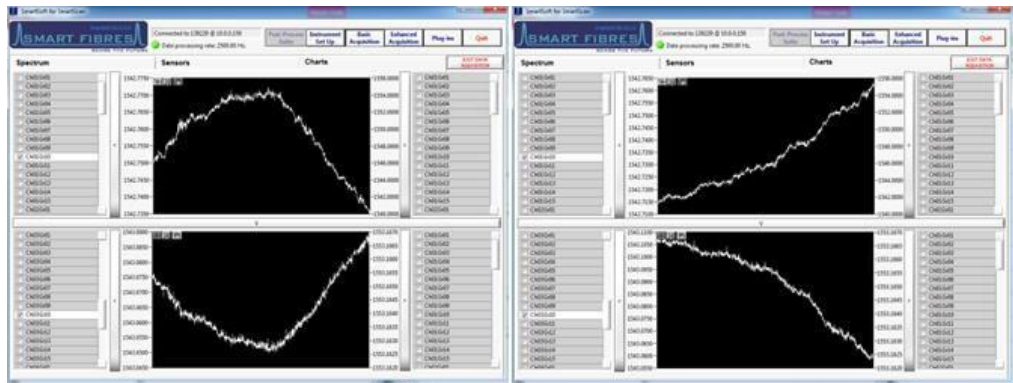
**Figure 5.8 Verification/Calibration of the fibre optic sensing system**



(a) Smartscan interrogator



(b) FBG reflectivity



(c) FBG sensors monitoring

Figure 5.9 FBG Interrogator

The auxiliary carriage was rigidly connected to the main towing carriage with Prolyte H30V trusses. The vertical supports were enabled with T slotted 90x90L aluminium profiles with fairings, which were fixed to both carriages and to the H30V trusses for the installation of the riser prototype and the underwater cameras of the motion capture system.

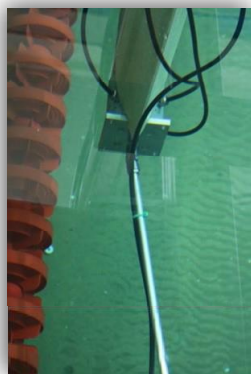


Figure 5.10 Auxiliary carriage and supports connections



**Figure 5.11 Installation of underwater cameras of the motion capture system**

A tri-axial load cell (Applied Measurements mod CCDXYZ-250kg-US) was calibrated and installed under the leading vertical support, to be used for pre-tension adjustments in the model and for the measurement of the dynamic tensions in the riser during the tests; the trailing vertical support included a swivel pulley in the bottom to allow a cable running through it up to a bottle screw tensioner in the top, as seen in figs. 5.12a and 5.12b.



(a) Load cell under lead-end support      (b) Tensioner above trail-end support

Figure 5.12 Lead-end and trail-end supports for the tensioned riser prototype

Final dimensions and properties of the model setup were taken to update a finite element model for analysis, as indicated in figs. 5.13, 5.14 and 5.15. The final length of the copper tube was  $L=18.0215$  m, with  $D=42$ mm gives an aspect ratio ratio of  $L/D=429.08$  at a yaw angle close to  $80^\circ$ .

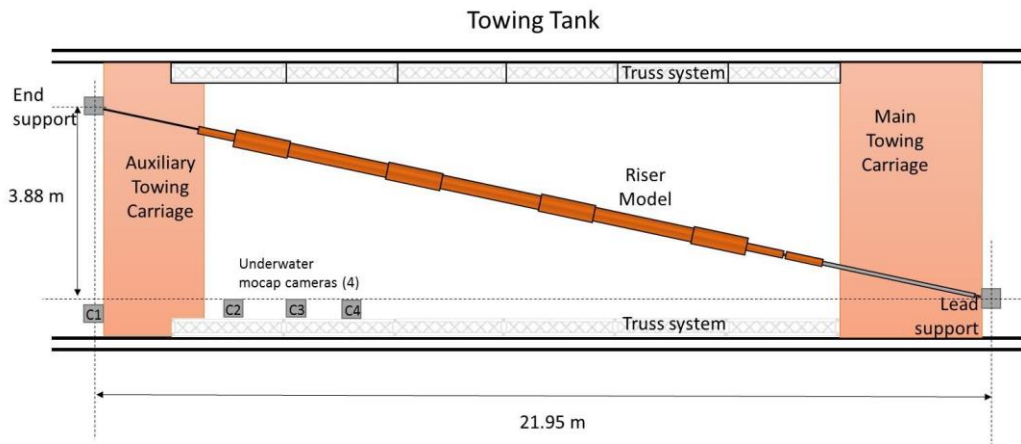


Figure 5.13 Plan view setup dimensions

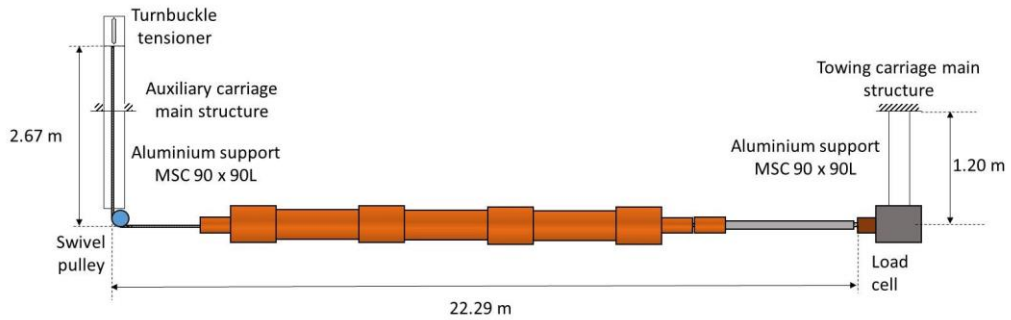


Figure 5.14 Elevation view setup dimensions

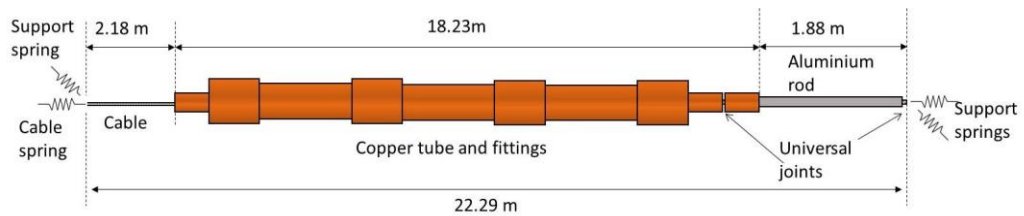


Figure 5.15 Beam model for Ansys FEA

The first depth for the tests series was set at  $25 \times OD = 1.05$  m from the water free surface to the top of the tube cross section; however, it was found that the model weight was lower than expected, causing an upward deflection of the riser prototype.

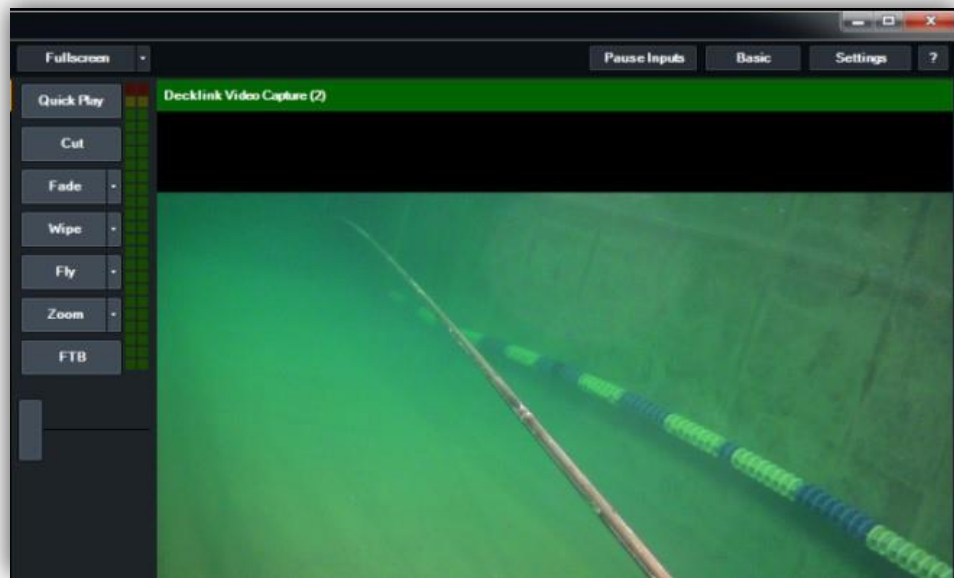


Figure 5.16 Riser upward deflection at 1.05 m tow depth at supports

The fabrication specs (BS EN 1057, 2006) for the copper tube indicates a thickness tolerance of  $\pm 10\%$ . After a carefully revision based on weights instead of measured dimensions, it was found that three additional sections of 6 metres length presented a constant mass per unit length of 10% less than the mass per unit length specified in brochure.

It was verified that the external diameter of the copper tube was correct, so the real thickness of the copper tube was in average 10% thinner and in the boundary of the fabrication tolerance, originating a change in the mass ratio of the intended neutrally buoyant condition from 0.988 to 0.897.

With the riser prototype already instrumented, we did not find any weight compensation method that could be implemented safely within the time frame assigned for the towing tank, so it was decided to conduct the tests in that condition with an initial pre-tension of 115 N, considering that the sub-surface towing method for riser installation generally adopts an upward deflection in real life conditions (see fig. 1.7).

During the initial towing tests, it was also found that the response of the riser prototype presented rotations with respect to the longitudinal axis, this possibility was expected due to the inherent condition of the cable strand construction in the tensioning system, so that the lead-end cable was replaced with an aluminium rod of 12.7 mm diameter with two universal joints between the load cell and the leading end of the riser, avoiding rotations over the longitudinal axis while allowing rotations with respect to both transverse axis.

The final model properties and geometric data of the model are summarised in table 5.5.

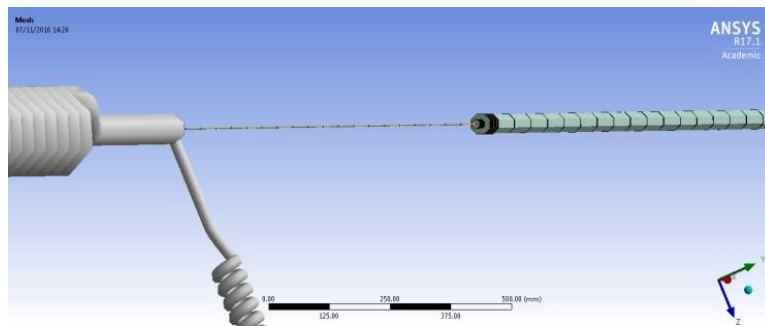
**Table 5.5 Riser model properties and geometric data for tests at a yaw angle about 80°**

<b>Tube Material</b>		<b>Copper R250 (Half-hard) BS EN 1057</b>
Length (inc end feed coupling)	L (m)	18.02
Outside Diameter	OD (mm)	42.00
Internal Diameter	ID (mm)	39.84
Thickness	t (mm)	1.08
Aspect ratio	L/OD	429.08
Copper density	$\rho$ (kg/m <sup>3</sup> )	8930.43
Mass per unit length	m (gr/m)	1242.68
Young's Modulus (0°)	E (Gpa)	117.00
Proof stress	$\sigma_{0.2\%}$ (Mpa)	150.00
Ultimate Tensile Strength	$\sigma_{UTS}$ (Mpa)	250.00
Bending Stiffness	EI (kNm <sup>2</sup> )	3.41
<b>Rod material at lead-end</b>		<b>Aluminium</b>
Rod length	(m)	1.88
<b>Cable material at trail-end</b>		<b>Stainless Steel</b>
Cable length	(m)	2.18

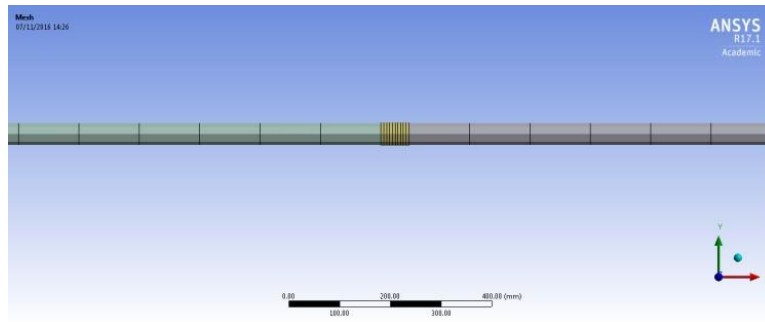
End reducers and universal joint length	(m)	0.21
---	-----	------

## 5.8 ANSYS model of the riser prototype

The “as-built” data of the riser prototype according to table 5.5, including fittings, real weights and length dimensions verified with laser distance measurer were used as an input to build the corresponding model in ANSYS FEA software. For the static analysis, the own weight and uniformly distributed loads equivalent to the buoyancy force per unit length of each element was considered to calculate the upward deflection presented in the riser prototype during the setup.

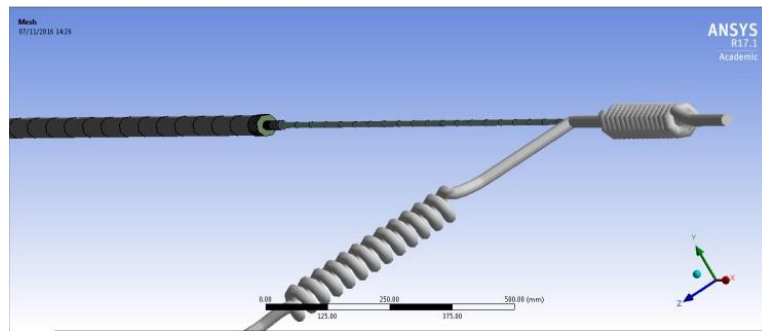


(a) Trailing end, cable and support modelling



(b) Straight fittings modelling





(c) Leading end (articulated rod and support modelling) **Figure 5.17 Ansys model for FEA**

The real upward deflection of the riser prototype pre-tensioned at 115 N, was determined from measurements at the centre of the model from the water free surface to the top of the tube, which gave a depth of 645 mm, so the deflection was  $1,050 - 645 = 405$  mm. The maximum calculated deflection in the Ansys model for the same axial tension of 115 N is showed in fig. 5.18 as 405.13 mm.

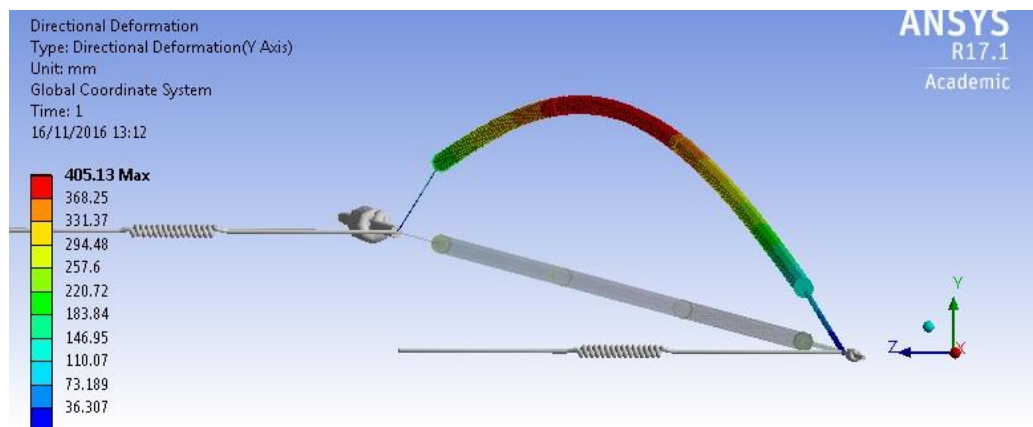


**Figure 5.18 Submerged Static deflection**

As a revision of the Ansys model, it was verified that the axial tension results were kept along the model and that the bending moments along the cable, the rod element connections to the tube ends and connections to both supports were zero or negligible, in order to secure the correct representation of the support conditions.

The Ansys model also included a consideration for the modal analysis, where the lateral stiffness of the aluminium supports in the cantilever condition ( $k_{\text{support}}=3EI/L^3$ ) was modelled as equivalent linear springs.

In the case of the axial stiffness for the trailing end, this was considered as a serial combination of the stiffness provided by the support, as in the leading end, plus the stiffness of the vertical length of the cable to the tensioner ( $k_{\text{cable}}=EA/L$ ), so,

$$1/k_{\text{eq\_axial}}=1/k_{\text{support}}+1/k_{\text{cable}}.$$

The added mass was considered by a modification of the material densities for equivalent densities accounting for the mass of the water displaced by the cylindrical elements, with an added mass coefficient of 1.0, within the same element cross section.

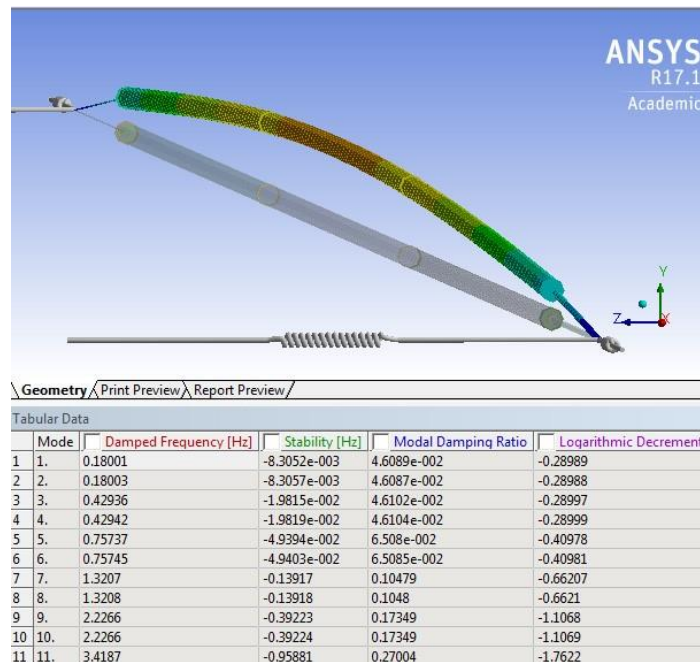


Figure 5.19 Modal analysis

A series of pluck tests were conducted to determine experimentally the damped natural frequencies of the model in still fluid and to estimate the damping by the logarithmic decrement method, although it was found that a low speed towing of the model with a sudden stop was a better method to induce an initial perturbation. Two tests with five decay

cycles were chosen for data analysis from the motion capture system with results in table 5.6.

The natural frequency of the fundamental mode was estimated by sinusoidal fitting of the experimental response, the 4 tests in table 5.7 were chosen considering similar values of the measured tension, the frequency values found were also verified respect to data from the fibre optic sensing system.

**Table 5.6 Experimental damping**

Test no.	Peak amplitude (mm)					$\delta$	$\zeta$
	1	2	3	4	5		
16IL	5.0150	3.4899	2.3623	2.1865	1.6494	0.2780	0.0442
93IL	4.8799	3.1207	2.0363	1.8509	1.4557	0.3024	0.0481
$\mu$							0.0461

**Table 5.7 Measured frequency of the fundamental mode**

Test no.	Damped freq. (Hz)	End tension (N)
16IL	0.173	109.70
17IL	0.178	110.78
35IL	0.175	112.54
36IL	0.179	111.71
$\mu$	0.176	111.184

The fundamental frequency of the submerged riser prototype in still water depends on tension as the characteristic response of a tensioned beam, so, this sensitivity was analysed in the Ansys model for a range of tensions, with results shown in table 5.8.

**Table 5.8 FEA modal analysis**

Tension (N)	Frequency 1st mode (Hz)	Frequency 2nd mode (Hz)	Frequency 3rd mode (Hz)	Frequency 4th mode (Hz)	Frequency 5th mode (Hz)	Frequency 6th mode (Hz)	Frequency 7th mode (Hz)
90	0.165	0.393	0.706	1.273	2.188	3.387	4.728

95	0.168	0.400	0.716	1.282	2.196	3.393	4.734
100	0.171	0.408	0.727	1.292	2.203	3.400	4.739
105	0.174	0.415	0.737	1.302	2.211	3.406	4.745
110	0.177	0.422	0.747	1.311	2.219	3.412	4.750
115	0.180	0.429	0.757	1.321	2.227	3.419	4.755
120	0.183	0.436	0.767	1.330	2.234	3.425	4.761
125	0.186	0.443	0.777	1.339	2.242	3.431	4.766
130	0.188	0.449	0.786	1.349	2.249	3.438	4.771
135	0.191	0.455	0.795	1.358	2.257	3.444	4.776
140	0.194	0.461	0.804	1.367	2.264	3.450	4.781
175	0.211	0.501	0.864	1.428	2.317	3.493	4.817
180	0.214	0.506	0.872	1.437	2.324	3.499	4.822
185	0.216	0.511	0.880	1.445	2.331	3.505	4.827
190	0.218	0.516	0.888	1.453	2.338	3.511	4.832

The difference found between the mean experimental value of the fundamental mode and the calculated results in the Ansys model, as indicated in tables 5.7 and 5.8, was about 0.001 Hz.

Considering the previous result for the measured natural frequency against the FEA model in Ansys, it is considered that the performance of both, the motion capture system and the fibre optic sensing system are adequate and validated for the intended measurements in VIV tests.

## 5.9 Lessons learned in the fabrication of the riser prototype

### 5.9.1 Buoyancy sensitivity

The work load of the test facilities in KHL is generally intense, this was the case around the dates of the experimental work, these conditions originate that all the work related with the prototype fabrication, setup activities and tests were scheduled within the time frame assigned.

The problem related with the buoyancy of the model due to the real average thickness of the copper tube supplied, could be tackle with some measures for distributed ballast, which

was not foreseen and could not be performed due to time constraints; hence, it is recommended:

To fabricate under any circumstance the un-instrumented model in advance for buoyancy tests and/or ballast assessment, considering the inherent sensitivity of a near neutrally buoyant condition for a slender cylinder.

Perform an exhaustive verification of material mass per unit length or consider higher requirements for dimensional tolerances than the commercial standard utilised.

### **5.9.2 Synchronisation of the FBG interrogator**

For the data acquisition of the fibre optic sensing technology in hydrodynamic tests is highly convenient to be synchronised with data acquired from other measurement systems, like force sensors or motion capture, hence the recommendation to consider and test an interrogator instrument equipped with SYNC capabilities to use an external trigger.

This was not available in the SmartScan interrogator used in the first application of this technology. Current SmartScan interrogators can synchronise their UTC time stamp to the host PC clock or to an NTP server via a LAN connection; unfortunately, it was not possible to link the used model to the same LAN/PC running the MOCAP system at the time of the test setup.

### **5.9.3 Reflections on metallic surfaces affecting the mocap system**

As commented in section 3.1, the motion capture system depends on the reflection of infrared light from markers over the object of interest, but natural and artificial light sources reflected from metallic surfaces can be a cause of problems for marker identification.

The mocap system has several ways to deal with undesired reflections, like exposure adjustments and mask utilities, but in towing conditions this reflections over metallic surfaces were found difficult to mitigate from adjustments in the mocap system.

Additional measures should be contemplated in the test scope, like a matte painting preparation over the model surface or any way to cover the section of the model subject to motion measurement from the direct exposure of natural and artificial light sources other than the invisible infrared light strobe (royal blue visible strobe for underwater cameras) coming from the mocap camera system.

#### **5.9.4 Fibre optic array design**

The application of the fibre sensing technology on the riser prototype required the use of bare optical fibres to be bonded over the tube. Near the tube end, a buffer for each fibre optic array was requested with a bundle jacket to group the 4 arrays for the downlead section, as showed in fig. 5.5.

During the customised fabrication of the arrays, it was reported that the typical buffer installation over the downlead length of 15 metres approached tensioning limits in the fibres, so a loose buffer tube was agreed; nonetheless, during the bonding installation over the copper tube, one of the arrays was found broken in the reel before the last three sensors with one sensor out of the specified distance, losing one point of measurement in one axis after performing a fusion splice.

From the previous experience, it is recommended to consider a fabrication inspection or other means of evidence for acceptance during procurement of the fibre optic arrays, especially if a replacement from the vendor is likely to compromise the execution of the intended tests.

The downlead length was determined according to the distances from the submerged tube end of the riser up to the data acquisition rack on the main towing carriage; the continuity of the fibre optic is mandatory for the immersed condition but one alternative can include a shorter downlead length to reach a dry position on the main carriage, then the arrays can be extended by connecting simple and inexpensive fibre optic patch leads, which can help to mitigate tensions in the fibres during buffer installation by the manufacturer of the FBG arrays.

Working with bare fibre optics is indeed a delicate job and fusion splicing equipment must be considered in place; the fusion splicer is the equipment used to perform the process of fusing two fibres together, being the most common method of splicing. We received support to perform the fusion splicing in the broken fibre array, here it was found that the polyimide coating of the fibre presented difficulties for the typical mechanic stripping of the coating required to prepare the splice.

The polyimide coating offers higher resistance to temperature for the fibres and this was selected due to the potential use of a heat shrink over the prototype, which could induce high temperatures during installation, therefore, it is recommended to be prepared with the specific tools required by potential splicing.

## **5.10 Definition of test conditions for current and wave flows**

In section 2.2, the geometric parameters for the test were initially established considering some practical and local environmental conditions and applied in the experimental setup covered in section 5.7.

In order to represent the current flows and wave characteristics of interest to investigate VIV responses in the towing tank, model scaling concepts needs to be considered.

### **5.10.1 Scaling concepts**

To analyse the scaling of the current flows and waves of interest, the geometrical similarity in scaling laws requires that all linear dimensions must be kept within the same scale ratio, which is given between linear dimensions of the full-scale structure and the model structure as  $R=L_f/L_m$ .

A general approach for wave scaling considers the dispersion relation of linear wave theory,

$\omega = \tanh(kd)$ , if  $kd \gg 1$ , then  $\omega \approx c$ , where  $\omega$  is the wave angular frequency and  $c$  is the wave number with  $L$  as the wave length, thus the wave speed  $c = \omega L$ ; from the scale ratio definition, we can use  $L_m=L_f/R$  to write the wave angular frequency of

the model as  $\frac{L_m}{L_f} = \frac{U_m}{U_f} = \frac{T_f}{T_m} = \frac{1}{R}$ , hence,  $\frac{U_m}{U_f} = \frac{1}{\sqrt{R}}$ , or  $\frac{2\pi}{T_m} = \frac{2\pi}{T_f} \sqrt{R}$ ,  
 therefore, the wave period can be scaled for the model structure as  $T_m = \frac{T_f}{\sqrt{R}}$ .

Water waves are gravity driven, where the Froude number, defined as a ratio between inertia and gravity forces, has provided in hydrodynamic studies an excellent parameter to secure the similarity of forces. The adoption of similarity of forces combined with geometrical similarity secures a dynamic similarity condition, which provides the kinematic similarity between the full structure and the model.

For Froude scaling, the inertia forces (mass multiplied by acceleration) is generally expressed proportionally in terms of the physical quantities of density  $\rho$ , volume  $L^3$  and velocity  $U$ , as  $F_i \propto \rho L^3 \frac{U^2}{L} = \rho L^2 U^2$ ; consequently, the gravity forces are expressed as  $F_g \propto \rho L^3 g$ , so the ratio between inertia and gravity force is  $\frac{F_i}{F_g} = \frac{U^2}{gL}$ .

With the previous concepts, the dynamic similarity between the full scale structure and the model structure can be achieved by equating their ratios between inertia and gravity forces, so,  $\frac{U_m^2}{g L_m} = \frac{U_f^2}{g L_f}$ , from which we get the Froude number as  $\frac{U_m}{\sqrt{g L_m}} = \frac{U_f}{\sqrt{g L_f}}$ , hence the Froude scaling for velocity is given as  $U_m = U_f \sqrt{\frac{L_m}{L_f}}$ .

In section 5.3, a scale ratio  $R=12.095$  was obtained during the selection of the material for the fabrication of the prototype; applying this ratio to the waves of table 2.1 with the scaling factors analysed above, the testing waves in the towing tank were defined as given in table 5.9.

**Table 5.9 Testing waves**

Waves of interest			Wave scaling			Waves in tank				
No.	H <sub>s</sub> (m)	T (s)	R	H <sub>s</sub> x R <sup>-1</sup> (m)	T x R <sup>-1/2</sup> (s)	f (Hz)	Amp (mm)	d (m)	H/gT <sup>2</sup>	d/gT <sup>2</sup>
1	1.00	6.00	12.095	0.08	1.73	0.58	41	2.18	0.0028	0.0747
2	2.00	7.50		0.17	2.16	0.46	83		0.0036	0.0478
3	4.50	10.00		0.37	2.88	0.35	186		0.0046	0.0269

In section 2.2, the typical offshore towing speeds for riser towers and pipe bundles were identified up to 1.75 m/s, applying the Froude scaling for velocities, the corresponding tank



towing speed for the model is  $U_m = \frac{1.75 \text{ m/s}}{\sqrt{12.095}} = 0.51$  / ; therefore, a range of towing speeds from 0.1 to 0.9 m/s were defined to assess VIV effects. The towing speed range and associated reduced velocities are not intended to cover the whole aspect of VIV but some representative conditions of interest within the resources and time window of the towing tank assigned for testing in this work.

Considering the fundamental frequency in still water for the range of tensions in table 5.7 and the yaw angle in the initial setup of the riser model, the range of reduced velocities for flow velocities normal to the member axis ( $U_r = U/fnD$ ) will be about  $U_r \approx 2 - 17$ .

The previous scaling concepts were considered sufficient for the scope, resources and purpose of the experimental work, where the selection of a commercial copper tube as a high density model material was initially implemented to achieve the neutrally buoyant condition, helping to keep the model fabrication within experimental budget; nonetheless, it must be mentioned that a proper scale model for a full scale structure must also consider the similarity of the interaction between the structural vibrations and hydrodynamic forces, namely hydro-elasticity and Reynolds number similarity.

For hydro-elasticity, the global stiffness of the full structure must be correctly scaled, with similar structural damping and mass distribution (Sverre Steen, 2014).

Considering the model as a beam element, is easy to see that the solutions derived in section 4.2.3 for beam deflections due to a distributed mass or load force, have the dependence  $\propto L^3$ ; if we consider a hydrodynamic force (e.g. a drag force)  $q = C_D \rho U^2 D$ , then the force  $q$  can be expressed as  $\propto U^2 D$ , so,  $\propto U^2 D$ ; applying geometric similarity to the response of a full scale structure,  $\frac{U_m}{U} = \frac{L_m}{L}$ , or  $\frac{U_m}{U} = \frac{L_m}{L}$ , hence:

$$\frac{U_m}{U} = \frac{L_m}{L}$$

Substituting  $\frac{U_m}{U} = \sqrt{\frac{L_m}{L}}$  and  $\frac{U_m}{U} = \frac{L_m}{L}$ , we get  $\frac{U_m}{U} = \frac{L_m}{L}$ , representing a scaling factor for structural rigidity of  $(\frac{L_m}{L})^3 = (\frac{L_m}{L})^3$ .

Additionally, the second moment of area  $\propto L^4$ , so, geometric similarity requires that  $\frac{I_m}{I} = (\frac{L_m}{L})^4$ .

, then  $\tau = \mu \frac{dv}{dy}$  is the equation defining the scaling of elasticity as  $\tau = \mu \frac{dv}{dy}$ , which means that the model structure requires a change of elasticity in respect to that of the full scale structure, which in our case would demand a model material change (e.g. fibre glass composite pipe).

Reynolds similarity requires the same Reynolds number (Re) value for two geometrically similar flows, being the non-dimensional Re defined as the ratio between inertia and viscous forces.

It was reviewed above that we can express an inertia force with physical quantities as  $F_i \propto \rho V^2 L$ . For viscous forces, the Newton's law of viscosity is considered for a shear stress  $\tau$  between adjacent fluid layers.

The shear stress is proportional to a flow velocity gradient and defined as  $\tau = \mu \frac{dv}{dy}$ , being  $\mu$  the viscosity of the fluid (a proportionality constant between shear stress and the velocity gradient), so  $\tau \propto \mu \frac{dv}{dy}$ , thus a viscous force can be expressed multiplying the shear stress by area quantities ( $A$ ) as  $F_v \propto \mu \frac{dv}{dy} A$ , then  $F_v = \mu \frac{dv}{dy} A$ , where  $\nu = \frac{\mu}{\rho}$  is called the kinematic viscosity.

Then, for Reynolds similarity, we need  $\frac{V_f L_f}{\nu_f} = \frac{V R L}{\nu}$ , and  $\frac{V_f L_f}{\nu_f} = \frac{V R L}{\nu}$ .

To satisfy both, Re and Froude scaling, we can substitute the Froude scaling velocity  $V_f = \sqrt{g L_f}$  in the previous equation, to get  $\frac{\sqrt{g L_f} L_f}{\nu_f} = \frac{V R L}{\nu}$ , this means that the fluid kinematic viscosity for model testing would require a reduction in the fluid viscosity by a factor of  $\frac{1}{R^2}$ .

Considering our scale ratio  $R=12.095$  and a typical kinematic viscosity value for sea water at 20 Celsius degrees  $\nu = 1.05 \times 10^{-6} \text{ m}^2/\text{s}$ ,  $\nu_f = 1.05 \times 10^{-6} / (12.095)^2 = 7.1 \times 10^{-9} \text{ m}^2/\text{s}$ , which is even a value well below the kinematic viscosity of mercury. This explain the difficulty to study Re effects on VIV responses of flexible risers for Re values close to practical applications (Resvanis et al., 2012), which would demand for our wave flows of interest an impractical reduction of the scale ratio with very large testing facilities or fullscale tests.

Notwithstanding the foregoing, our test setup has the potential to be adapted for the study of Re effects, within practical ranges, on VIV responses from current flows at tow depths out of the effects of the free surface by setting the scale ratio  $R=1$ , although for this specific case a flume tank could be a better option due to the limitations of a towing tank length.

Further guidelines and recommendations for detailed planning and design of model testing for specific applications were found well documented in DNV-RP-C205 (2007) section 10.

### **5.10.2 Wave theory selection**

The dimensionless wave steepness  $H/gT^2$  and the dimensionless relative depth  $d/gT^2$  parameters were evaluated considering the water depth in the towing tank of 2.18 metres.

Using the values obtained for the dimensionless parameters and the diagram showed in fig. 2.1.6a in the work of Barltrop et al. (1990), the appropriate wave theories can be identified for non-linear Stokes 5th order or Stream function wave theories.

The Stokes 5<sup>th</sup> order wave theories of Skjelbreia and Hendrickson (1960) and Fenton (1990) were reviewed and programmed in Mathcad for calculation of wave particle velocities, the examples contained in the previous references were reproduced to validate the Mathcad worksheets. Fenton's theory was selected considering his demonstration of higher accuracy based on the wave steepness expansion term (Fenton, 1985).

The computed horizontal wave particle velocities for the testing waves are plotted and compared against the velocities given by the "Airy" linear wave theory in fig. 5.20.

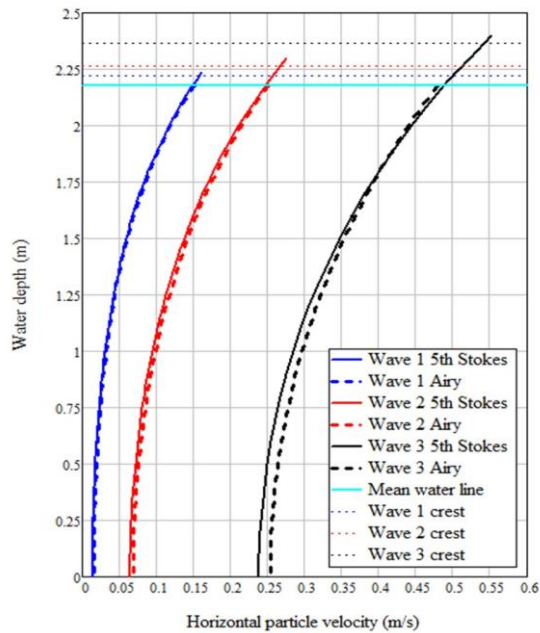


**Figure 5.20 Wave particle velocities**

In the towing tank, generated wave periods and heights were measured with a fixed wave probe instrument; the measured values were inserted into the Mathcad worksheet to calculate the experimental wave particle velocities used in the analysis of results.

### **5.11 Instrumentation systems and data acquisition**

The experimental data acquisition encompasses measurements from the motion capture system (MOCAP) for motion response at a zone of interest over the model, the fibre optic sensing system (FOSS) for curvature/bending strains along the span and the load cell at the lead-end for pre-tension settings and dynamic force responses.

The load cell data was integrated to data from the towing carriage and tank instrumentation for the measurement of the tow speed and generated waves, using the CED 1401 (mkII) data acquisition system and Spike2 software.

The data acquisition system CED 1401 and the motion capture system can be and were synchronised with the same external trigger for time series data, unfortunately the available

interrogator was not able to be synchronised since it does not have sync/external trigger capability.

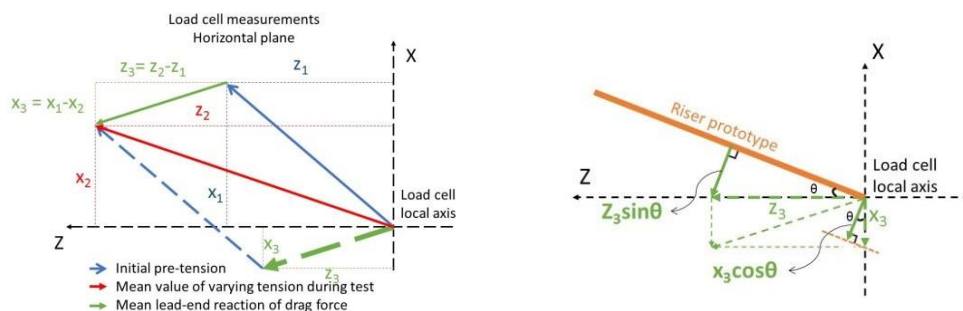
Wave height and frequency were measured with both, a wave probe fixed in the towing tank and a sonic probe mounted in the towing carriage, to obtain a direct measurement of the encounter wave frequency during current plus wave tests.

After installation and calibration of the 3 underwater cameras for the motion capture system, it was found that the setup allowed acceptable marker visualisation about a third of the model length, where more underwater cameras will be required to cover the full span; so, the trail-end sector was chosen to conduct the motion capture response with this system.

### 5.12 Approximation of steady drag force/coefficients for towing requirements and a method to estimate local mean drag coefficients along the axis of the model

For pre-tension settings, the axial tension at the lead end was computed and monitored in real time with the norm of the measured values in the tri-axial load cell. The reaction in the lead-end due to time varying lift forces was measured directly in the “Y” vertical axis of the load cell, whereas the lead-end reactions to the general mean drag forces were initially considered from the horizontal plane differential measurements showed in fig. 5.21a.

For each test, the temporal mean reaction at the lead-end due to drag forces normal to the model was approximated from the load cell measurements according to the components showed in fig. 5.21b. Assuming preliminary that the magnitude of this force at the lead-end represents about half of the total drag force in the model, an equivalent temporal mean total drag force per unit length can be set as  $\approx ( \sin + )$ .



(a) Horizontal plane vector forces

(b) Normal drag force components

Figure 5.21 Mean drag force estimation from load cell data

Assuming a total drag force acting over the whole length of the model, including the main copper tube section, the rod and the cable elements; a consideration was made over the geometric properties of each element in the typical drag force equation mentioned in 5.10.1, in this way, it was estimated that the copper tube element would take about 96% of the total force if a constant global drag coefficient is assumed to be acting over the length of each element of the model string, i.e. the copper tube, the rod and the cable, subject to a current flow.

A higher drag coefficient was considered for the copper tube element due to a higher motion response respect to that of the rod and cable elements during higher towing speeds (say up to 2 times the drag coefficient corresponding to the cable and the rod), in this case the participation of the copper tube would be about 98% of the total drag force.

The experimental data from the load cell showed that in the worst case, the horizontal load vector at the lead end reached up to 3.5 degrees of deviation with respect to the initial or un-deflected longitudinal axis.

For these deflections and considering that the normal drag component is compensated along the copper tube but decremented for the rod and incremented for the cable element according to the mentioned maximum deviation angles, the corresponding contributions in the drag equation was assessed for a participation of the copper tube between 97 to 98% in the total force, using either the same global drag coefficient or differentiated coefficients as discussed in the previous paragraphs.

The average of participation and standard deviation of the previous estimations gives a percentage of 97.1% and 0.7% respectively, so under previous considerations, the general participation of the main copper tube element in the model for the equivalent drag force per unit length was approximated as  $= (0.97 \pm 0.01)(\sin + )$ .

A temporal mean drag coefficient to estimate towing capacity requirements is then preliminary approximated as:

$$= \frac{1}{1 + 1.043 \left( \frac{A}{D} \right)^2} \quad (5.5)$$

In reality, the drag force is generally affected by CF vibration amplitudes, this effect has been studied extensively, where a common expression used to calculate the drag amplification factor ( ) respect to that of a rigid cylinder ( ) is used in SHEAR7, the offshore industry standard software for VIV analysis (Jhingran et al., 2008), and is given as a function of the ratio of the CF amplitude and the cylinder diameter as: =

$$1 + 1.043 \left( \frac{A}{D} \right)^2$$

Thus, the drag forces and corresponding drag coefficients in long flexible cylinders can be expected to present local variations due to variations in local vibration amplitudes and variations of the flow velocity along the length considering the relative velocities of the moving cylinder and the oscillatory velocities in the presence of wave flows among other factors.

The total hydrodynamic loading is generally calculated by the relative motion form of Morison's equation, see Annex 11c in Barltrop (1998) or Appendix C in Sparks (2007), which can be used to determine inertia or added mass coefficients associated to the non-steady terms of the Morison's equation in laboratory tests.

For the current scope, a method to estimate a local mean drag coefficient can be derived from the beam equations of motion previously analysed, considering a forcing term  $F(x,t)$  representing a VIV response. Adding the viscous term of eq. (A.35) to eq. (A.64) and the forcing term, we have:

$$m \ddot{w} + c \dot{w} + EI w'''' = F(x,t) \quad (5.6)$$

As proposed in the work of Jhingran et al. (2008), the acceleration and velocity terms will vanish for a temporal mean of zero-mean oscillatory processes, then:  $\ddot{w} = \dot{w} = 0$  ( ), the authors also mention that for a tensioned dominated beam, the bending stiffness term can also be dropped; in order to assess this in our experimental setup, a quick review can be made comparing the model's fundamental frequency ( $n=1$ ) against that obtained by ignoring the bending stiffness with the frequency equation of a simple taut string.

For the same tension and hydrodynamic mass values used in Ansys analysis:

$$\frac{n}{2L} \sqrt{\frac{T}{m}} = \frac{1}{\sqrt{\frac{115 N}{m}}} = 0.183 \text{ s}^{-1}$$

The fundamental frequency obtained in the finite element modal analysis with a detailed model, considering experimental damping values, was of 0.18 Hz as shown in fig. 5.19, hence it is considered that the assumption of a tensioned dominated beam is reasonable to drop the bending stiffness term.

So,  $\omega = \frac{1}{2L} \sqrt{\frac{T}{m}}$ , but  $\omega = \frac{v}{D_{op}}$ , where  $D_{op}$  is an optical diameter, i.e. the diameter for the opposed optical fibres with FBG sensors for measurement of the bending strains, then the local mean drag force per unit length can be approximated for time averaged bending strains as  $F_D = \frac{1}{2} \rho C_D v^2$ .

A local drag coefficient is finally obtained applying the drag force equation as  $C_D = \frac{2F_D}{\rho v^2}$ , although for our setup with bare fibres bonding directly to the external diameter, we can write:

$$C_D = \frac{2F_D}{\rho v^2} \tag{5.7}$$

### 5.13 Reduced velocity and Strouhal number for long flexible cylinders

The reduced velocity is generally expressed as  $V_r = \frac{U}{f_n D}$ , where  $U$  is the current flow velocity normal to the member axis,  $f_n$  is the natural frequency of the cylindrical member and  $D$  is the diameter; however, the experimental data showed that the flexible long cylinder exhibits multiple frequency peak responses.

So the reduced velocity can be more conveniently expressed as  $V_r = \frac{U}{f_n D}$ , where



represents the first peak in the cross flow frequency response or “1 x” frequency, as named by other researchers (Vandiver et al., 2009) (Jhingran et al., 2008), which can be determined by PSD analysis from data of either, the MOCAP or the FOSS.

The data corresponding to marker No. 3 in the MOCAP system, located about L/7, was selected to perform PSD analysis to identify the frequency responses; consequently, the 1 x frequency was also considered to determine the Strouhal number as = \_\_\_\_.

## 6 Data analysis and results of the riser towing test

### 6.1 Data analysis

#### 6.1.1 Load cell and MOCAP system data processing

Analysis of measured data from the load cell and the optical tracking system, related with the first tests series for current flow alone was performed for mean values and RMS amplitudes of tensions and motion responses, conducting PSD analysis for IL and CF directions, some of the main results of interest are summarised in table 6.1; here, the flow velocity normal to the cylinder was preliminary calculated using the initial horizontal angle of the cylinder's longitudinal axis during the setup.

PSD analysis of the motion capture system for marker No. 3 was performed, identifying the lowest and highest frequency responses in each case for CF and IL directions, where the first peak in the CF direction corresponded generally to the dominant "1 x" frequency.

**Table 6.1 Current flow alone, tow depth = 1.05 m (25 OD), PSD analysis from marker no.3 of MOCAP system**

Test No.	Tow speed (m/s)	Ur	Initial Tension (N)	Re	IL freq. response			CF freq. reponse			CF/IL Dom.	St
					Dom. (Hz)	Low. (Hz)	High. (Hz)	Dom. (Hz)	1 x (Hz)	High. (Hz)		
16	0.10	2.20	115.67	6.56E+02	0.19	0.19	0.42	0.39	0.19	0.39	2.05	0.45
17	0.20	2.19	112.39	1.30E+03	0.43	0.38	0.43	0.38	0.38	0.38	0.88	0.46
18	0.30	5.18	115.06	1.95E+03	0.47	0.24	0.47	0.24	0.24	0.47	0.51	0.19
19	0.40	6.64	114.08	2.60E+03	0.55	0.25	0.55	0.25	0.25	0.25	0.45	0.15
11	0.50	7.39	115.49	3.25E+03	0.55	0.28	0.82	0.28	0.28	0.28	0.51	0.14
12	0.60	5.52	115.66	3.89E+03	0.45	0.45	0.9	0.45	0.45	0.45	1.00	0.18
13	0.70	5.68	116.69	4.54E+03	1.01	0.16	1.01	0.51	0.51	0.51	0.50	0.18
14	0.80	5.81	115.50	5.19E+03	1.13	0.57	1.13	0.57	0.57	0.57	0.50	0.17
15	0.90	5.90	116.53	5.83E+03	0.28	0.28	1.24	0.63	0.63	0.63	2.25	0.17

#### 6.1.2 Fibre Optic Sensing System (FOSS) data processing

The RMS amplitudes of the time varying CF and IL bending strains at sensor locations along the model were analysed from data of the FOSS, considering the settled motion response achieved over the second half of the time at the full speed of each test.

For the plotted bending strain responses, the sensor pair No. 15 correspond to the leadingend side during towing. Some data for the sensor pairs Nos. 1, 2 and 3 in CF direction near the trail-end is not presented due to the fabrication/installation issues commented in section 5.9.4 for one of the fibre optic arrays.

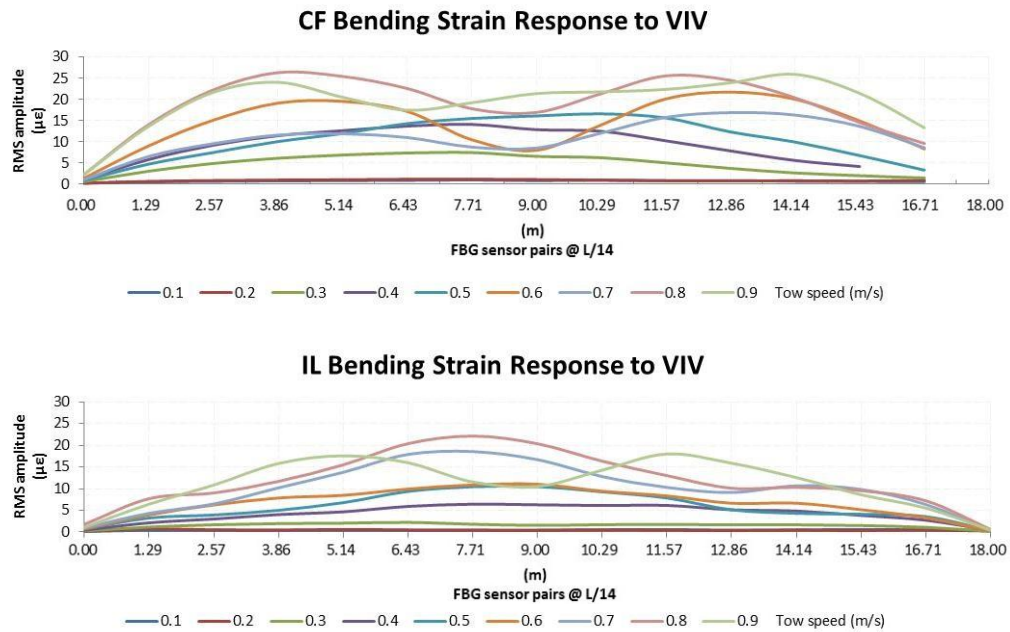


**Figure 6.1 Bending strain responses due to current flow alone**

The plotted profiles of the bending strain RMS amplitudes, constructed with smoothed (spline) lines over data points at FBG location as showed in fig. 6.1, correspond to the time varying response due to vortex shedding and were found useful as an indicative of the participating vibrational modes and the location zones (anti-nodes) with the highest bending strain response in CF and IL directions.

It was verified that peak frequencies determined in PSD analysis from data of the FOSS generally corresponds with those obtained from the optical tracking system in the location of the marker No. 3, as indicated in table 6.1; although the advantage of distributed FBG sensors in the fibre arrays allowed to identify harmonic responses in other locations along

the model and a more clear indication of the dominant frequencies, considering the variation of amplitudes along the model for vibrations with multiple frequencies/mode shapes.

The differences of performing PSD analysis over the whole-time series in FOSS data respect to analysis over just the second half of the test, where the response is reasonably more settled, was generally about 0.01 Hz for the dominant frequencies, thus the PSD results are reported with two decimal places.

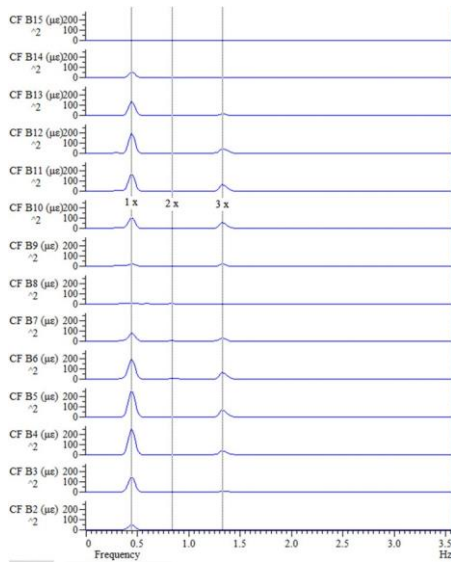
Fig. 6.2 shows the PSD analysis of FBG data in test No. 12 for current flow at 0.6 m/s. The typical dominant frequency of 1 x for the CF direction can be identified with higher peaks about  $1/4L$  and  $3/4L$  sectors, which indicates the location of the anti-nodes for the 1 x standing wave with largest amplitudes. In the same way, the anti-node zone for the 3 x harmonic standing wave also becomes evident.

For the IL direction, the typical dominant frequency of 2 x showed higher peaks nearby  $1/2L$ , identifying also 1 x and 5 x harmonic peaks.

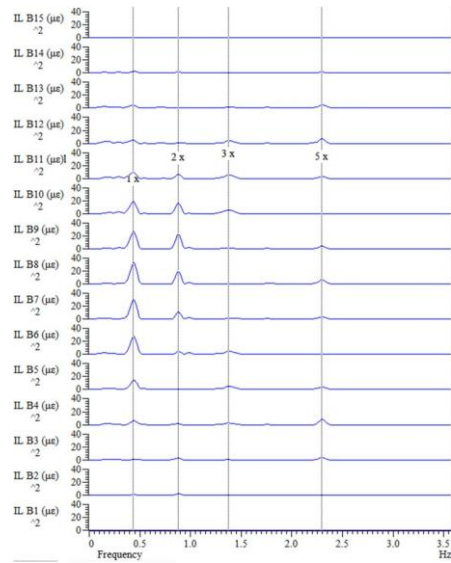
These variations in the PSD peak magnitudes over FBG sensors along the model, can explain the limitations of the MOCAP system to capture frequency components if the visualisation of markers is restricted nearby node zones or sectors of low amplitude response for certain frequencies, which was the case for some of the frequencies included in table 6.1; nonetheless, the integration of the FOSS can assist to select a particular setup for the available underwater cameras, providing the motion capture for total displacement response data, including rigid body motions.

The RMS amplitude of bending strains can be approximated with the square root of the area under the PSD curve, thus a fraction of the maximum RMS amplitude can be set as a minimum value to identify the peak frequencies with a reasonable contribution in the response. Setting this minimum value as, say 10%, will provide a general criterion to define weak responses, e.g. the 2 x CF, 3 x IL and 4 x IL harmonics, so the frequency responses in test No. 12 (fig. 6.2) can be identified as 1 x and 3 x for CF and 2 x, 1 x and 5 x for IL.

The previous procedure can be extended to any test to characterise the multi-frequency CF and IL response from the FOSS data.



(a) CF direction

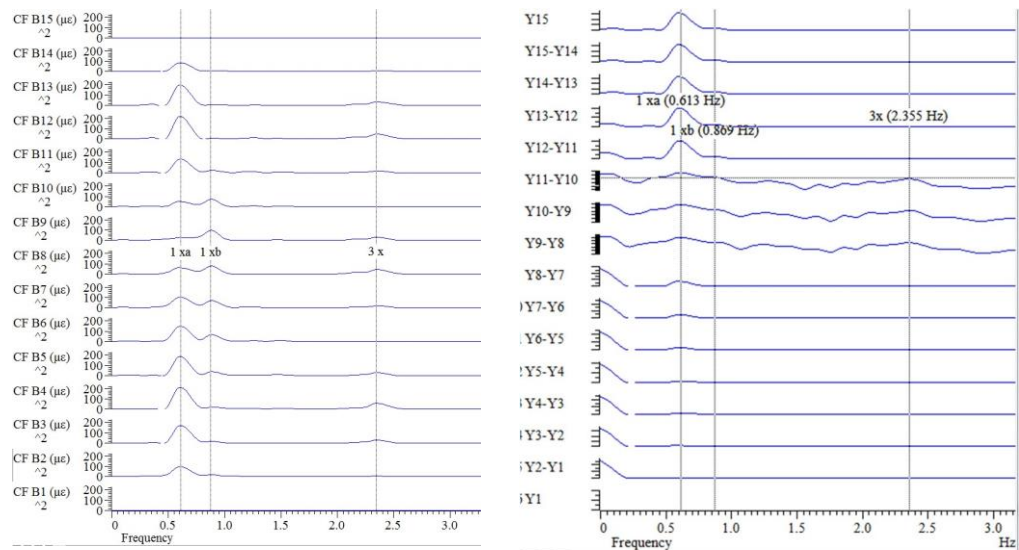


(b) IL direction

**Figure 6.2 PSD frequency peaks from the FOSS data, test No. 12.**

From table 6.1, it was found that the PSD analysis in test No. 15, from MOCAP data corresponding to the marker No. 3, showed an atypical dominant IL frequency.

A detailed inspection of the peak frequencies in PSD analysis from the FOSS is shown in fig. 6.3b, where the strain range in the graph is amplified for the FBG pair sensors corresponding to the location of marker no. 3, identifying the peak frequencies found with MOCAP data, nonetheless, the real dominant frequencies becomes evident if we consider results at other FBG locations along the model.



(a) CF direction

(b) CF direction from displacements

**Figure 6.3 PSD frequency peaks from the FOSS data, test No. 15.**

### 6.1.3 Indications of vortex shedding patterns and response branch transitions

In test no. 15, peak frequencies 3 x and 2 x were identified for CF and IL directions respectively, although the corresponding 1 x CF response appears to be within the two frequency peaks 1 xa and 1xb shown in fig. 6.3a. Additionally, the CF time varying bending strain in fig. 6.1, shows a change from the second mode shapes of previous tests to a third mode shape response in test no. 15.

A close inspection of the time varying bending strain response measured in FBG sensors about sectors of maximum amplitude for the third mode identified in the CF direction (see Fig. 6.12, location CF B9), showed a somewhat modulated response that could be related with the two frequency peaks 1 xa and 1 xb, and a typical double peak associated with the combined frequency response of 1 x and 3 x. It is considered that this combined response could be also associated with the 2P shedding mode described by Williamson and Roshko (1988), or the four concentrated regions of vorticity per cycle mentioned for the 2P mode by Blackburn et al. (2001).

Bending strain responses measured in high response zones for FBG sensor locations 9 and 6 corresponding to 7.71 m and 11.57 m from the trail-end (see Fig. 6.14), are shown in figures

6.4 to 6.12 for IL and CF directions of the first tests series for current flow.

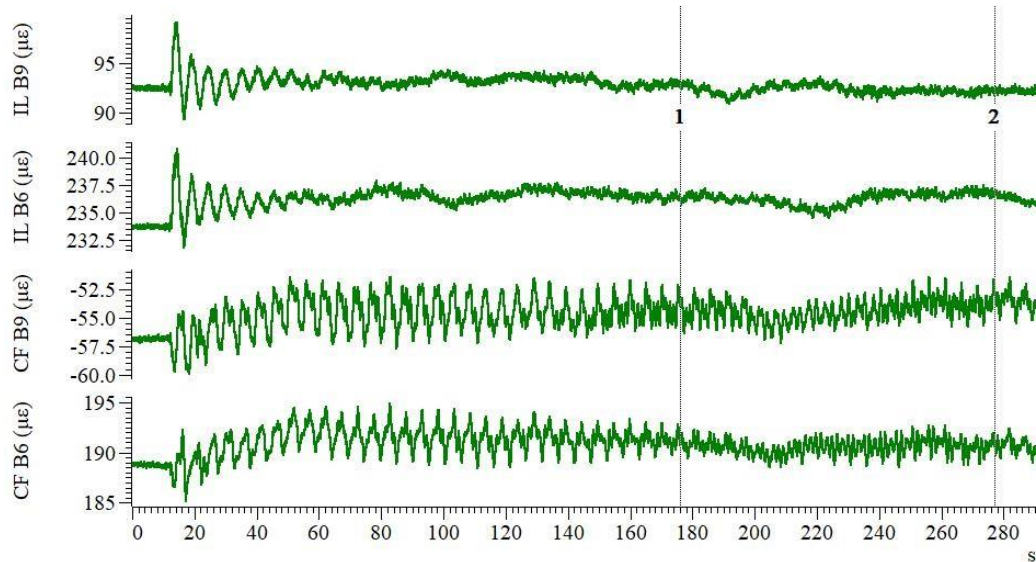


Figure 6.4 IL and CF bending strain responses in test no. 16 (0.1 m/s).

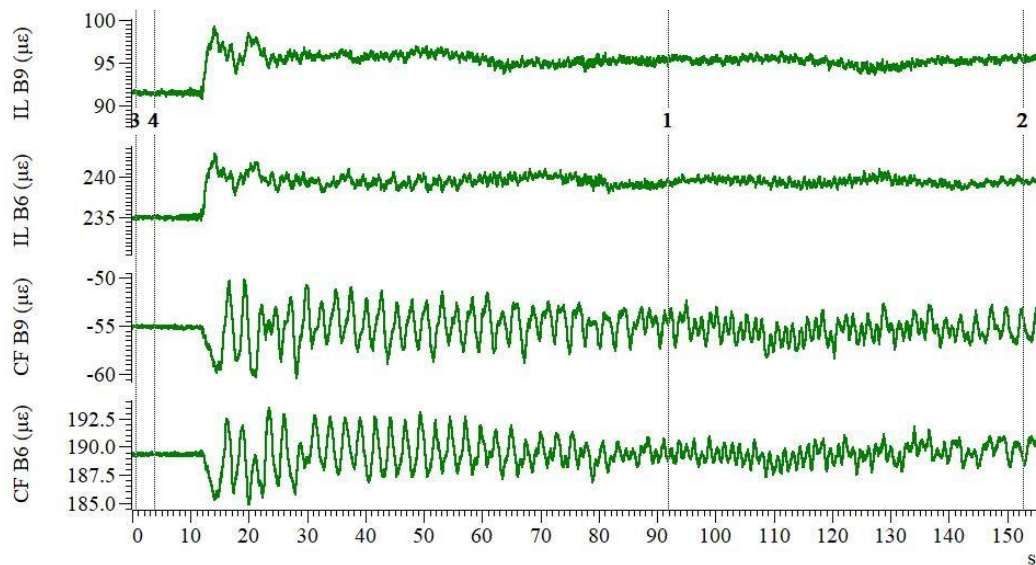


Figure 6.5 IL and CF bending strain responses in test no. 17 (0.2 m/s)

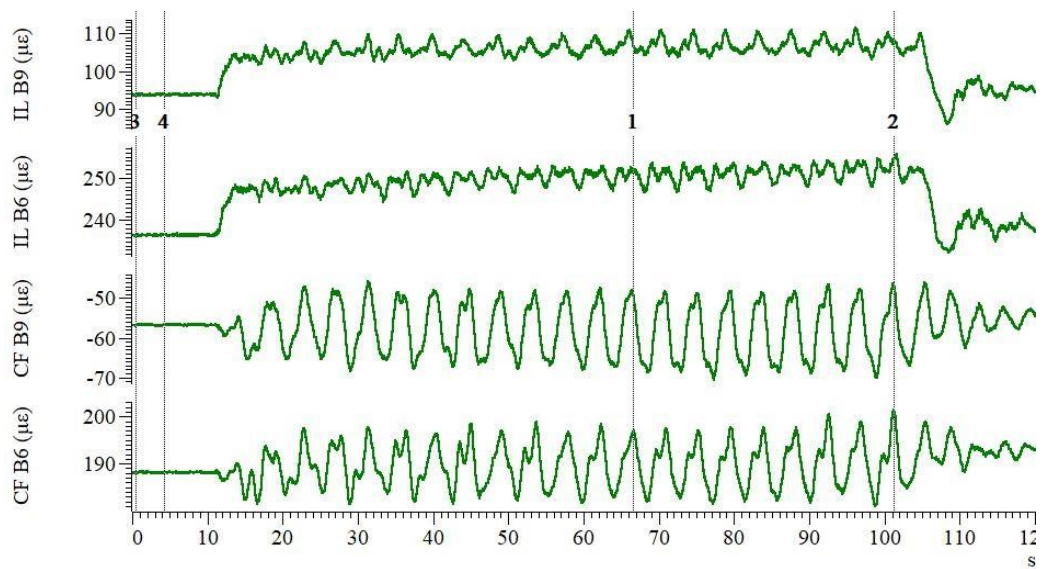


Figure 6.6 IL and CF bending strain responses in test no. 18 (0.3 m/s)

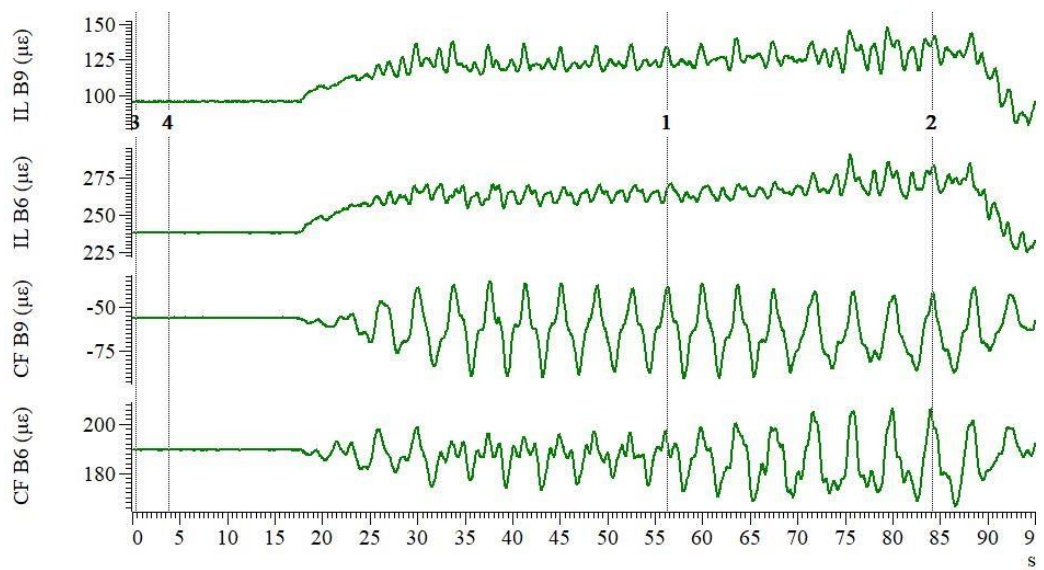


Figure 6.7 IL and CF bending strain responses in test no. 19 (0.4 m/s)



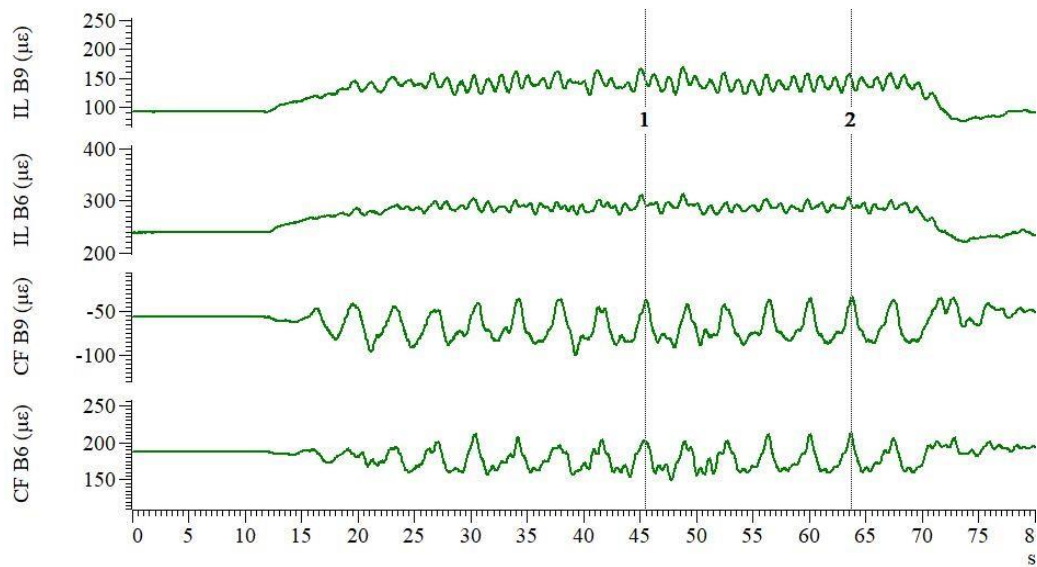


Figure 6.8 IL and CF bending strain responses in test no. 11 (0.5 m/s)

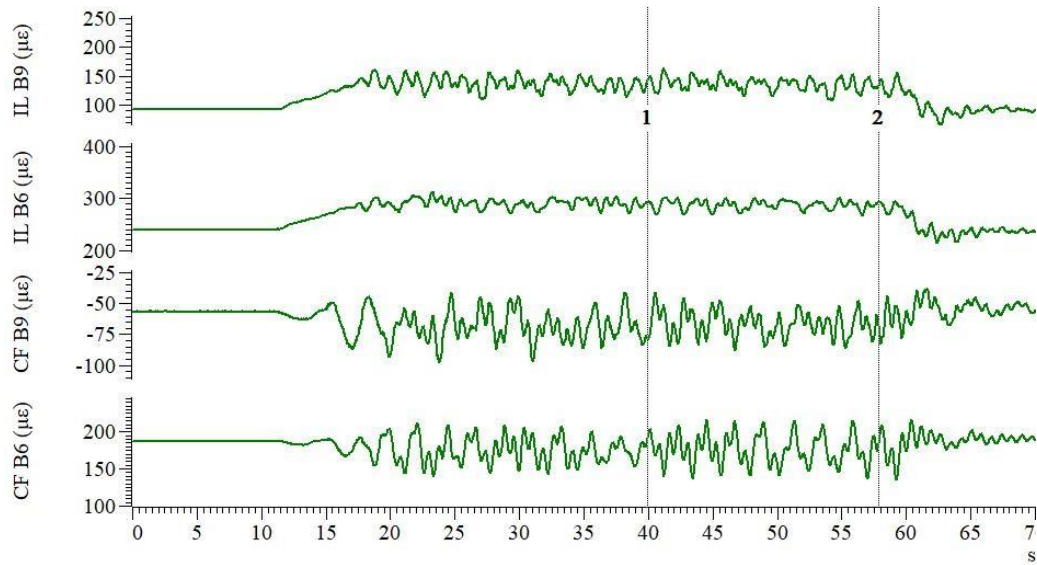


Figure 6.9 IL and CF bending strain responses in test no. 12 (0.6 m/s)

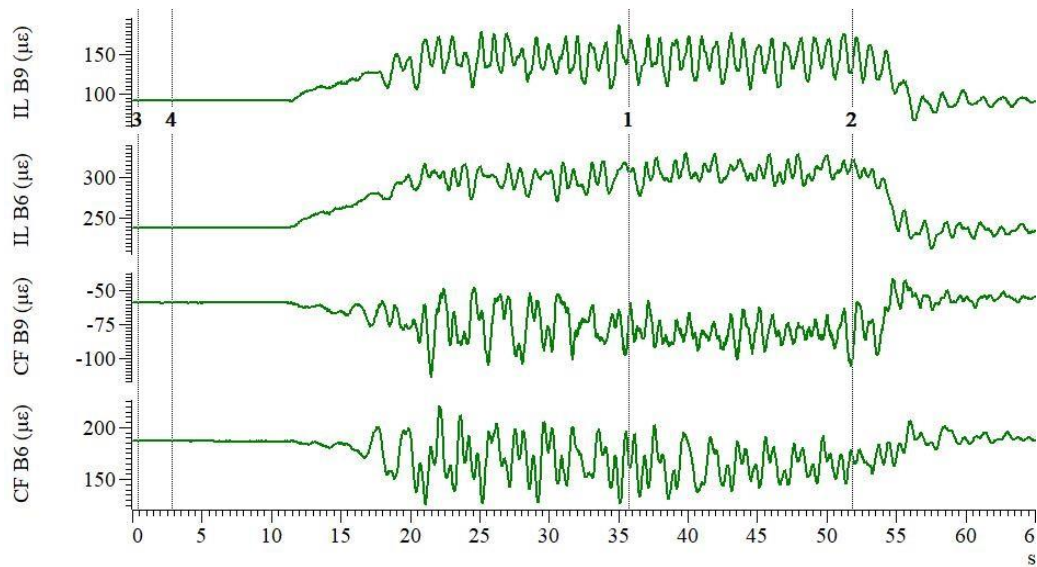


Figure 6.10 IL and CF bending strain responses in test no. 13 (0.7 m/s)

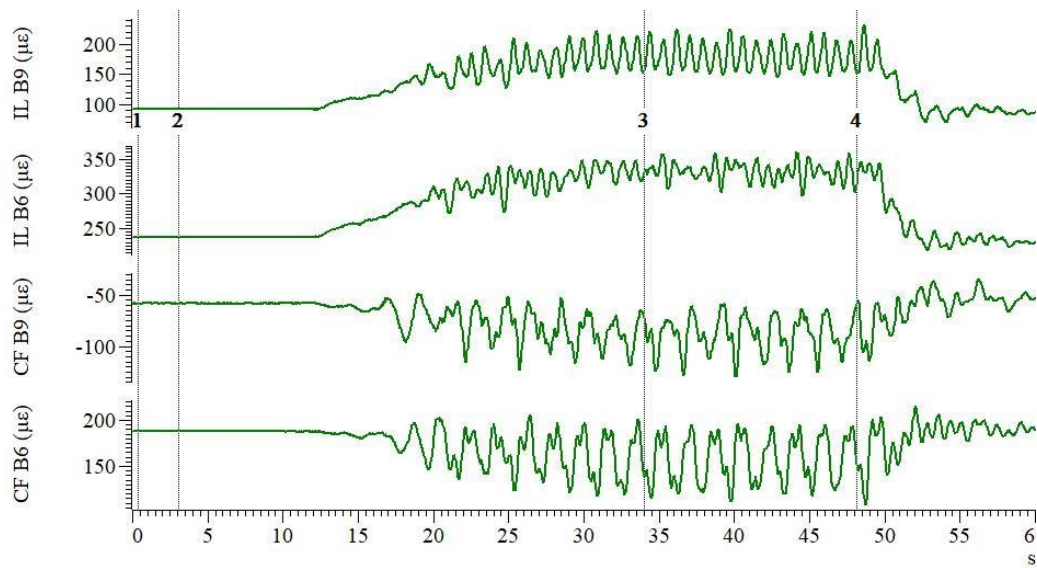
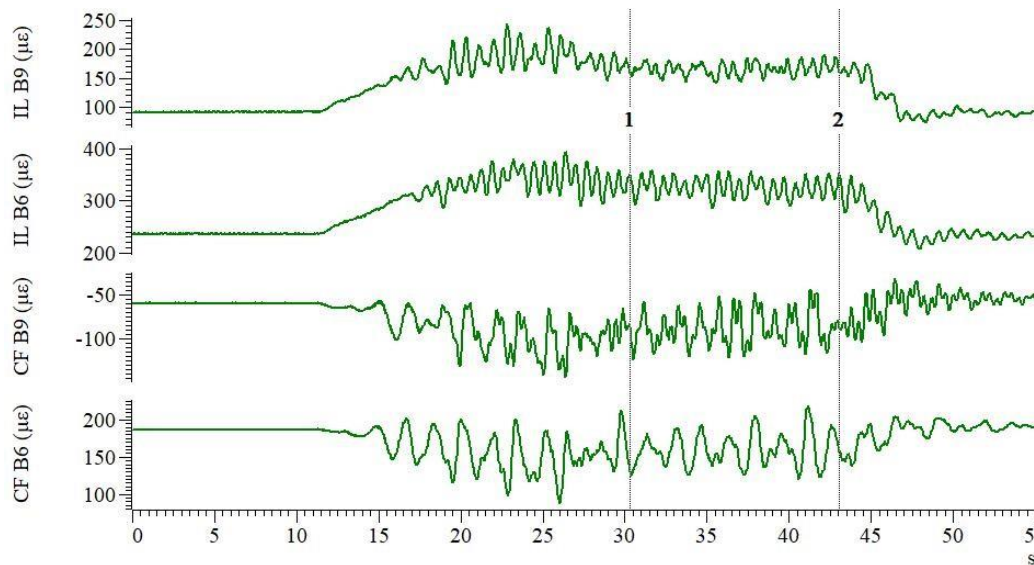


Figure 6.11 IL and CF bending strain responses in test no. 14 (0.8 m/s)



**Figure 6.12 IL and CF bending strain responses in test no. 15 (0.9 m/s)**

The previous observations together with the topics reviewed in section 2.1.1, lead us to verify indications of the vortex shedding patterns in the CF response of previous tests, where we found that double peaks associated to a combined response of 1 x and 3 x (probably also associated with the 2P mode) were consistent from tests no. 12, 13 and 14, especially at FBG sensors located about antinodes of the dominant second mode of vibration for these tests, where the bending amplitudes are higher.

At lower velocities, we found indications likely associated to different patterns, test no. 11 showed responses where the double peak is predominant at only one side of the oscillations, as the typical combined frequency response of 1 x and 2 x, It is considered that this combined response could be also associated with the S + P mode, interestingly this test also presents a change in the vibrational mode with respect to tests at higher flow velocities where the double peak response at both sides was dominant.

It is believed that these indications suggest a transition between an initial-upper response branch, on the other hand, a next branch transition could be related with the two coexisting frequencies 1 xa and 1 xb in test no. 15 by the intermittent switch response behaviour of the upper-lower transition described by Khalak and Williamson (1999).

Additional tests will be required to support the previous vortex shedding mode indications, probably with integration of a PIV system in selected tests; nonetheless, it is considered that the integration of the MOCAP system and the FOSS represents a good approach and a potential tool to conduct detailed investigations and characterisation of response branches and associated shedding mode patterns for the current model conditions, although larger towing tank facilities or ocean basin tanks will be required for a good representation of the response, in order to capture a larger number of oscillations at the flow velocities of the upper-lower transitions.

### 6.1.4 Estimation of local flow velocities and local drag coefficients

Local flow velocities normal to the cylinder can be estimated by adjusting the normal component of the flow velocity for local angles of deviation from the initial and undeflected longitudinal axis of the model, since the longitudinal axis will present a mean deflection due to the steady component of the drag force, which increases as the tow speed increases for each test series.

To calculate the angle of deviation for the deflected profile in the horizontal plane due to an acting mean drag force, the mean value of the IL curvature during the second half of each test can be considered from FOSS data, see fig. 6.13.

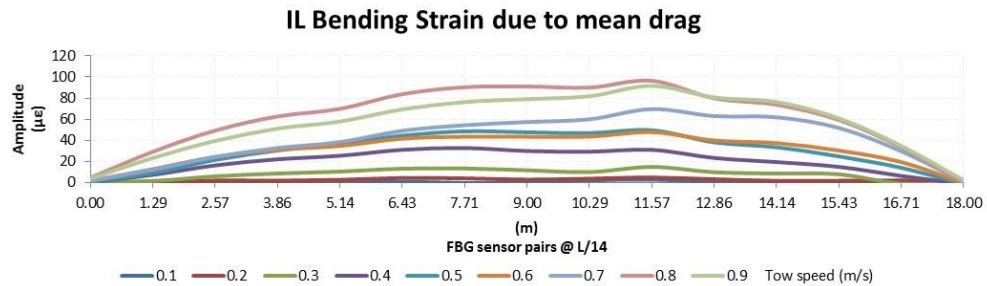


Figure 6.13 IL Mean bending strain

The deviation at each FBG sensor location can be estimated using the curvature obtained from the mean value of the measured IL bending strain, as  $\theta = \frac{\Delta y}{\Delta x}$ ; then,  $\theta = \frac{\Delta y}{\Delta x}$

– , where  $L_{FBG}$  is the arc length given by the distance between sensors of 1.285 m.

Thus, the local angle respect to the towing tank axis at any FBG sensor number/location “ ” can be approximated as  $\theta = \theta_0 + \sum \dots$  , considering that the local angle varies monotonically for the deflection associated to the mean drag. The index arrangement accounts for the sensors numbering in this case (1-15 starting from the trail-end towards the lead-end).

The starting angle  $\theta_0$  at the lead-end, which corresponds to the location of sensor no. 15, was taken as the departure angle respect to the initial longitudinal axis, given by the measured components of the mean varying tension at the load cell (the angle given by the red vector in fig. 5.21a).

Under the previous methodology, the local values for the angles and corresponding flow velocities normal to cylinder at FBG sensors locations were calculated for the test No. 15; both frequency responses, 1 xa and 1 xb, associated to a second and third mode shapes respectively, were considered to calculate a reduced velocity range with results showed in table 6.2.

**Table 6.2 Local reduced velocities and drag coefficients, test no. 15**

	IL15	IL14	IL13	IL12	IL11	IL10	IL9	IL8	IL7	IL6	IL5	IL4	IL3	IL2	IL1
$\theta$ (deg)	7.01	7.09	7.23	7.41	7.61	7.85	8.12	8.39	8.68	9.00	9.28	9.55	9.76	9.88	9.89
U (m/s)	0.11	0.11	0.11	0.12	0.12	0.12	0.13	0.13	0.14	0.14	0.14	0.15	0.15	0.15	0.15
Ur [1 xa]	4.28	4.33	4.41	4.52	4.64	4.79	4.95	5.12	5.29	5.49	5.66	5.82	5.94	6.02	6.02
Ur [1 xb]	2.97	3.01	3.06	3.14	3.22	3.33	3.44	3.56	3.68	3.81	3.93	4.04	4.13	4.18	4.18

The local mean axial strain at FBG sensor locations and associated to the steady drag component was computed from FOSS data according to the procedure indicated at the end of section 5.5.

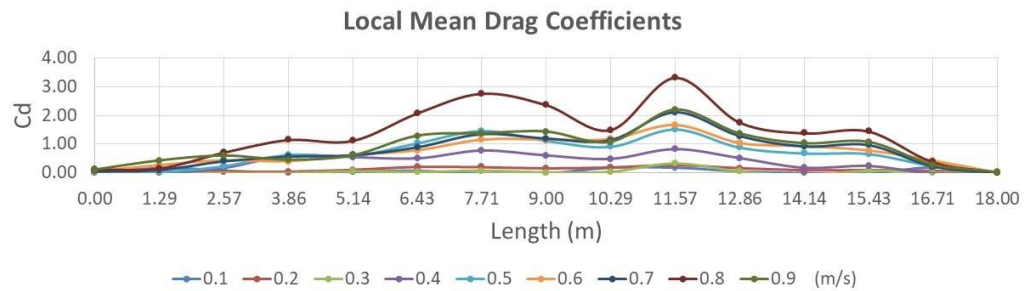
This allowed to obtain the local mean axial strain with respect to the initial static tension, then the tension values were obtained applying Hook’s law ( $\sigma = E \epsilon$ ), adding the initial static tension values for each test measured with the load cell at the trail end.

Table 6.3 summarises the calculated results for the first test series, showing the initial and final local angle of deviation for the deflected longitudinal axis of the model respect to the towing tank, with corresponding normal flow and reduced velocity ranges.

**Table 6.3 Local reduced velocity range and maximum drag coefficients for current flow alone**

Tow speed (m/s)	St	$\theta_{15}$ (deg)	$\theta_1$ (deg)	$\Delta\theta$ (deg)	$U_{15}$ (m/s)	$U_1$ (m/s)	$\Delta U$ (m/s)	Ur range	
0.1	0.454	10.01	10.05	-0.04	0.02	0.02	0.00	1.07	1.07
0.2	0.458	9.89	10.01	-0.12	0.03	0.03	0.00	2.16	2.18
0.3	0.193	9.45	9.85	-0.40	0.05	0.05	0.00	4.88	5.08
0.4	0.151	8.74	9.76	-1.02	0.06	0.07	0.01	5.79	6.46
0.5	0.135	8.27	9.85	-1.58	0.07	0.09	0.01	6.10	7.26
0.6	0.181	8.05	9.64	-1.58	0.08	0.10	0.02	4.43	5.30
0.7	0.176	7.80	9.94	-2.14	0.09	0.12	0.03	4.43	5.63
0.8	0.172	6.63	9.82	-3.19	0.09	0.14	0.04	3.85	5.69
0.9	0.169	7.01	9.89	-2.88	0.11	0.15	0.04	4.28	6.02
								2.97	4.18

Finally, the local mean drag coefficients were approximated using eq. 5.7, the distribution along the axis of the model is shown in Fig. 6.14 for the first test series.



**Figure 6.14 Preliminary local drag coefficient distributions along the riser length for current flow, tow depth = 1.05 m (25 OD)**

Unlike bending strain calculations, where the temperature sensitivity is compensated with FBG sensors in diametrically opposed fibre optic arrays, the temperature sensitivity is not compensated in the scope of this work for tension strains, which will require dedicated FBG sensors and additional calibration work, considering that FBG sensors are more sensitive to temperature than strain (see eq. 5.4); therefore, the previous results for local drag coefficients are presented only as part of the methodology developed and cannot be considered for reference without specific calibration tests.

### 6.1.5 Future work and potential of the FOSS/MOCAP integration

As a way to validate the method to estimate local velocities and local drag coefficients, an additional load cell located at the trail-end of the model could be used to compute the mean angle of the vector forces due to an IL mean drag, as done for the lead-end, in order to compare those measurements against the final angle calculated under the methodology discussed in the previous section.

A load cell at the trail-end could be mounted over a linear guide system to keep it connected back to the tensioning system; alternatively, a tiltmeter or other ways to measure the cable departure angle at the trail-end could also be implemented.

Tension distribution calculations from FOSS data using eq. 5.7 could be calibrated against traditional strain sensor measurements and assess the sensibility of the method to response amplitudes, number of sensors and lead/trail-end effects.

The method could be used to approximate the deflected profile of the model from FOSS data, where the position of each FBG sensor can be found projecting the geometric chord of length  $2 \text{ } \_\_\_\_\_\_$  at the angle from the starting angle .

Moreover, some extrapolation techniques can be explored to discretise the chord lengths between sensors and assess with the MOCAP system during additional tank testing if the accuracy can be improved, using extrapolated values of measured curvatures, e.g. the values from the spline function as used in the smooth curve construction of the chart tools to plot the bending strain amplitude responses, as in Fig. 6.1

Furthermore, using an interrogator with synchronisation capability, future work could also assess the possibility to calculate motion response from FOSS data at FBG sensor locations and at discretised points between sensors, by processing in real time the initial angle given by load cells force vectors and the time series bending strain/curvature data for the projections of the chords and respective angles.

The MOCAP system could assist to provide boundary displacements at one end, with the potential to get velocities and accelerations at all FBG sensor locations and discretised points.

The additional load cell could be used to assess the measurement capability of axial drag forces under determined setup conditions, considering aspect ratios and yaw angles for

towing tests, to investigate if the skin friction forces related to axial drag can be obtained from differential measurement between temporal mean tension values at the lead-end and the trail-end load cells, considering tension distribution measurement with the FOSS.

As commented in section 5.10.1, the similarity of the interaction between the structural vibrations and hydrodynamic forces needs to be considered in the model for hydroelasticity, looking for similar structural damping and mass distribution. A model based on a more flexible material, such as a fibre glass composite pipe could be considered, although the strain transfer of the bonding methods for the FBG sensors of the FOSS may need a specific evaluation to verify eq. 5.4 for the wavelength shift of the FBG sensors.

To provide the initial pre-tension in the model setup, a turnbuckle tensioner was implemented within the scope and resources of this experimental work (see figs. 5.12b and 5.14), applying pre-tensions about 115N and 190N. The maximum peak tensions measured in the load cell for the hardest conditions at maximum speed, free surface and/or highest waves, where below 300N, thus, it is recommended to implement in future tests a constant tension mechanism, e.g. a top pulley with a suspended weight equivalent to the peak tension expected instead of a turnbuckle, as a way to approach the test setup to real towing conditions; additionally, physical springs in the tension line could model the stiffness of full scale towing lines.

Current and wave tests were conducted in a heading seas condition, i.e. the towing direction against the direction of wave propagation in the towing tank; additional testing can explore the response for following seas, were the towing is conducted in the same direction of the wave propagation.

Nonetheless, it is considered that this type of VIV tests on relative long flexible pipeline/riser models in the towing tank of the Kelvin Hydrodynamic Laboratories, allowed an understanding of the basic response characteristics for tow-out operations, gaining experience in the first application of latest technologies for underwater motion capture and fibre optic sensing systems, that enabled integration with other University departments to innovate with instrumentation of research in these complex models, aiming to provide additional tools for future applications.



A potential to develop a methodology to exploit motion response measurement capabilities along the model span, including positions, velocities and accelerations with a proper integration and synchronisation of the FOSS, was also identified for future work, which can assist to investigate local hydrodynamic parameters, in order to avoid a high number of underwater cameras for a MOCAP system and the implications to avoid undesired turbulence to the model, due to the required locations in tank towing conditions.

Even when irregular waves could be tested in the towing tank facilities, regular waves were selected due to tank time constraints and considering that these represent a more adverse condition during tow operations.

The technology could be applied for greater length to diameter ratios in ocean basin/wave tank laboratories, to allow for testing in multiple combinations of current and wave flow directions, where the test time would not be restricted by the length to speed test ratio of a towing tank, avoiding limitations for response settlement and frequency resolution from PSD data analysis.

Moreover, ocean basin tanks can provide extended testing subject to sea spectra correlated with specific sea states according to metocean statistics of potential towing routes in different seasons.

The hydrodynamic parameters investigated in this way, can be used for further investigations and calibrations of VIV prediction models included in current software used by the offshore industry.

Additionally, several fluid-structure interactions related with tow installation methods can be further investigated in towing tank tests for future specific designs, such as hydrodynamic coefficients of multi-line hybrid risers or structural damping contributions of peripheral lines due to friction forces during axial sliding through the riser guides fitted on the core pipe of riser towers, since these are still modelled as a single equivalent pipeline for towing analysis.

The availability of the Flowave, a new circular basin tank facility for research, can also be of interest to conduct some tests, since it can provide combinations of wave and current flows in any relative direction (Ingram et al., 2014), although the tank size can restrict the scale

and maximum length to diameter ratios for specific designs, but with a flexible model correctly scaled for hydro-elasticity and Re similarity, there is a high potential for detailed VIV studies of flexibles at any yaw angles to further investigate aspects reviewed in section 2.1.3.

## 6.2 Test series results

Within the scope and assigned resources in this research, the test series were defined for a limited number of conditions.

These were conducted for a range of towing speeds from 0.1 to 0.9 m/s, with the submerged model at a depth equivalent to 25 times the outside diameter (25 OD) of the copper tube, considering the submerged depth from the free surface to the top of the tube's cross section at supports locations under towing carriages. The conditions encompass:

- i) Current flow alone
- ii) Current flow plus heading wave no. 1
- iii) Current flow plus heading wave no. 2
- iv) Some current flows plus heading wave no. 3
- v) Increment of initial tension for some cases in ii, and iii.
- vi) Induced turbulence for some cases in i, ii, iii and v.

To assess the effects of the tow depth, most of the tests in i, ii and iii were repeated for a tow depth of 10 OD and some at the free surface condition 0 OD, representing the conditions:

- vii) Change in tow depth (10 OD) for cases i, ii and iii.
- viii) Change in tow depth at free surface (0 OD) for cases i, ii and iii.

### 6.2.1 Current flow alone

The results of this first test series were presented in section 6.1, the main global parameters of interest are included in table 6.1 and figure 6.1, being these formats selected for analysis, discussions and comparison of the different conditions to be tested, the tabulated drag force per unit length is based in the first approximation indicated in section 5.12 from reactions measured in the lead-end for a first insight of the drag behaviour; the local mean drag coefficients along the axis and further details can be explored by data processing methods covered in sections 6.1.3 and 6.1.4.

Table 6.1 was updated in table 6.4, considering the PSD analysis of the FOSS system to get a clearer identification of dominant frequencies for comparative purposes of other tests.

The reduced velocities reported, were calculated initially with the normal component of the current flow velocity  $U_c$ , respect to the initial longitudinal axis.

**Table 6.4 Current flow (PSD analysis from FOSS data), tow depth = 1.05 m (25 OD)**

Test No.	Tow speed (m/s)	$\alpha_c$	$U_r$	Initial Tension (N)	Fd (N/m)	Re	IL freq. response			CF freq. reponse			CF/IL Dom.	St
							Dom. (Hz)	Low. (Hz)	High. (Hz)	Dom. (Hz)	1 x (Hz)	High. (Hz)		
16	0.10	1.00	2.20	115.67	-0.01	6.56E+02	0.19	0.19	0.77	0.39	0.19	0.77	2.05	0.45
17	0.20	1.00	2.19	112.39	0.03	1.30E+03	0.43	0.43	1.16	0.77	0.38	0.77	1.79	0.46
18	0.30	1.00	5.40	115.06	0.12	1.95E+03	0.46	0.23	0.46	0.23	0.23	0.23	0.50	0.19
19	0.40	1.00	6.39	114.08	0.29	2.60E+03	0.54	0.26	0.54	0.26	0.26	0.26	0.48	0.16
11	0.50	1.00	7.72	115.49	0.43	3.25E+03	0.81	0.27	1.33	0.27	0.27	0.54	0.33	0.13
12	0.60	1.00	5.58	115.66	0.53	3.89E+03	0.89	0.44	2.29	0.44	0.44	1.34	0.50	0.18
13	0.70	1.00	5.68	116.69	0.65	4.54E+03	1.00	0.49	2.35	0.51	0.51	0.51	0.51	0.18
14	0.80	1.00	5.81	115.50	1.26	5.19E+03	1.11	0.54	1.11	0.57	0.57	0.57	0.51	0.17
15	0.90	1.00	6.10	116.53	1.09	5.83E+03	1.52	0.61	1.52	0.61	0.61	2.35	0.40	0.16

The main findings for current flow alone are described as follows:

- (a) For tow speeds of 0.1-0.2 m/s, corresponding to reduced velocities up to about 2.2, the IL and CF time varying bending strain responses were negligible.
- (b) At higher tow speeds, the response and reduced velocities showed a typical lock-in range about  $5.4 < U_r < 7.7$ ; CF response presented 1 x and 3 x peak frequencies in PSD analysis, whereas IL response showed 2 x, 1 x and for some cases up to 5 x harmonics.
- (c) The bending strain profiles for CF response presented a dominant first vibrational mode shape for the dominant 1 x frequency for tests between 0.1 to 0.5 m/s ( $2.2 <$

$U_r < 7.7$ ), a dominant second mode shape response for tests between 0.6 to 0.8 m/s ( $5.6 < U_r < 5.8$ ) and a likely hybrid second-third mode shape for the highest towing speed tested at 0.9 m/s ( $U_r = 6.1$ ).

- (d) Similarly, the vibrational modes for the IL response can be identified in Fig. 6.1, although the effect of the harmonics is higher over the more familiar standing wave mode shapes shown for the CF direction.
- (e) It was noted a reduction of the CF bending response in test No. 13 at 0.7 m/s respect to test No. 12 at lower tow speed, before a high increase of the drag in test No. 14.
- (f) The global mean drag force reached maximum values at test no. 14 with a tow speed of 0.8 m/s and a reduced velocity of 5.8, then a reduction of drag can be noted for test no. 15 at a higher tow speed of 0.9 m/s, with a reduced velocity of 6.1; these results summarised in table 6.1 are coherent with the mean IL bending strains response profile showed in fig. 5.34, where test no. 14 showed higher amplitudes over test no. 15, which together with the observations in incise c), suggest the possibility of an intermittent switch within the upper-lower transition discussed in section 6.1.3.
- (g) Within typical lock-in range, the Strouhal number ( $St$ ) found in this series had a range from 0.19 to 0.13 within the first mode of vibration, where the lowest  $St$  value corresponded with the highest reduced velocity before a change to the second mode response, where  $St$  range was 0.18 to 0.17, then a value of 0.16 in the next mode.

## 6.2.2 Current flow plus heading wave no. 1

Table 6.5 summarise the results of this section, which was conducted for the same towing speed range of the first series but subject to the test wave no.1 defined in section 2.3, 5.10.1 and table 5.8. For tests with combinations of current and wave flows the measured wave frequency generated in the tank was included with the measured encounter wave frequency.

In the same way as presented in Fig. 6.1, the RMS amplitudes of the time varying CF and IL bending strains measured with the FOSS are showed in fig. 6.15.

The maximum horizontal wave particle velocities were calculated as per section 5.10.2, using Fenton’s 5<sup>th</sup> order theory. Considering the initial upward deflection of the model and that the wave particle velocities varies with depth from the free surface, the velocities were calculated for the maximum and minimum depths of the model along the span, to identify the magnitude of the difference in velocities and report the range of KC numbers.

According to recommended practices (DNV-RP-H103, 2010), for combinations of current and wave flows the governing parameters are the Reynolds number (Re), KeuleganCarpenter number (KC) and the current flow velocity ratio ( $\alpha_c$ ).

Re is based on the maximum velocity of the water particles solved normal to the cylinder, i.e. the normal component of the current flow velocity plus the maximum wave particle or orbital velocity.

KC, the dimensionless quantity to express the ratio of drag over inertia forces in oscillatory fluid flows, is defined as  $KC = \frac{U_{wm} T}{D}$ , where  $U_{wm}$  is the maximum wave particle velocity resolved normal to the cylinder, T is the wave period and D is the cylinder’s outside diameter.

$\alpha_c$  is the ratio of the current flow velocity respect to the total flow velocity, i.e.  $\alpha_c = \frac{U_c}{U_c + U_{wm}}$ .

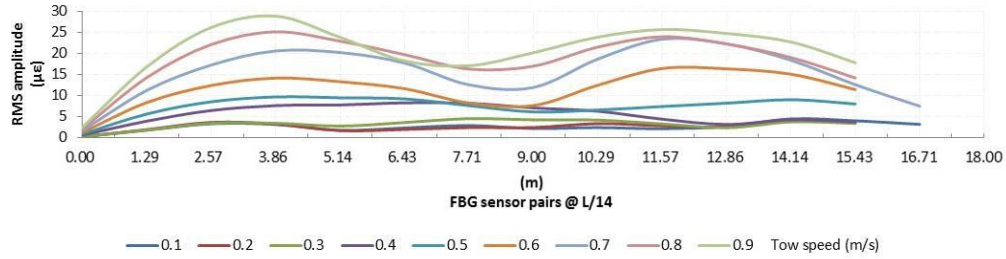
**Table 6.5 Current flow plus heading wave no. 1, tow depth = 1.05 m (25 OD)**

Test No.	Tow speed (m/s)	Enc. freq. (Hz)	Wave freq. (Hz)	$\alpha_c$	Ur	Initial Tension (N)	Fd (N/m)	Re	KC min	KC max	Uk	Uk/KC range	
24	0.10	0.60	0.58	0.59	0.69	118.94	0.01	1.11E+03	0.30	0.51	0.69	2.32	1.36
25	0.20	0.62	0.58	0.75	1.34	120.90	0.04	1.73E+03	0.28	0.47	1.33	4.78	2.82
26	0.30	0.64	0.58	0.82	1.91	121.04	0.11	2.36E+03	0.27	0.46	1.92	7.13	4.20
27	0.40	0.67	0.58	0.86	5.71	119.34	0.22	3.01E+03	0.27	0.45	2.49	9.36	5.51
28	0.50	0.69	0.58	0.88	5.91	119.78	0.34	3.70E+03	0.29	0.50	3.01	10.29	6.04
29	0.60	0.71	0.58	0.90	5.16	119.28	0.50	4.32E+03	0.28	0.47	3.48	12.53	7.37
30	0.70	0.73	0.58	0.91	5.47	118.11	0.85	4.97E+03	0.27	0.47	3.96	14.47	8.50
31	0.80	0.75	0.58	0.92	5.80	118.32	1.18	5.64E+03	0.29	0.50	4.39	14.91	8.75
32	0.90	0.77	0.58	0.93	6.10	120.29	1.41	6.26E+03	0.27	0.47	4.80	17.53	10.30

(continued)

Test No.	IL freq. response			CF freq. response			CF/IL Dom.	St
	Dom. (Hz)	Low. (Hz)	High. (Hz)	Dom. (Hz)	1 x (Hz)	High. (Hz)		
24	0.60	0.58	0.60	0.60	0.60	0.60	1.00	0.85
25	0.59	0.59	1.25	0.62	0.62	0.62	1.06	0.56
26	0.77	0.77	0.77	0.65	0.65	0.77	0.84	0.43
27	0.29	0.29	1.32	0.29	0.29	0.66	1.00	0.15
28	0.85	0.35	0.85	0.35	0.35	0.69	0.41	0.15
29	0.95	0.49	0.95	0.48	0.48	1.42	0.51	0.17
30	1.04	1.04	1.04	0.53	0.53	1.57	0.51	0.17
31	1.10	1.10	1.47	0.57	0.57	1.66	0.52	0.16
32	1.22	0.61	2.44	0.61	0.61	0.61	0.50	0.15

### CF Bending Strain Response to VIV



### IL Bending Strain Response to VIV

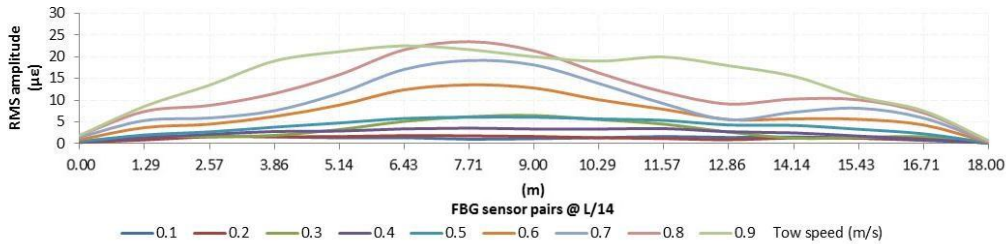


Figure 6.15 Bending strain responses due to current flow plus heading wave no. 1, tow depth = 1.05 m (25 OD)

From examination of results, the findings were:

- For tow speeds of 0.1-0.3 m/s, corresponding to reduced velocities less than 2.0 ( $\alpha_c < 0.85$  or  $U_{wm} > U_c/6$ ) the dominant CF frequency response is about the measured encounter wave frequency, so the CF response was driven by the inertia and frequency of the wave flow induced forces at those towing speeds.
- At higher tow speeds, the response and reduced velocities showed a typical lock-in range about  $5.2 < U_r < 6.1$ , CF and IL responses were more dominated by 1 x and 2 x peak frequencies respectively, with very weak harmonic peak responses.
- Comparing the time varying bending strain amplitudes (fig. 6.15) against the previous results for current flow alone (fig. 6.1), the combined current plus wave

flows produced a decrement in amplitudes for tow speeds between 0.3 to 0.6 m/s, being the response amplitude higher at 0.7 m/s, and similar at 0.8-0.9 m/s.

- (d) Within typical lock-in range, the Strouhal number (St) found in this series had a value of 0.15 in tests nos. 27 and 28, presenting a mode of vibration in CF between first and second mode (fig. 6.15); for increasing tow speeds in tests nos. 29 to 32, a more dominant second mode shape profile is observed, with a St range decreasing from 0.17 to 0.15.

### 6.2.3 Current flow plus heading wave no. 2

Following the considerations of the two previous sections, the results for the test series with wave no. 2 are summarised in table 6.6 and fig. 6.16 below.

**Table 6.6 Current flow plus heading wave no. 2, tow depth = 1.05 m (25 OD)**

Test No.	Tow speed (m/s)	Enc. freq. (Hz)	Wave freq. (Hz)	$\alpha_c$	Ur	Initial Tension (N)	Fd (N/m)	Re	KC min	KC max	Uk	Uk/KC range	
85	0.10	0.47	0.46	0.35	0.87	116.75	0.05	1.87E+03	1.24	1.69	0.88	0.71	0.52
86	0.20	0.49	0.46	0.52	1.69	118.44	0.17	2.52E+03	1.24	1.68	1.70	1.38	1.01
87	0.30	0.50	0.46	0.62	2.47	117.75	0.27	3.16E+03	1.23	1.68	2.47	2.01	1.47
88	0.50	0.53	0.46	0.73	3.86	118.72	0.51	4.46E+03	1.23	1.68	3.90	3.17	2.33
89	0.70	0.56	0.46	0.80	7.36	116.54	0.76	5.69E+03	1.17	1.59	5.18	4.43	3.25
90	0.90	0.59	0.46	0.84	6.15	113.79	1.06	6.97E+03	1.15	1.57	6.34	5.50	4.03

(continued)

Test No.	IL freq. response			CF freq. reponse			CF/IL Dom.	St
	Dom. (Hz)	Low. (Hz)	High. (Hz)	Dom. (Hz)	1 x (Hz)	High. (Hz)		
85	0.87	0.47	0.87	0.48	0.48	0.87	0.55	0.40
86	0.85	0.49	1.34	0.49	0.49	0.86	0.57	0.31
87	0.87	0.50	1.37	0.50	0.50	0.87	0.58	0.25
88	0.88	0.88	1.42	1.42	0.54	1.42	1.61	0.19
89	0.94	0.54	1.32	0.54	0.39	0.74	0.58	0.11
90	1.46	0.59	1.46	0.61	0.61	0.84	0.41	0.14

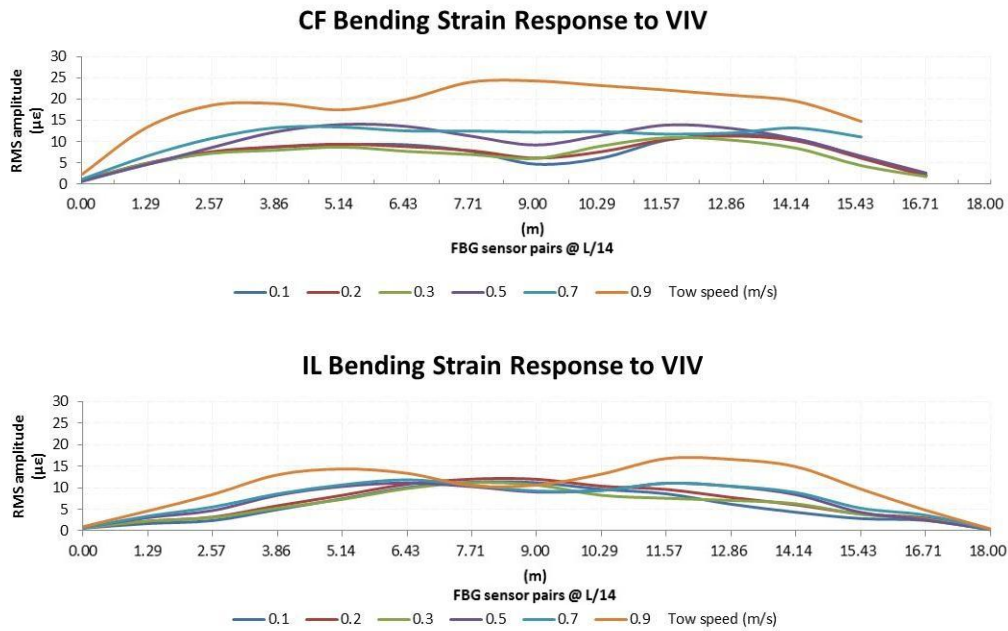


Figure 6.16 Bending strain responses due to current flow plus heading wave no. 2, tow depth = 1.05 m (25 OD)

The findings for this condition were:

- (a) For all of the tow speeds, the dominant frequencies for CF responses are about the measured encounter wave frequency, the response showed a more generalised influence of the inertia and frequency of the wave flow induced forces, with one exception in test no. 88, where the 1 x frequency was not the dominant response frequency but a frequency corresponding to the addition of the wave encounter frequency plus the IL dominant frequency, although the 1 x CF frequency of this test was also about the wave encounter frequency.
- (b) Time varying bending strain amplitudes for tests with  $Ur < 5.0$  were greater than those measured for the wave no.1, whereas tests with  $Ur > 5.0$  presented lower response amplitudes, i.e. the wave flow increased the response until the vortex shedding within typical lock-in range caused a decrement in vibration amplitudes with respect to tests with wave no. 1.
- (c) Strouhal numbers for the tests nos. 89 and 90 with  $Ur > 5.0$  were lower than the previous series, with a range of  $0.11 < St < 0.14$ . It must be mentioned that in test



no. 89 there was a non-dominant first peak in the PSD analysis giving the reported values of  $U_r = 7.36$  and  $St = 0.11$ , however if the dominant frequency is considering for these parameters instead of the first peak frequency, the values for the reduced velocity and Strouhal number would be 5.34 and 0.15 respectively, so  $St$  will be decreasing from 0.15 to 0.14 as  $U_r$  increases from 5.34 to 6.15.

### 6.2.4 Current flow plus heading wave no. 3

Wave no. 3 considers the extreme value case mentioned in section 2.3. Due to concerns about the model response and strength of the instrumentation, the test was left to the end of the tank time assigned and towed at 0.1 and 0.5 m/s in one single run. Results are summarised in table 6.7 and fig. 6.17 as follows:

**Table 6.7 Current flow plus heading wave no. 3, tow depth = 1.05 m (25 OD)**

Test No.	Tow speed (m/s)	Enc. freq. (Hz)	Wave freq. (Hz)	$\alpha_c$	$U_r$	Initial Tension (N)	$F_d$ (N/m)	Re	KC min	KC max	$U_k$	Uk/KC range	
120	0.10	0.36	0.35	0.18	1.12	185.82	0.12	3.52E+03	4.41	5.25	1.16	0.26	0.22
120	0.50	0.40	0.35	0.56	5.30	185.82	0.72	5.79E+03	3.92	4.65	5.22	1.33	1.12

(continued)

Test No.	IL freq. response			CF freq. reponse			CF/IL Dom.	St
	Dom. (Hz)	Low. (Hz)	High. (Hz)	Dom. (Hz)	1 x (Hz)	High. (Hz)		
120	0.96	0.37	1.42	0.37	0.37	0.37	0.39	0.16
120	0.98	0.19	1.47	0.39	0.39	0.39	0.40	0.11

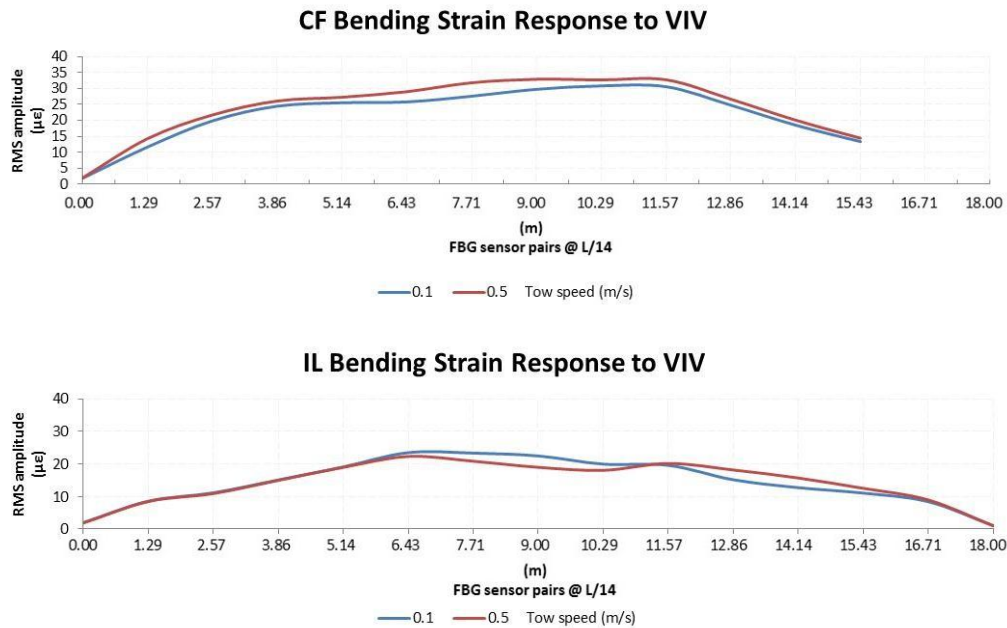


**Figure 6.17 Bending strain responses due to current flow plus heading wave no. 3, tow depth = 1.05 m (25 OD)**

The findings for this condition with the extreme wave case were:

- (a) For both tow speeds, the dominant CF frequencies were about the measured encounter wave frequency.
- (b) Time varying bending strain amplitudes showed a clear dominance of the inertia of the wave flow induced forces, regardless that the second part of the test reached a reduced velocity value within typical lock-in range.

**6.2.5 Current flow plus heading wave no. 1 (increment of initial tension respect 6.2.2)**

To assess the effects of an increment for the initial tension during the response, an additional test with a repetition at the maximum towing speed were performed for current and wave flows, the results for the case with wave no.1 are indicated in table 6.8 and fig. 6.18 below.

**Table 6.8 Current flow plus heading wave no. 1 with tension increment, tow depth = 1.05 m (25 OD)**

Test No.	Tow speed (m/s)	Enc. freq. (Hz)	Wave freq. (Hz)	$\alpha_c$	Ur	Initial Tension (N)	Fd (N/m)	Re	KC min	KC max	Uk	Uk/KC range	
118	0.90	0.77	0.58	0.93	5.85	184.43	1.61	6.26E+03	0.28	0.47	4.80	17.35	10.19
119	0.90	0.77	0.58	0.93	5.90	185.07	1.10	6.26E+03	0.28	0.47	4.80	17.35	10.17

(continued)

Test No.	IL freq. response			CF freq. response			CF/IL Dom.	St
	Dom. (Hz)	Low. (Hz)	High. (Hz)	Dom. (Hz)	1 x (Hz)	High. (Hz)		
118	1.27	1.27	2.54	0.64	0.64	0.64	0.50	0.16
119	1.56	*1.28	1.56	0.63	0.63	0.63	0.40	0.16

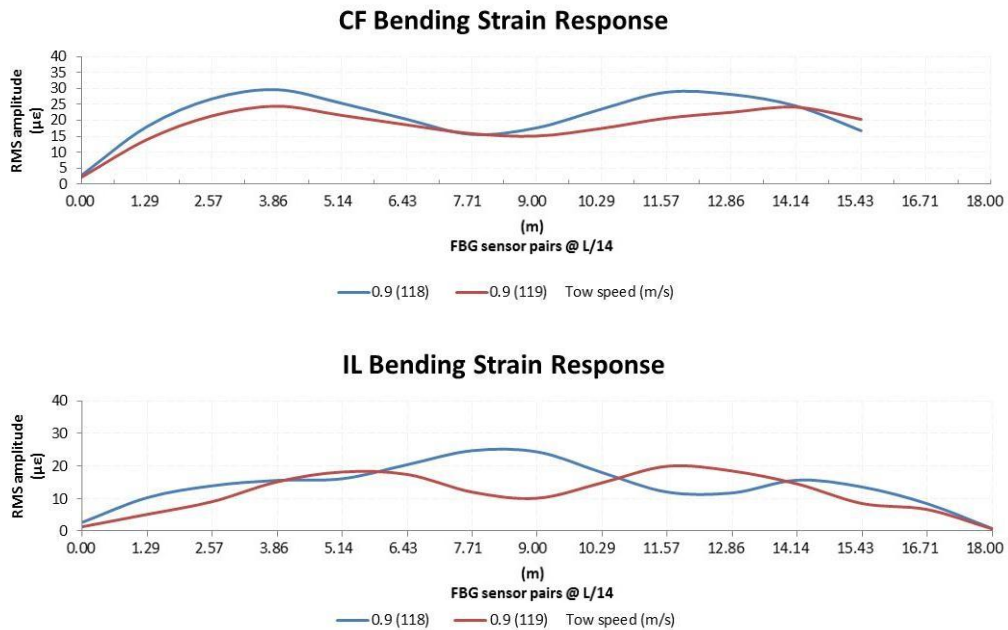


Figure 6.18 Bending strain responses due to current flow plus heading wave no. 1 with tension increment, tow depth = 1.05 m (25 OD)

The findings were:

- (a) The CF and IL frequency response presented increments within expected values, considering the tension effects evaluated in table 5.7, although the IL response in test no. 119 experimented a shift from a \*weak 2 x peak of 1.28 Hz to a dominant IL frequency response about 1.56 Hz, with the modification in the IL mode shape as showed in fig. 6.18, the lower CF bending strain response amplitudes in test no. 119

respect to test no. 118, corresponded to the observed shift in the dominant IL frequency.

### 6.2.6 Current flow plus heading wave no. 2 (increment of initial tension respect 6.2.3)

As in previous section, two tests at the maximum towing speed were considered for the conditions of this section subject to a higher initial tension and wave no. 2, with results indicated in table 6.9 and fig. 6.19 below.

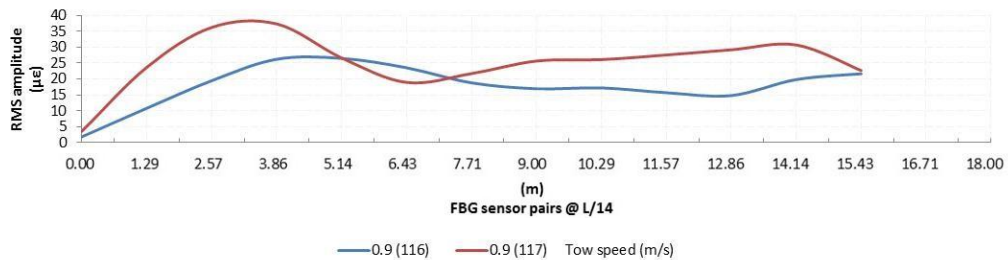
**Table 6.9 Current flow plus heading wave no. 2 with tension increment, tow depth = 1.05 m (25 OD)**

Test No.	Tow speed (m/s)	Enc. freq. (Hz)	Wave freq. (Hz)	$\alpha_c$	Ur	Initial Tension (N)	Fd (N/m)	Re	KC min	KC max	Uk	Uk/KC range	
116	0.90	0.59	0.46	0.84	5.81	184.24	1.27	6.98E+03	1.17	1.59	6.34	5.42	3.98
117	0.90	0.59	0.46	0.84	6.00	185.59	1.39	6.96E+03	1.15	1.57	6.34	5.51	4.04

(continued)

Test No.	IL freq. response			CF freq. response			CF/IL Dom.	St
	Dom. (Hz)	Low. (Hz)	High. (Hz)	Dom. (Hz)	1 x (Hz)	High. (Hz)		
116	1.56	*1.28	1.56	0.64	0.64	0.64	0.41	0.14
117	1.22	**1.22	2.44	0.62	0.62	0.62	0.51	0.14

#### CF Bending Strain Response



#### IL Bending Strain Response

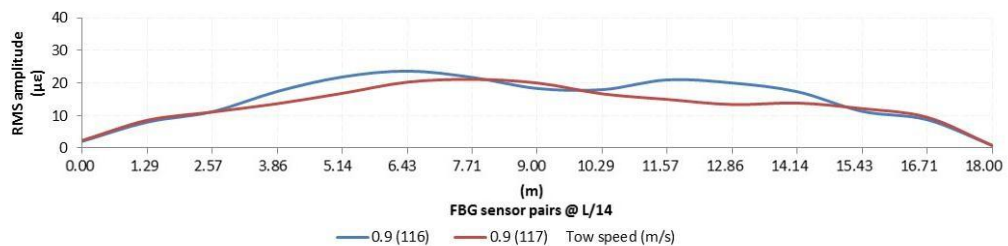


**Figure 6.19 Bending strain responses due to current flow plus heading wave no. 2 with tension increment, tow depth = 1.05 m (25 OD)**

The findings were:

- (a) Both IL responses presented peaks in PSD analysis about the 2 x harmonic at 1.28 and 1.22 Hz, but the dominant IL frequency of test no. 116 showed a peak at the shifted frequency of 1.56 Hz.
- (b) Time varying IL bending strains showed similar amplitudes toward the centre of the length with some differences according to the change in the mode shape along the model, but the CF bending strain response in test no. 116 showed a reduction against test no. 117. Again, as in the previous section the shift in the dominant IL frequency of test no. 116 showed a relation with the reduction of the bending strain amplitudes in the CF response.

### 6.2.7 Current flow with induced turbulence

There was an interest to explore the effects of some induced turbulence in the response of the model respect to the previous test series, thus three squared 90x90L aluminium profiles structural elements, like the used as vertical supports for the riser model and the underwater cameras, were distributed and installed in front of the main towing carriage to generate separation and turbulent flows for the riser model towed behind. The turbulent velocity fluctuations in the wakes of the three vertical elements were not measured due to time restrictions, although it could be useful to perform tests with a range of turbulence intensities in future detailed investigations.

The tests results are presented in the same formats of tables and figures (see table 6.10 and fig. 6.20 below) to be compared against results of tests conducted without induced turbulence.

**Table 6.10 Current flow with induced turbulence, tow depth = 1.05 m (25 OD)**

Test No.	Tow speed (m/s)	$\alpha_c$	Ur	Initial Tension (N)	Fd (N/m)	Re	IL freq. response			CF freq. reponse			CF/IL Dom.	St
							Dom. (Hz)	Low. (Hz)	High. (Hz)	Dom. (Hz)	1 x (Hz)	High. (Hz)		

93	0.10	1.00	2.15	108.00	0.01	6.55E+02	0.19	0.19	0.39	0.19	0.19	0.77	1.00	0.46
94	0.30	1.00	5.46	107.55	0.11	1.95E+03	0.46	0.23	0.46	0.23	0.23	0.23	0.50	0.18
95	0.50	1.00	8.78	107.29	0.33	3.25E+03	0.76	0.39	0.76	0.39	0.24	0.68	0.51	0.11
96	0.70	1.00	5.53	106.41	0.97	4.54E+03	1.03	1.03	1.03	0.52	0.52	1.56	0.51	0.18
97	0.90	1.00	5.91	107.48	1.61	5.83E+03	1.25	1.25	2.50	0.63	0.63	1.88	0.50	0.17

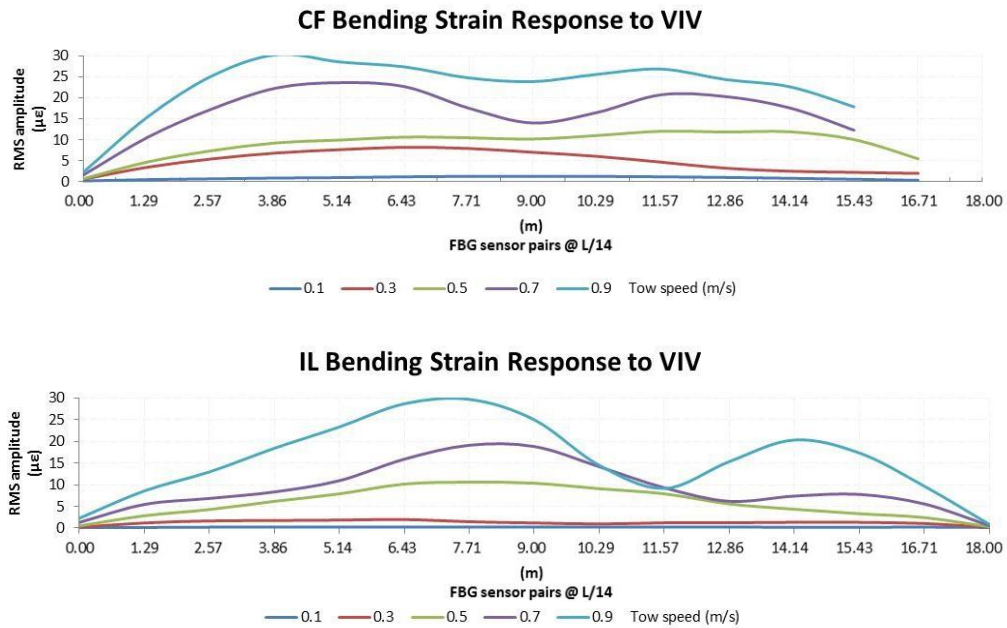


Figure 6.20 Bending strain responses due to current flow with induced turbulence, tow depth = 1.05 m (25 OD)

The findings were:

- (a) For the towing speeds of 0.1, 0.3 and 0.7 m/s the CF and IL frequency responses were similar, whereas 0.5 and 0.9 m/s towing speeds presented slightly lower IL and higher CF frequency responses than those for the current flow alone case; being the last two cases in tests nos. 95 and 97 at the flow velocity conditions related with indications of the response branch transitions reviewed in sections 6.1.3 and 6.2.1.
- (b) PSD analysis in test no. 95 showed a typical 2 x IL dominant response frequency respect to the 1 x CF frequency, whereas test no. 11 without induced turbulence presented a lower dominant CF response frequency of 0.27 Hz with a weak 2 x IL response frequency, being a 3 x harmonic the dominant IL frequency.

- (c) As in test no. 89 of section 6.2.3, test no. 95 presented a non-dominant CF first peak in the PSD analysis, which leads to a high value for the reduced velocity of 8.78 and low St of 0.11, if the dominant frequency is considering for these parameters instead of the first peak frequency, the values for the reduced velocity and Strouhal number would be 5.37 and 0.19 respectively.
- (d) Time varying bending strains in test no. 97 were found slightly higher than test no. 15 without turbulence at the same maximum towing speed, where it can be noted that the dominant IL frequency in test no. 15 also presents a shift to a higher frequency than that of the 2 x harmonic.

### 6.2.8 Current flow plus heading wave no. 1 with induced turbulence

**Table 6.11 Current flow plus heading wave no. 1 with induced turbulence, tow depth = 1.05 m (25 OD)**

Test No.	Tow speed (m/s)	Enc. freq. (Hz)	Wave freq. (Hz)	$\alpha_c$	Ur	Initial Tension (N)	Fd (N/m)	Re	KC min	KC max	Uk	Uk/KC range	
98	0.10	0.60	0.58	0.60	2.12	106.44	0.02	1.09E+03	0.28	0.48	0.69	2.43	1.43
99	0.50	0.69	0.58	0.88	5.17	106.42	0.32	3.68E+03	0.28	0.48	3.01	10.58	6.23
100	0.90	0.78	0.58	0.93	5.90	106.42	1.22	6.29E+03	0.30	0.51	4.79	16.14	9.47
106	0.90	0.77	0.58	0.93	5.39	107.84	1.07	6.25E+03	0.27	0.46	4.80	17.81	10.47

(continued)

Test No.	IL freq. response			CF freq. reponse			CF/IL Dom.	St
	Dom. (Hz)	Low. (Hz)	High. (Hz)	Dom. (Hz)	1 x (Hz)	High. (Hz)		
98	0.60	0.20	0.66	0.60	0.20	0.60	1.00	0.28
99	0.81	0.40	0.81	0.40	0.40	1.23	0.49	0.17
100	1.47	0.20	1.47	0.63	0.63	0.63	0.43	0.16
106	1.47	1.47	1.47	0.69	0.69	0.73	0.47	0.17

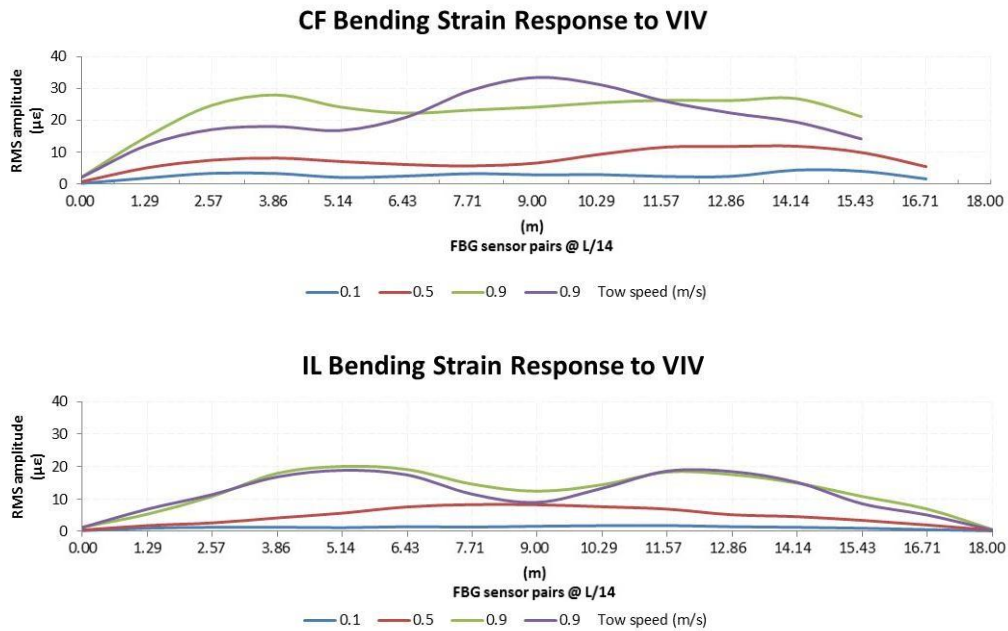


Figure 6.21 Bending strain responses due to current flow plus heading wave no. 1 with induced turbulence, tow depth = 1.05 m (25 OD)

From results in table 6.11 and fig. 6.21 above, the findings were:

- (a) For  $U_r > 5.0$ , CF and IL dominant frequency responses showed some increments with respect to the tests without turbulence.
- (b) Time varying bending strains are within the same range, although a mode shape change is evident for the difference in the CF dominant frequencies between repeated tests 100 and 106, where the PSD showed some additional non-harmonic frequency peaks after the dominant response, as in fig. 6.3a, which again suggest each of the repeated tests responding to the different intermittent response of the upper-lower transition, although longer run times will be required to support this hypothesis.

### 6.2.9 Current flow plus heading wave no. 2 with induced turbulence

During this series, there was a failure in the triggering of test no. 102 for the data acquisition of the mocap system and the load cell, thus it was repeated as test no. 103 (see table 6.12);



however, FOSS data was captured for test no. 102 and is included in fig. 6.22, showing the agreement of the time varying bending strain response with test no. 103.

**Table 6.12 Current flow plus heading wave no. 2 with induced turbulence, tow depth = 1.05 m (25 OD)**

Test No.	Tow speed (m/s)	Enc. freq. (Hz)	Wave freq. (Hz)	$\alpha_c$	Ur	Initial Tension (N)	Fd (N/m)	Re	KC min	KC max	Uk	Uk/KC range	
101	0.10	0.47	0.46	0.35	0.87	106.99	0.05	1.86E+03	1.22	1.67	0.88	0.72	0.53
103	0.50	0.53	0.46	0.73	3.88	106.90	0.52	4.44E+03	1.22	1.66	3.90	3.20	2.35
104	0.90	0.59	0.46	0.84	6.41	106.80	1.14	6.97E+03	1.15	1.57	6.33	5.49	4.03
105	0.90	0.59	0.46	0.84	6.26	107.28	1.08	6.96E+03	1.14	1.56	6.33	5.54	4.06

(continued)

Test No.	IL freq. response			CF freq. response			CF/IL Dom.	St
	Dom. (Hz)	Low. (Hz)	High. (Hz)	Dom. (Hz)	1 x (Hz)	High. (Hz)		
101	0.87	0.48	0.87	0.48	0.48	0.87	0.55	0.41
103	0.89	0.54	1.42	0.53	0.53	1.42	0.60	0.19
104	1.50	0.59	2.40	0.58	0.58	2.40	0.39	0.13
105	1.18	0.24	2.36	0.59	0.59	1.35	0.50	0.13

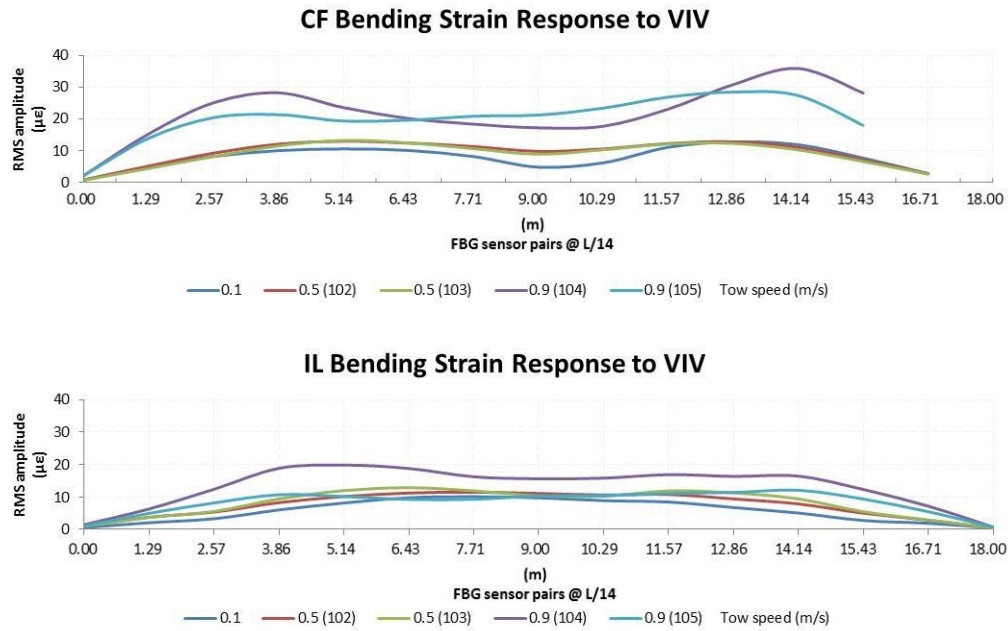


**Figure 6.22 Bending strain responses due to current flow plus heading wave no. 2 with induced turbulence, tow depth = 1.05 m (25 OD)**

The findings were:

- (a) The response showed a similar general behaviour as commented for the results in section 6.2.3.
- (b) Time varying bending strains showed amplitudes within the same range, except for the maximum tow speed tested in test no. 104, which presented higher amplitudes and higher IL dominant frequency respect to the response without induced turbulence, although test no. 105 presented lower dominance and more distributed peak frequencies in the IL response.
- (c) Tow speeds up to 0.5 m/s, which correspond to the maximum practical towing speed at full scale, was below typical lock-in range with  $Ur < 4.0$ , being the response mainly dominated by the inertia of the wave flow induced forces.

### 6.2.10 Current flow plus heading wave no. 1 with increment of initial tension and induced turbulence

**Table 6.13 (Induced turbulence over 6.2.5 case), tow depth = 1.05 m (25 OD)**

Test No.	Tow speed (m/s)	Enc. freq. (Hz)	Wave freq. (Hz)	$\alpha_c$	Ur	Initial Tension (N)	Fd (N/m)	Re	KC min	KC max	Uk	Uk/KC range	
112	0.90	0.78	0.58	0.93	5.81	182.85	1.65	6.29E+03	0.29	0.50	4.80	16.43	9.64
113	0.90	0.78	0.58	0.93	5.90	184.07	1.20	6.27E+03	0.28	0.48	4.78	16.89	9.90

(continued)

Test No.	IL freq. response			CF freq. reponse			CF/IL Dom.	St
	Dom. (Hz)	Low. (Hz)	High. (Hz)	Dom. (Hz)	1 x (Hz)	High. (Hz)		
112	1.27	1.27	2.55	0.64	0.64	0.64	0.50	0.16
113	1.57	1.23	2.48	0.63	0.63	2.44	0.40	0.16

Figure 6.23 includes RMS amplitudes of the time varying bending strains of section 6.2.5 for comparative purposes.

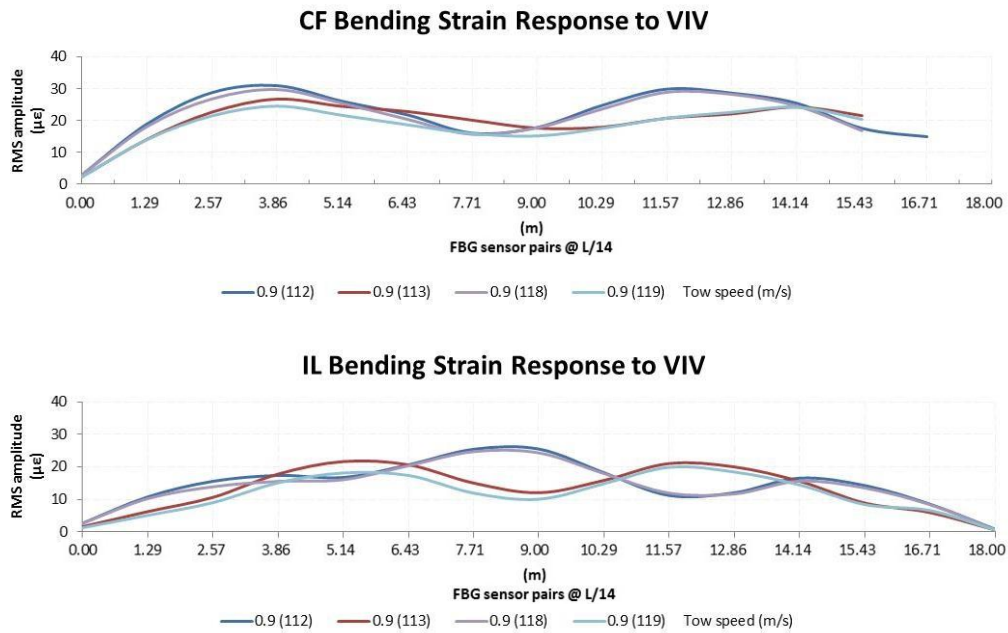


Figure 6.23 Bending strain (induced turbulence over 6.2.5 case), tow depth = 1.05 m (25 OD)

From results in table 6.13 and fig.6.23, the findings were:

- (a) Similar general behaviour as commented for results in section 6.2.5 without turbulence.
- (b) The shift in the dominant IL frequency of test no. 113 cannot be explained by induced turbulence effects, since it is experienced either in this section or in 6.2.5; nonetheless, it can be again observed that as the IL dominant frequency shift to higher values than that of a typical 2 x harmonic, a decrease in the time varying bending strains is noted for the CF direction.
- (c) Induced turbulence effects, if any, were restricted to a very small increment in the time varying bending strain amplitudes of tests nos. 112 and 113 over tests 118 and 119.

### 6.2.11 Current flow plus heading wave no. 2 with increment of initial tension and induced turbulence

Table 6.14 (Induced turbulence over 6.2.6 case), tow depth = 1.05 m (25 OD)

Test No.	Tow speed (m/s)	Enc. freq. (Hz)	Wave freq. (Hz)	$\alpha$	Ur	Initial Tension (N)	Fd (N/m)	Re	KC min	KC max	Uk	Uk/KC range	
114	0.90	0.59	0.46	0.84	6.30	183.45	1.33	6.98E+03	1.17	1.59	6.33	5.42	3.98
115	0.90	0.59	0.46	0.84	6.20	183.88	1.07	6.98E+03	1.17	1.59	6.33	5.40	3.97

(continued)

Test No.	IL freq. response			CF freq. response			CF/IL Dom.	St
	Dom. (Hz)	Low. (Hz)	High. (Hz)	Dom. (Hz)	1 x (Hz)	High. (Hz)		
114	1.22	0.59	2.50	0.59	0.59	0.59	0.49	0.13
115	1.20	1.20	2.45	0.60	0.60	1.48	0.50	0.13

The figure 6.24 includes RMS amplitudes of the time varying bending strains of section 6.2.6 for comparative purposes.

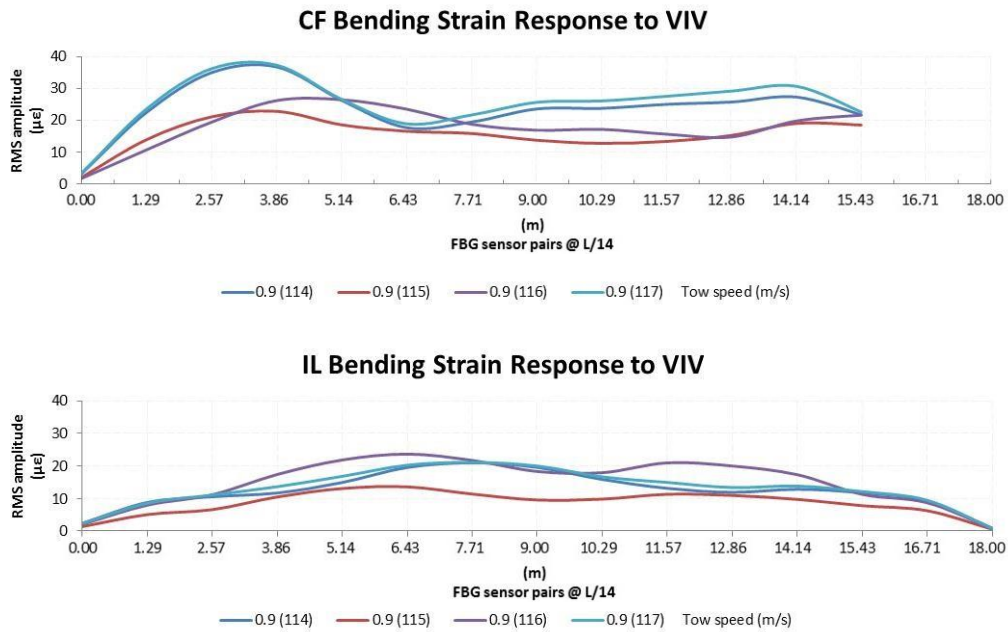


Figure 6.24 Bending strain (induced turbulence over 6.2.6 case), tow depth = 1.05 m (25 OD)

From results in table 6.14 and fig. 6.24, the findings were:

- Similar general behaviour as commented for results in section 6.2.6.
- The shift in the dominant IL frequency was experienced only in test 116, with the effect in the mode shape response shown in fig. 6.24 respect to the tests of this section.

- (c) The induced turbulence effects, if any, are restricted to small decrements in the time varying bending strain amplitudes of tests 114 and 115 over tests 116 and 117.

A greater number of tests, turbulence intensities or longer times of exposure in an ocean basin tank could be performed in future work to conduct a better assessment of turbulence effects in current plus wave flow conditions.

### 6.2.12 Tow depth change to 10 OD and 0 OD for current flow alone

To assess the effects of the proximity to the free surface, the test series in 6.2.1 were repeated, changing the tow depth to 10 OD and to the towing tank free surface at 0 OD, thus the tables and figures summarising the results will be compared accordingly.

**Table 6.15 Current flow alone, tow depth = 0.42 m (10 OD)**

Test No.	Tow speed (m/s)	$\alpha_c$	$U_r$	Initial Tension (N)	Fd (N/m)	Re	IL freq. response			CF freq. reponse			CF/IL Dom.	St
							Dom. (Hz)	Low. (Hz)	High. (Hz)	Dom. (Hz)	1 x (Hz)	High. (Hz)		
35	0.10	1.00	2.16	116.33	0.00	6.54E+02	0.58	0.19	1.34	0.58	0.19	0.78	1.00	0.46
36	0.20	1.00	2.16	116.86	0.04	1.30E+03	0.39	0.39	1.16	0.38	0.38	0.77	1.00	0.46
37	0.30	1.00	5.18	117.42	0.09	1.95E+03	0.24	0.24	0.58	0.24	0.24	0.58	1.00	0.19
38	0.40	1.00	6.14	117.49	0.24	2.60E+03	0.27	0.27	0.81	0.27	0.27	0.27	1.00	0.16
39	0.50	1.00	6.90	117.35	0.45	3.24E+03	0.78	0.39	1.34	0.30	0.30	0.40	0.38	0.14
40	0.60	1.00	5.39	118.24	0.55	3.89E+03	0.93	0.48	1.32	0.46	0.46	1.41	0.49	0.19
41	0.70	1.00	5.37	117.58	0.98	4.54E+03	1.07	0.53	2.42	0.54	0.54	1.60	0.50	0.19
42	0.80	1.00	5.61	118.56	1.30	5.19E+03	1.17	0.59	1.17	0.59	0.59	1.75	0.50	0.18
43	0.90	1.00	6.10	118.70	1.54	5.83E+03	1.22	1.22	1.55	0.61	0.61	2.49	0.50	0.16

**Table 6.16 Current flow alone, tow depth = 0.00 m (free surface, 0 OD)**

Test No.	Tow speed (m/s)	$\alpha_c$	Ur	Initial Tension (N)	Fd (N/m)	Re	IL freq. response			CF freq. reponse			CF/IL Dom.	St
							Dom. (Hz)	Low. (Hz)	High. (Hz)	Dom. (Hz)	1 x (Hz)	High. (Hz)		
60	0.10	1.00	2.19	124.36	-0.07	6.54E+02	0.63	0.19	1.08	0.58	0.19	0.96	0.92	0.46
61	0.20	1.00	2.13	124.23	0.00	1.30E+03	0.65	0.38	1.17	0.77	0.39	1.15	1.18	0.47
62	0.30	1.00	2.18	129.95	0.04	1.95E+03	0.58	0.58	1.15	0.57	0.57	1.15	0.99	0.46
66	0.40	1.00	4.04	117.05	0.11	2.60E+03	0.54	0.42	1.06	0.78	0.41	0.93	1.44	0.25
68	0.43	1.00	4.11	119.15	0.15	2.77E+03	0.55	0.43	1.64	0.82	0.43	0.91	1.49	0.24
67	0.45	1.00	3.66	119.45	0.16	2.92E+03	0.51	0.51	1.01	0.51	0.51	0.87	1.00	0.27
65	0.50	1.00	3.98	114.79	0.27	3.25E+03	0.52	0.52	1.05	0.52	0.52	1.05	1.00	0.25
64	0.60	1.00	4.43	113.91	0.42	3.89E+03	1.12	0.56	1.68	1.12	0.56	1.68	1.00	0.23
63	0.70	1.00	4.75	132.51	0.67	4.55E+03	1.22	0.61	1.22	1.22	0.61	1.84	1.00	0.21
69	0.80	1.00	4.87	120.54	0.90	5.19E+03	0.68	0.68	1.36	0.68	0.68	2.70	1.00	0.21
70	0.90	1.00	4.94	120.28	1.27	5.83E+03	1.52	0.76	1.52	0.75	0.75	3.02	0.50	0.20

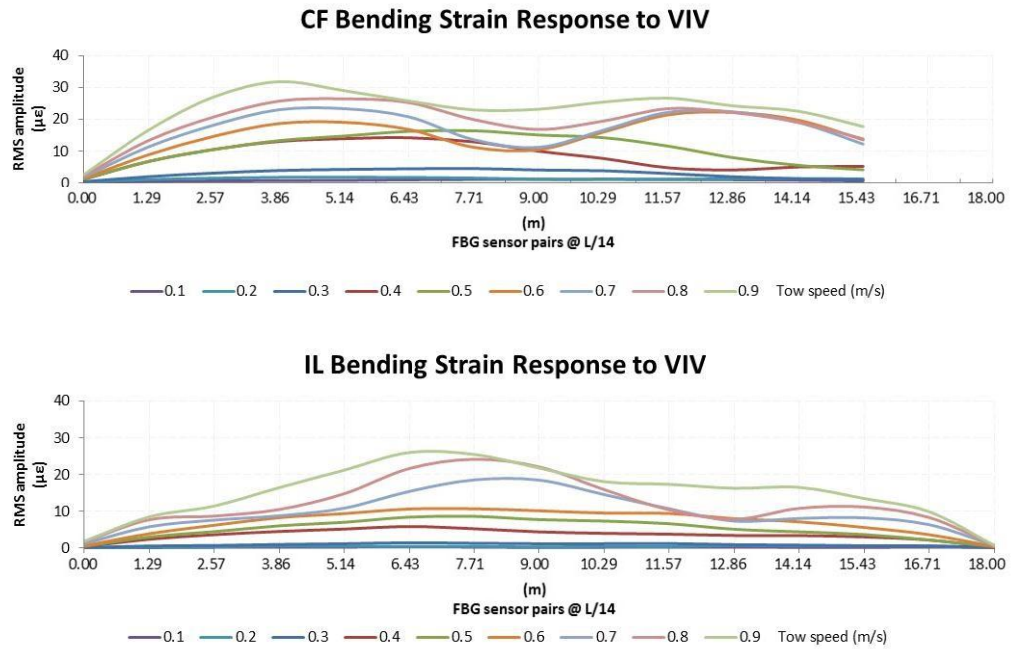


Figure 6.25 Bending strain responses due to current flow alone, tow depth = 0.42 m (10 OD)

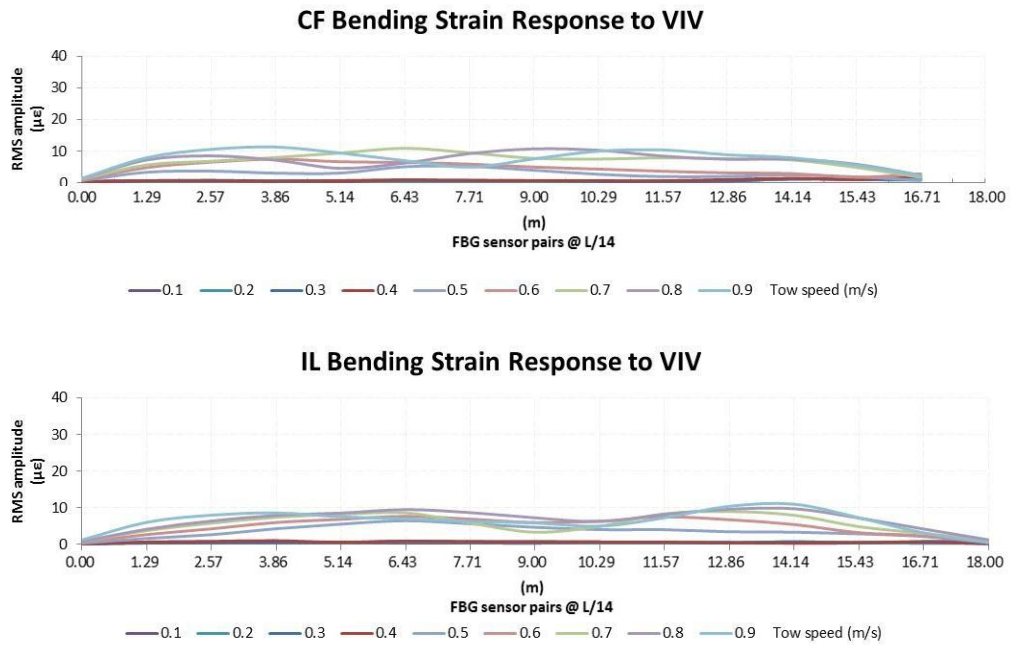


Figure 6.26 Bending strain responses due to current flow alone, tow depth = 0.0 m (free surface, 0 OD)

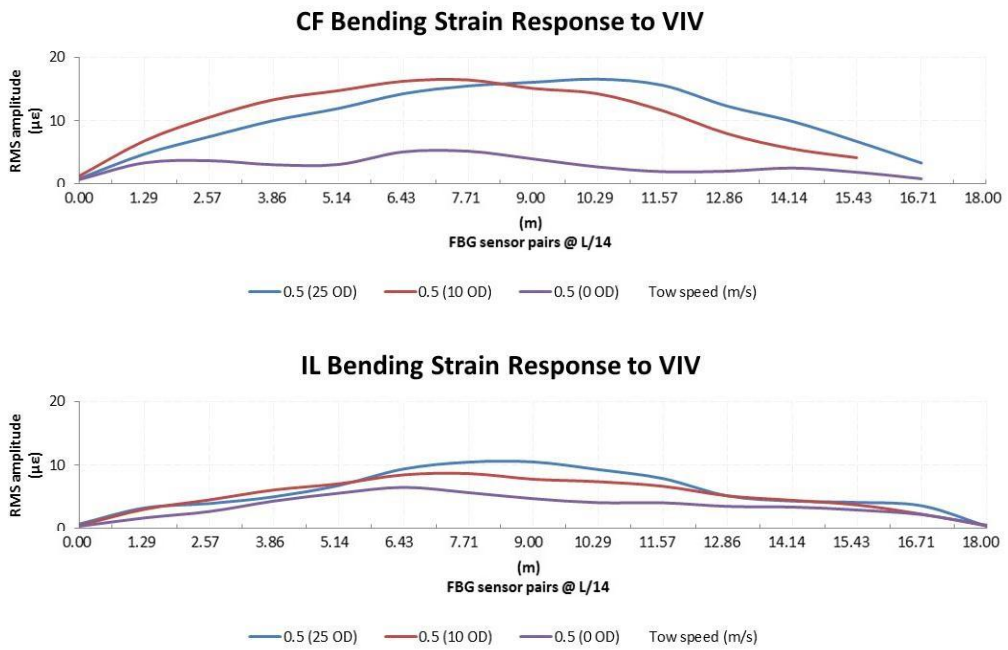


Figure 6.27 Bending strain responses due to current flow alone, tow depth effects at 0.5 m/s.

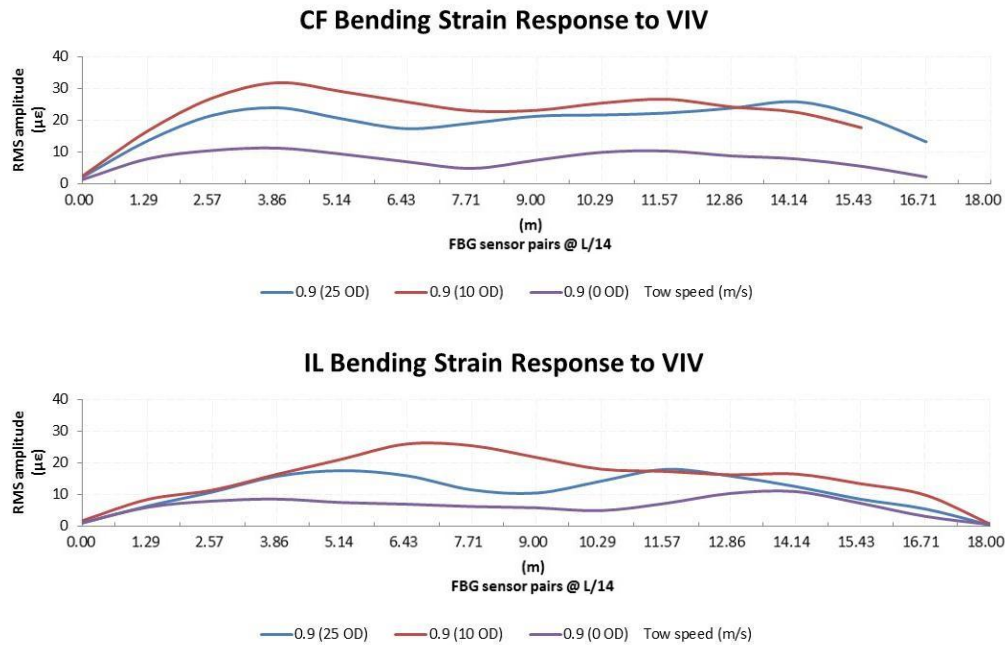


Figure 6.28 Bending strain responses due to current flow alone, tow depth effects at 0.9 m/s.

From results in tables 6.15 and 6.16 and figs. 6.25, 6.26, 6.27 and 6.28, the findings for the test conditions with change in tow depth were:

- (a) The results in tables 6.4, 6.15 and 6.16, showed that generally the CF and IL frequency responses and Strouhal number increases as the tow depth decreases, with the consequent reduction in reduced velocities for the same towing speeds as the model is tested at tow depths approaching the free surface.
- (b) The time varying bending strains also showed a general decrease in response amplitudes as the tow depth approaches the free surface, with one exception for the maximum speed in test no. 43, where the response was higher when reducing the tow depth from 25 OD to 10 OD (see fig. 6.25).

### 6.2.13 Tow depth change to 10 OD and 0 OD for current flow plus wave no.1

The effects of the proximity to the free surface were also tested, considering the conditions of section 6.2.2 by changing depths to 10 OD and 0 OD.

Table 6.17 Current flow plus wave no. 1, tow depth = 0.42 m (10 OD)



Test No.	Tow speed (m/s)	Enc. freq. (Hz)	Wave freq. (Hz)	$\alpha$	Ur	Initial Tension (N)	Fd (N/m)	Re	KC min	KC max	Uk	Uk/KC range	
46	0.10	0.60	0.58	0.38	0.69	119.02	0.05	1.72E+03	0.68	1.17	0.69	1.02	0.59
47	0.20	0.62	0.58	0.56	1.34	119.22	0.11	2.31E+03	0.64	1.11	1.33	2.06	1.20
48	0.30	0.64	0.58	0.67	1.91	119.20	0.21	2.91E+03	0.62	1.06	1.92	3.12	1.81
49	0.40	0.67	0.58	0.72	2.51	120.33	0.33	3.61E+03	0.64	1.11	2.49	3.86	2.24
50	0.50	0.69	0.58	0.76	3.00	121.09	0.46	4.26E+03	0.65	1.12	3.01	4.64	2.69
51	0.60	0.71	0.58	0.78	3.49	120.99	0.60	4.97E+03	0.69	1.18	3.49	5.08	2.94
52	0.70	0.73	0.58	0.81	4.60	121.66	0.78	5.62E+03	0.68	1.18	3.96	5.79	3.35
53	0.80	0.75	0.58	0.84	5.09	121.16	0.97	6.21E+03	0.65	1.12	4.40	6.75	3.91
54	0.90	0.77	0.58	0.85	5.81	121.18	1.46	6.84E+03	0.64	1.11	4.80	7.51	4.34

(continued)

Test No.	IL freq. response			CF freq. reponse			CF/IL Dom.	St
	Dom. (Hz)	Low. (Hz)	High. (Hz)	Dom. (Hz)	1 x (Hz)	High. (Hz)		
46	1.20	0.58	1.20	0.60	0.60	1.20	0.50	0.55
47	1.20	0.59	1.20	0.62	0.62	1.20	0.52	0.42
48	1.18	1.18	1.30	0.65	0.65	0.65	0.55	0.35
49	0.96	0.66	2.32	0.66	0.66	0.66	0.69	0.29
50	1.38	0.69	1.38	0.69	0.69	1.37	0.50	0.25
51	1.41	0.71	1.41	0.71	0.71	1.37	0.50	0.22
52	1.08	1.08	1.40	0.73	0.63	1.46	0.68	0.18
53	1.46	0.65	1.46	0.77	0.65	0.77	0.53	0.16
54	1.27	1.27	1.27	0.64	0.64	1.90	0.50	0.15

**Table 6.18 Current flow plus wave no. 1, tow depth = 0.00 m (free surface, 0 OD)**

Test No.	Tow speed (m/s)	Enc. freq. (Hz)	Wave freq. (Hz)	$\alpha$	Ur	Initial Tension (N)	Fd (N/m)	Re	KC min	KC max	Uk	Uk/KC range	
73	0.10	0.60	0.58	0.37	0.69	116.93	0.02	1.78E+03	1.24	1.24	0.69	0.56	0.56
76	0.20	0.62	0.58	0.55	1.33	105.29	0.13	2.36E+03	1.17	1.17	1.33	1.14	1.14
77	0.30	0.65	0.58	0.65	1.91	112.28	0.23	2.99E+03	1.15	1.15	1.92	1.68	1.68
78	0.40	0.67	0.58	0.71	2.47	115.01	0.43	3.68E+03	1.19	1.19	2.49	2.08	2.08
79	0.50	0.69	0.58	0.74	3.00	116.93	0.66	4.36E+03	1.23	1.23	3.01	2.45	2.45
80	0.60	0.71	0.58	0.78	3.49	119.81	0.82	5.00E+03	1.23	1.23	3.49	2.84	2.84

(continued)

Test No.	IL freq. response			CF freq. reponse			CF/IL Dom.	St
	Dom. (Hz)	Low. (Hz)	High. (Hz)	Dom. (Hz)	1 x (Hz)	High. (Hz)		
73	1.20	0.60	2.40	0.60	0.60	1.20	0.50	0.53
76	1.87	0.62	2.49	0.62	0.62	1.87	0.33	0.41
77	1.94	0.64	2.59	0.65	0.65	2.58	0.34	0.34
78	1.33	0.64	1.33	0.67	0.67	0.67	0.50	0.29
79	1.37	0.69	2.75	0.69	0.69	2.75	0.50	0.25

80	1.41	0.71	2.84	0.71	0.71	2.84	0.50	0.22
----	------	------	------	------	------	------	------	------

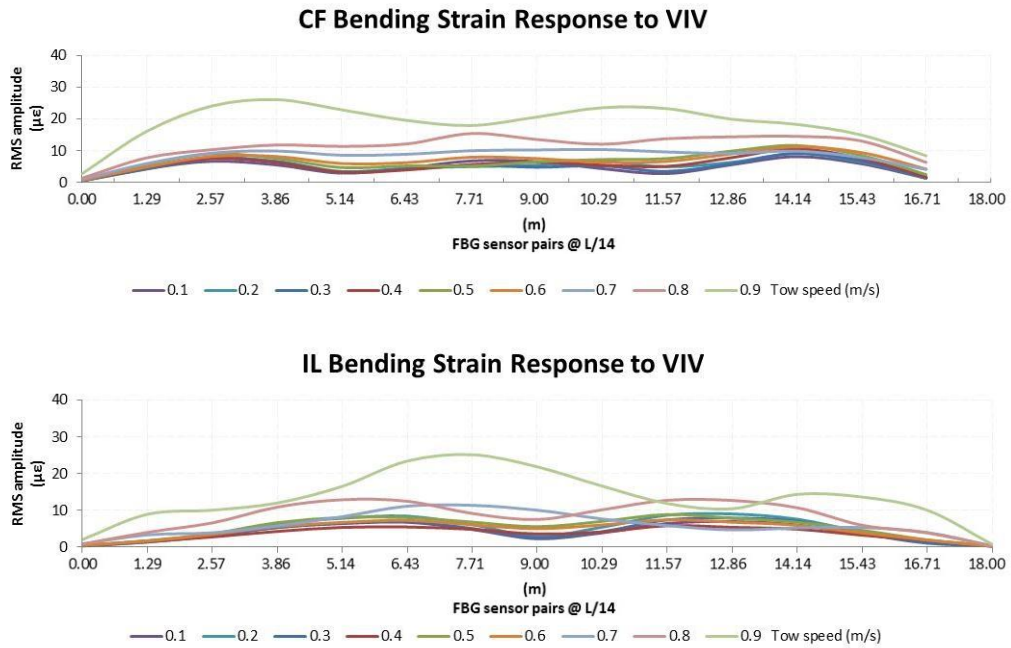


Figure 6.29 Bending strain responses due to current flow plus wave no. 1, tow depth = 0.42 m (10 OD)

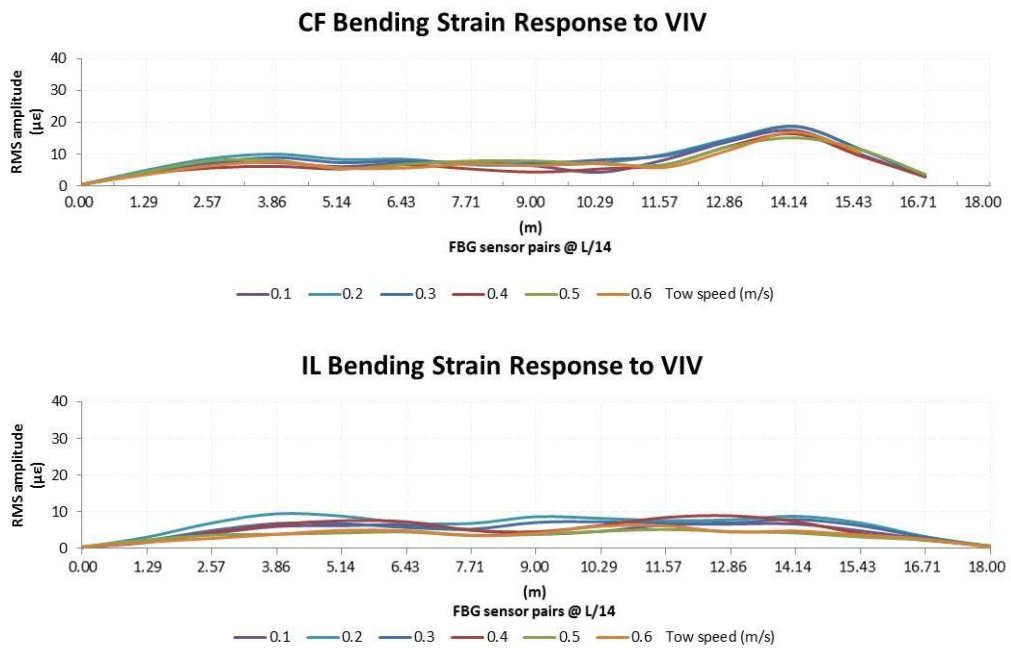


Figure 6.30 Bending strain responses due to current flow plus wave no. 1, tow depth = 0.0 m (free surface, 0 OD)

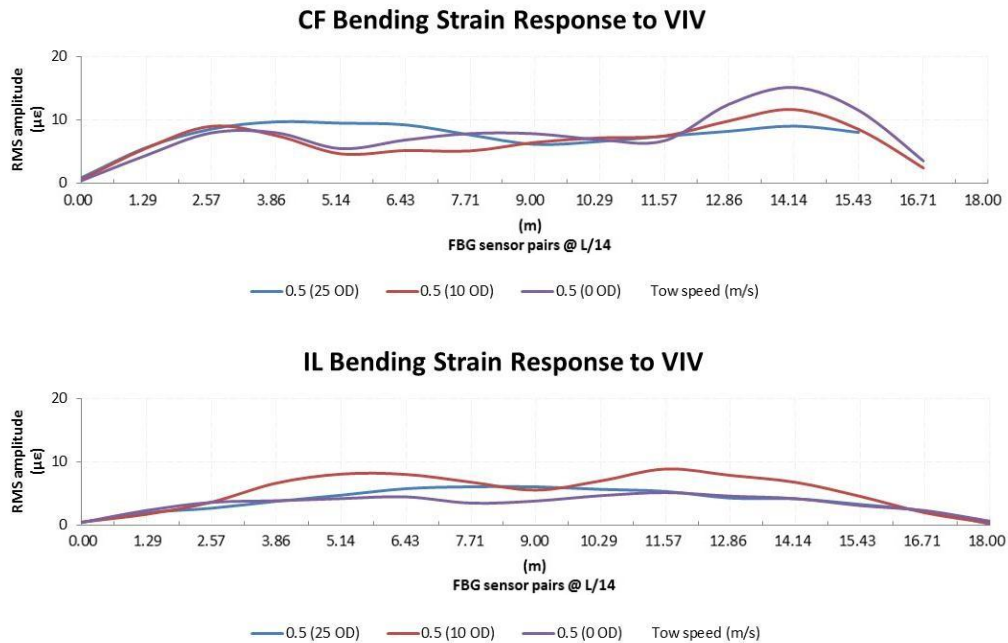


Figure 6.31 Bending strain responses due to current flow plus wave no.1, tow depth effects at 0.5 m/s.

From results in tables 6.17, 6.18 and figs. 6.29, 6.30 and 6.31, the findings for this test conditions with change in tow depth were:

- (a) The results in tables 6.5, 6.17 and 6.18 confirm that the dominant CF frequency response will shift to the encounter wave frequency in the cylinder when  $\alpha_c$  reach values lower than 0.85 as the tow depth decreases.
- (b)  $St$  for tests with  $Ur > 5.0$  showed similar values from 25 OD to 10 OD tow depths (tests 53 and 54 vs. tests 31 and 32).
- (c) The time varying bending strains also showed a decrease in response amplitudes as the cylinder depth approaches the free surface, where the wave flow dominated the responses, being the current flow component of little influence in the response at the free surface condition.
- (d) A zone of high bending strain responses about the FBG sensors location no. 4 ( $L = 14.14$  m) was persistent in the CF direction for the free surface condition at any tow speed (see fig. 6.30a). It was verified that this was also experienced in wave flow

only conditions. A probable cause of this high CF response zone could be explained by the different lateral stiffness respect to the lead-end support conditions (see figs. 5.14, 5.15 and section 5.8) and by a range of encounter wave frequencies close to the third natural mode of the model.

### 6.2.14 Tow depth change to 10 OD and 0 OD for current flow plus wave no.2

In the same way, the effects of the approximation to the free surface were tested, considering the conditions of section 6.2.3, but changing depths to 10 OD and 0 OD.

**Table 6.19 Current flow plus wave no. 2, tow depth = 0.42 m (10 OD)**

Test No.	Tow speed (m/s)	Enc. freq. (Hz)	Wave freq. (Hz)	$\alpha_c$	Ur	Initial Tension (N)	Fd (N/m)	Re	KC min	KC max	Uk	Uk/KC range	
55	0.10	0.47	0.46	0.24	0.89	122.32	0.08	2.70E+03	2.01	2.84	0.88	0.44	0.31
57	0.30	0.50	0.46	0.48	2.48	115.88	0.36	4.02E+03	2.03	2.88	2.47	1.22	0.86
56	0.50	0.53	0.46	0.61	3.83	121.08	0.66	5.29E+03	2.01	2.84	3.91	1.95	1.38
58	0.70	0.56	0.46	0.70	5.18	115.45	1.01	6.52E+03	1.94	2.74	5.19	2.67	1.89

(continued)

Test No.	IL freq. response			CF freq. reponse			CF/IL Dom.	St
	Dom. (Hz)	Low. (Hz)	High. (Hz)	Dom. (Hz)	1 x (Hz)	High. (Hz)		
55	0.92	0.45	0.92	0.47	0.47	0.47	0.51	0.27
57	0.94	0.50	1.45	0.50	0.50	0.50	0.53	0.19
56	0.95	0.88	1.42	0.54	0.54	0.54	0.57	0.16
58	1.47	0.78	1.47	0.56	0.56	1.63	0.38	0.13

**Table 6.20 Current flow plus wave no. 2, tow depth = 0.00 m (free surface, 0 OD)**

Test No.	Tow speed (m/s)	Enc. freq. (Hz)	Wave freq. (Hz)	$\alpha_c$	Ur	Initial Tension (N)	Fd (N/m)	Re	KC min	KC max	Uk	Uk/KC range	
81	0.10	0.47	0.46	0.23	0.89	120.49	0.12	2.78E+03	2.95	2.95	0.88	0.30	0.30
82	0.30	0.50	0.46	0.48	2.48	124.34	0.41	4.07E+03	2.94	2.94	2.47	0.84	0.84
83	0.50	0.53	0.46	0.61	3.90	127.13	0.82	5.32E+03	2.87	2.87	3.90	1.36	1.36

(continued)

Test No.	IL freq. response			CF freq. reponse			CF/IL Dom.	St
	Dom. (Hz)	Low. (Hz)	High. (Hz)	Dom. (Hz)	1 x (Hz)	High. (Hz)		
81	0.47	0.47	0.95	0.47	0.47	0.95	1.00	0.27
82	0.50	0.50	0.93	0.50	0.50	1.00	1.00	0.19

83	0.53	0.53	1.59	0.53	0.53	1.05	1.00	0.16
----	------	------	------	------	------	------	------	------

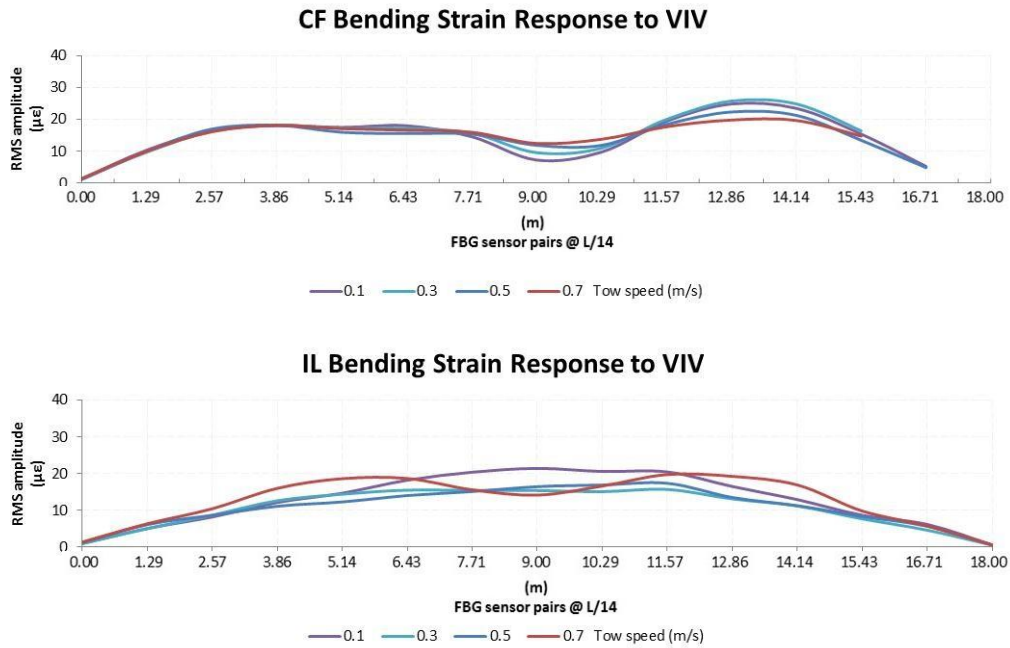


Figure 6.32 Bending strain responses due to current flow plus wave no. 2, tow depth = 0.42 m (10 OD)

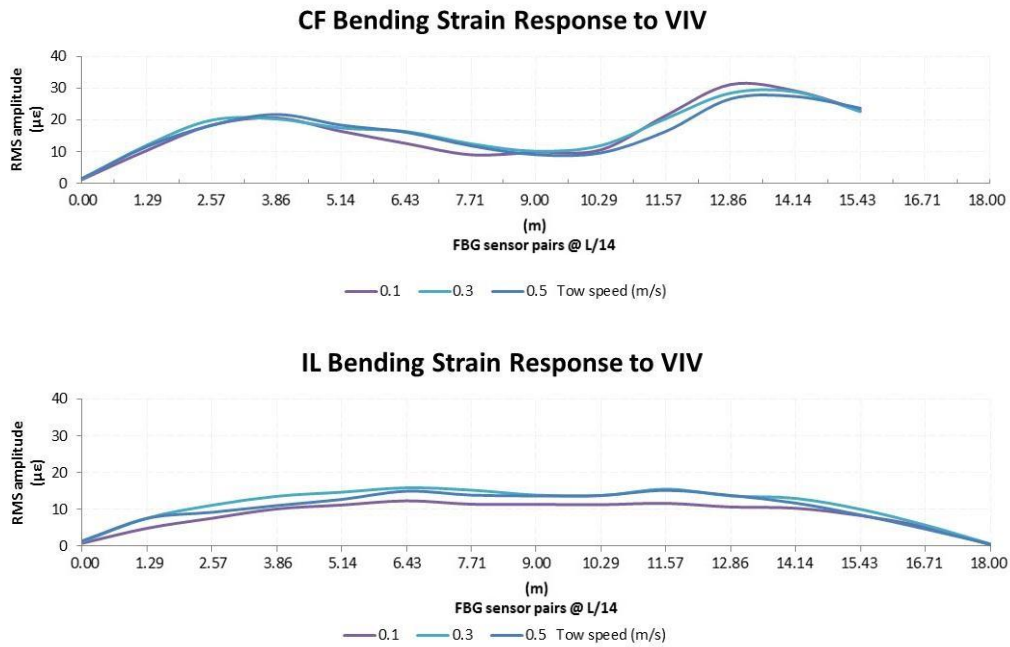


Figure 6.33 Bending strain responses due to current flow plus wave no. 2, tow depth = 0.0 m (free surface, 0 OD)

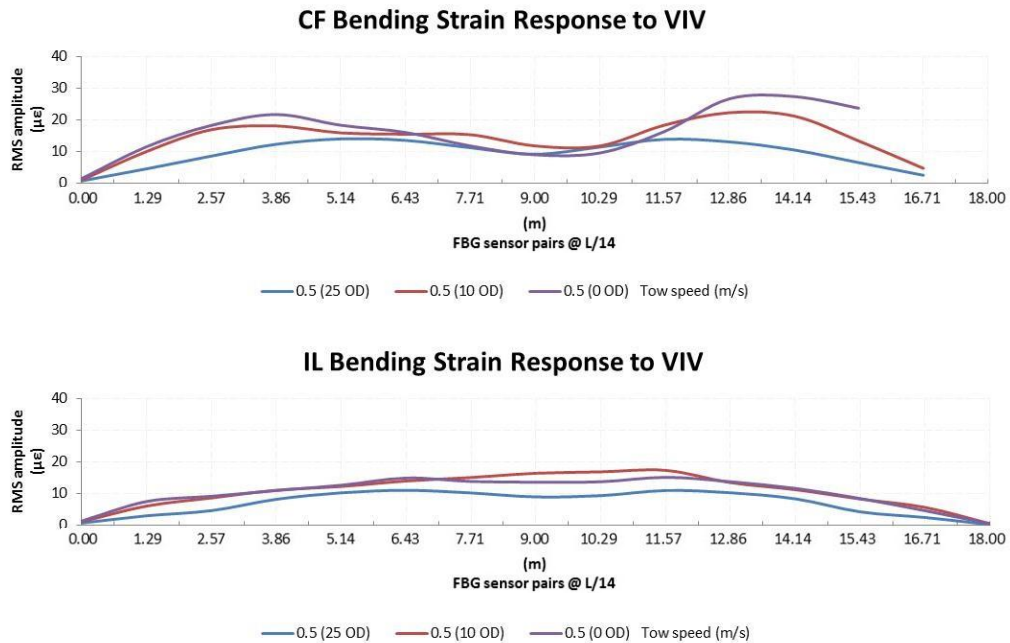


Figure 6.34 Bending strain responses due to current flow plus wave no.2, tow depth effects at 0.5 m/s.

From results in tables 6.19, 6.20 and figs. 6.32, 6.33 and 6.34, the findings for this test conditions with change in tow depth were:

- (a) Results in tables 6.5, 6.19 and 6.20, showed again the dominant CF frequency responses dominated by the encounter wave frequency while the current flow velocity ratio  $\alpha_c$  is lower than a value of 0.85.
- (b) For the Strouhal number, the tests showed decreased results from 25 OD to 10 and 0 OD, although they showed similar values at 10 and 0 OD tow depths within the towing speed tested. Reduced velocities also showed similar values with a very small increment as the tow depth change from 25 OD to the free surface.
- (c) The time varying bending strains showed an increase in response amplitudes as the tow depth approaches the free surface (see fig. 6.34), where the wave flow showed more dominance in responses than tests with wave no. 1

- (d) The zone with larger CF responses about FBG sensors nos. 4-5 in fig. 6.32 and 6.33, showed a tendency to vanish as the encounter wave frequency and tension increases with the current flow speed.

## 6.2.15 General remarks of tests results

### Current flow alone (depth 25 OD)

- At the lowest towing speed, the 1 x CF and dominant IL frequency responses were close to the fundamental frequency found in still water.
- The first peak or 1 x CF frequency was the dominant CF frequency when the reduced velocity was within typical lock-in range ( $5 < Ur < 8$ ), with the Strouhal number  $St$  decreasing from 0.19 to 0.13 for the first mode of vibration, from 0.18 to 0.17 for the second and a value of 0.16 in the third mode.

### Current plus wave flows (depth 25 OD)

The combinations of wave flow forces and current flows showed that the encounter wave frequency experienced by the cylinder at low speeds becomes the dominant CF frequency response, and this influence expands to higher speeds as the wave flow increases. In general, it was found that the encounter wave frequency sets the dominant CF frequency when the current flow velocity ratio was lower than a value of 0.84 ( $\alpha_c < 0.84$ ).

For time varying bending strains, the results showed that the wave flow forces increased the amplitudes at low speeds with respect to responses with current flow alone, but then the effect is reversed, showing decreased values in most cases when  $Ur > 5.0$  (fig. 6.35c); the effects on the estimated equivalent mean drag force per unit length is shown in fig. 6.36.

With wave no. 1

- 1 x CF frequency was the dominant CF frequency for all the tests in the series.

- The encounter wave frequency was the dominant CF frequency only for tests at low tow speed and below typical lock-in range frequencies ( $U_r < 5$ ). Within lock-in range,  $St$  was varying from 0.15 to 0.17.

With wave no. 2

- The wave encounter frequency established the dominant CF frequency or the 1 x CF frequency.
- Time varying bending strains were greater than those subject to wave no. 1, until vortex shedding at  $U_r > 5.0$  caused lower amplitude responses.
- At  $U_r > 5.0$ ,  $St$  presented lower values than those of the wave no. 1, with a range from 0.15 to 0.14.

With wave no. 3

- The wave encounter frequency established the dominant CF frequency.
- Bending strains were dominated by the wave flow inertia, regardless the change in the tow speed up to  $U_r = 5.3$  during the test.



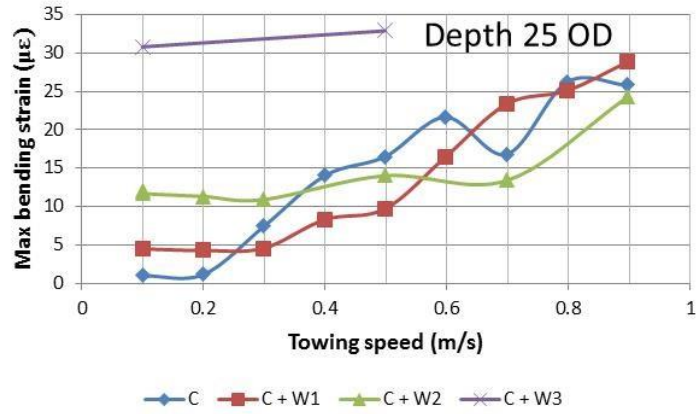
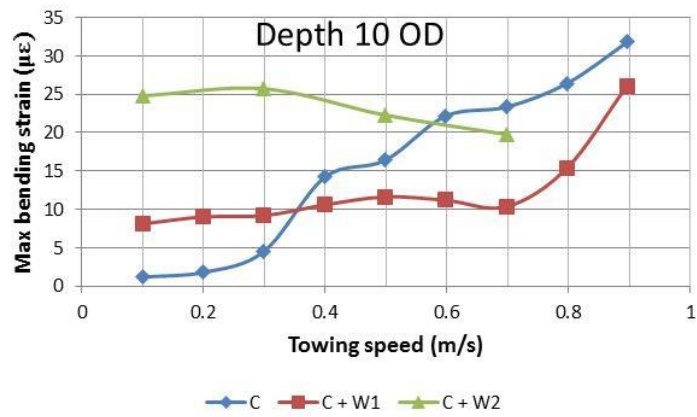
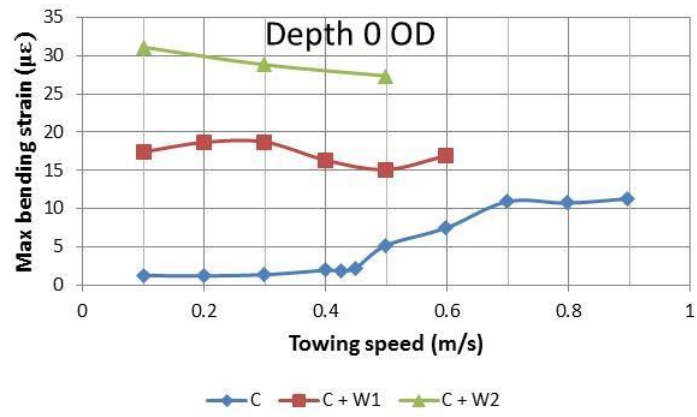


Figure 6.35 Effect of waves on maximum bending strain responses due to VIV and wave forces.

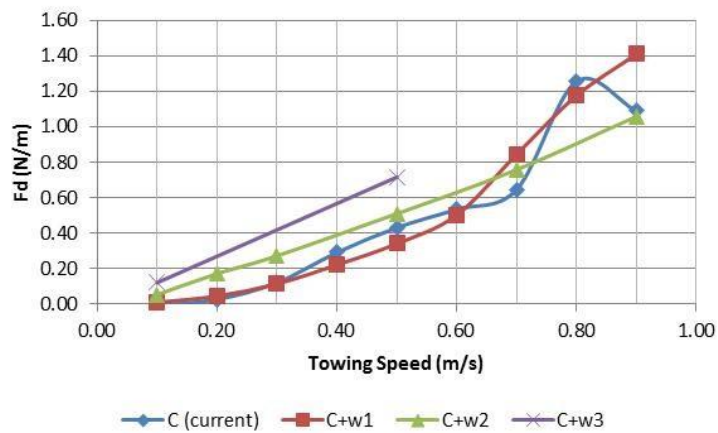


Figure 6.36 Approximation of mean drag forces per unit length at 25 OD in different test conditions.

### Increment of initial tension for Current plus wave flows (tow depth 25 OD)

The frequency responses showed expected increments according to the higher initial tension and in agreement with the increasing fundamental mode as calculated in table 5.7 for a range of tensions; however, it was noted that some results showed similar time varying bending strain responses at different conditions, this motivated that a few tests were repeated at the maximum towing speed of 0.9 m/s, which then showed different responses in dynamic tensions and time varying bending strain.

After comparison of data, it was found that both, dynamic tensions and time varying bending strains can experience an important reduction, of about 45%, during repeated tests; the higher responses occur when the typical 2 x IL frequency was dominant with some harmonics components as 4 x or small components of the CF peak frequencies.

Some tests presented IL responses where the dominant IL frequency shifted from the typical 2 x to about twice the encounter wave frequency, even when the corresponding encounter wave frequency showed weak peaks in the CF response spectrum.

In any case, the shift of the IL dominant frequency to a higher value than that of a 2 x frequency was related in the three cases of occurrence in tests nos. 113, 116 and 119, to the reduction of the response amplitudes for CF bending strains.

It was also of interest the fact that the more familiar VIV response with dominant IL frequencies at 2 x, led to very similar bending response amplitudes along the model for the maximum tow speed of 0.9 m/s but in different flow conditions, as in test no. 111 subject to current + induced turbulence, test no. 118 subject to current + wave1 and test no. 112 subject to current + wave1 + induced turbulence.

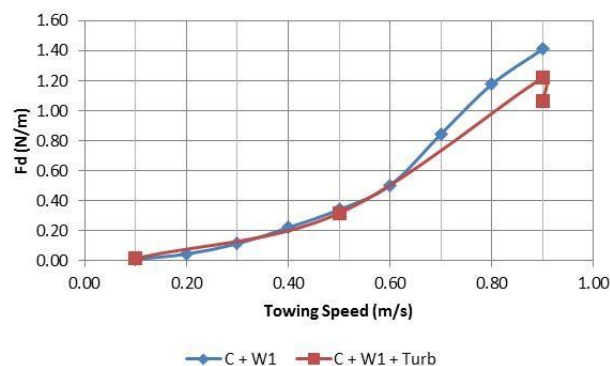
The behaviour reinforces the hypothesis of an upper-lower transition, where the flow velocity in the upper branch appears to be the dominant factor for time varying response amplitudes rather than the wave flow or induced turbulence indicated in the previous paragraph; hence it makes sense to set towing speeds below the initial-upper transition during design.

### Induced turbulence for current flow and current plus wave flows (tow depth 25 OD)

For turbulence with current flow, the tests results showed that there were not shifts to higher responses from the 2 x dominant IL frequencies; unlike the shifts experienced in tests nos. 11 and 15 without induced turbulence.

Current and wave flows showed similar behaviour as tests without induced turbulence, although a small increment in the frequency responses were observed.

For tests with current and wave flows subject to an increment of the initial tension, a similar behaviour was found again with respect to tests without induced turbulence, possible effects were restricted to a small decrease in bending strain amplitudes for wave1 and a small increase for wave2, which showed some coherence with the mean drag forces plotted in fig. 6.37.



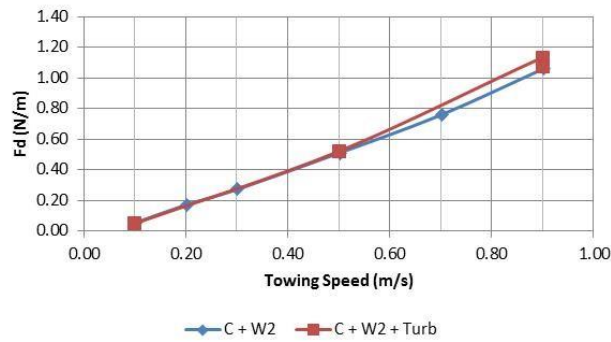


Figure 6.37 Effects of induced turbulence on drag forces for current + wave flows.

### Effects of the tow depth

#### Current flow alone

- It was found that frequency responses and Strouhal number increases as the tow depth decreases for the same towing speeds.
- The time varying bending strains experienced smaller amplitudes as the tow depth approached the free surface.
- At free surface (0 OD) the CF and IL dominant frequencies tends to match each other; for the cases where this do not occur, the match occurs for the first peaks of the CF and IL frequencies.
- The equivalent mean drag force per unit length showed lower values as the tow depth approached the free surface condition, the results also showed a large change in the slopes for 10 OD and 25 OD at 0.6 and 0.7 m/s respectively (see fig. 6.39a).

#### Current + wave no. 1

- Frequency responses and Strouhal number increases as the tow depth decreases as found for current flow alone, although the increased values of  $St$  were similar at 0 and 10 OD tow depths from the initial reference depth of 25 OD.
- The bending strain amplitudes also experienced reductions toward the free surface, where the current component was of little influence in the response at all speeds.

- Drag forces increase as tow depth decreases, although a change in the curve slope can be identified for tests at 25 OD above a speed of 0.6 m/s (fig. 6.39b), presenting higher drag forces than tests at 10 OD after a tow speed of about 0.65 m/s.

#### Current + wave no. 2

- The CF frequency response remained driven by the encounter wave frequency at all tow depths, where only the IL frequency response showed slight increments as the tow depth decreased.
- St presented similar values at 10 and 0 OD tow depths, although in both cases these were smaller values respect to results at 25 OD.
- Unlike the previous two conditions for current alone and current +wave no. 1, the higher dominance of the wave no. 2 led to higher bending strain amplitudes as the tow depth approached the free surface.
- The higher wave flow showed a clear increment of the drag forces as the tow depth approached the free surface.

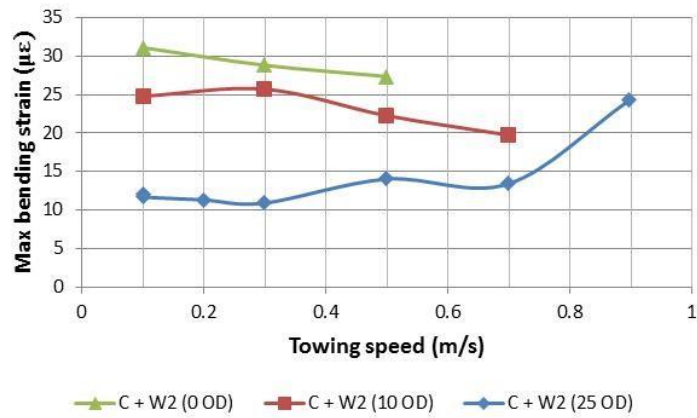
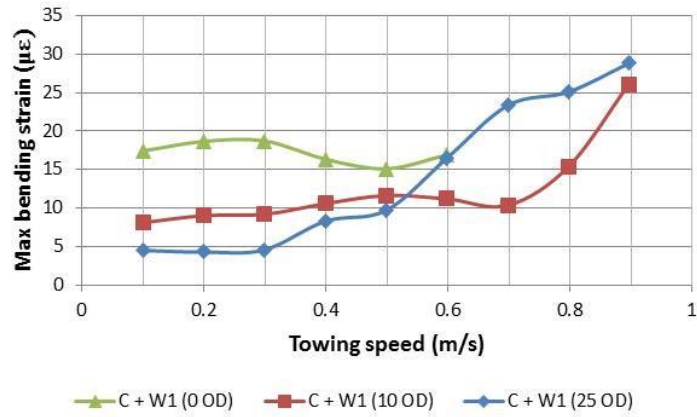
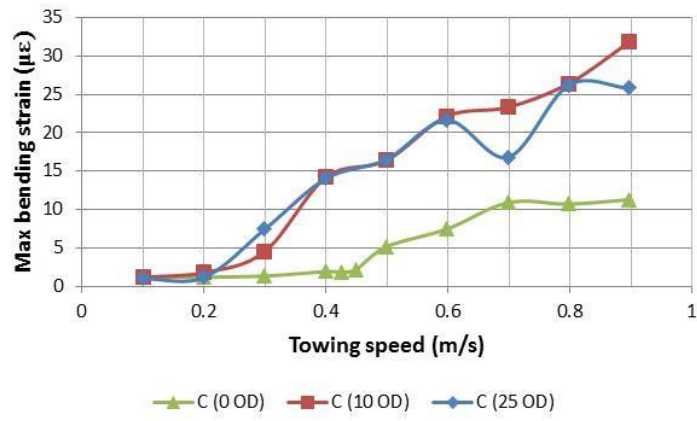
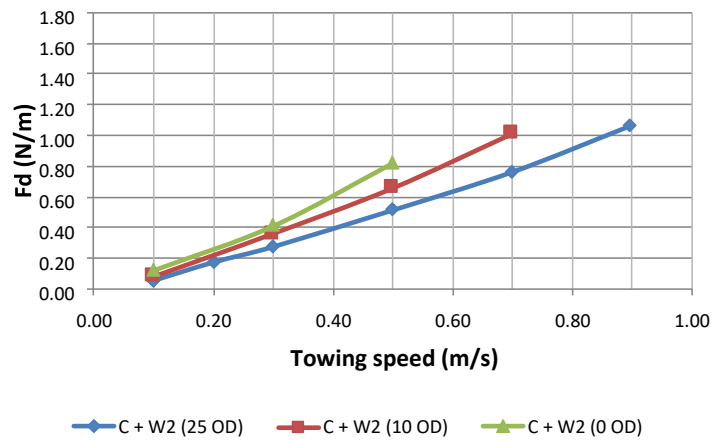
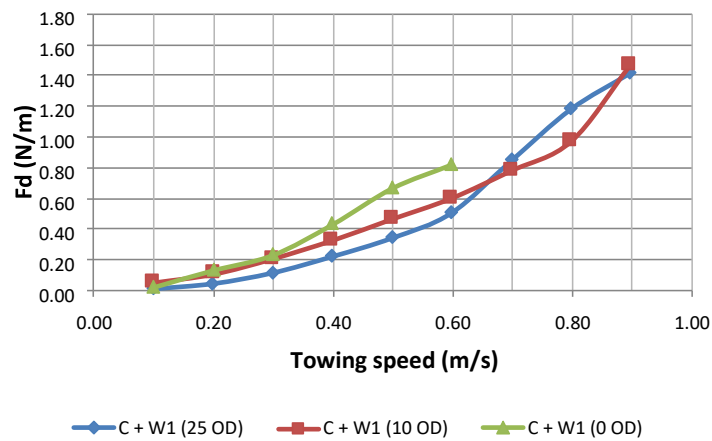
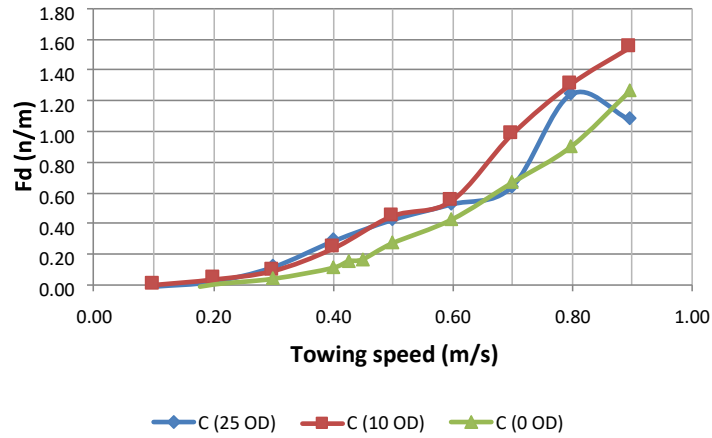


Figure 6.38 Tow depth effects on bending strain responses due to VIV and wave induced forces (current and current plus wave flows).

### Approximation of mean drag force per unit length

The effect of the tow depth of the riser model on the approximated mean drag force per unit length has been already described above for each flow condition tested, an insight of the behaviour is plotted in fig. 6.39, integrating results from all tables of section 6.2.



**Figure 6.39 Tow depth effects on approximated mean drag forces for current and current + wave flows.**

A feature of interest in previous plots is represented by large changes in the slopes of the curves at certain tow speeds (being identified about 0.6 and 0.7 m/s for current flows at 10 and 25 OD (fig. 6.39a), and 0.6 m/s for current + wave1 flow at 25 OD (fig. 6.39b) from which drag forces increase substantially their rate of change against the towing speed, probably associated with the transition zones between the initial and upper branches.

The identification of the towing speeds within soft slopes in the experimental results discussed above for current plus wave flows, are not far from the typical offshore maximum speeds mentioned in section 2.2 and their scaled quantity determined in section 5.10.1 of 0.51 m/s, which was considered to define the range of towing speeds for this experimental work.

Hence, it is considered that the experimental assessment of the branch transitions for responses under several representative conditions will be of value to assist the setting of maximum towing speeds during design, avoiding higher responses and tensions associated to the upper branch, providing benefits in the operational bollard pull capacity that the offshore tug arrangement can provide.

Keeping responses in the initial branch can help to design towing routes within acceptable levels of fatigue damage, considering that the drag force and corresponding drag coefficients represents one of the largest stochastic variables governing the uncertainty in fatigue damage to define safety factors, as indicated in section 6.3.5 of the offshore standard DNV-RP-F204 (2005).

## **6.2.16 Towing Tests Conclusions**

### **Current flow alone**

For the setup and conditions of the tests, current flows showed vortex induced vibrations with 1 x dominant frequency response in the cross-flow direction over the riser model, with odd harmonic components. For the in-line direction the response showed the typical 2 x



dominant frequency with even harmonic components, although weak even and odd peak components can be present in the response spectra for either CF or IL direction.

The Strouhal number “St” experimentally determined can be used to predict the range for the dominant frequency response during design. For  $U_r > 2.0$ , St presented a decreasing range as  $U_r$  increased during the first vibrational mode from 0.19 to 0.13, then St decreased from 0.18 to 0.17 for the second vibrational mode and a value of 0.16 for the third mode at the highest speed tested. The behaviour suggest that St could be approaching a value about 0.16 within lock-in conditions as the vibrational mode increases, although a riser model with a longer aspect ratio could be tested for verification of St values at higher vibrational modes.

There were some response characteristics that suggest an association with the initial-upper and upper-lower response branch transitions; as these transitions and the upper response branch are of large influence for high VIV response amplitudes and are sensitive to the test conditions, I recommend during design model testing to determine the towing speed range where the initial-upper transition occurs for different conditions. This will more reliably define a maximum towing speed to be used offshore.

As a reference, in our tests the response characteristics associated to an initial-upper transition was identified at a tow speed about 0.6 m/s (see fig. 6.39a), which can be compared to the typical maximum towing speed for offshore installations mentioned in section 5.10, corresponding to a scaled velocity in the towing tank of 0.51 m/s.

In the absence of wave flows, our results show that VIV response amplitudes and drag coefficients at the free surface and for all speeds are lower than those experienced in tests with the model submerged (see figs. 6.38a and 6.39a), thus a provision to perform a surface tow installation method should be considered by designers in installation manuals, considering a potential weather forecast for sea state conditions with small wave amplitudes.

### **Current plus regular wave flows**

In our tests with combinations of current and regular waves, we found that the current flow velocity ratio  $\alpha_c$  represents an important parameter to determine whether the response is dominated by vortex shedding or by inertia forces of the wave flow. Within our test

conditions at tow depth of 25 OD for the riser model, the cylinder frequency response was dominated by the encounter wave frequency for values of  $\alpha_c < 0.84$ ; otherwise, other vortex shedding frequencies than the wave encounter frequency becomes dominant.

Within lock-in range and for current flow velocity ratios about  $0.90 < \alpha_c < 0.84$ , the effect of waves on VIV was measured as a decreased response in bending strain amplitudes with a slight frequency increase in comparison to towing tests with current flow alone. For current flow velocity ratios larger than 0.90, the bending strain amplitudes and frequency responses were similar to the results for current flow alone.

For cases where the encounter wave frequency dominated the response at  $\alpha_c < 0.84$ , the effect of waves and VIV also showed a decrease in bending strain amplitudes in comparison with tests for current flow alone. The decrease was found at all towing speeds within typical lock-in range, except for the response to the wave no. 3 representing the extreme value case during towing for installation, where the strains were higher, and a deeper tow depth will be required to mitigate the wave forces.

### **Tow depth effects**

The change in tow depth for the riser model from 25 OD to 10 OD and from 25 OD to 0 OD at free surface, presented increased responses for maximum bending strain amplitudes during tests subject to current plus wave no. 2 (fig. 6.38c).

There was also an increased response in maximum bending strain amplitudes for current plus wave no.1 when changing from 25 OD to 0 OD, with the responses mainly driven by the wave induced forces with reduced velocities below typical lock-in range; conversely, the response showed lower bending strain amplitudes when changing from 25 OD to 10 OD for towing speeds within typical lock-in range (fig. 6.38b).

The previous behaviour was identified for maximum bending strains measured with the FOSS, and it was consistent with results shown in fig. 6.39b and fig. 6.39c for the approximated mean drag coefficients computed from load cell data according to section 5.12, which provides an indication of the effects of tow depth and current plus wave flows on drag forces within our test conditions.

In summary, the methodologies followed for the tests scope based on geometric parameters and environmental conditions of interest, allowed to identify maximum towing speeds below the characteristic response associated to a lower-upper transition of the VIV response branch about a speed of 0.5 m/s, which is about the maximum towing speed found in literature for offshore operations.

The measurement technologies implemented in the experimental tests, show the capability to provide hydrodynamic parameters to estimate the response frequencies and bending strains due to VIV and wave induced forces that can be scaled to assist response predictions for fatigue design and for calibration of present state of practice software models.

Further experimental work in ocean basin tanks with representative sea states/irregular waves, model materials for hydro-elastic similarity and additional combinations of the relative directions between current and waves and modelling of tensioning/support mechanism is recommended.

### 6.3 Integration of the FOSS, MOCAP and Load Cell data for motion response

Following the ideas of section 6.1.5, the methodology for the IL and CF motion response calculation is set for the representative tests of the first series in section 6.2.1 by integration and data processing of the fibre optic sensing system (FOSS), the motion capture system (MOCAP) and the load cell installed at the lead-end of the model.

As mentioned in section 5.7, for circular cylinders the bending strains are determined by the radius of the cylinder divided by the radius of curvature, i.e.  $\epsilon = \frac{r}{R}$ , so  $\Rightarrow$ , then the geometric projection of chords between FBG sensor location segments for deflected shapes in our test setup are obtained from bending strain data, using angles =

$\theta_{i-1,i} = \frac{2\epsilon_i R_i}{1 + \epsilon_i R_i}$ , with chords lengths given by  $L_{chord,i} = 2 R_i \sin(\frac{\theta_{i-1,i}}{2})$ .

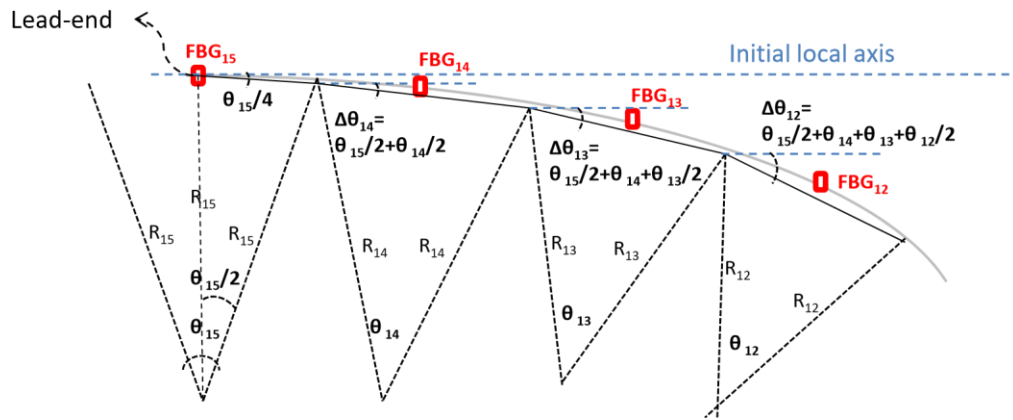


Figure 6.40 Chord projection angles from bending strain data

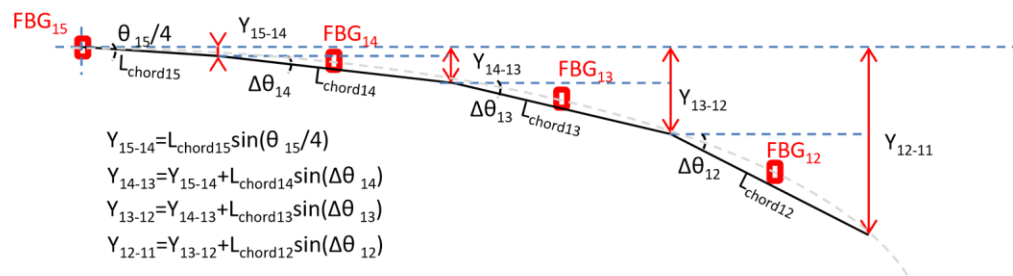


Figure 6.41 Deflected profile from chord projections

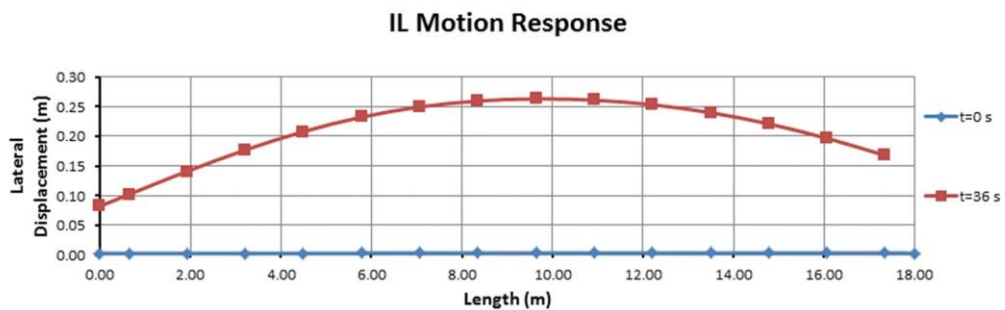
For IL direction, the geometric chord projection methodology to obtain the profile of deflected shapes from bending strain data in the FOSS is shown in fig. 6.40 and 6.41; it considers chord projections from the horizontal positive axis of the Cartesian coordinate system and an adjustment for the half chord of the curvature measured in the FBG sensor near the lead-end. These time varying deflected shapes will require a rotation according to measured positions with the MOCAP near the trail-end and calculated positions at the leadend from the load cell data.

The lead-end positions were calculated by solving the departure angles from the IL components of the tensions measured at the load cell, and used to project the aluminium rod length connected to the riser model for the time varying positions.

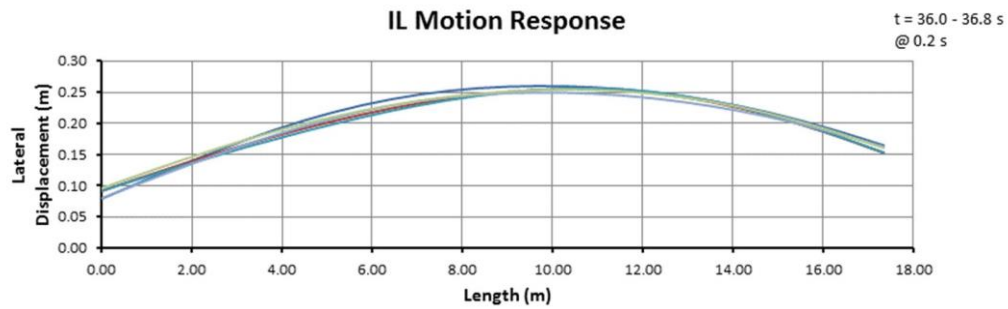
These calculated positions are neglecting the inertia effects of the aluminium rod in the measurements at the load cell, although the effect is expected to be small against the reaction forces measured at the load cell due to the hydrodynamic and inertia response of the riser model. This uncertainty could be experimentally assessed in future tests by comparing the calculations against measurements from the motion capture system with relocations of the underwater cameras for this purpose.

The lead-end positions were added to the time series data of deflected shapes, and then rotated (with a 2D rotation matrix) to fix the time varying position near the trail-end according to measurements performed with the MOCAP system.

The intersection of the horizontal plane and the axis of the initial position setup for the riser model (see fig. 5.13) is the axis of reference; the initial position at  $t=0$  s and the IL response for a selected time range is shown in fig. 6.42 for test no. 15.



a) Initial position at  $t=0$  s and deflected shape at  $t=36$  s.



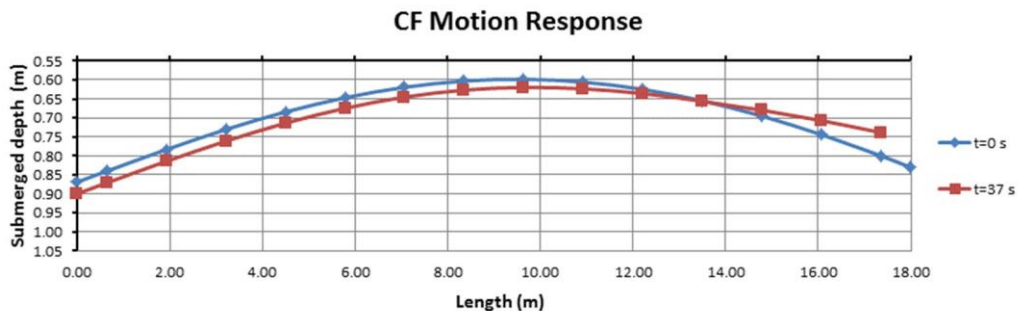
b) Motion response in a time interval

**Figure 6.42 IL Motion response**

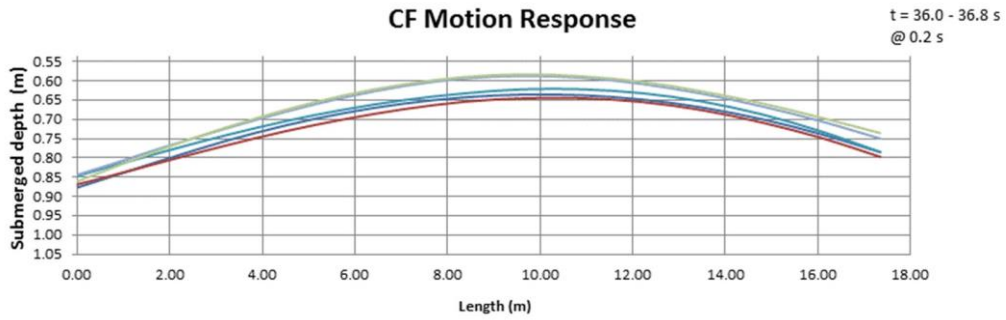
For CF direction, the initial upward deflection of the model was considered using the vertical bending moment distribution along the axis of the riser model, which was obtained from the finite element analysis results mentioned in section 5.8, the curvature distribution was computed dividing the bending moment distribution by the bending stiffness  $EI$  and used as starting values in the time series data of the FOSS.

The angle of variation between each FBG sensor location points and chord projections were then processed as done for the IL direction, followed by the input of the vertical lead-end positions approximated from the load cell data, and the rotations of the deflected shapes to fix the vertical positions near the trail-end measured with the MOCAP system.

The intersection of the still water surface in the towing tank and the vertical plane for the initial position setup of the riser model (see fig. 5.14) is the axis of reference; the initial upward deflection at  $t=0$  s and the CF response for a selected time range is shown in fig. 6.43 for test no. 15.



a) Initial position at  $t=0$  s and deflected shape at  $t=37$  s.

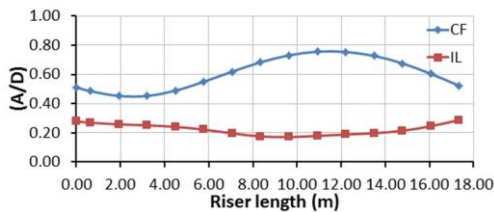


b) Motion response in a time interval

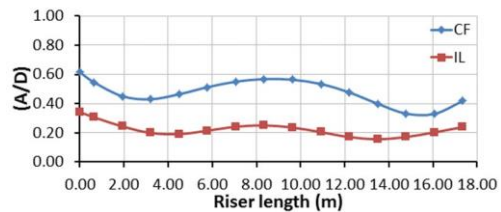
Figure 6.43 CF Motion response

IL and CF motion response processed in the time series data can be analysed for trajectories and response amplitudes along the axis, the RMS amplitudes were analysed during the second half of each test, using the non-dimensional amplitude A/D shown in fig.

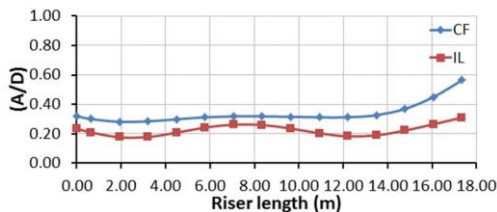
6.44 and summarised in table 6.21 with coefficients of interest from table 6.4.



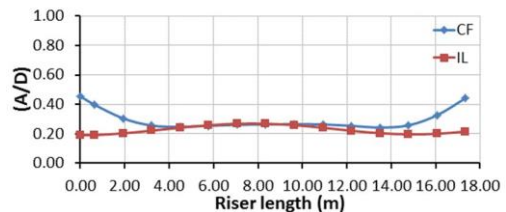
a) Test 15 (tow speed 0.9 m/s)



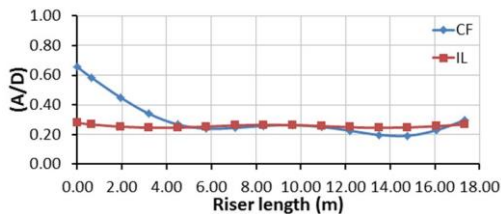
b) Test 14 (tow speed 0.8 m/s)



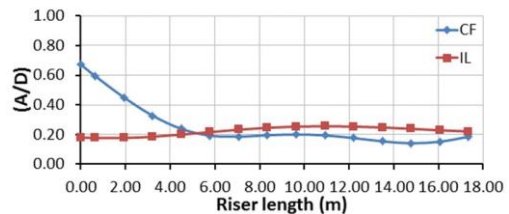
c) Test 13 (tow speed 0.7 m/s)



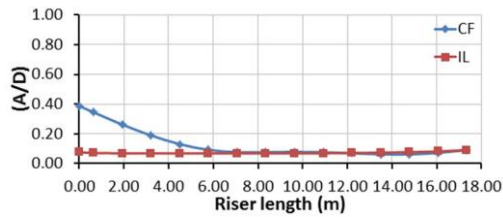
d) Test 12 (tow speed 0.6 m/s)



e) Test 11 (tow speed 0.5 m/s)



f) Test 19 (tow speed 0.4 m/s)



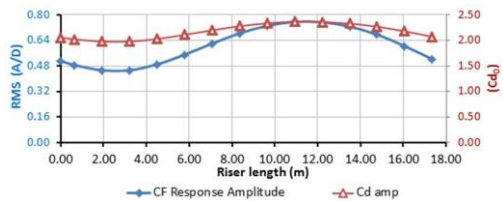
g) Test 18 (tow speed 0.3 m/s)

Figure 6.44 CF and IL RMS response amplitudes (A/D)

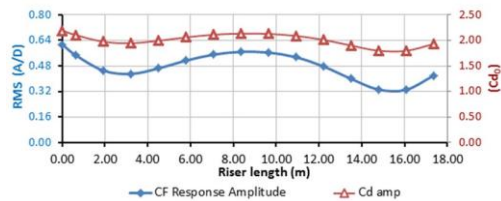
Table 6.21 RMS response amplitudes (A/D) and main parameters

Test No.	Tow Speed (m/s)	Initial Tension (N)	Re	Dom Freq		Ur		Cd <sub>amp</sub>		IL RMS Amplitude		CF RMS Amplitude	
				IL (Hz)	CF (Hz)	min	max	min (Cd <sub>0</sub> )	max (Cd <sub>0</sub> )	min (A/D)	max (A/D)	min (A/D)	max (A/D)
18	0.30	115.06	1.95E+03	0.46	0.23	4.88	5.08	1.27	1.88	0.07	0.09	0.06	0.39
19	0.40	114.08	2.60E+03	0.54	0.26	5.79	6.46	1.46	2.26	0.18	0.26	0.14	0.67
11	0.50	115.49	3.25E+03	0.81	0.27	6.10	7.26	1.56	2.24	0.25	0.28	0.19	0.66
12	0.60	115.66	3.89E+03	0.89	0.44	4.43	5.30	1.65	1.98	0.19	0.27	0.24	0.45
13	0.70	116.69	4.54E+03	1.00	0.49	4.43	5.63	1.72	2.13	0.18	0.31	0.28	0.56
14	0.80	115.50	5.19E+03	1.11	0.54	3.85	5.69	1.80	2.19	0.16	0.34	0.33	0.62
15	0.90	116.53	5.83E+03	1.52	0.61	4.28	6.02	1.98	2.37	0.17	0.29	0.45	0.76

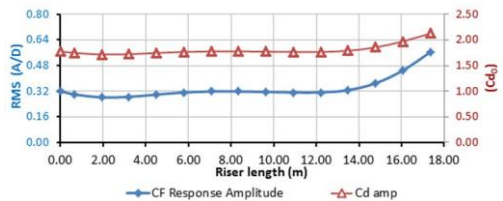
The drag amplification factors ( $C_{damp}$ ) in table 6.21 are based in the CF response amplitude A/D, using the well-known formulation proposed by Vandiver (1983) for predictions of drag coefficients and mentioned in section 5.12 as  $C_{damp} = 1 + 1.043 \frac{C_{d0}}{C_{d0} + C_{d0}}$ , with distributions along the riser length as shown in fig. 6.45.



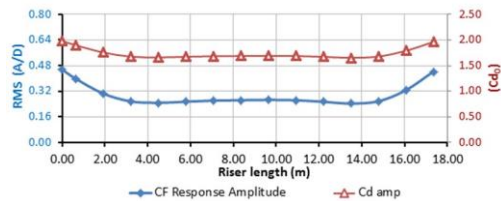
a) Test 15 (tow speed 0.9 m/s)



b) Test 14 (tow speed 0.8 m/s)



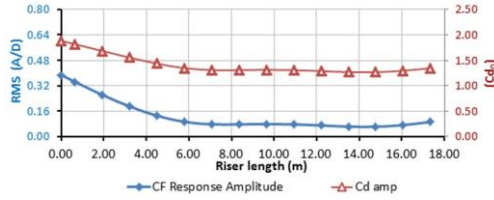
c) Test 13 (tow speed 0.7 m/s)



d) Test 12 (tow speed 0.6 m/s)



e) Test 11 (tow speed 0.5 m/s)

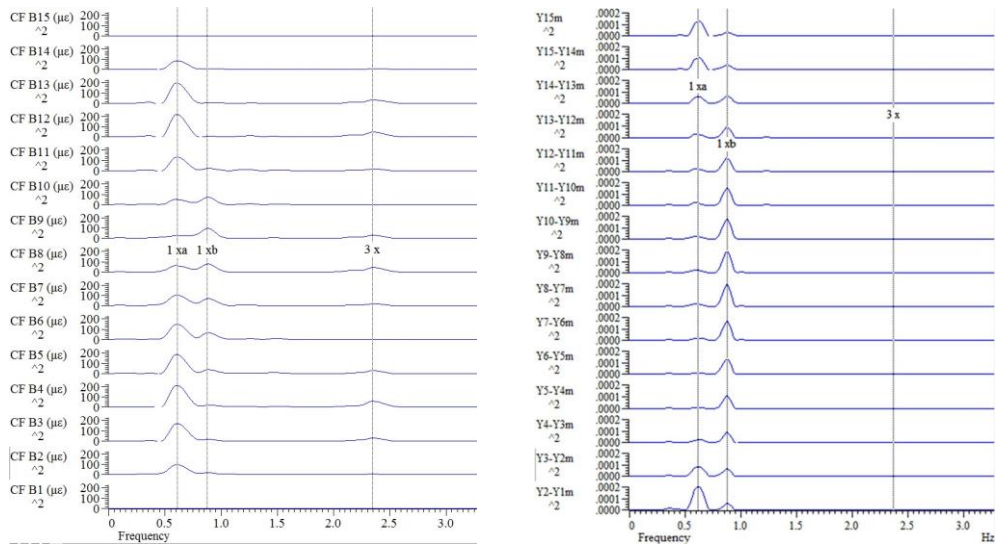


f) Test 19 (tow speed 0.4 m/s)

g) Test 18 (tow speed 0.3 m/s)

Figure 6.45 RMS Amplitude responses and drag coefficients

PSD analysis of the processed time series data for motion response showed the same frequency responses obtained from PSD of bending strain data, where harmonic responses are also identified, although spectral distribution differences are evident between bending strain and motion response, as showed in fig. 6.46 for PSD comparison of CF frequencies in test no. 15.



(a) CF direction from bending strain

(b) CF direction from motion response

Figure 6.46 PSD frequency peaks from the FOSS data, test No. 15.

The previous results shows differences between spectrum areas along the length and are indicative of differences in the locations of maximum amplitudes between bending strains and CF motion response, thus the bending strain amplitudes in fig. 6.1 were compared against motion response amplitudes along the riser length, with results shown in fig. 6.47.

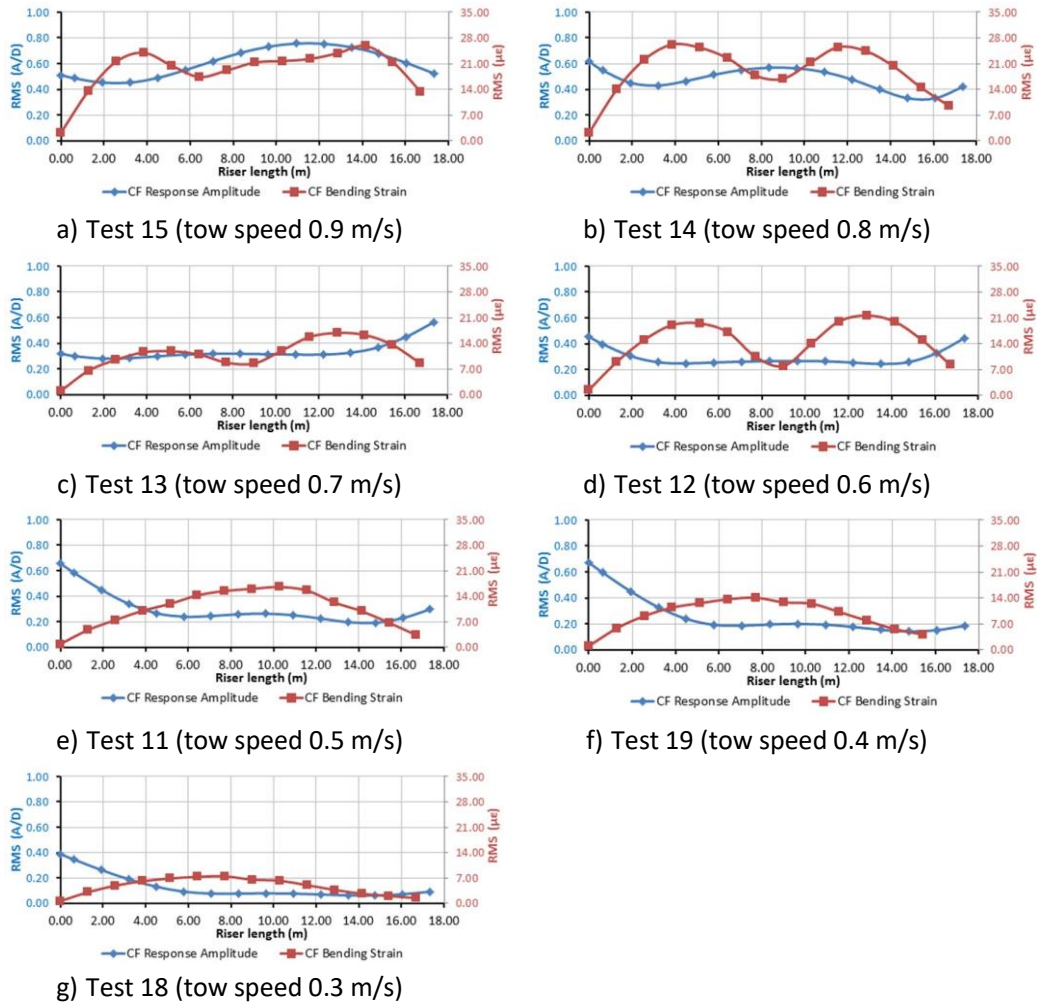


Figure 6.47 CF motion response against bending strain response

For our particular test setup at a large yaw angle, see table 5.5, the differences found between bending strains and motion response amplitudes along the riser length are of relevance for fatigue analysis, considering that the fatigue life during VIV of long slender cylinders is highly dependent on stress range cycles and the ratios between spectrum areas of the frequency responses along the cylinder, which will be addressed in the next chapter; nonetheless, the capability of the systems to evaluate the motion responses of long flexible cylinders in hydrodynamic testing is presented, with the methodologies that can be considered for further topics of research.

## 7 Fatigue damage design

### 7.1 Software tools

The procedures and methodologies for estimation of the overall fatigue damage, including VIV induced fatigue during riser design, were reviewed in section 2.4, according to relevant design codes, where guidance is provided for VIV fatigue analysis through state-of-practice software.

The availability of Orcaflex, one of the leading software packages for riser analysis and design, was explored for a few towing simulations to test some of the time domain VIV models.

The software requires setting load cases from simulations of several load conditions that the system can experience in its life time, thus, representative load conditions for towing routes can be defined to perform the fatigue damage analysis of tow-out operations for particular towing routes and environmental conditions, dividing the range of sea states in wave classes, where each wave class will require a simulation file.

Three types of analysis can be selected: a regular analysis for regular wave classes and corresponding simulations; a rain flow analysis for a set of random wave simulations; and a spectral analysis to calculate damage in frequency domain. The rain flow method is indicated as the most accurate but also the most time consuming, thus several recommendations are provided for selection of load cases and duration of random wave simulations in the software manual.

The damage is calculated at line end points and mid segment cross-sections of the line model, considering stress ranges results larger than the endurance limit over the response time history of each load case, and then scaled for the total exposure time of each representative load case.

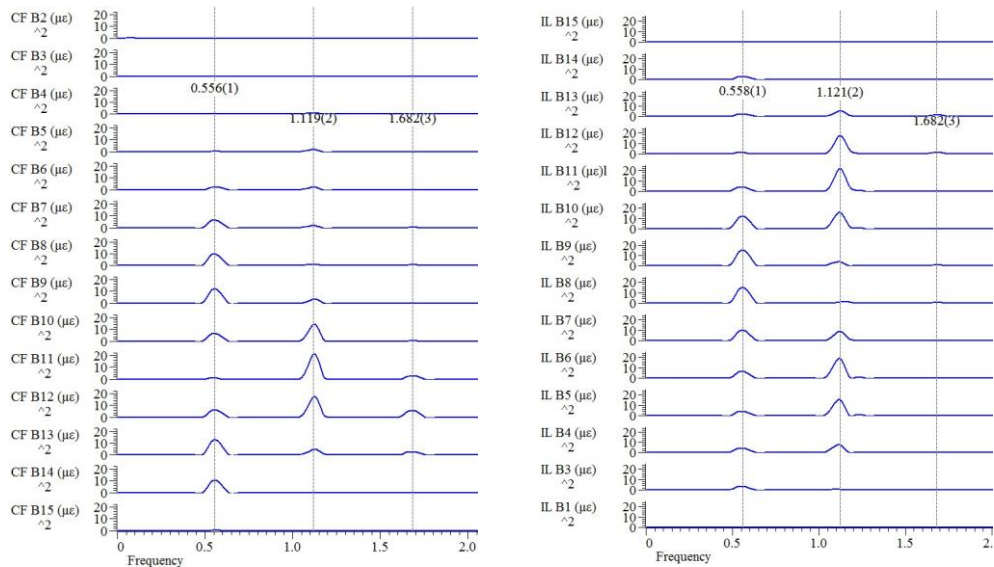
Alternatively, the software allows VIV induced fatigue damage to be computed externally, using the VIV frequency domain model in SHEAR7, as third-party software tool interface. Other riser analysis packages (e.g. FLEXCOM) also offers SHEAR7 interfaces to compute fatigue damage, although not tested within the scope and resources of this research.

## 7.2 Spectral fatigue analysis

Even when current VIV prediction tools and state of practice software have proven to predict well the VIV 1 x frequency response for riser analyses, neither of the harmonic responses nor their locations are included in the solutions based in current prediction models (Fontaine et al., 2011).

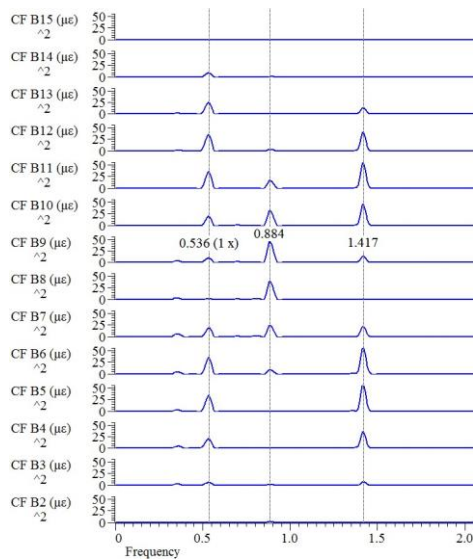
Our measurements in the riser towing tests and other referenced experiments previously mentioned, show that the response for long flexible cylinders contains higher harmonics, so energy is not solely concentrated about the Strouhal frequency associated to the 1 x frequency, i.e. the response is not narrow banded for the typical application of a Rayleigh probability density function used in spectral fatigue analysis.

For our test setup, large spectral areas of the higher harmonics were identified in tests at free surface condition for current flow alone with towing speeds between 0.6 to 0.8 m/s (tests no. 64, 63 and 69), and for current plus wave no. 1 combination with a towing speed of 0.5 m/s (test no. 79). The largest spectral areas for higher harmonics were identified in test no. 88, with a tow depth of 25 OD and for a combination of current plus wave no. 2, with a towing speed of 0.5 m/s.

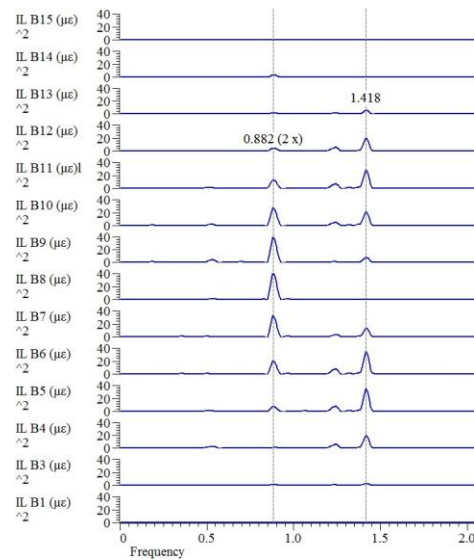


(a) CF direction  
**Figure 7.1 Broad band spectrum, test No. 64**

(b) IL direction



(a) CF direction



(b) IL direction

**Figure 7.2 Broad band spectrum, test No. 88**

DNV-OS-F201 (2010) in Appendix B, D 200, states that rainflow counting is the recommended method to provide the estimation of the stress probability density function, although it also mentions about the statistical uncertainties associated to time domain estimates of fatigue damage, indicating that sensitivity analyses should be considered, making reference to semi-empirical methods for corrections of typical narrow band fatigue damage estimation, e.g. Wirsching’s correction factor or Dirlik’s method for the rainflow density function.

The Dirlik’s method is identified as a promising alternative in the DNV standard, where the expression for the rainflow range uses the spectral moments from the zeroth to the fourth moment of area of the PSD, see section 11.3.6 for broad band spectra in Bartrop and Adams (1991).

In the work of Jhingran and Vandiver (2007), Dirlik’s method was evaluated against a Rayleigh PDF, which is only based on the zeroth spectral moment, identifying the former as a more appropriate method to predict stress range PDFs for responses with higher harmonics; then a modified Dirlik method is proposed to account for higher harmonics, considering the proven accuracy of VIV prediction tools for the 1 x response, so the spectral

moments for a total cross flow stress spectrum with 1 x frequency response plus 3 x and 5 x harmonics are estimated as:

$$\begin{aligned}
 &= \sigma_1^2 + \sigma_3^2 + \sigma_5^2 \\
 &= \sigma_1^2 (1 + h + k) \\
 &= \sigma_1^2 (1 + 9h + 25k) \\
 &= \sigma_1^2 (1 + 81h + 625k)
 \end{aligned}$$

Being  $\sigma_1$ ,  $\sigma_3$  and  $\sigma_5$  the zeroth, first, second and fourth spectral moments;  $A_1$ ,  $A_3$  and  $A_5$  the areas under the stress spectrum corresponding to 1 x, 3 x and 5 x frequencies.

In the cited paper, it is considered that  $\sigma_1 = h$ , with  $\sigma_1$  as the RMS of the stress for the 1 x component, it is also assumed that  $\sigma_3 = 3h$  and  $\sigma_5 = 5h$ , and since  $h \approx 3$  and

$k \approx 5$ , the spectral moments are finally expressed as:

$$\begin{aligned}
 &= (1 + h + k) \\
 &= (1 + 3h + 5k) \\
 &= (1 + 9h + 25k) \\
 &= (1 + 81h + 625k)
 \end{aligned}$$

The Dirlik stress range is then proposed to be estimated with previous spectral moments, where the unknown ratios of the spectral areas,  $h$  and  $k$ , are indicated as areas of on-going research.

For horizontal towing at large yaw angles, our preliminary findings showed that odd and even harmonic frequencies can be present in both, cross flow and in-line directions, moreover, for combined conditions of current plus large wave flows, the harmonics can differ from the typical integer multiples with respect to the 1 x frequency governed by the encounter wave frequency as shown in fig. 7.2.

As previously mentioned, VIV tests with longer exposure times in ocean basin tanks would be ideally required for experimental statistical data, especially if spectral analysis methods are intended to be considered in sensitivity analyses.

The results of these extended tests can be used to determine the ratios of spectral areas, either for maximum values or at desired locations along the span of the model, and to update the ratios of the first and second harmonics with respect to the 1 x frequency (assumed as the typical 3 x and 5 x CF harmonics in the previous equation for and their powers for and ), to define the spectral moments of representative conditions selected during model testing, following the proposal in Jhingran and Vandiver (2007).

Using the spectral moments as proposed in the previous paragraph, a modified Dirlik's probability density function ( ) can be computed according to eq. 11.61 in Barltrop and Adams (1991) and continue with the procedure to evaluate the stress range parameter or weighted average stress range, representing a constant amplitude stress range which causes an equivalent fatigue damage of that determined by rainflow counting, as =

$$(\ ) .$$

Finally, the damage in a time T can be estimated for the representative conditions by

$$= \frac{1}{A}$$

Where A and m defines the S-N curve as = , represents a mean period between peaks or crests per unit time, so / represents the number of stress ranges or stress cycles.

Then, Miner's rule can finally be applied for the accumulated fatigue damage during towing operations involving different testing conditions.

The proposed steps to investigate the ratios of spectral areas together with the ratios of first and second harmonics defining the spectral moments in a Dirlik modified method, can be then used to compare predictions against measured fatigue damage during model testing, full scale tests or monitoring measurements during tow-out installations methods, in order to assess the contribution towards a better understanding and characterisation of the VIV phenomena, aiming to reduce the uncertainties between experimental and field data.

### 7.3 Extreme event fatigue analysis

Although not related to the planned towing method of installation, extreme events such as hurricanes and strong eddies from the loop current in the GOM are important during the operation stage due to the potential that a single event can cause fatigue damage, which could not be correctly represented in the long term fatigue damage calculated from the wave scatter diagram data (API-RP-2RD, 2013).

An accumulated damage value of 1.0 represents the limit defined by the design fatigue curve and the API standard set accumulated damage limits as:

$$\text{Damage} \leq \begin{array}{ll} 0.1, & \text{during service life} \\ 0.1, & \text{during a single ULS event, for S-N approach} \\ 1.0, & \text{during a single ALS event} \end{array}$$

Section 4.3 of the standard relates the serviceability limit state (SLS) to normal operational conditions and normal temporary events; the ultimate limit state (ULS) to extreme operational conditions and abnormal temporary events; and the accidental limit state (ALS) to survival conditions or rare accidental loads.

A typical load case matrix relating the limit state categories (SLS, ULS and ALS) to return periods of different environmental conditions can be consulted for reference in Annex B of the code, although these relations are required to be identified by each project with Failure Mode and Effects Analysis (FMEA) and HAZOP procedures during design reviews.

## 8 Conclusions

The research topic arises from the need to understand the risks and challenges associated to solutions for oil production infrastructure in deep and ultra-deep waters, representing conditions and technical complexity that often demands the frontier of knowledge and industry practices, given the important environmental, social and economic impacts associated with unwanted events during project execution.

Although current codes and industry standards indicated in section 2.4 provides the recommendations to set design guidelines to assess VIV damage during towing installation methods, there was clearly a need to assimilate the basic principles in the structural response of slender cylindrical elements, thus the approach to conduct simplified analysis



along with the use of programs for application of the finite element method during the qualification of the motion capture (MOCAP) system in chapters 3 and 4, as well as the corresponding analysis for planning and design of the towing tests in chapter 5.

In order to identify some parameters and representative test conditions to be considered for the research scope, a series of visits and interviews were arranged with Subsea7 fabrication yard in Wick, Scotland, and engineering facilities in Aberdeen, Scotland for bundles and Paris, France for risers.

Subsea7 is a pioneer and leading subsea contractor and service provider, involved in the execution of projects where tow-out installation methods of risers and pipeline bundles have proved to be a competitive solution. This approach provided a first insight into practical procedures, current capabilities and operational aspects, which helped to model some scenarios to conduct this research work.

From this practical approach, a few simulations and analysis for a pipeline towing operation were performed with the availability of software Orcaflex, for a first insight into the use of prediction models, as included in section 1.5.

The experimental work to assess the applicability of the optical tracking system for motion capture (MOCAP) over flexible beams subject to forced harmonic excitation in chapter 3, provided an introduction to lab instrumentation, training and skills development for data processing and analysis, which are of intensive application during research and model testing activities required in engineering, design and monitoring of riser, bundles and other slender structural elements subject to potential fatigue damage due to flow induced vibrations.

The successful application of the aerial MOCAP system in flexible beams for motion response measurements, allowed a first implementation of recent motion capture technology, using underwater cameras courtesy of Qualisys motion capture systems, with enthusiastic support from the staff of the Kelvin Hydrodynamics Laboratory, which were mounted under the towing carriage of the towing tank to perform VIV tests on a partially submerged vertical cantilever, in order to assess the underwater system performance against the aerial cameras as a twin MOCAP system, included in chapter 4.

The planned work to evaluate the application of the new underwater cameras for the MOCAP system over flexibles, was used by the system provider and the University department to conduct a first workshop in 2014, with the participation of several delegates from towing and basin tank laboratories around the world, which has been carried out annually in different locations since then, (Flowave tank, Edinburgh, Scotland 2015 and Marintek, Trondheim, Norway 2016), which we attended with presentations of our implementation for this research work, having the opportunity to visit and learn about other current applications of the system at leading hydrodynamic research facilities.

Additionally, the innovation with this underwater motion capture system application was included in a research report of the Marine Renewables Infrastructure Network, an ECfunded consortium of 29 partners bringing together a network of 42 specialist marine renewable energy testing facilities (Bourdier et al., 2015).

During literature review, it was found that some of the most recent VIV research and monitoring on long slender cylinders was performed with fibre optic sensing systems for direct measurements of bending strains/curvatures and frequency responses along structural members (Vandiver et al., 2009).

The technology was assimilated and implemented with support from the NAOME department, constituting another first application in the Kelvin Hydrodynamics Laboratory, using the results of estimated motion responses to design a fibre optic sensing system (FOSS) based on Fibre Bragg Grating (FBG) sensors inscribed in optical fibre arrays.

This fostered a close cooperation and support of our colleagues from the Centre for Microsystems and Photonics of the Department of Electronic and Electrical Engineering in the University of Strathclyde, whom provided an approach and guidance about the technology, facilitating installation advice, support and the FBG interrogator equipment during the time window assigned to conduct towing tests.

The riser model was designed and built for the experimental towing tests, with a model aspect ratio about 430, a final mass ratio of 0.9, damping ratio in still fluid  $\zeta = 0.046$  ( $m*\zeta=0.04$ ), Reynolds number ranges about  $3.77E+03 < Re < 3.35E+04$  considering total flow velocities or  $6.56E+02 < Re < 5.83E+03$  considering the velocity component normal to the

cylinder, with combinations of wave flows at low Keulegan-Carpenter number range of  $0.3 < KC < 5.25$ .

The implementation of new technologies for motion capture and strain/curvature measurements during experimental work described in chapters 5 and 6 and their tested capabilities, provided methods and sets the basis for development of additional work to obtain high quality data and hydrodynamic parameters at localised points of interest over long flexible cylinders, aiming to explore the improvement of VIV prediction models available in commercial software or in new research works, by means of experimental calibrations with hydrodynamic coefficients obtained from more representative flexible models, as an alternative to the use of general default coefficients obtained from forced excitations in rigid cylinders.

Additionally, future work can assess a proposed method for estimation of motion response from the FOSS, which can potentially provide valuable information during both, model testing and installation monitoring of towed risers/bundles.

The experience in the execution of the experimental work in the towing tank was found to provide an inexpensive first stage for the execution of further model testing in ocean basin tanks, where a more suitable time of flow exposure and combinations with different wave directions can be tested. Newly available facilities such as the circular Flowave tank can represent an opportunity to take advantage for testing current and wave flows in any relative direction, subject to the limitations of the tank dimensions.

The results of the towing tests for the riser model carried out in limited combinations of current velocities, waves, initial tension and tow depths chosen for this research scope, provides an insight of the response behaviour for the main fluid loading conditions during towing operations, through measurements and analysis of the frequency and amplitudes of the flow induced vibrations within a range of parameters, as well as the response analysis of tension forces to obtain mean drag force components and time varying force reaction at end supports in each case.

This provides a notion to set limits and risk conditions to be considered in the analysis and design of tow-out installation methods and for towing route planning, considering the circulation and metocean forecast data for any given season, as reviewed in section 2.2.

The results also provided indications to identify response branch transitions and associated vortex shedding patterns, confirming some of the main characteristics of VIV responses over a fully submerged and relatively short horizontal cantilever model in the work of Williamson and Roshko (1988) and Khalak and Williamson (1999), although in our case within a particular range of reduced velocities, according to the excited vibration modes of the long flexible model, however, longer aspect ratios tests will be of great contribution to evaluate the behaviour for higher modes of vibration.

Further tests were also identified to improve the understanding of these responses under towing conditions, to assess the effects of a model setup where the initial tension can be kept nearly constant, and a proper elasticity scaling can be implemented for the use of models with longer aspect ratios (L/D), enabling responses at higher modes of vibration to be investigated.

Currently, the Petroleum Mexican Institute is about to open new research and test facilities during the second half of 2017 as a deep water technology centre in Boca del Río, Veracruz. The construction of an ocean basin tank is planned in the medium term, where large opportunities are identified to apply and develop the knowledge and methods of the present work for hydrodynamic model testing involved in Pemex's next challenges for oil production projects in the Gulf of Mexico.

## References

- ALAMILLA, J., CAMPOS, D., ORTEGA, C., MORALES-CONTRERAS, J. L. & SORIANO, A. 2007. Estimation of the design wave height for offshore structures transportation. *10th International Conference on Applications of Statistics and Probability in Civil Engineering (ICASP10)*. Tokyo.
- ALLIOT, V. & LEGRAS, J. L. Lessons Learned From The Evolution And Development Of Multiple-Lines Hybrid Riser Towers For Deep Water Production Applications. 2005. OTC: Offshore Technology Conference, OTC-17683.
- ALLIOT, V., ZHANG, H., PERINET, D. & SINHA, S. Development of Towing Techniques for Deepwater Flowlines and Risers. 2006. OTC: Offshore Technology Conference, OTC17826.
- API-RP-2RD 1998. Design of Risers for Floating Production Systems (FPSs) and Tension-Leg Platforms (TLPs). *RECOMMENDED PRACTICE 2RD*. AMERICAN PETROLEUM INSTITUTE.
- API-RP-2RD 2013. Dynamic Risers for Floating Production Systems. *API STANDARD 2RD*.

- BARLTROP, N. & ADAMS, A. 1991. Dynamics of Fixed Offshore Structures. ButterworthHeinemann.
- BARLTROP, N., MITCHELL, G. M. & ATKINS, J. 1990. *Fluid Loading on Fixed Offshore Structures: Background to the 4th Edition of Offshore Installations: Guidance on Design and Construction*, HM Stationery Office.
- BARLTROP, N. D. P. 1998. *Floating structures : a guide for design and analysis*, London, CMPT (Centre for Marine and Petroleum Technology).
- BLACKBURN, H. M., GOVARDHAN, R. & WILLIAMSON, C. 2001. A complementary numerical and physical investigation of vortex-induced vibration. *Journal of Fluids and Structures*, 15, 481-488.
- BLEVINS, R. D. 1977. Flow-induced vibration. *New York, Van Nostrand Reinhold Co., 1977. 377 p.*
- BLEVINS, R. D. 1994. *Flow-induced vibration*, Malabar, Fla., Malabar, Fla. : Krieger Pub. Co.
- BOURDIER, S., THIEBAUT, F., ROUSSET, J.-M., OHANA, J., LE BOULLUEC, M., GERMAIN, G., JOHANNING, L., DAMY, G., TASSAIN, A. & CASTILLON, F. 2015. Remote Underwater Motion Measurement. *WP4: Research to innovate and improve infrastructures, technologies and techniques*. MARINET.
- BOURGUET, R., EM KARNIADAKIS, G. & TRIANTAFYLLOU, M. S. 2015. On the validity of the independence principle applied to the vortex-induced vibrations of a flexible cylinder inclined at 60°. *Journal of Fluids and Structures*, 53, 58-69.
- BOURGUET, R. & TRIANTAFYLLOU, M. S. 2015. Vortex-induced vibrations of a flexible cylinder at large inclination angle. *Philosophical Transactions of the Royal Society A: Mathematical, Physical and Engineering Sciences*, 373.
- BS EN 1057 2006. Copper and copper alloys. Seamless, round copper tubes for water and gas in sanitary and heating applications. BSI.
- CHEN, J., GONG, H., JIN, S. & LI, S. The influence of adhesive on fiber Bragg grating strain sensor. 2009. 751419-751419-8.
- CHIEN-CHING, G.-S. H. Dynamic Strain Measurement Using Improved Bonding Fiber Bragg Grating. Abstracts of 17th World Conference on Non-Destructive Testing, 2008.
- CICESE 2013a. REPORTE ANUAL DE LA INTERPRETACIÓN DINÁMICA GENERAL DEL GOLFO DE MÉXICO, AÑO 2013. *MEDICIÓN Y ANÁLISIS METOCEÁNICO DEL GOLFO DE MÉXICO, ETAPA 2009-2013*. Revisión 1 ed.
- CICESE 2013b. REPORTE DE LOS DATOS OBTENIDOS CON LA BOYA METOCEÁNICA. *MEDICIÓN Y ANÁLISIS METOCEÁNICO DEL GOLFO DE MÉXICO, ETAPA 2009-2013*. Rev 0 ed.: CICESE.
- COMISION NACIONAL DE HIDROCARBUROS. 2016. *4TH BIDDING PROCESS DEEP-WATER BLOCKS ROUND 1* [Online]. Available: <http://rondasmexico.gob.mx/wpcontent/uploads/2016/07/4th-Bidding-Round-Deep-Water-blocks-v.25.pdf> [Accessed 18/10 2016].
- DAHL, J. M., HOVER, F. S., TRIANTAFYLLOU, M. S., DONG, S. & KARNIADAKIS, G. E. 2007. Resonant Vibrations of Bluff Bodies Cause Multivortex Shedding and High Frequency Forces. *Physical Review Letters*, 99, 144503.
- DE LA CRUZ, D., ZIMMERMANN, C. A., NEVEUX, P. & LOUVETY, F. The Greater Plutonio Riser Tower. Offshore Technology Conference, 4-7 May 2009 Houston, TX., OTC 19929.
- DESERTS, L. D. OTC 11875 Hybrid Riser for Deepwater Offshore Africa. ANNUAL OFFSHORE TECHNOLOGY CONFERENCE, 2000. 37-46.

- DNV-OS-F101 2010. SUBMARINE PIPELINE SYSTEMS, (DET NORSKE VERITAS, OFFSHORE STANDARD).
- DNV-OS-F201 2010. DYNAMIC RISERS (DET NORSKE VERITAS. OFFSHORE STANDARD).
- DNV-RP-C205 2007. ENVIRONMENTAL CONDITIONS AND ENVIRONMENTAL LOADS (DET NORSKE VERITAS. OFFSHORE STANDARD).
- DNV-RP-F204 2005. RISER FATIGUE (DET NORSKE VERITAS. OFFSHORE STANDARD).
- DNV-RP-H103 2010. MODELLING AND ANALYSIS OF MARINE OPERATIONS (DET NORSKE VERITAS. OFFSHORE STANDARD).
- DRECHSLER, K., HEINE, M., MITSCHANG, P., BAUR, W., GRUBER, U., FISCHER, L., ÖTTINGER, O., HEIDENREICH, B., LÜTZENBURGER, N. & VOGGENREITER, H. 2009. Carbon Fiber Reinforced Composites. *Ullmann's Encyclopedia of Industrial Chemistry*. John Wiley and Sons.
- DUBRANNA, J., PÉREZ-BRUNIUS, P., LÓPEZ, M. & CANDELA, J. 2011. Circulation over the continental shelf of the western and southwestern Gulf of Mexico. *Journal of Geophysical Research: Oceans*, 116, n/a-n/a.
- FEMTOFIBERTEC. 2016. *Femtosecond-Laser-Written Fiber Bragg Gratings* [Online]. Available: <http://www.femtofibertec.de/en/> [Accessed 02/11 2016].
- FENG, C. 1968. *The measurement of vortex induced effects in flow past stationary and oscillating circular and D-section cylinders*. University of British Columbia.
- FENTON, J. 1990. Nonlinear wave theories. *the Sea*, 9, 3-25.
- FENTON, J. D. 1985. A fifth-order Stokes theory for steady waves. *Journal of waterway, port, coastal, and ocean engineering*, 111, 216-234.
- FONTAINE, E., MARCOLLO, H., VANDIVER, K., TRIANTAFYLLOU, M., LARSEN, C., TOGNARELLI, M., CONSTANTINIDES, Y. & OAKLEY, O. Reliability based factors of safety for VIV fatigue using NDP riser high mode VIV tests. ASME 2011 30th International Conference on Ocean, Offshore and Arctic Engineering, 2011. American Society of Mechanical Engineers, 511-522.
- GABBAI, R. & BENAROYA, H. 2005. An overview of modeling and experiments of vortexinduced vibration of circular cylinders. *Journal of Sound and Vibration*, 282, 575616.
- GOVARDHAN, R. & WILLIAMSON, C. 2000. Modes of vortex formation and frequency response of a freely vibrating cylinder. *Journal of Fluid Mechanics*, 420, 85-130.
- HBM. 2010. *Polyimide Strain Sensor Installation* [Online]. Available: [https://www.youtube.com/watch?v=gjRmB-X\\_lcw](https://www.youtube.com/watch?v=gjRmB-X_lcw) [Accessed 02/11 2016].
- HOWE, R. Evolution of offshore drilling and production technology. Offshore Technology Conference, 1986. Offshore Technology Conference, OTC-5354.
- HUERA-HUARTE, F. & BEARMAN, P. 2009. Wake structures and vortex-induced vibrations of a long flexible cylinder—part 1: dynamic response. *Journal of Fluids and Structures*, 25, 969-990.
- INGRAM, D., WALLACE, R., ROBINSON, A. & BRYDEN, I. The design and commissioning of the first, circular, combined current and wave test basin. OCEANS 2014 - TAIPEI, 710 April 2014 2014. 1-7.
- JAIN, A. & MODARRES-SADEGHI, Y. 2013. Vortex-induced vibrations of a flexibly-mounted inclined cylinder. *Journal of Fluids and Structures*, 43, 28-40.
- JHINGRAN, V., JAISWAL, V. & VANDIVER, J. K. Spatial variation of drag on long cylinders in sheared flow. ASME 2008 27th International Conference on Offshore Mechanics and Arctic Engineering, 2008. American Society of Mechanical Engineers, 919-927.

- JHINGRAN, V. & VANDIVER, J. K. Incorporating the higher harmonics in VIV fatigue predictions. ASME 2007 26th International Conference on Offshore Mechanics and Arctic Engineering, 2007. American Society of Mechanical Engineers, 891-899.
- JU, G. T., LITTELL, H. S., COOK, T. B., DUPRE, M. H., CLAUSING, K. M., SHUMILAK, E. E., SCHOPPA, W. & BLIZZARD, W. A. Perdido Development: Subsea and Flowline Systems. 2010. OTC: Offshore Technology Conference, OTC-20882.
- KHALAK, A. & WILLIAMSON, C. 1999. Motions, forces and mode transitions in vortex-induced vibrations at low mass-damping. *Journal of fluids and Structures*, 13, 813851.
- KIM, Y.-H., VANDIVER, J. & HOLLER, R. 1986. Vortex-induced vibration and drag coefficients of long cables subjected to sheared flows. *Journal of Energy Resources Technology*, 108, 77-83.
- KUTZ, M. 2006. *Mechanical Engineers' Handbook, Volume 1: Materials and Engineering Mechanics*, John Wiley & Sons.
- LEGRAS, J.-L. & PILLET, B. 2013. Tethered Catenary Riser: A New Deepwater Concept. V04BT04A025.
- LIROLA, F., PIONETTI, F. R., BRUGUIER, C. & ALTMANN, L. 2013. Deep And Ultra Deep Riser Concepts Allowing to Maximize Local Content. Offshore Mediterranean Conference.
- MEXICAN PRESIDENCY. 2012. *Nuevo yacimiento de petróleo en el Golfo de México* [Online]. Available: <http://calderon.presidencia.gob.mx/2012/10/nuevo-yacimiento-depetroleo-en-el-golfo-de-mexico/> [Accessed 10/10 2016].
- NANNINGA, N. E. 2008. *HIGH CYCLE FATIGUE OF AA6082 AND AA6063 ALUMINUM EXTRUSIONS*. DOCTOR OF PHILOSOPHY, MICHIGAN TECHNOLOGICAL UNIVERSITY.
- NATIONAL INSTRUMENTS. 2016. *Fiber-Optic Sensing* [Online]. Available: <http://www.ni.com/opticalsensing/> [Accessed 02/11 2016].
- NURWANTO, T., KARUNAKARAN, D. & FRANCISS, R. 2013. COBRA Riser Concept for Ultra Deepwater Condition. V04BT04A030.
- OFFSHORE TECHNOLOGY 2016. *Stones Field, Gulf of Mexico, United States of America* [Online]. Available: <http://www.offshore-technology.com/projects/stones-fieldgulf-mexico/> [Accessed 18/10 2016].
- OIL & GAS JOURNAL 2012. CASCADE AND CHINOOK, DEVELOPING THE LOWER TERTIARY WITH THE FIRST FPSO IN THE U.S. GULF OF MEXICO. *OIL & GAS JOURNAL*. ORCINA LTD. 2006. The OrcaFlex VIV Toolbox User Guide to the Time Domain Models. Available: <https://www.orcina.com/SoftwareProducts/OrcaFlex/Documentation/Time%20Domain%20VIV%20Models.pdf> [Accessed 22/11/2013].
- ORCINA LTD. 2007. ORCAFLEX VIV TOOLBOX VALIDATION. Available: <https://www.orcina.com/SoftwareProducts/OrcaFlex/Validation/R648-01-02%20OrcaFlex%20VIV%20Validation%20Summary.pdf> [Accessed 16/11/2013].
- PEMEX. 2016. *Call for bids of Trion block will strengthen Pemex* [Online]. Available: [http://www.pemex.com/en/press\\_room/press\\_releases/Paginas/2016-049national.aspx](http://www.pemex.com/en/press_room/press_releases/Paginas/2016-049national.aspx) [Accessed 18/10 2016].
- PETRUSKA, D. J., ZIMMERMANN, C. A., KRAFFT, K. M., THURMOND, B. F. & DUGGAL, A. Riser System Selection and Design for a Deepwater FSO in the Gulf of Mexico. 2002. OTC: Offshore Technology Conference, OTC-14154.
- RAMBERG, S. E. 2006. The effects of yaw and finite length upon the vortex wakes of stationary and vibrating circular cylinders. *Journal of Fluid Mechanics*, 128, 81-107.
- RESVANIS, T. L., JHINGRAN, V., VANDIVER, J. K. & LIAPIS, S. Reynolds number effects on the vortex-induced vibration of flexible marine risers. ASME 2012 31st International

- Conference on Ocean, Offshore and Arctic Engineering, 2012. American Society of Mechanical Engineers, 751-760.
- RITTO, T., AGUIAR, R., SAMPAIO, R. & CATALDO, E. How to match theoretical and experimental boundary conditions of a cantilever beam. Proceedings of the 7th European Conference on Structural Dynamics E, 2008.
- RÖSLER, J., HARDERS, H. & BAEKER, M. 2007. *Mechanical behaviour of engineering materials: metals, ceramics, polymers, and composites*, Springer Science & Business Media.
- SAINT-MARCOUX, J.-F., ABELANET, M. & BOMBINO, S. 2010. Lessons Learnt From Recent Deepwater Riser Projects. International Society of Offshore and Polar Engineers.
- SAINT-MARCOUX, J.-F. & LEGRAS, J.-L. Lessons Learned on the Design and Construction of Hybrid Riser Towers. 2011. OTC: Offshore Technology Conference, OTC-21271.
- SARPKAYA, T. 1979. Vortex-Induced Oscillations: A Selective Review. *Journal of Applied Mechanics*, 46, 241-258.
- SARPKAYA, T. 2010. *Wave forces on offshore structures*, Cambridge University Press.
- SBM OFFSHORE. 2016. *FPSO Turritella* [Online]. Available: <http://www.sbmoffshore.com/wp-content/uploads/2016/05/FACTSHEETTURRITELLA.pdf> [Accessed 18/10 2016].
- SBM OFFSHORE. GLOSSARY. 2013. *Glossary* [Online]. Available: [http://www.sbmoffshore.com/wp-content/uploads/2013/09/SBMO-Glossary\\_Original\\_2045.pdf](http://www.sbmoffshore.com/wp-content/uploads/2013/09/SBMO-Glossary_Original_2045.pdf) [Accessed 18/10 2016].
- SCHLICHTING, H. 1979. *Boundary-layer theory*, McGraw-Hill.
- SERTÁ, O. B., LONGO, C. E. V. & ROVERI, F. E. Riser Systems for Deep and Ultra-Deepwaters. 2001. OTC: Offshore Technology Conference, OTC-13185.
- SHARMA, P. P., SONG, R., APOS, DONNELL, J., MORRIS, K. J. & KAVANAGH, W. K. Design Methods in ISO 13628-12 and Implications for Gulf of Mexico SCRs. 2010. OTC: Offshore Technology Conference, OTC-20778.
- SKJELBREIA, L. & HENDRICKSON, J. 1960. Fifth order gravity wave theory. *Coastal Engineering Proceedings*, 1, 10.
- SPARKS, C. P. 2007. *Fundamentals of marine riser mechanics: basic principles and simplified analyses*, PennWell Books.
- SVERRE STEEN 2014. *Experimental Methods in Marine Hydrodynamics*. Revised August 2014 ed. Trondheim, Norway: Marine Technology Centre.
- SWORN, A. Hybrid Riser Towers from an Operator's Perspective. Offshore Technology Conference, 2-5 May 2005 Houston, TX., OTC 17397.
- TIMOSHENKO, S. 1974. *Vibration problems in engineering*, New York, New York : Wiley.
- UNAM. 2013a. *Hydrodynamic Forecast Operational System* [Online]. Available: <http://grupo-ioa.atmosfera.unam.mx/pronosticohidrodinamico/index.php/es/principal/rapidez-hycom> [Accessed 14/10/2016 2016].
- UNAM. 2013b. *Operational Numerical, Weather and Wave Forecasting System* [Online]. Available: <http://grupo-ioa.atmosfera.unam.mx/sipronomo/index.php/menu-altura> [Accessed 14/10/2016 2016].
- VANDIVER, J. K. 1983. *Drag coefficients of long flexible cylinders*, ; Massachusetts Inst. of Technology.
- VANDIVER, J. K. 1993. Dimensionless Parameters Important to the Prediction of Vortex-Induced Vibration of Long, Flexible Cylinders in Ocean Currents. *Journal of Fluids and Structures*, 7, 423-455.



- VANDIVER, J. K., ALLEN, D. & LI, L. 1996. THE OCCURRENCE OF LOCK-IN UNDER HIGHLY SHEARED CONDITIONS. *Journal of Fluids and Structures*, 10, 555-561.
- VANDIVER, J. K., JAISWAL, V. & JHINGRAN, V. 2009. Insights on vortex-induced, traveling waves on long risers. *Journal of Fluids and Structures*, 25, 641-653.
- VIKESTAD, K., VANDIVER, J. & LARSEN, C. 2000. Added mass and oscillation frequency for a circular cylinder subjected to vortex-induced vibrations and external disturbance. *Journal of Fluids and Structures*, 14, 1071-1088.
- WERNECK, M. M., ALLIL, R., RIBEIRO, B. A. & DE NAZARÉ, F. V. 2013. A Guide to Fiber Bragg Grating Sensors. *Current Trends in Short and Long-period Fiber Gratings*, ed. C. Cuadrado-Laborde.
- WILLIAMSON, C. & ROSHKO, A. 1988. Vortex formation in the wake of an oscillating cylinder. *Journal of fluids and structures*, 2, 355-381.
- WILLIAMSON, C. H. K. & JAUVTIS, N. 2004. A high-amplitude 2T mode of vortex-induced vibration for a light body in XY motion. *European Journal of Mechanics - B/Fluids*, 23, 107-114.
- WINDOLF, M., GÖTZEN, N. & MORLOCK, M. 2008. Systematic accuracy and precision analysis of video motion capturing systems—exemplified on the Vicon-460 system. *Journal of biomechanics*, 41, 2776-2780.
- WU, X., GE, F. & HONG, Y. 2012. A review of recent studies on vortex-induced vibrations of long slender cylinders. *Journal of Fluids and Structures*, 28, 292-308.
- ZAVALA-HIDALGO, J., GALLEGOS-GARCÍA, A., MARTÍNEZ-LÓPEZ, B., MOREY, S. L. & O'BRIEN, J. J. 2006. Seasonal upwelling on the Western and Southern Shelves of the Gulf of Mexico. *Ocean Dynamics*, 56, 333-338.

## Appendix A

### A.1 Analysis of a simply supported beam with harmonic ground motion (fig. 3.1 in section 3.1.2)

#### Free vibration analysis

Free transversal vibrations occur when no ground motion but an initial perturbation is present in the system, from figure 3.1 the dynamic equilibrium condition for forces in the “y” direction (neglecting rotary inertia and shearing deformation) is:

$$- \frac{\partial V}{\partial x} - \frac{\partial H}{\partial x} = 0$$

$$\frac{\partial V}{\partial x} = - \frac{\partial H}{\partial x}$$

The moment equilibrium condition gives:

$$+ \frac{d^2 M}{dx^2} = 0$$

Neglecting higher order terms:

$$\frac{d^2 M}{dx^2} = 0$$

From Euler-Bernoulli beam theory, we have

$$M = EI \frac{d^2 w}{dx^2}$$

Then, the governing equation for free vibration of the beam is:

$$EI \frac{d^4 w}{dx^4} + \rho A \omega^2 w = 0 \tag{A.1}$$

Assuming a solution of the form:  $w(x) = W(x) e^{i\omega t}$ , subst. into (A.1):

$$EI \frac{d^4 W}{dx^4} - \rho A \omega^2 W = 0 \tag{A.2}$$

$$\frac{d^4 W}{dx^4} - k^4 W = 0$$

To solve the previous 4<sup>th</sup> order ODE, we try:  $W(x) = e^{\lambda x}$ , then:

$$\lambda^4 - k^4 = 0 \tag{A.3} \quad \lambda = \pm k, \pm ik \tag{A.4}$$

The general solution therefore is:

$$W(x) = C_1 e^{kx} + C_2 e^{-kx} + C_3 e^{ikx} + C_4 e^{-ikx}$$

Using the identities:

$$\begin{aligned} e^{\pm ikx} &= \cos(kx) \pm i \sin(kx) \\ e^{\pm kx} &= \cosh(kx) \pm \sinh(kx) \end{aligned}$$

The general solution can be expressed as:

$$\begin{aligned}
\phi(x) &= [\cosh(\alpha x) + \sinh(\alpha x)] + [\cosh(\alpha x) - \sinh(\alpha x)] + [\cos(\beta x) + i \sin(\beta x)] \\
&\quad + [\cos(\beta x) - i \sin(\beta x)] \\
\phi(x) &= (C_1 + C_2)[\cosh(\alpha x)] + (C_3 - C_4)[\sinh(\alpha x)] + (C_5 + C_6)[\cos(\beta x)] + (C_7 - C_8)[\sin(\beta x)] \\
\phi(x) &= [C_1 \cosh(\alpha x) + C_2 \sinh(\alpha x) + C_5 \cos(\beta x) + C_7 \sin(\beta x)] \quad (A.5)
\end{aligned}$$

And

$$\begin{aligned}
&\frac{\omega^2}{a^2} \\
&= \pm \sqrt{\frac{\omega^2}{a^2}} \qquad \qquad \qquad = \pm \sqrt{\frac{\omega^2}{a^2}} = \pm \frac{\omega}{a}
\end{aligned}$$

$$\frac{d\phi}{dx} = [\sinh(\alpha x) + \cosh(\alpha x)] - [\sin(\beta x) + \cos(\beta x)] \quad (A.6)$$

$$\frac{d^2\phi}{dx^2} = [\cosh(\alpha x) + \sinh(\alpha x)] - [\cos(\beta x) - \sin(\beta x)] \quad (A.7)$$

The 4 boundary conditions (BC) for free vibration in a simply support beam are:

$$= 0 \quad = 0$$

$$(a) = 0 \quad =$$

$$(b)$$

$$\frac{d^2y}{dx^2} = 0 \quad = 0 \quad (c)$$

$$\frac{d^2y}{dx^2} = 0 \quad = \quad (d)$$

Substituting BC (a) and (c) in eq. (A.5) and (A.7) respectively yields to  $C_1=C_3=0$ , and BC (b) and (d) in eq. (A.5) and (A.7) respectively:

$$\sinh(\lambda a) + \sin(\lambda a) = 0$$

$$(e) \sinh(\lambda a) - \sin(\lambda a) = 0$$

$$(f)$$

In matrix form:

$$\begin{matrix} \sinh(\lambda a) & \sin(\lambda a) & 0 \\ \sinh(\lambda a) & -\sin(\lambda a) & 0 \end{matrix} = \begin{matrix} 0 \\ 0 \end{matrix}$$

For a non-trivial solution, the determinant of the first matrix must be zero:

$$= = \quad (A.9) \sqrt{\quad}$$

From eq. A.9, we get the angular natural frequency for any vibration mode as:

$$= \frac{i^2 \pi^2 a}{l^2} = \frac{i^2 \pi^2}{l^2} \sqrt{\frac{EI}{m}} \quad (A.10)$$

Then the natural frequency of the  $i$ th mode for the beam in Hertz is:

$$-2 \sinh(\dots) \sin(\dots) = 0 \tag{A.8}$$

If

$$=$$

(Where  $i = \text{integer} = 1, 2, 3, \dots$ ), the equation (A.8) is satisfied, then:

$$\tag{A.11}$$

Now, from eq. (A.8) since  $\sinh(i\pi) \neq 0$ , from eq. (e) C2 must be zero, then:

$$= = = 0 \tag{g}$$

Substituting eq. (g) and (A.9) in eq. (A.5):

$$\begin{aligned} (\dots) &= \sin \frac{\dots}{\dots} \\ &= \frac{i^2 \pi}{\dots} \sqrt{\frac{EI}{\dots}} \end{aligned} \tag{A.12}$$

### Normal mode method

The normal mode method consist in the utilisation of the principal modes of vibration as generalised coordinates, where the equations of undamped motion become uncoupled, in these coordinates, each equation may be solved as if it pertained to a system with only one degree of freedom, which allows to calculate the response of the  $i$ th vibrational mode by the Duhamel integral (Timoshenko, 1974).

The mode shapes of deflections in eq. A.12 are sine curves for free vibrations, and this function is clearly orthogonal (two functions,  $f$  and  $g$ , are called orthogonal if their inner product  $\langle f, g \rangle$  is zero for  $f \neq g$ ), which mean that it can be normalised:

$$(\dots) \rightarrow (\dots)$$

For normalized functions

$$= 1$$

Then:

$$-C_4 \left[ \frac{\sin \left( \frac{\pi x}{2l} \right)}{2} \right] = 1$$

$$= 1 \quad \frac{-C_4}{i\pi} \left[ \frac{\pi}{2} \right]$$

$$C_4 = \sqrt{\frac{2}{l}}$$

Thus, the shape of natural modes of vibration as a normal function is:

$$= \sqrt{\frac{2}{l}} \sin \left( \frac{i\pi x}{l} \right) \tag{A.13}$$

We can rewrite the governing equation A.1 as:

$$+ = 0 \tag{A.14}$$

It is clear that “y” is a function of position and time, then for any vibrational mode we can attempt a solution in the form of (method of separation of variables):

$$(,) = \sum ( ) ( ) \tag{A.15}$$

Subst. eq. (A.15) into (A.14):

$$+ = 0$$

Multiplying by :

$$= -$$

The left hand side of the previous equation is only f(t) and the right hand side is only f(x), therefore the equation holds if and only if both terms are equal to a constant, say - :

$$\begin{aligned}
 & \ddot{u}_i = -\omega_i^2 u_i \\
 & + = 0 \quad (A.16)
 \end{aligned}$$

$$\begin{aligned}
 & \ddot{v}_i = -\omega_i^2 v_i \\
 & - \ddot{u}_i = 0 \quad (A.17)
 \end{aligned}$$

Eq. (A.16) represents the simple harmonic oscillator equation, with general solution of the form

$$u_i = A_i \cos(\omega_i t) + B_i \sin(\omega_i t) \quad (A.18)$$

Subst. eq. (A.18) into eq. (A.15), we get the harmonic motion of the beam when vibrates in its  $i$ th natural mode:

$$u_i(t) = \sum [A_i \cos(\omega_i t) + B_i \sin(\omega_i t)] \quad (A.19)$$

Subst. eq. (A.19) into eq. (A.14):

$$-\ddot{u}_i = \omega_i^2 u_i = 0 \quad (A.20)$$

$$-\ddot{v}_i = 0 \quad (A.21)$$

We can write this eq. in the form of an eigenvalue problem:

$$L u_i = -\omega_i^2 u_i \quad (A.22)$$

Where

$$L u_i = \frac{d}{dx} \left( EI \frac{d^3 u_i}{dx^3} \right) + \rho A \omega_i^2 u_i = 0 \quad (A.23)$$

To examine the orthogonality properties, we will consider two modes  $i$  and  $j$  of the eigenvalue problem:

$$L u_i = -\omega_i^2 u_i \quad (h)$$

$$L v_j = -\omega_j^2 v_j \quad (i)$$

Multiplying eq. (h) by  $X_j$  and eq. (i) by  $X_i$  and integrating the products over the length of the beam, we have:

$$\int_0^L X_j L u_i dx = -\omega_i^2 \int_0^L X_j u_i dx \quad (j)$$

$$= \quad (k)$$

For  $i=j$ , the Eigen functions are normalised:

$$= = 1 \quad (l)$$

Then

$$= = \_ \quad (m)$$

### Support Motion

For this experiment the right support will experience a vertical ground translation, according to the harmonic function:

$$= (\ ) = \sin(\Omega) \quad (n)$$

Where  $y_1$  is the amplitude in "y" direction and  $\Omega$  is the impressed angular frequency.

Then, the eq. (A.1) of motion may be written:

$$+ - (\ ) = 0 \quad (o)$$

The term  $(\ ) = /$ , is the displacement function that needs to be multiplied by the corresponding support motion  $g(t)$ , in order to get the relative response along the beam to produce the flexible-body motions. Thus eq. (o) represents the effect of the support motion on the bending stiffness component of eq. (A.1).

To solve this equation, we introduce the notation

$$* = - (\ ) \quad (p)$$

Which represent the relative response to the rigid body translation of the support, so the absolute acceleration of any point will be:

$$= * + (\ ) \quad (q)$$

Subst. eq. (p) and (q) into (o):

$$* + (\ ) + (*) = 0$$

$$* + * = - (\ ) = - (\ ) \quad (A.24)$$



The right term from equation (A.24) is equivalent to the “force” term in a typical forced vibration beam equation but in relative coordinates.

For  $EI/m=a^2$  and multiplying eq. (A.24) by  $dx$ :

$$*+ \quad * \quad = -()() \quad (A.25)$$

We can transform this equation to normal coordinates by subst. eq. (A.15) into eq. (A.25), multiplying by  $X_j$  and integrating over the length of the beam:

$$\Sigma \quad + \quad = -() \quad () \quad (A.26)$$

Substituting eq. (l) and (m) into eq. (26):

$$+ = -() \quad () \quad (A.27)$$

The right hand term of eq. (A.27) is the  $i$ th equivalent normal mode load “ $q$ ”, which is equivalent to a force term per unit of mass. The response of the  $i$ th vibrational mode is found by the Duhamel’s integral as:  $= \_ \sin(t - t)'$ , then:

$$= - \_ () \quad (') \sin \quad (t - t) ' \quad (A.28)$$

Superimposing all of the normal mode responses to the previous time function, according to eq. (A.15):

$$* = - \Sigma \quad \_ () \quad (') \sin \quad (t - t) ' \quad (A.29)$$

This represents the vibrational motion of any point along the beam, relative to the rigid body projection between supports, during the excitation at one end.

The total solution is obtained from eq. (p) by adding the vibrational and rigid-body motions:  $= () \quad () + \quad * \quad (A.30)$

### Solution of the dynamic response

Substituting eq. (A.13) and (n) into (A.29), we have:

$$* = -\frac{2}{l} \sum_{\omega} \frac{1}{\omega} \sin\left(\frac{i\pi x}{l}\right) \frac{1}{l} \int^l x \sin\left(\frac{i\pi x}{l}\right) dx (-\Omega^2 y_1) \int^t \sin \Omega t' \sin \omega (t - t)'$$

$$* = \sum_{i=1}^{\infty} \left( \frac{2\Omega}{\omega} - 1 \right) \sin \sin \Omega' \sin (t - t)'$$

Solving the first integral by parts, with  $u = x$  and  $dv = \sin\left(\frac{i\pi x}{l}\right) dx$ , we have  $du = dx$  and  $v = -\frac{l}{i\pi} \cos\left(\frac{i\pi x}{l}\right)$ :

$$= \frac{x l i \pi x}{i \pi} \left( \frac{i \pi x}{l} \right) \sin \frac{i \pi x}{l} - \cos \left( \frac{i \pi x}{l} \right) \cos = + \sin \left[ \frac{x l i \pi x}{i \pi} \left( \frac{i \pi x}{l} \right) \right] -$$

Then:

(A.31)

To solve the integral in eq. (A.31), we use the trigonometric identities:

$$\cos(-) = \cos(+) \cos(0) + \sin(+) \sin(0) \cos(+) = \cos(+) \cos(0) - \sin(+) \sin(0)$$

Subtracting the second identity to the first one, we have:

$$\cos(-) - \cos(+) = 2 \sin(+) \sin(0), h$$

$$* = \sum_{i=1}^{\infty} \left( \frac{2\Omega}{\omega} - 1 \right) \sin \sin \Omega' \sin (t - t)'$$

$$\sin(+) \sin(0) = \frac{1}{2} [\cos(-) - \cos(+)]$$

Substituting the last identity for the integral, we have that:

$$\begin{aligned}
 \sin \Omega' \sin (t-t) &= \frac{1}{2} (\cos [\Omega - (t-t)] - \cos [\Omega + (t-t)]) \\
 &= \frac{1}{2} (\cos [(\Omega + ) - (t)] - \cos [(\Omega - ) + (t)]) \\
 &= \frac{1}{2} \left[ \frac{1}{\Omega + } \sin [(\Omega + ) - (t)] - \frac{1}{\Omega - } \sin [(\Omega - ) + (t)] \right] \\
 &= \frac{1}{2} \left[ \frac{1}{\Omega + } [\sin(\Omega t) + \sin( t)] - \frac{1}{\Omega - } [\sin(\Omega t) - \sin( t)] \right] \\
 &= \frac{1}{2} \left[ \frac{(\Omega - \omega_i) [\sin(\Omega t) + \sin(\omega_i t)] - (\Omega + \omega_i) [\sin(\Omega t) - \sin(\omega_i t)]}{\Omega^2 - \omega_i^2} \right] \\
 + \frac{1}{2} \left[ \frac{\Omega \sin(\Omega t) + \Omega \sin( t) - \sin(\Omega t) - \sin( t) - \Omega \sin(\Omega t) + \Omega \sin( t) - \sin(\Omega t)}{\Omega} \right] \\
 &= \frac{1}{2} \left[ \frac{\Omega \sin( t) - \sin(\Omega t) + \Omega \sin( t) - \sin(\Omega t)}{\Omega^2 - \omega_i^2} \right] \frac{\Omega \sin( t) - \sin(\Omega t)}{\Omega - } \\
 &= \frac{\Omega}{-1} \frac{\sin( t) - \sin(\Omega t)}{1 - \frac{\Omega}{\Omega}} = \frac{1}{1 - \frac{\Omega}{\Omega}} \left[ \frac{1}{\Omega} \right] \sin(\Omega t) - \frac{\Omega}{\Omega} \sin( t)
 \end{aligned}$$

If the term  $\frac{1}{(1 - \frac{\Omega^2}{\Omega^2})} =$  (the magnification factor)

$$\sin \Omega' \sin (t - t) = - ( ) \sin(\Omega t) - \sin( t) \quad (A.32)$$

Subst. eq. (A.32) into eq. (A.31):

$$* \quad (A.33)$$

From eq. (A.10), we know that:

$$= \sum_{i=1}^{\infty} \left( \frac{1}{i^5} \right) \left[ \sin \sin(\Omega t) - \sin( t) \right]$$

$$= \text{_____}$$

Then:

$$* = \frac{2l^4 \Omega^2 y_1}{\pi^5 a^2} \sum_{i=1}^{\infty} \frac{\beta_i}{i^5} \sin \left( \frac{i\pi x}{l} \right) \left[ \sin(\Omega t) - \frac{\Omega^2}{i^2 \pi^2 a} \sin(\omega_i t) \right]$$

The first part of the previous equation represents steady-state forced vibrations of the beam, whereas the second part represents transient free vibrations.

Since transient vibrations disappear after a short time due to damping, for the steady and harmonic disturbing support motion we have:

$$y^* = \left[ \frac{2l^4 \Omega^2}{\pi^5 a^2} - \left( \frac{1}{\sin [ \sin(\Omega )] \right) \right]$$

And the total dynamic solution from eq. (p) and (n) is found as:

$$= - \sum - \left( \frac{1}{+ \sin [ \sin(\Omega )] \right)$$

It is important to point out that in the previous solution, damping was neglected. The effect of damping in the response is only important for impressed frequencies close to the natural frequency of each vibration mode where resonance takes place.

This total dynamic solution represents displacements measured from the static equilibrium position; therefore we can get the final response profile adding the static and dynamic profiles.

The static equilibrium profile is defined by the own weight of the beam element, from bending theory we have:

$$= -$$

And the moment due to the own weight of the beam is:

$$= - \frac{\quad}{2} + \frac{\quad}{2}$$

Equating the previous equations, and integrating twice with the corresponding boundary conditions, the static equilibrium profile is found as that of a simply supported beam:

$$= - \frac{\quad}{24} ( \quad + \quad - 2 \quad )$$

Adding the static equilibrium profile to the dynamic solution, we get the response profile:

$$(A.34) \quad = - \frac{\quad}{\quad} \sum_{i=1}^{\infty} \sin \left( \frac{\quad}{\quad} + \sum [ \quad ( \quad ) ] - \frac{\quad}{\quad} ( + \quad - 2 \quad ) \right)$$

### Damping estimation

The damping forces on vibrating beams are dissipation processes of the stored energy in the oscillation system, they can reduce or even prevent the oscillations, these forces are originated either from external interactions or internal effects.

External damping can be due to surrounding fluids and contacts, while internal effects are generally due to visco-elasticity and internal friction in the beam element.

The mathematical model representation of external damping as a simple viscous damping (proportional to velocity) can show that a damping factor diminishes at higher vibrational modes by  $(n^{-2})$ , while the model of internal damping (e.g. Kelvin-Voigt) shows that the damping factor increases quadratically  $(n^2)$  with the vibration mode.

Since the proposed experiments are intended to force an excitation below the first modes of vibration, a simple viscous model (proportional to velocity) can be analytically derived to estimate the damping in the system.

Adding the viscous term to eq. (A.1), we have:

$$\begin{aligned}
 \ddot{y} + \dot{y} + y &= 0 & (A.35) \\
 \ddot{y} + \dot{y} + y &= 0
 \end{aligned}$$

If we use the notation of eq. (A.23) and

$$2n = \dots \quad (A.36)$$

The convenience of using the notation of eq. (A.36), becomes evident in eq. (A.43) and their scenarios.

$$+ 2 \dots + \dots = 0 \quad (A.37)$$

Assuming a solution in the form of:

$$y(t) = e^{\dots t} \quad (A.38)$$

Subst. eq. (A.38) into eq. (A.37):

$$\begin{aligned}
 + 2 \dots + \dots &= 0 \\
 2 \dots + \dots &= 0 \\
 + \dots &= 0
 \end{aligned}$$

We try:

$$\begin{aligned}
 y(t) &= \\
 2 \dots + \dots &= 0
 \end{aligned}$$

$$\begin{aligned}
&= -\frac{r}{a^2} \left(1 + \frac{r}{r}\right) \\
&= \pm \frac{ir}{a} \sqrt{\left(1 + \frac{2n}{r}\right)}_2 \\
&\sqrt{\frac{ir^4}{a}} \sqrt{\left(1 + \frac{2n}{r}\right)} \quad , = \pm = \pm \\
\text{(A.39)} & \\
&\sqrt{\frac{ir^4}{a}} \sqrt{\left(1 + \frac{2n}{r}\right)} \\
& , = \pm = \pm \qquad \qquad \qquad \text{(A.40)}
\end{aligned}$$

In this way, we can express the general solution as in eq. (A.5) and solve for BC of the simple support beam to get the solution of eq. (A.8),  $kl=i^{\text{th}}\pi$ , then subst. into eq. (A.39) or (A.40):

$$\sqrt{\frac{ir^4}{a}} \sqrt{\left(1 + \frac{2n}{r}\right)} = \frac{i^{\text{th}}\pi}{l} \qquad \qquad \qquad \text{(A.41)}$$

$$ir \sqrt{\left(1 + \frac{2n}{r}\right)} = \left(\frac{i^{\text{th}}\pi}{l}\right)^2 \sqrt{\frac{EI}{m}} \qquad \qquad \qquad \text{(A.41)}$$

$$= \qquad \qquad \qquad \text{(A.42)}$$

Squaring left and right terms and arranging:

$$+ 2 \quad + \quad = 0$$

damping value of n.

$$= \frac{-2n \pm \sqrt{4n^2 - 4\omega_n^2}}{2} = - \quad \pm \quad - \qquad \qquad \qquad \text{(A.43)} \sqrt{\quad}$$

There are 3 possible scenarios for the roots (i.e.  $n < \omega_n$ ,  $n = \omega_n$  and  $n > \omega_n$ ), depending on the For the first scenario, where  $n < \omega_n$ , we can define a quantity

$$= \quad - \qquad \qquad \qquad \text{(A.44)}$$

And we obtain two complex roots as:

$$= - \quad +$$

$$= - \quad -$$

Substituting the roots in eq. (A.38):

$$x(t) = C_1 e^{(-n + i\omega_d)t} + C_2 e^{(-n - i\omega_d)t} = e^{-nt} [\cos(\omega_d t) + \dots]$$

$$x(t) = C_3 e^{(-n + i\omega_d)t} + C_4 e^{(-n - i\omega_d)t} = e^{-nt} [\cos(\omega_d t) - \dots]$$

The sum or difference of the previous solutions multiplied by any constant is also a solution, then:

$$x(t) = C_5 e^{-nt} [\cos(\omega_d t)]$$

$$x(t) = C_6 e^{-nt} [\sin(\omega_d t)]$$

The general solution of eq. (A.37) is obtained by addition of the previous solutions as:

$$x(t) = e^{-nt} [\cos(\omega_d t) + \sin(\omega_d t)] \tag{A.45}$$

This general solution is of the same form as that in eq. (A.19) for the undamped case, with two important differences:

- (a) The decay factor  $e^{-nt}$ , which decreases with time to damped out vibrations.
- (b) The angular frequency is  $\omega_d$  for damped vibrations, and is given by eq. (44) as:

$$\omega_d = \sqrt{\omega_n^2 - n^2} \tag{A.46}$$

So:

$$n = \sqrt{\omega_n^2 - \omega_d^2}$$

$$\frac{n}{\omega_n} = \sqrt{1 - \frac{\omega_d^2}{\omega_n^2}}$$

This first scenario for the root value in eq. A.43 represents the underdamped solution; in this way it can be shown that the third scenario represents an over damped solution.

The second scenario occurs when  $n = \omega_n$ , and it becomes relevant since we can get an special damping value from eq. (36), known as critical damping  $c_c = 2m\omega_n$ , and a damping ratio can be defined as:



$$\zeta = \frac{2mn}{w} = \frac{n}{w} = \sqrt{1 - \frac{\omega_d^2}{\omega^2}} \quad (2)$$

Then we can express:

$$= \frac{1}{\sqrt{1 - \zeta^2}} \quad (A.47)$$

$$= \frac{1}{\sqrt{1 - \zeta^2}} \quad (A.48)$$

The damping ratio can be obtained from experimental data analysis by the logarithmic decrement method.

Eq. (A.48) and the trigonometric relationship  $y(x)\cos(\omega_d t - \phi) = y(x)[\cos(\omega_d t)\cos(\phi) + \sin(\omega_d t)\sin(\phi)]$  can be used in eq. (A.45), for a phase form:

$$= (A) \cos(\omega_d t - \phi)$$

$$= (A) \cos(\omega_d t) \cos(\phi) + \sin(\omega_d t) \sin(\phi)$$

$$\sqrt{1 - \zeta^2} = \frac{1}{\sqrt{1 - \zeta^2}} \quad (A)$$

$$\tan(\phi) = \frac{\sin(\phi)}{\cos(\phi)} = \frac{\sin(\omega_d t)}{\cos(\omega_d t)}$$

$$y(t) = (A) e^{-\zeta \omega_n t} \cos(\omega_d t - \phi) \quad (A.49)$$

Eq. (A.45) or (A.49) represents a harmonic oscillation with exponential decay (with some amplitude as function of x at any point of the beam), then we can express two consecutive amplitudes with  $t_1=t$  and  $t_2=t+td$ , where  $td$  is the oscillation period ( $td=2\pi/\omega_d$ ), as:

$$y_1(t) = (A) e^{-\zeta \omega_n t} \cos[\omega_d t - \phi]$$

$$y_2(t) = (A) e^{-\zeta \omega_n (t+td)} \cos[\omega_d (t+td) - \phi]$$

Dividing  $y_1$  by  $y_2$ , we have:

$$\frac{y_1}{y_2} = \frac{y(x)e^{-\zeta \omega_n t} \cos[\omega_d t - \phi]}{y(x)e^{-\zeta \omega_n (t+td)} \cos[\omega_d (t+td) - \phi]}$$

Since the magnitude of the cosine term is the same after one period, these terms cancel each other, so we have:

$$\frac{A_2}{A_1} = e^{-\zeta \omega_n T} \quad (A.50)$$

Taken logarithms at both sides of the equation, the logarithmic decrement of two consecutive amplitudes in any exponential decay oscillation is given by the LHS as:

$$\ln \left( \frac{A_2}{A_1} \right) = -\zeta \omega_n T \quad (A.51)$$

And,

$$\ln \left( \frac{A_2}{A_1} \right) = -\zeta \omega_n T$$

Using eq. (47) we have:

$$\ln \left( \frac{A_2}{A_1} \right) = \frac{\zeta \omega_n 2\pi}{\sqrt{1 - \zeta^2}}$$

Arranging:

$$\zeta = \frac{\delta}{\sqrt{4\pi^2 + \delta^2}} \quad (A.52)$$

## A.2 Analysis of a partially submerged cantilever beam (section 3.2.1)

### Free vibration analysis (fig. 3.23 in section 3.2.2)

Free transversal vibrations occur when an initial perturbation is present in the system, from figure 3.23 the dynamic equilibrium condition for forces in the “y” direction (neglecting rotary inertia and shearing deformation) results the same as that analysed in Appendix A.1 to get the general solution as in equations A.5, so:

$$y(x,t) = [cosh(\lambda x)] + [sinh(\lambda x)] + [\cos(\omega t)] + [\sin(\omega t)] \quad (A.53)$$

$$y(x,t) = [sinh(\lambda x)] + [cosh(\lambda x)] - [\sin(\omega t)] + [\cos(\omega t)] \quad (A.54)$$

$$C_1 \cosh(\beta x) + C_2 \sinh(\beta x) - C_3 \cos(\beta x) - C_4 \sin(\beta x) \quad (\text{A.55})$$

$$C_1 \sinh(\beta x) + C_2 \cosh(\beta x) + C_3 \sin(\beta x) - C_4 \cos(\beta x) \quad (\text{A.56})$$

The boundary conditions for free vibration in the cantilever beam are:

$$w = 0 \quad \theta = 0 \quad (\text{a})$$

$$M = 0 \quad V = 0 \quad (\text{b})$$

$$w = 0 \quad \theta = 0 \quad (\text{c})$$

$$M = 0 \quad V = 0 \quad (\text{d})$$

Substituting BC (a) and (b) in eq. (A.53) and (A.54) respectively yields to  $C_1 = -C_3$  and  $C_2 = -C_4$ , with this results and BC (c) and (d) in eq. (A.55) and (A.56) respectively:

$$[\cosh(\beta L) + \cos(\beta L)] + [\sinh(\beta L) + \sin(\beta L)] = 0 \quad (\text{e})$$

$$[\sinh(\beta L) - \sin(\beta L)] + [\cosh(\beta L) + \cos(\beta L)] = 0 \quad (\text{f})$$

In matrix form:

$$\begin{bmatrix} \cosh(\beta L) + \cos(\beta L) & \sinh(\beta L) + \sin(\beta L) \\ \sinh(\beta L) - \sin(\beta L) & \cosh(\beta L) + \cos(\beta L) \end{bmatrix} \begin{bmatrix} C_1 \\ C_2 \end{bmatrix} = \begin{bmatrix} 0 \\ 0 \end{bmatrix}$$

For a non-trivial solution, the determinant of the first matrix must be = 0

$$[\cosh(\beta L) + \cos(\beta L)][\cosh(\beta L) + \cos(\beta L)] - [\sinh(\beta L) + \sin(\beta L)][\sinh(\beta L) - \sin(\beta L)] = 0$$

$$\cosh^2(\beta L) + 2 \cosh(\beta L) \cos(\beta L) + \cos^2(\beta L) - \sinh^2(\beta L) - \sin^2(\beta L) = 0$$

Since  $\sin^2 + \cos^2 = 1$  and  $\cosh^2 - \sinh^2 = 1$ , then:

$$\cosh(\beta L) \cos(\beta L) = -1 \quad (\text{A.57})$$

Eq. A.57 represents a transcendental function, i.e. there is no algebraic solution. The roots can be found by the Newton-Raphson numerical method or any other root finding methods, the first 4 roots are  $kl = (1.875, 4.694, 7.855, 10.996)$

Setting the root values of  $kl=\lambda_i$ ,  $k=\lambda_i/L$  and from eq. A.2 and A.3, we have:

$$\frac{\lambda_i}{L} = \sqrt{\frac{\omega}{a}}$$

$$\frac{\lambda_i^2}{\sqrt{EI}} = \quad (A.58)$$

So, the natural frequencies (in hertz) are:

$$(A.59)$$

Solving for the mode shapes, from eq. A.53:

$$(\ ) = [\cosh(\ )] + [\sinh(\ )] + [\cos(\ )] + [\sin(\ )]$$

It was determined from BC that  $C1 = -C3$  and  $C2 = -C4$ , then:

$$(\ ) = [\cosh(\ )] + [\sinh(\ )] - [\cos(\ )] - [\sin(\ )]$$

$$(\ ) = [\cosh(\ ) - \cos(\ )] + [\sinh(\ ) - \sin(\ )]$$

$$= \frac{\lambda_i^2}{\sqrt{EI}}$$

From eq. (e) we have:

$$= - \frac{\cosh(kl) + \cos(kl)}{\sinh(kl) + \sin(kl)}$$

Doing the term:

$$\frac{\cosh(kl) + \cos(kl)}{\sinh(kl) + \sin(kl)} =$$

Since  $kl = \lambda_i$ , the equation for the mode shapes can be written as:

$$y(x) = C_1 (\cosh \lambda_i x - \cos \lambda_i x) + C_2 (\sin \lambda_i x - \sinh \lambda_i x) \quad (A.60)$$

Setting arbitrary values for the constants C1 and L, say C1 = 1 and L = 10, the mode shapes can be plotted for each root value  $\lambda_i$ :

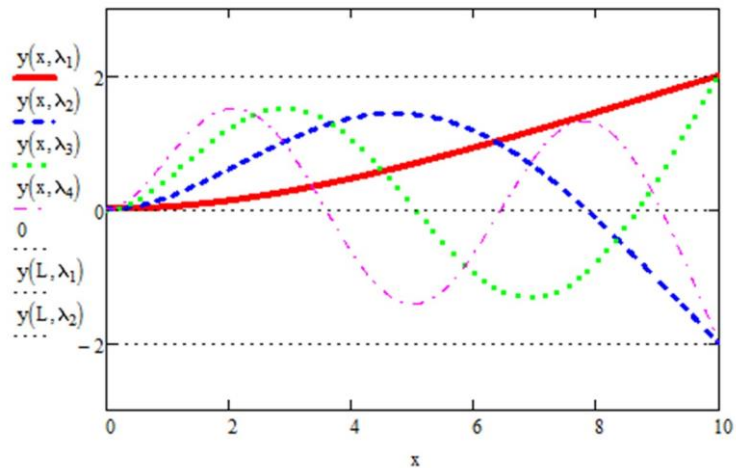


**Figure A.1 Mode shapes for free vibrations of a cantilever beam**

The plot of eq. A.60 in fig. A.1 shows that the constant C1 represents the half of the maximum vibration amplitude at the free end of the mode shapes for free transversal vibrations ( $C1 = 1/2 A_{max}$ ).

In the proposed experiment, the cantilever beam will be in vertical position with the fixed end at the top and partially submerged with a plug at the bottom, which will be tested for a range of towing speeds.

Drag and lift forces are expected to be induced by the fluid flow around the submerged section of the tube which can let to some form of oscillatory response of the cantilever.

It is also expected a decrease of the natural frequencies of the cantilever beam, once this has been mounted in the partially submerged condition in still water, due to the added mass effect (added inertia of the fluid around the submerged section), thus the mass along the beam cannot be considered constant.

The natural frequency "in vacuum" of the fundamental mode for the geometric and material properties can be estimated from eq. A.59.

### Rayleigh's method

For the partially submerged condition of the cantilever in still water, the fundamental frequency can be estimated for the simplified model by Rayleigh's energy method.

Rayleigh's method approximates the fundamental frequency by equating the kinetic and potential energies of a vibrating beam (better approximations and higher modes can be estimated by the Ritz method, which is a further development of the Rayleigh's method).

The kinetic energy ( $1/2mv^2$ ) is integrated over the length of the beam as:

$$= \frac{1}{2} \int_0^L \rho A \dot{w}^2 dx$$

It was shown that a solution of the form:  $w(x,t) = W(x)e^{i(\omega t - kx)}$ , satisfies the governing eq. A.5, thus:

$$-EI \frac{d^4 W}{dx^4} = \rho A \omega^2 W = \rho A [\cos(kx) + i \sin(kx)]$$

Maximum velocities can be found when  $t = (n-0.5)\pi/\omega$ :

$$-EI \frac{d^4 W}{dx^4} = \rho A [0 + i(\pm 1)] = \pm \rho A$$

Thus,

$$= - \frac{1}{2} \int_0^L \left( \frac{d^2 w}{dx^2} \right)^2 dx \quad (A.61)$$

The maximum potential energy is that of the flexural strain energy in a beam, which is determined by the strain energy density in a volume  $= V$ , where the strain energy density is  $= u$ .

From Young's modulus,  $E$ , then  $\epsilon = \frac{\sigma}{E}$ ; also, for bending stress  $\sigma = E y \kappa$  and from bending theory  $\kappa = \frac{d^2 w}{dx^2}$ , then  $\sigma = E y \frac{d^2 w}{dx^2}$ , so  $\epsilon = y \frac{d^2 w}{dx^2}$ .

Then,  $u = \frac{1}{2} \sigma \epsilon = \frac{1}{2} E y^2 \left( \frac{d^2 w}{dx^2} \right)^2$ .

Hence, the maximum potential energy in a beam is:

$$= - \frac{1}{2} \int_0^L E y^2 \left( \frac{d^2 w}{dx^2} \right)^2 dx \quad (A.62)$$

Equating eq. A.61 and A.62, and solving for the frequency:

$$= \frac{(\dots)}{\dots} \quad (A.63)$$

### A.3 Analysis of a tensioned free-free beam (section 3.3.2)

#### Free vibration analysis (fig. 3.45)

For the response of the riser prototype in a horizontal towing test, it seems reasonable to assume small angle deflections ( $\theta$  is assumed small), then  $\cos\theta \approx 1$  and  $\sin\theta \approx \theta$ ; since  $dy/dx = \tan\theta$ ,  $dy/dx = \sin\theta/\cos\theta \approx \sin\theta \approx \theta$ , so  $\theta$  can be approximated as  $\theta \approx dy/dx$ , thus:

$$\frac{dy}{dx} = \theta$$

$$+ \frac{d^2y}{dx^2} = \frac{d\theta}{dx} = \frac{d^2y}{dx^2}$$

Then, the force component in fig. 3.45

$$+ \frac{d^2y}{dx^2} = \frac{d^2y}{dx^2} \left( \frac{dy}{dx} \right)^2 = \frac{d^2y}{dx^2} \theta^2$$

$$- \frac{d^2y}{dx^2} + \frac{d^2y}{dx^2} \theta^2 + \left( \frac{dy}{dx} \right)^2 = \frac{d^2y}{dx^2} \theta^2$$

$$- \frac{d^2y}{dx^2} \left( T \frac{dy}{dx} \right)^2 = \frac{d^2y}{dx^2} \theta^2$$

With the previous approximations, the dynamic equilibrium condition for forces in the "y" direction of fig. 3.45 can be written as:

$$- \frac{d^2y}{dx^2} + \frac{d^2y}{dx^2} \theta^2 + \left( \frac{dy}{dx} \right)^2 = 0$$

$$- \frac{d^2y}{dx^2} - \frac{d^2y}{dx^2} \theta^2 + \left( T \frac{dy}{dx} \right)^2 = 0$$

$$- \frac{d^2y}{dx^2} - \frac{d^2y}{dx^2} \theta^2 + \frac{d^2y}{dx^2} = 0$$

The moment equilibrium condition gives:

$$+ \frac{d^2y}{dx^2} - \frac{d^2y}{dx^2} - \frac{d^2y}{dx^2} = 0$$



Neglecting higher order terms:

$$\dots =$$

$$\dots = \dots$$

From bending theory we have

$$=$$

Then, the governing equation for free vibration of the beam is:

$$\dots - (T \dots) \dots - + \dots = 0$$

If the tension is considered constant:

$$\dots - \dots + \dots = 0 \tag{A.64}$$

Assuming a solution of the form:  $y(x) = e^{\lambda x}$ , subst. into (A.64):

$$\dots - \dots = 0$$

$$\dots - \dots = 0$$

We try:  $y(x) = e^{\lambda x}$ , then:

$$\lambda^4 - \frac{T}{EI} \lambda^2 - \frac{m\omega^2}{EI} = 0$$

$$= \frac{T}{2EI} + \sqrt{\left(\frac{T}{2EI}\right)^2 + \frac{m\omega^2}{EI}}$$

$$\lambda = \pm \sqrt{\frac{T}{2EI} + \sqrt{\left(\frac{T}{2EI}\right)^2 + \frac{m\omega^2}{EI}}} = \pm \tag{A.65}$$

$$= -\frac{T}{2EI} \pm \sqrt{\left(\frac{T}{2EI}\right)^2 + \frac{m\omega^2}{EI}}$$

$$, = \pm \sqrt{\sqrt{\left(\frac{T}{2EI}\right)^2 + \frac{m\omega^2}{EI}} - \frac{T}{2EI}} = \pm \tag{A.66}$$

If the term

$$- = \tag{A.67}$$

and

$$\tag{A.68}$$

We can write eq. (A.65) and (A.66) as:

$$- =$$

$$= \frac{A^2}{2} + \sqrt{\frac{A^4}{4} + B^4} \tag{A.69}$$

$$= -\frac{A^2}{2} + \sqrt{\frac{A^4}{4} + B^4} \tag{A.69}$$

$$\tag{A.70}$$

Useful relationships are derived as follows:

From eq. (A.69):

$$= - \tag{A.71}$$

From eq. (A.70):

$$= + \tag{A.72}$$

Multiplying eq. (A.69) and (A.70):

$$= \tag{A.73}$$

Subtracting eq. (A.70) to (A.69):

$$= + \tag{A.74}$$

The general solution therefore is:

$$() = + + +$$

But

$$\pm = \cosh( ) \pm \sinh( )$$

$$\pm = \cos( ) \pm i \sin( )$$

So,

$$() = [\cosh( ) + \sinh( + )] + [\cosh( ) - \sinh( )] + [\cos( ) + i \sin( )]$$

$$() = ( + )[\cosh( )] + ( - )[\sinh( )] + ( - )[\sin( )] = 0$$

$$() = [\cosh( )] + [\sinh( )] + [\cos( )] +$$

And

$$= [\sinh( )] + [\cosh( )] - [\sin( )] +$$

$$= [\cosh( )] + [\sinh( )] - [\cos( -$$

$$= [\sinh( )] + [\cosh( )] + [\sin( = 0$$

The boundary conditions for a free-free tensioned beam are:

$$= 0$$

$$= 0$$

$$= 0$$

Substituting BC (a) in eq. (A.77):

$$+ \dots) [\cos(\dots)] + (\dots) \quad (d)$$

$$[\sin(\dots)] \quad (A.75)$$

(a) (b)

$$[\cos(\dots)] \quad (A.76) \quad (c)$$

$$\dots) - [\sin(\dots)] \quad (A.77) \quad - \dots = 0$$

$$\dots) - [\cos(\dots)] \quad (A.78) \quad - \dots \quad (A.79)$$

Substituting BC (c) and eq. (A.67) in eq. (A.78) and (A.76):

$$- \dots - [ \dots + \dots ] = 0$$

$$+ \dots$$


---


$$-$$

Using eq. (A.71) and (A.72):

$$- \dots \quad (A.80)$$

Substituting BC (b), eq. (A.79) and (A.80) in eq. (A.77):

$$- [\cosh(\dots)] + - [\sinh(\dots)] - [\cos(\dots)] - [\sin(\dots)] = 0$$

$$[\cosh(\dots) - \cos(\dots)] + - \sinh(jl) - \sin(\dots) = 0$$

$$[\cosh(\dots) - \cos(\dots)] + - \sinh(jl) - \sin(\dots) = 0 \quad (A.81)$$

Substituting BC (d), eq. (A.67), (A.79) and (A.80) in eq. (A.78) and (A.766):

---


$$- [\sinh(\dots)] + - [\cosh(\dots)] + [\sin(\dots)] - [\cos(\dots)]$$

$$\begin{aligned}
 & - \frac{1}{h} [\sinh(\beta)] + \frac{1}{h} [\cosh(\beta)] - \frac{1}{h} [\sin(\beta)] + \frac{1}{h} [\cos(\beta)] = 0 \\
 & \frac{1}{h} (-\beta) \sinh(\beta) + \frac{1}{h} (\beta) \sin(\beta) \\
 & + \frac{1}{h} (-\beta) \cosh(\beta) - \frac{1}{h} (\beta) \cos(\beta) = 0
 \end{aligned}$$

Using eq. (A.71) and (A.72):

$$\begin{aligned}
 & \frac{1}{h} \left[ \frac{1}{h} \sinh(\beta) + \sin(\beta) \right] + \frac{1}{h} [\cosh(\beta) - \cos(\beta)] = 0 \\
 & \frac{1}{h} \sinh(\beta) + \sin(\beta) + [\cosh(\beta) - \cos(\beta)] = 0 \quad (A.82)
 \end{aligned}$$

Arranging eq. (A.81) and (A.82) in matrix form:

$$\begin{aligned}
 & \cosh(\beta) - \cos(\beta) \quad \frac{1}{h} \sinh(\beta) - \sin(\beta) \\
 & \hspace{15em} = 0 \\
 & \frac{1}{h} \sinh(\beta) + \sin(\beta) \quad \cosh(\beta) - \cos(\beta) \\
 & \hspace{15em} = 0
 \end{aligned}$$

For a non-trivial solution, the determinant of the first matrix must be = 0

$$\begin{aligned}
 & h(\beta) - 2 \cosh(\beta) \cos(\beta) + \beta^2 \\
 & - h(\beta) + \frac{1}{h} \sinh(\beta) \sin(\beta) - \frac{1}{h} \sinh(\beta) \sin(\beta) - \beta^2 = 0
 \end{aligned}$$

Since  $\cosh^2 - \sinh^2 = 1$  and  $\sin^2 + \cos^2 = 1$ ,

$$2[1 - \cosh(\beta) \cos(\beta)] + \frac{1}{h} \sinh(\beta) \sin(\beta) = 0$$

Using eq. (A.73), the characteristic equation is found as:

$$2 [1 - \cosh(\lambda) \cos(\lambda)] + (\lambda^2 - k^2) \sinh(\lambda) \sin(\lambda) = 0 \quad (\text{A.83})$$

We can rewrite eq. (A.83) using eq. (A.74) to find  $k$  roots, as:

$$\begin{aligned} & \sqrt{A^2 + 2k^2} \cosh(\lambda) - k^2 \cos(\lambda) \\ + & \left( -\sqrt{A^2 + 2k^2} \sinh(\lambda) + \sqrt{A^2 + k^2} \sin(\lambda) \right) = 0 \end{aligned} \quad (\text{A.84})$$

$B^4$  can then be found with eq. (A.72) to solve for the frequency of vibration from eq. (A.68) as:

$$B_i^2 = \sqrt{\frac{EI}{k^3}} \quad (\text{A.85})$$

Using eq. (A.79) and (A.80), the mode shape equation (A.75) can be expressed as:

$$y(x) = C_1 [\cosh(\lambda x)] + C_2 [\sinh(\lambda x)] + C_3 [\cos(\lambda x)] + C_4 [\sin(\lambda x)]$$

From eq. (A.81):

$$= - \frac{[k^3 \sinh(jl) - \sin(kl)]}{[\cosh(\lambda) - \cos(\lambda)]}$$

If

$$= - \frac{-\sinh(\lambda) \cos(\lambda)}{[\cosh(\lambda) - \cos(\lambda)]} \quad (\text{A.86})$$

Then:

$$y(x) = C_1 \cosh(\lambda x) + C_2 \cos(\lambda x) + C_3 \sinh(\lambda x) + C_4 \sin(\lambda x)$$

$$y(x) = E \cosh(\lambda x) - \sinh(\lambda x) + \cos(\lambda x) + \sin(\lambda x) \quad (\text{A.87})$$